UNIVERSITÉ DU LUXEMBOURG

PhD-FSTC-2012-03
The Faculty of Sciences, Technology and Communication

DISSERTATION

Defense held on 19/01/2012 in Luxembourg

to obtain the degree of

DOCTEUR DE L'UNIVERSITÉ DU LUXEMBOURG

EN PHYSIQUE

by

Dominik Matthias BERG
Born on 02 December 1981 in Wadern (Germany)

KESTERITE EQUILIBRIUM REACTION AND THE DISCRIMINATION OF SECONDARY PHASES FROM Cu_2ZnSnS_4

Dissertation defense committee

Dr. Phillip Dale, Dissertation supervisor
Université du Luxembourg

Prof. Dr. Susanne Siebentritt, Vice chairman
Professor, Université du Luxembourg

Prof. Dr. Laurence Peter
Professor, University of Bath

Prof. Dr. Susan Schorr
Professor, Helmholtz Zentrum Berlin

Prof. Dr. Roland Sanctuary, Chairman
Professor, Université du Luxembourg

Table of contents

Acknowledgements

First and foremost, I thank my supervisors, Susanne Siebentritt and Phillip Dale, for giving me the opportunity to do my Ph.D. in Luxembourg. Susanne and Phil, thank you both very much for your guidance, your help and enthusiasm, all the very fruitful discussions, your endless pool of ideas, and for your advice and patience.

Furthermore, I would like to thank Laurence Peter for being part of my CET committee, as well as Susan Schorr and Roland Sanctuary for being part in the jury.

I would like to thank all members of the LPV team, past and present, for being excellent company as well as for their great help, support, and teamwork throughout the past years. Especially, I am very grateful to:

- Thomas Schuler for all his help inside and outside the lab
- Danielle Schoder and Patricia Ramoa for taking care of all the small organizational things
- Alex Redinger for his advice and support with the panning of experiments, for all the helpful discussions, and for proof reading
- Johannes Fischer for his great teamwork and his help with the various experimental issues
- Monika Arasimowicz for her last minute help with some measurements
- David Regesch for his help with analyzing some PL data
- Katja Hönes and Rabie Djemour for collaboration with PL and Raman measurements
- Yasuhiro Aida for performing CdS depositions
- Levent Gütay and Marc Steichen for proof reading
- Vicente Reis-Adonis for fabricating the various electrodeposition and annealing tools

Furthermore, I am very thankful to Guillaume Zoppi of the University of Northumbria, Newcastle, for all his work to provide me with enough molybdenum substrates throughout the past years.

I am very grateful to Susan Schorr and Christiane Stephan from the Helmholtz Zentrum Berlin for allowing me to use their equipment for some XRD measurements as well as for introducing and helping me to and with Rietveld refinement analysis.

Also, I am very grateful to Alejandro Pérez-Rodriguez and his group from the University of Barcelona for performing Raman measurements and for answering all my questions patiently.

I would like to thank Jonathan Scragg from the University of Uppsala, Sweden, for all the fruitful discussions.

I am thankful to Lili Deligianni and Shafaat Ahmed from the IBM T.J. Watson Research Center in New York for providing me with some very uniform electrodeposited precursors.

I thank Michael Kirsch from the Helmholtz Zentrum Berlin for depositing the ZnO layers as well as the front contact onto my absorber layers.

Furthermore, I am very thankful to Jean-Christophe Lambrecht, Jérôme Guillot, Thierry Girot, Johanna Ziebel, and all other members of the CRP Gabriel Lippmann that helped me with the various analytical tools.

I thank all my friends (you all know who I am talking about) for their great support throughout the tough times, especially my girlfriend for being so positive, supportive, and helpful!

Zu guter Letzt möchte ich mich herzlichst bei meiner ganzen Familie, speziell bei meinen Eltern sowie meinem Bruder, für Ihre vielfältige Unterstützung in den letzten Jahren bedanken.

Herzlichen Dank!

Work done in conjunction with others

All the work presented in this thesis was carried out by the author, with the following exceptions:

1. The Auger electron spectroscopy measurements were performed by Jérôme Guillot and co-workers from the “CRP Gabriel Lippmann” in Belvaux, Luxembourg.
2. The inductively coupled plasma mass spectroscopy measurements were performed by Johanna Ziebel from the “CRP Gabriel Lippmann” in Belvaux, Luxembourg.
3. Raman spectroscopy measurements were partly performed by Prof. Dr. Pérez-Rodriguez and co-workers from the University of Barcelona, and partly by Rabie Djemour from the Laboratory for Photovoltaics of the University of Luxembourg.
4. Photoluminescence measurements were performed by Dr. Katja Hönes and Rabie Djemour from the Laboratory for Photovoltaics of the University of Luxembourg.
5. Preparation of two precursors containing Cu, Zn, Sn, and Se by vapour deposition for the study presented in section 5.10.1 was performed by Dr. Alex Redinger from the Laboratory for Photovoltaics of University of Luxembourg.
6. Preparation of some precursors containing Cu, Zn, and Sn for the study shown in section 5.10.2 was performed by the group of Dr. Lili Deligianni from the IBM T.J. Watson Research Center in New York.
7. Deposition of the ZnO window layers to finalize solar cell devices were performed by Michael Kirsch from the “Helmholtz Zentrum Berlin”.
8. Deposition of the CdS layer were performed together with Yasuhiro Aida, guest-researcher from TDK, Japan.

The evaluation of all the results was carried out by the author.

List of abbreviations

AAS	**A**tomic **a**bsorption **s**pectroscopy
AES	**A**uger **e**lectron **s**pectroscopy
ALD	**A**tomic **l**ayer **d**eposition
BSE	**B**ack-**s**cattered **e**lectrons
CB	**C**onduction **b**and
CE	**C**ounter **e**lectrode
CTS	**C**u_2Sn**S**$_3$
CV	**C**yclic **v**oltammogram
CZTS	**C**u_2**Z**nSn**S**$_4$
CZTSSe	**C**u_2**Z**nSn(**S/Se**)$_4$
DIW	**D**e-**i**onized **w**ater
EC-ALE	**E**lectro**c**hemical **a**tomic **l**ayer **e**pitaxy
ED	**E**lectro**d**eposition
EDA	**E**lectro**d**eposition and **a**nnealing
EDX	**E**nergy-**d**ispersive **X**-ray spectroscopy
EQE	**E**xternal **q**uantum **e**fficiency
FF	**F**ill **f**actor
FWHM	**F**ull **w**idth of **h**alf **m**aximum
GIXRD	**G**razing **i**ncidence **X**-**r**ay **d**iffraction
HER	**H**ydrogen **e**volution **r**eaction
ICP-MS	**I**nductively **c**oupled **p**lasma **m**ass **s**pectroscopy
IV	Current-voltage characteristics
KCN	Potassium cyanide
NHE	**N**ormal **h**ydrogen **e**lectrode
OCP	**O**pen **c**ircuit **p**otential
PL	**P**hoto**l**uminescence
PV	**P**hoto**v**oltaics
PVD	**P**hysical **v**apour **d**eposition
QE	**Q**uantum **e**fficiency
RDE	**R**otating **d**isc **e**lectrode
RPM	**R**otations **p**er **m**inute
RE	**R**eference **e**lectrode
RR	**R**esonant **R**aman
RTP	**R**apid **t**hermal **p**rocesser
SE	**S**econdary **e**lectrons
SEL	**S**tacked **e**lemental **l**ayer
SEM	**S**canning **e**lectron **m**icroscopy
SIMS	**S**econdary **i**ons **m**ass **s**pectrometry
SR	**S**pectral **r**esponse
VB	**V**alence **b**and
WDX	**W**avelength-**d**ispersive **X**-ray spectroscopy
WE	**W**orking **e**lectrode
XRD	**X**-**r**ay **d**iffraction

List of symbols

Chapter 1

(in order of appearance)

Symbol	Quantity
α	Absorption coefficient

Chapter 2

(in order of appearance)

Symbol	Quantity
ρ	Density
z	Depth
Z	Atomic number
λ	Wavelength
Θ	Angle
d_{hkl}	Lattice spacing
α	Grazing angle
F_{hkl}	Structure factor
f_n	Form factor
x, y, z	Cartesian coordinates
A_{abs}	Absorption factor
Θ_c	Critical angle
$Y_{i,obs}$	Observed XRD data
$Y_{i,cal}$	Calculated XRD data
W_i	Statistical weight
c_s	Overall scale factor
R_B	Bragg factor
$\hbar$	Planck constant (over 2π)
$\omega_{i,s}$	Frequency of incident/scattered light
$\|0\rangle$	Ground state
$\|e\rangle, \|e'\rangle$	Excited states
$E_{e,e'}$	Energy of excited states
Ω	Phonon frequency
$\omega(cm^{-1})$	Raman shift
$I_{i,s}$	Intensity of incident/scattered light
$\vec{E}(\omega_{i,s})$	Electric field of incident/scattered light
V_{vol}	Scattering volume
$e_{i,s}$	Polarization unit vector of incident/scattered light
$\tilde{\chi}_{\alpha,\beta}$	Generalized susceptibility tensor in direction α, β
$p_{\alpha,\beta}$	Dipole operators in direction α, β
$H_{E\text{-}L}$	Electron-phonon interaction Hamiltonian
Y_{PL}	Photon flux
c	Speed of light
$a(E)$	Absorptivity
E	Energy
$\Delta\mu$	Quasi Fermi level splitting
k_B	Boltzmann constant
T	Temperature

R_f	Surface reflectivity
d	Layer thickness
α_{abs}	Absorption coefficient
E_{kin}	Kinetic energy
E_{high}	Energy of higher shell
E_{low}	Energy of lower shell
E_{bind}	Binging energy
η_{eff}	Power conversion efficiency
P_{ill}	Power of illumination
V	Voltage
I	Current
I_{sc}	Short circuit current
V_{oc}	Open circuit potential
P_{out}	Output power
P_{max}	Maximum power
I_{max}	Current of maximum power
V_{max}	Voltage of maximum power
FF	Fill factor
R_s	Serial resistance
R_{sh}	Shunt resistance
QE	Quantum efficiency
EQE	External quantum efficiency
W	Width of space charge region
L_n	Diffusion length of space charge region
E_G	Band gap
A	Constant
$h\nu$	Photon energy

Chapter 3
(in order of appearance)

Symbol	**Quantity**
$e\phi_M$	Work function of the metal
$\overline{\mu}$	Electrochemical potential
μ	Chemical potential
$\frac{dn}{dt}$	Rate of growth/stripping
J	Current density
q	Charge of deposited ion
F	Faraday constant
V	Potential
E_M^0	Standard reduction potential
E_M	Reduction potential
R	Molar gas constant
T	Temperature
a	Concentration/activity
E	Potential value
η	Overpotential
J_0	Current at interface

α	Reversibility
D	Diffusion coefficient
t	Time
$\left[M^{q+}\right]$	Initial concentration of reducible species
ω	Angular velocity
ν	Kinematic velocity
Q_{tot}	Total charge
Q_M	Deposited charge of metal
Q_{H2}	Charge due to hydrogen evolution
φ_M	Plating efficiency
Q_{dep}	Deposited charge
Q_{strip}	Stripped charge
m_{ICPMS}	Mass measured with ICP-MS
m_{calc}	Mass calculated from the deposited charge

Chapter 4

(in order of appearance)

Symbol	Quantity
α	Absorption coefficient
E_G	Band gap
a, b, c	Lattice parameter (directions)
α, β, γ	Lattice parameter (angles)
G	Gibbs free energy
ΔG	Change in gibbs free energy
H	Enthalpy
ΔH	Change in enthalpy
T	Temperature
S	Entropy
ΔS	Change in entropy
p	Pressure
V	Volume
$\Delta G^0_{f,298}$	Standard Gibbs free energy of formation
Q	Reaction quotient
a_x	Activity
K_{eqm}	Equilibrium constant
R	Gas constant
$[A]$	Concentration of compound A
p_x	Partial pressure of reactant X
B_{ov}	Overall temperature coefficient
$B_{iso,X}$	Temperature coefficient for element X
B	Temperature coefficient
Pref1/Pref2	Texture factors
R_{Bragg}	Bragg factor (quality coefficient)
d	Layer thickness
$a(E)$	Absorptivity
FWHM	Full width of half maximum
V_{OC}	Open circuit voltage
J_{SC}	Short circuit current density

FF	Fill factor
η	Power conversion efficiency
R_{sh}	Shunt resistance
R_s	Series resistance
A	Area
EQE	External quantum efficiency
$J_{SC;gridcorrected}$	Grid corrected short circuit current density
$J_{SC;EQEeff}$	Short circuit current density obtained from the effect. EQE

Chapter 5

(in order of appearance)

Symbol	**Quantity**
T	Temperature
$\Delta G^0_{f,298}$	Standard Gibbs free energy of formation
R	Gas constant
K_{eqm}	Equilibrium constant
p_x	Partial pressure of reactant X
η_{eff}	Power conversion efficiency
J_{sc}	Short circuit current density
V_{oc}	Open circuit potential
FF	Fill factor

1 Introduction

As the Earth's population exceeds the seven-billion-people marker [1], the steady growth in energy consumption is one of the big challenges of the present time. The fact that fossile energy sources are finite, and due to increasing concerns about the cause and effect of climate change, the sector of renewable energies, including that of photovoltaics (PV), is gaining increasingly greater influence in the energy generation sector. At present, the solar cell market is dominated by silicon based devices, but due to the high cost of purification of silicon and due to the high material necessities, low cost alternatives are being investigated. Hereby, so called "compound thin film" materials, such as $Cu(In,Ga)Se_2$ (CIGS) and CdTe, have proven to be alternatives for silicon based devices. This is resulting in a steady increase of the PV market share of this "compound thin film" sector over the past few years. The power conversion efficiency record for CIGS devices has recently exceeded 20 % at laboratory scale while the record for module efficiencies currently lies at 15.7 % [2]. The former value is comparable to those obtained from polycrystalline silicon solar cells. The success of CIGS and CdTe based thin films is only reduced by the fact that they contain less abundant materials, such as In, Se, Cd, and Te, as can be seen in Figure 1-1. The cost and availability of indium in particular is an issue of concern, as its use in flat screens led to an increase of the market price by a factor of ten between the years 2002 and 2006 [3]. Anticipating an additional increase in the production of CIGS modules would lead to an even stronger increase in the material cost for indium.

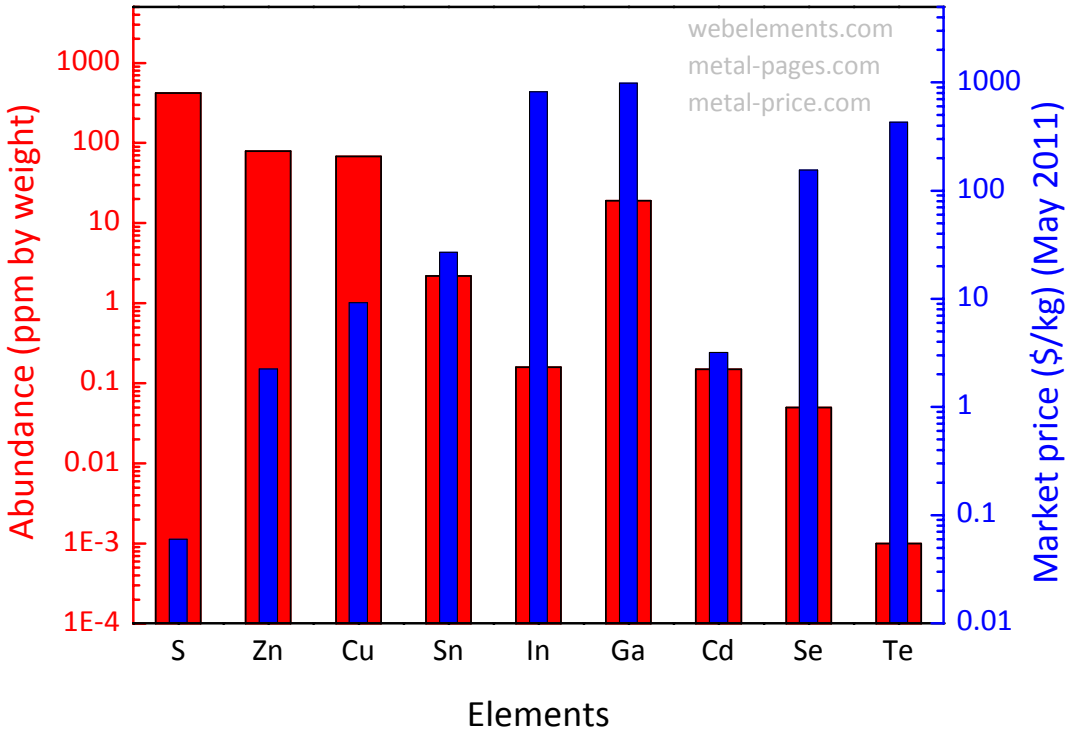

Figure 1-1 Abundance in the Earth's crust and market price (May 2011) of elements used for CZTS, CIGS, and CdTe thin films, according to given web pages as seen in the Figure.

As a possible alternative to those compound thin films, $Cu_2ZnSn(S,Se)_4$ (CZTSSe) has been suggested, as it only contains mostly abundant and cheap materials. Hereby, the substitution of In and Ga (from the CIGS compound) with Zn and Sn is expected to lead to a compound with similar properties. Already in 1988, Ito and Nakazawa recognized the potential of this compound for photovoltaic applications [4]. In various other publications, the p-type

conductivity, a high absorption coefficient of $\alpha > 10^4 cm^{-1}$, and its band gap of between 1.0 and 1.5 eV for a pure selenium CZTSe and a pure sulfur CZTS have been reported, respectively [5-11]. All these properties lie within the optimal range for solar energy conversion [12]. In the past two decades, major improvements in device efficiency for pure sulfur CZTS has been made by Katagiri et al., who reported a 6.8 % efficient device from a co-sputtered process followed by an annealing step [13]. Since then, further improvements, especially on the mixed sulfur-selenide $Cu_2ZnSn(S,Se)_4$ (CZTSSe) obtained from various different techniques have been made. At the present time, the record device reaches a power conversion efficiency of 10.1 %, as shown by IBM, indicating great potential of CZTSSe as an alternative for the known thin film solar cells [14].

Despite those good results, there are several challenges that researchers need to face in order to grow high quality CZTSSe thin films. As it is pointed out in more detail in chapter 4, it appears to be extremely difficult to grow single phase $Cu_2ZnSn(S,Se)_4$, as the existence region of single phase CZTS was reported to be fairly small [15]. As a result, the un-desired formation of secondary phases of the Cu-Zn-Sn-S/Se system is seemingly inevitable. Connected to this issue, the challenge of identification of the possible secondary phases, as well as their discrimination from the CZTS phase, exhibits another major concern of the present CZTS research. Besides those two, there are many other challenges, such as the choice of the right buffer and window layers, etc., which are not in the focus of this work.

The objective of the present work is twofold and closely connected to the two mentioned challenges in CZTS research: One focus was set to find the right tool that can be used to identify secondary phases of the Cu-Zn-Sn-S system and to discern them from Cu_2ZnSnS_4 (chapter 4), and the second focus was set to find a way to grow absorber layers for high quality CZTS thin film solar cells by avoiding secondary phases (at the surface of the absorber) (chapter 5).

In order to study both of those questions, the samples were typically prepared by a two-stage electrodeposition and annealing (EDA) approach. Electrodeposition (ED) is a widespread technique for fabricating metallic thin films and it has already been used successfully in the fabrication of CIGS thin films, producing devices with efficiencies above 12 % [16]. The advantage of ED is the relatively low equipment cost and energy consumption, the relatively efficient material utilization, its ability to be used at ambient temperatures, and that it is relatively easy to upscale.

Besides the “Introduction” and “Conclusion” chapters, this report is structured into four chapters. Chapter 2 discusses all techniques used to analyze the prepared samples. The emphasis is to explain why the respective measurement conditions/settings are used. In chapter 3, the uniform electrodeposition of the precursors is discussed. Chapter 4 deals with the question how to identify secondary phases of the Cu-Zn-Sn-S system and how to discern them from CZTS. In chapter 5, a novel annealing strategy is introduced that is based on the reversibility of the CZTS decay reaction (“equilibrium reaction”). It is shown that as a consequence of this “equilibrium reaction”, secondary phases at the absorber’s surface can be avoided and solar cell performance can be improved. Furthermore, a novel approach to form CZTS is introduced and examined.

Every experimental chapter itself is structured in “Goal”, “Background”, “Experiment”, “Results and Discussion”, and “Conclusion” sections. At the end of the thesis (chapter 6), a general conclusion as well as recommendations for future work are given.

2 Fabrication and characterization techniques

This chapter briefly introduces the techniques used for the fabrication and characterization of the samples that have been prepared in conjunction with this work. It covers the basic principles of each technique, shortly explains approaches to measure the data, lists the used settings, and briefly discusses important issues of the techniques with respect to the analysis of thin film semiconductors.

This chapter shall only provide a brief overview. References to more detailed literature will be given in the corresponding sections.

2.1 Physical vapour deposition of admixed precursors

Physical vapour deposition (PVD) processes are commonly used techniques to deposit thin films of a few nanometer to a few micrometer thickness. The materials to be deposited are vapourized from a solid or liquid source in the form of atoms or molecules and transported in the form of a vapour through a low pressure environment to the substrate, where they condense and form a layer [17].

The samples of the study shown in section 5.10.1 (Cu-Zn-Sn-Se precursors) have been prepared in a molecular beam epitaxy system with a base pressure of $1 \cdot 10^{-8}$ mbar without bake-out. Effusion cells are used to evaporate Zn, Sn, Cu, and Se on commercially available Mo coated soda lime glass. Sample temperature is measured by a pyrometer and the deposition rates are controlled by a quartz crystal monitor, an electron impact emission spectroscopy system, and a pressure gauge. The chosen deposition temperature of 330°C is low enough to prevent loss of Sn and therefore enables the thorough control of the film composition [18]. The deposited thin films had a thickness or around 2 μm.

2.2 Annealing of precursors

The annealings of all electrodeposited as well as vapour deposited precursors have been carried out in a tube furnace (Elite Thermal System Limited – Type "TSH 12/38/250-2416") with a home-build low vacuum/gas chamber that allows the variation of the kind of background gas and its pressure in a range between 10^{-3} and 1300 mbar. The samples were placed together with ca. 100 mg elemental sulfur into a graphite box which then is moved into the tube furnace before the process. For the samples discussed in section 4.12 (CTS) and chapter 5, besides the sulfur, there was also 10-25 mg of SnS powder added to the graphite box before the annealing. The graphite box was equipped with a small hole of a diameter of ca. 2 mm enabling to fill the box with the background gas prior to the annealing. The inner volume of the graphite box is around 20 cm^3. A sketch of both, the oven as well as the graphite box is shown in Figure 2-1.

In the standard annealing process, the precursors have been annealed for two hours at 550 °C in 500 mbar of forming gas (90 vol% N_2 + 10 vol% H_2), with either only sulfur (standard annealing I) or with sulfur **and** tin sulfide (standard annealing II). Figure 2-2 shows a typical temperature profile of an annealing run. Hereby, the thermocouple was placed outside the graphite box, where the glass rod and graphite are connected. Considering that the thermal conductivity of graphite with 6.67 W/(cmK) at 800 K is fairly large [19], it is assumed that the measured temperature represents the actual sample temperature fairly well. An error of a few degrees should however be considered. Furthermore, it shall be noticed that the exhaust of the tube furnace was lead through a Zn acetate containing scrubber in order to neutralize all possible H_2S molecules from the annealing gas used.

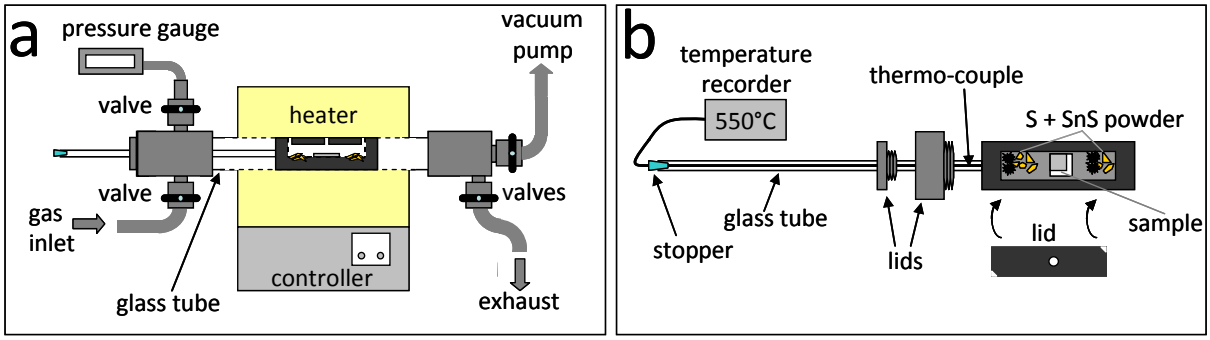

Figure 2-1 Sketches of (a) the general setup of the annealing oven (tube furnace), and (b) the graphite box, the arrangement of the sample and the sulfur and SnS powder inside the box and the thermo-couple.

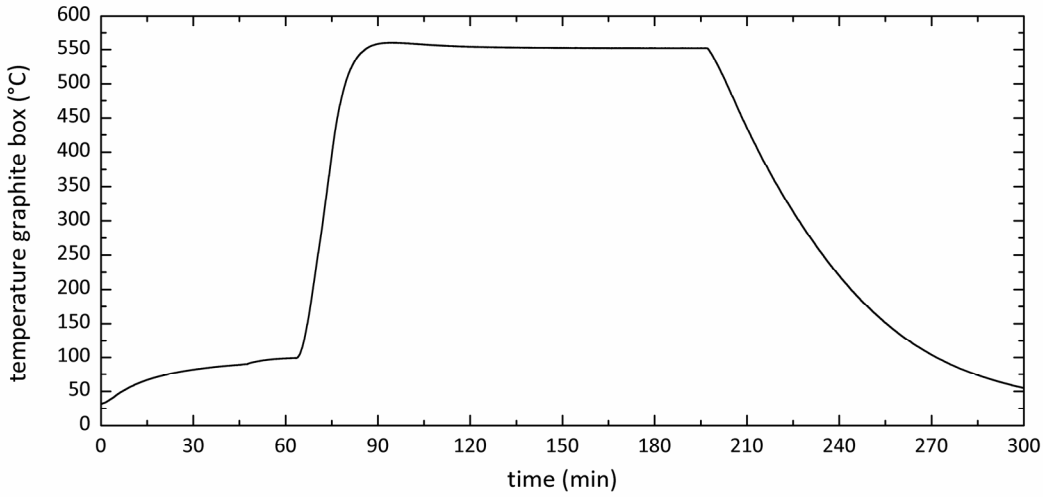

Figure 2-2 Temperature profile of a typical annealing run as measured. In the first 60 min the box was heated to 100°C while pumping down the system, then the box was heated to 550°C at a rate of 20.7 °C/min after which the temperature was kept constant for approx. 120 min, and finally the box was cooled at an initial cooling rate of 7.8 °C/min.

2.3 Scanning electron microscopy and energy/wavelength dispersive X-ray spectroscopy

Since it is very difficult for optical instruments to resolve nano-scale objects (such as morphological details) on the surface of materials, an electron beam is typically used to "illuminate" the surface. The interaction of this so-called *primary electron beam* is manifold. Figure 2-3 sketches the most common interaction, amongst which the creation of *Auger electrons* (see section 2.7) and *secondary electrons* (SE) are fairly surface near, and those of *back-scattered electrons* (BSE) and *characteristic X-rays* occur further in the bulk (< 3 μm).

By selectively looking at the emitted electrons or X-rays, one can get information about the very surface near region (from Auger electrons or SE) or about the bulk (looking at BSE of X-rays). To examine and visualize the morphology of a sample's surface, for example, one typically looks at the secondary electrons. This is typically done using scanning electron microscopy. To learn more about the composition of the bulk material, one needs to look at the characteristic X-rays, for example using energy or wavelength dispersive X-ray spectroscopy (EDX or WDX, respectively).

In the following sections the mentioned techniques are briefly introduced. For further details, the reader is referred to the following reference [20].

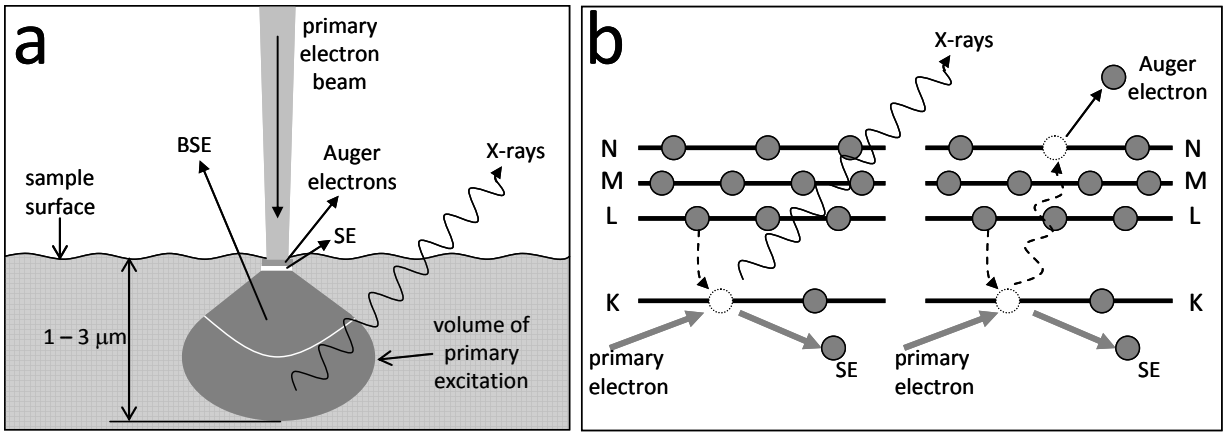

Figure 2-3 (a) Interaction of a primary electron beam with a sample's surface generating Auger electrons and secondary electrons (SE) in the first 50 nm of the sample, leading to back-scattered electrons (BSE) deeper down in the film, and creating characteristic X-rays from the shown volume of primary excitation. (b) Schematic picture of the creating of secondary and Auger electrons and the characteristic X-rays.

2.3.1 SEM

Scanning electron microscopy is probably the most common technique to examine and analyze micro-structural characteristics of samples [20]. Since a focused electron beam is used to "illuminate" the sample, the spatial resolution can be up to 1 - 5 nm [20]. By scanning the primary electron beam over a two dimensional grid, the escaping secondary and back-scattered electrons can be detected per point on the grid by collecting them in a scintillator detector. The more electrons are detected per point on the grid, the brighter the pixel on a computer generated image becomes. By scanning over a given area, a two dimensional image of the area is created.

Typically, SE as well as BSE are detected together, so the information partly comes from the surface, but partly also from the bulk. To make sure that the majority of SE is measured, e.g. to gain information mainly about the surface morphology, the SE detector is geometrically arranged in a way that a majority of SE arrive. This is possible since back-scattered electrons follow more defined trajectories while secondary electrons are emitted more randomly. To ensure a high quality picture in which also fine details can be observed, it is recommended to use a high electron current during the measurement [20]. Furthermore, the use of a low energy primary electron beam is favored for surface sensitive measurements, since less energetic electrons have a smaller penetration depth into the sample.

While the surface-near emitted SE make it possible to visualize the surface morphology, BSE that are scattered also from the bulk of the sample are typically used to visualize areas of elemental differences. Since heavy atoms typically have a larger scattering cross section for electrons than light atoms do, the amount of back-scattered electrons coming from a heavy atom is larger than that coming from a light atom. This leads to a much brighter spots in the recorded image and makes it possible to distinguish areas of elemental differences even if they have the same surface morphology.

The measurements done within the scope of this work were performed on a Hitachi SEM (SU-70). SEM images were typically taken in the SE mode at an acceleration voltage of the primary electron beam of 7 or 8 keV and at the high current mode. Furthermore, the working distance was set to 5 mm to ensure a good resolution.

2.3.2 EDX/WDX

While the emitted SE and BSE can be used to visualize the sample's morphology and differences in the elemental distribution, respectively, the emitted characteristic X-rays from the bulk can be used to determine the relative composition of the elements in the sample. As sketched in Figure 2-3 (b), when a primary electron hits and releases SE from for example the K shell of the atom, an electron from energetically higher shell will fall down, filling the hole and releasing energy. This energy is then either given to an Auger electron (see section 2.7) or is emitted directly as an X-ray. Due to energy conservation, the energy of the X-ray has to have the same value as the energy difference of the two shells involved in that process (here the L and K shell) and since the shells in different elements typically have different energetic positions, the energy of the X-ray is a characteristic information of the atom (see *Moseley's law*). By a spectral analysis of the emitted X-rays (as can be seen in Figure 2-4 (a)), one can qualitatively determine which elements are in the sample. By comparing the integral intensities of the obtained peaks one can even obtain quantitative information about the elemental ratios contained in the sample. The latter case, however, is not as straight forward but contains certain difficulties which are related to the chemical environment of the atoms (*matrix*) in the sample under investigation. As an example, the interactions of the incoming primary electron beam and of the outgoing X-rays with the sample are surely different in a densely packed Cu-Sn alloy, than in a less dense Cu-Sn-S compound, leading to different measured Cu/Sn ratios, even if they should be equal. Hereby, three main effects are typically named that account for these differences and they can be used in calculations to generate more precise composition ratios:

(1) *Atomic number effect* (Z)
(2) *X-ray absorption effect* (A)
(3) *X-ray fluorescence effect* (F)

The atomic number effect describes the X-ray generation with depth z as a function of the atomic number Z and the density ρ. For example, a possible decrease in X-ray generation can be due to an increase in elastic scattering with atomic number [20]. The X-ray absorption effect, on the other hand, describes the possible loss of X-rays that are generated deep in the sample on their way out to the detector. Finally, the X-ray fluorescence describes the creation of secondary X-ray from a photoelectric ionization of inner atomic shells from the primary X-ray [20]. These ZAF factors certainly depend on the matrix of the sample. To take those factors in a measurement into account, reference material of a similar matrix and know composition has to be used to calibrate the system. For further details, please refer to [20].

In energy dispersive X-ray spectroscopy (EDX), X-rays can be detected with a spectral resolution of 130 eV [20]. An EDX spectrum measured on a Cu_2ZnSnS_4 thin film on molybdenum at 20 keV primary beam energy is shown in Figure 2-4 (a). One can see that the K as well as the L lines for Cu (K_α = 8.0413 keV, L_α = 0.9297 keV) and Zn (K_α = 8.6313 keV, L_α = 1.0118 keV) are present, that for S (K_α = 2.3075 keV) only the K lines and for Mo (L_α = 2.2932 keV), and Sn (L_α = 3.4440 keV) only the L lines can be seen. Important to notice is that the L lines for Cu and Zn and those for S and Mo lie very close to each other, respectively. This makes it hard to evaluate the correct Cu/Zn and Mo/S ratios. It shall be noted that the ratio of Mo/S is the more problematic case. Here, both lines are only separated by 14.3 eV while in the case of Cu and Zn the line position is a little bigger with 82.1 eV, in both cases below the spectral resolution. In practice, this means that by using the L lines to evaluate the Cu/Zn ratio, the errors will be fairly large, where it is almost impossible to discern S and Mo from one another. To solve the

problems, the K lines for Cu and Zn, which are well separated, can be used, if the primary beam energy was chosen to be higher enough. For the case of discerning S and Mo, one has to use wavelength dispersive X-ray spectroscopy (WDX), which has a factor of 10 better spectral resolution than EDX, as shown in Figure 2-4 (b) and (c) [20].

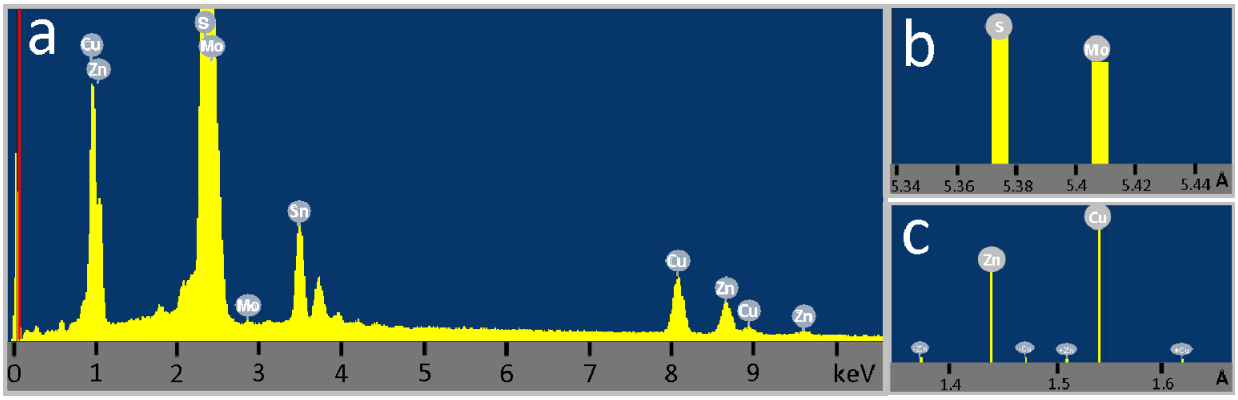

Figure 2-4 (a) EDX spectrum measured on a Cu_2ZnSnS_4 containing sample. One can see the K lines of Cu, Zn, and S at 8.0413 keV, 8.6313 keV, and 2.3075 keV, respectively, and the L lines of Cu, Zn, Sn, and Mo at 0.9297 keV, 1.0118 keV, 3.4440 keV, and 2.2932 keV, respectively. Spectra (b) and (c) show small sections of a WDX spectrum, where the possible resolution of S and Mo (in (b)) and the one of the L lines of Cu and Zn (in (c)) is shown. In all images the y-axis represents EDX/WDX counts.

To be able to compare EDX/WDX measurements of one sample with those taken of another, one needs to make sure that always the same primary beam energy was used. The reason for this can be found in the different information depths that a lower or a higher energetic primary beam will cause. In Figure 2-5 the results of a CASINO simulation of a 7 keV primary beam in comparison to a 20 keV primary beam on a CZTS sample is shown. Both graphs show the interaction volume of the incident electrons with the sample. As a first result, it can be seen that the electron interaction volume for the 7 keV beam does not reach deeper into the film than 300 nm, while that of the 20 keV beam reaches down to 1200 nm. This indicates that a low energy beam is much more surface sensitive than a higher energy beam, which makes a direct comparison difficult in case the sample inherits a compositional gradient. Winthin those interaction volumes, characteristic X-rays are produced. Hereby, characteristic X-rays can only be produced in those regions, in which the kinetic energy of the primary electron beam is still larger than the characteristic X-ray energy, for example larger than 8.04 keV for the Cu K line, and 3.44 keV for the Sn L line. As a result, characteristic X-rays of different elements are typically produced in differently sized interaction volumes and hence have their origin in different depths of the films. This indicates that the direct comparison of EDX/WDX results of different samples with different in-depth composition gradients or different thicknesses is difficult.

In the measurements performed within the scope of this work, a 20 keV primary beam was typically used to ensure a good average composition measurement in depth, and a very low magnification of “300 times” was used to ensure a good lateral composition average. To calibrate the WDX measurement, standards that were provided with the machine have been used. In the case of EDX, a quant-optimization was performed on a copper foil before each measurement unit in order to account for possible changes in the beam current. Furthermore, the software was set to correct for the ZAF effects. In the analysis of the composition ratios, the K lines were used for S, Cu and Zn, and the L lines for Sn and Mo. The S/Mo ratio has mostly

been ignored (a sufficient amount of S has been assumed) and has only been measured with WDX in some important cases.

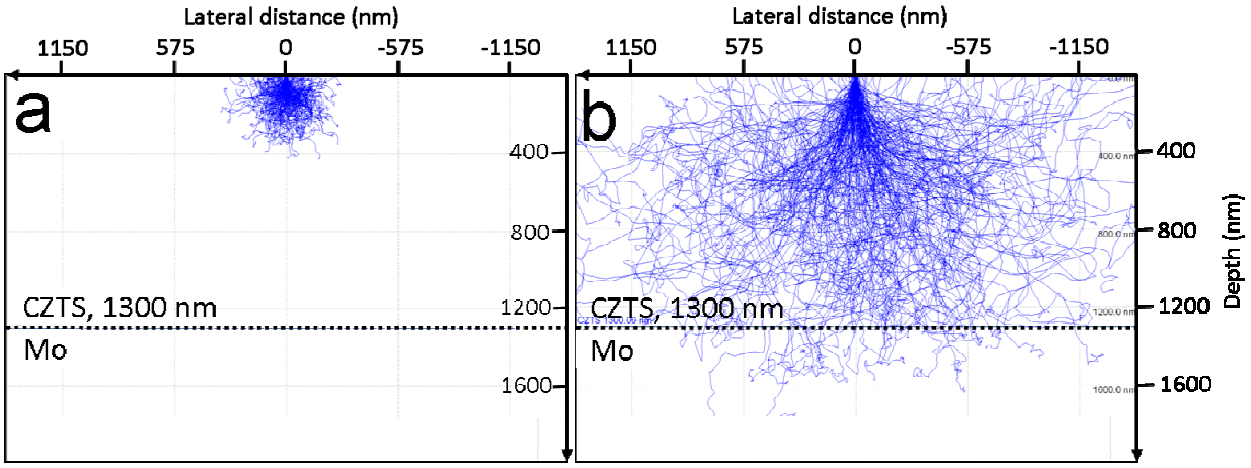

Figure 2-5 CASINO simulation of a (a) 7 keV and (b) 20 keV primary electron beam that interacts with a Cu_2ZnSnS_4 sample (thickness of 1300 nm) on a Mo substrate.

The software that calculates the elemental composition also provides an error for the measurements, which is typically of the order of 2 rel.%. On top of that, a statistical error of the measurements has been investigated by measuring the same spot on a Cu_2ZnSnS_4 sample ten times in a row. The compositional results for each element have been averaged and a standard deviation from this average has been calculated for the different elements to be: ±0.2 rel.% for Cu, ±0.4 rel.% for Zn, ±0.2 rel.% for Sn, ±0.3 rel.% for S, ±0.3 rel.% for Mo. These standard deviations of the measurement are smaller than that given by the machine and lead to errors for the Zn/Sn, Cu/(Zn+Sn), and Cu/Sn ratios of ±0.03, ±0.06, ±0.05, respectively.

Apart from those statistical errors, a systematic error of the EDX measurements can occur, when measuring the composition of a thin sample or of a sample with open morphology, or when chosing the measurement conditions such that a Mo signal from the underlying molybdenum substrate is measured. The analyzing software typically assumes that all measured elements are evenly distributed within the film. As the X-ray yield from the Mo L line at around 2.4 keV is much different than that of, for example, the Cu K line at around 8.1 keV, and as these X-rays have their origin from different interaction volumes, the analyzing software makes a systematic error in the simulation of the EDX spectrum by assuming an even distribution of the elements. Figure 2-6 shows an example of the simulated spectrum (red line) overlaying the measured spectrum (yellow). One can see a small discrepancy in both spectra. As a cause, the calculated relative amounts are not totally correct. The higher the amount of detected Mo in the film, the larger this discrepancy becomes and the larger the systematic error becomes. Within a measurement series, where the detected molybdenum content is comparable, this systematic error only leads to a general shift of the elemental ratios into one direction. Relative changes in the samples composition, however, stay un-effected. On the other hand, when comparing samples with different molybdenum content, this systematic error is different for each sample and can lead to false conclusions. Therefore, when comparing samples with compositions containing different amounts of Mo, an overall error of 1 at% is assumed for all elements in order to account for the error. This value is not evaluated but rather based on experience. For all other measurements, where the Mo content is comparable, the statistical errors mentioned in the previous paragraph were used, bearing in mind that there might also be a small systematic error in addition.

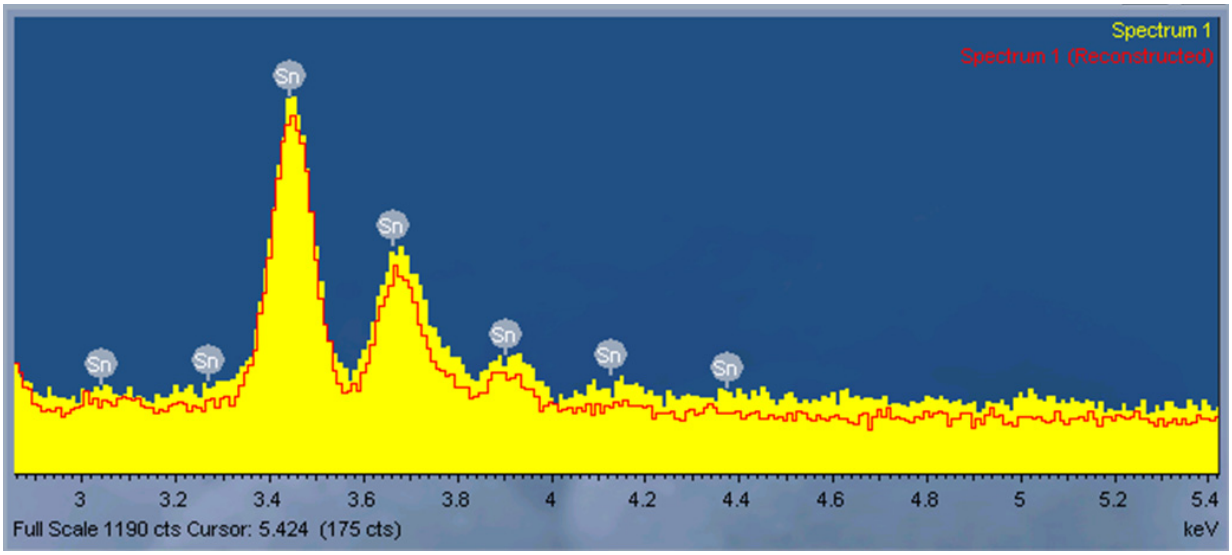

Figure 2-6 EDX spectrum as measured (yellow) on a sample with a very open morphology (80 at% of Mo) and as simulated (red line), assuming that all detected elements (Mo, S, Sn, Cu, and Si) are distributed evenly.

2.4 X-ray diffraction (XRD)

The content of the following subchapters were taken from the standard textbooks as referenced here [21, 22]. For further details, the reader is referred those references.

2.4.1 General background

X-ray diffraction is besides neutron scattering one of the key techniques in the study of crystal structures amongst the various fields of physics, chemistry, biology, and material science. When X-rays interact with a crystalline material, the electrons around the atom start to oscillate at the frequency of the incoming beam. At the same time, these oscillating electrons will emit electromagnetic radiation, following the laws of electromagnetism. Since this radiation is scattered into all directions, destructive as well as constructive interference occurs in a radially distributed region around the sample. Since the atoms in a crystal are arranged in a regular pattern, a law can be derived that describes the condition that must be given such that constructively interfering X-rays of a wavelength λ have been scattered into an angular position Θ after interacting with a crystal with a lattice spacing d_{hkl}. This law is called Bragg's law and is given as follows [22]:

$$n\lambda = 2d_{hkl}\sin(\Theta)$$

Equation 2-1

The lattice spacing d_{hkl} varies for the different crystal systems (see textbooks for more details) and hence contains the desired structural information. To obtain this information, one can either keep λ fixed and look at the scattering intensity while varying Θ, or vice versa. Typically, the former method is used. Standard setups are shown in Figure 2-7.

While the angular position of the constructively interfering diffracted X-rays is given by Braggs law, the scattering amplitude F_{hkl} (the so-called *structure factor*) of a unit cell can be derived from the summation of the individual scattering amplitudes f (so-called *form factor*) from all atoms in the unit cell [22]:

$$F_{hkl} = \sum_{n=0}^{N} f_n \exp\{2\pi i(hx_n + ky_n + lz_n)\}$$

Equation 2-2

The intensity I_{hkl} of the scattered X-rays is then given via $I_{hkl} \propto A_{abs}\left|F_{hkl}\right|^2$ and is, amongst others, dependent on an absorption factor A_{abs}.

X-ray diffraction can primarily be used to check the crystal structures available in a film by comparing the obtained X-ray pattern with those of standards taken from a crystal structure database [23]. For further investigation, line profile analysis can be used to reveal information about the microstructure of the sample, such as unit cell parameters, stress and strain in the layers, grain sizes, etc. Within the scope of this work (in chapter 4), the *Rietveld Refinement* method (discussed in section 2.4.3) has been used to evaluate the percentage of a secondary phase to the main phase in a sample.

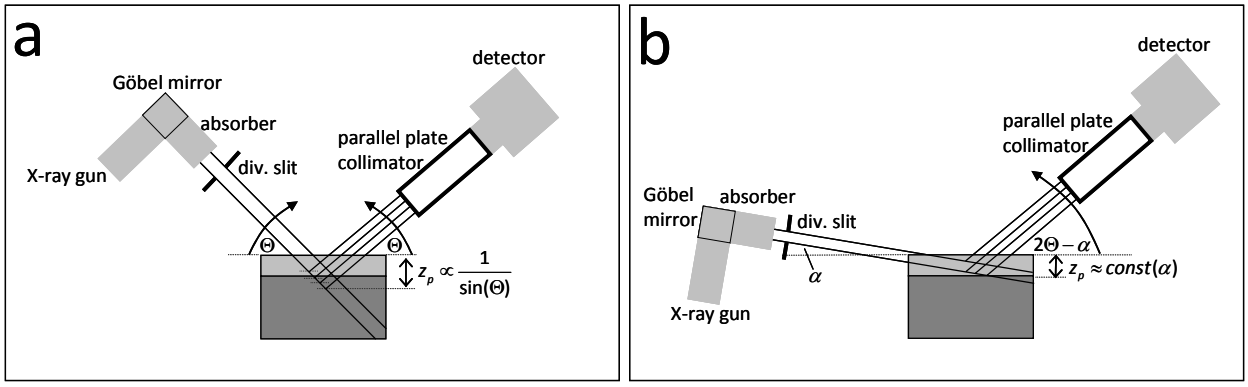

Figure 2-7 Experimental setups for (a) a $\Theta - 2\Theta$ scan in parallel beam mode and (b) a grazing incidence X-ray diffraction scan, where α is the grazing angle, Θ the scanning angle, and z_p the penetration depth in each case.

2.4.2 X-ray diffraction on thin films

Commonly, X-ray pattern are measured in a symmetrical ($\Theta - 2\Theta$) setup, as sketched in Figure 2-7 (a). Hereby, both arms, the X-ray source arm as well as the detector arm, scan in parallel along an angle Θ (each) around the sample that sits in the center of the arrangement, while the intensity of the X-rays is detected. While in this arrangement X-rays only diffract from those lattices that are parallel to the sample holder's surface, it is suitable to investigate texture in the film. For thin films, however, this arrangement has several disadvantages, resulting in a low diffraction intensity, as can be seen in Figure 2-8 (top). This low intensity is mainly related to the path length of the X-ray in the thin film is too short. Using the Lambert-Beer law, typical penetration depths lie in the range of 1 to 100 μm for Cu K_α radiation, which is far bigger than the thickness of typical thin films [22]. While for a low angle most of the X-rays are still diffracted by the thin film, the contribution from the underlying substrate increases dramatically for higher angles since most of the X-rays simply travel through the thin film without interactions. The outcome of this is that the absorption factor A_{abs} of the $\Theta - 2\Theta$ scan decreases dramatically for higher angles lowering the peak to background ratio. Furthermore, the substrate signal might increase and might superimpose that of the thin film, making a detailed investigation difficult [22].

As a solution it is suggested to keep the X-ray source arm at a constant small angle while the detector arm is scanned along 2Θ. This experimental arrangement is called *grazing incidence XRD* (GIXRD) and is sketched in Figure 2-7 (b). Since here, the grazing angle α is kept very

shallow (typically between 0.7 and 5°), the X-rays mainly penetrate and diffract within the thin film (as sketched in Figure 2-7 (b)), leading to a fairly constant absorption factor throughout the angular range and increasing the peak to background ratio [22]. In this configuration, X-rays will not longer only diffract on lattice planes parallel to the sample holder's surface but also from lattice planes of a different orientation. For polycrystalline and non-textured samples, this helps to make sure that most of the small peak contributions can be detected, as shown in Figure 2-8 (bottom). For highly textured material, however, this configuration might result in no measurable signal. The grazing angle should also be chosen with care. If chosen to be too small, it might get close to a critical angle Θ_c of total reflection ($\Theta_c \approx 0.1-0.5°$) resulting in a shift of peak positions. Furthermore, in a multilayered film, being close to the critical angle might cause unwanted total reflection of one of the layers.

For this work, the use of the GIXRD configuration has been chosen since a better signal to background ratio could be achieved throughout the angular range, as a comparison of a $\Theta-2\Theta$ and grazing incidence scan performed on the same sample shows (Figure 2-8). Further experimental details are given later in this section.

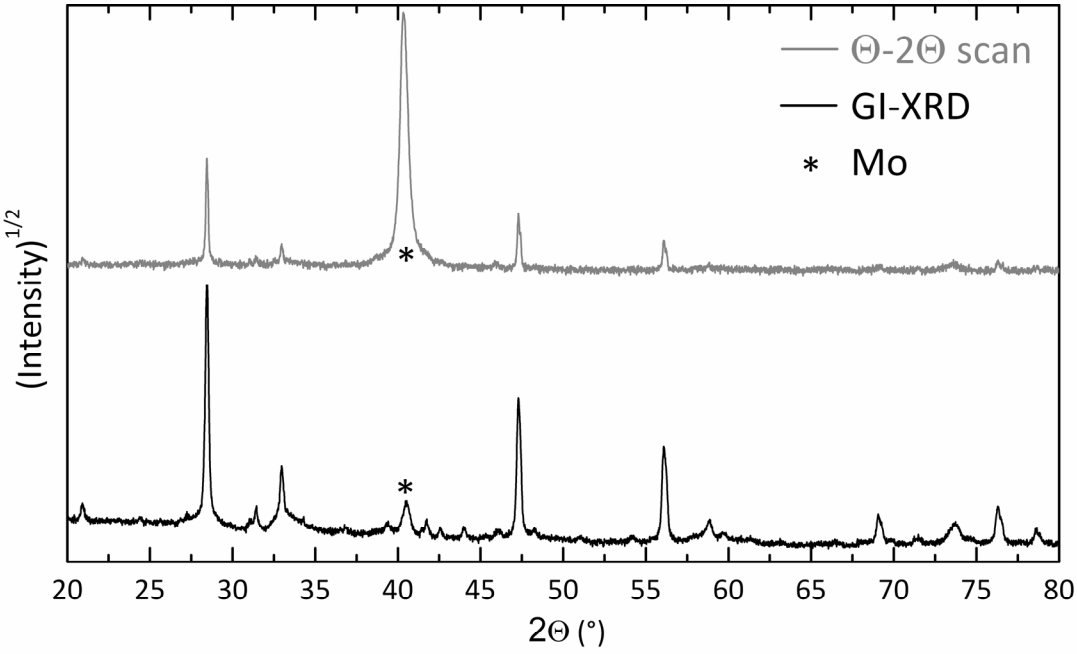

Figure 2-8 X-ray diffraction pattern of a monoclinic Cu_2SnS_3 thin film grown on a Mo substrate measured in a $\Theta-2\Theta$ (grey) and in a grazing incidence (black) setup. "*" indicates the main peak of the contribution of the Mo substrate which is the majority phase detected in the $\Theta-2\Theta$ scan suppressing the other phase of the thin film.

2.4.3 Rietveld Refinement

General Background

Rietveld Refinement is a method introduced by H. Rietveld to characterize the microstructure of crystalline materials. The principle of this profile refinement method is to minimize a function M which describes the difference between the observed data $y_{i,obs}$ and the calculated profile $y_{i,cal}$ [24]:

$$M = \sum_i W_i \left\{ y_{i,obs} - \frac{1}{c_s} y_{i,cal} \right\}^2$$

Equation 2-3

Here, W_i describes the statistical weight and c_s the overall scale factor such that $y_{i,cal} = c_s \cdot y_{i,obs}$ [24]. Amongst many more, the least-squares parameters comprise the half-width parameters, unit cell parameters, preferred orientation parameters, strain parameters, scale factors, etc., all revealing information about the samples microstructure. As a measure for the goodness of the refinement, the Bragg factor R_B is used [25]:

$$R_B = 100 \cdot \frac{\sum_i \left| y_{i,obs} - y_{i,cal} \right|}{\sum_i \left| y_{i,obs} \right|}$$

Equation 2-4

A refinement is typically seen as good, if $R_B \leq 6$ [25].

Furthermore it shall be noted that for refinement of thin films it is important to have a minimum of around 2000 counts for the highest peak of the pattern that is supposed to be refined. This value has been obtained through experience and suggested by Prof. Dr. Susan Schorr.

In this work, Rietveld analysis has been utilized to obtain a percentage value of a secondary phase in a sample with respect to the main phase (see chapter 4). For this, the free and online available software Fullprof has been used.

Refined parameters

In the refinement analyses performed within this work, only a small set of variables were refined. Hereby, the order of refinement as suggested by the Fullprof manual has been followed [25]:

After choosing the best possible starting model by considering the lattice constants for CZTS (as obtained from a database), and after removing peak contributions due to the Mo substrate, the *scale* factor was refined, which scales the calculated pattern to the measured one in terms of signal intensity.

The next step was to refine the *background* of the measured XRD pattern. For the refinements in this work, this step was done semi-manually, where the user fixed several background points manually after which those points were refined.

In the next step, the *lattice parameters* (*a, b, c*) were refined one after the other.

This step was followed by the refinement of the *UVW values*, where the W value was refined first, followed by the V value, before finally the U value was refined. Hereby, the UVW values describe the broadening of the measured pattern, which is generally dependent on the used X-ray diffraction instrument as well as on the sample itself. Measuring and analyzing the pattern of a reference sample, for example, where the angular dependent peak broadening is assumed to only dependent on the instrument function, the UVW values can be obtained for a certain instrument and a certain instrument configuration (e.g. a certain grazing angle, etc.). Hereby, the relation of UVW values to the full width half maximum (FWHM) of the peaks is given via the Caglioti function [26] and describes the instrument function:

$$H_G = U \tan^2(\Theta) + V \tan(\Theta) + W \,,$$

Equation 2-5

where H_G is the FWHM of the Gaussian component of the Bragg peak and Θ is the angle.

In the next refinement step, a *shape1* factor is refined, which refines the shape of the measured peaks.

Following this, the *texture* factors *pref1* and *pref2* are being refined, which describe a preferred orientation of the crystals in the analyzed sample. Hereby, *pref2* describes the fraction of the sample that is not textures (hence the values lie within 0 and 1), while *pref1* described the way of texturing. For *pref1* > 1 implies a needle like habit, *pref1* < 1 a platy habit, and *pref1* = 1 implies no preferred orientation.

As a last step of a first refinement run, the *temperature factors* B_{iso} or B_{ov} were refined. Hereby, both B values describe the atomic displacement of either individual atoms (B_{iso}) or of all atoms (B_{ov}) in terms of the area of displacement, as their units are given in $Å^2$.

In order to find out whether the measured pattern can be refined better with a secondary phase (CTS or ZnS), a second refinement run has been performed by choosing a starting model which contains a CZTS phase **together** with a secondary phase (CTS or ZnS). In this second run, all the previously explained steps were performed again in the same sequence for the added secondary phase.

In order to obtain the best refinement for the individual patterns, the R-Bragg values for the different intermediate steps were compared.

At this point it shall be noted that in the performed refienement analyses, parameters like *peak asymmetry* or *strain* were not considered due to complexity reasons.

2.4.4 Used settings

Figure 2-7 (b) shows the schematic of the grazing incidence setup used for the measurements done within the scope of this work. Most measurements have been performed at a Bruker D8 DISCOVER, where 1.2 mm divergence slit as well as a soller slit have been used on the X-ray source arm, and where a parallel plate collimator has been used at the detector arm together with a scintillator detector. Furthermore, the grazing angle α was set to 0.75°. The few measurements discussed in chapter 4 were obtained on a PANAlytical X'Pert PRO, using a soller slit as well as a ¼° divergence slit at the source arm and a parallel plate collimator at the detector arm. The grazing angle was set to 1°. In all cases, X-rays from a Cu $K_{\alpha_{1+2}}$ source have been used.

Before each measurement, a height alignment of the sample has been performed in order to avoid peak shifts. The typical scan range for the investigation of Cu_2ZnSnS_4 thin films and its possible secondary phases was between 10 and 80°. A step length of 0.01° and an integration time of 3 s/step were chosen. Phase identification is based on the JCPDS data base 2009 [23].

2.5 Raman spectroscopy

Raman spectroscopy is an optical, non-destructive technique with a widely spread use in life sciences, chemistry, and physics and it has even been used in a mission to Mars [27]. Within those fields, it is utilized to reveal the molecular significance of bacteria, to study structural rearrangements during chemical reactions, and gives information about crystalline quality and chemical compositions of crystalline materials, respectively [28-30].

2.5.1 General background

The principle of Raman spectroscopy lies in the inelastic scattering of incident light off a sample. Hereby, as sketched in Figure 2-9, an incident photon transfers its energy $\hbar\omega_i$

(incident) onto the sample, exciting an electron from its ground state $|0\rangle$ into a state $|e\rangle$ with the energy E_e. This excited electron then interacts with the lattice under the exchange of energy $\pm\hbar\Omega$, annihilating ("+", anti-Stokes process) or creating ("-", Stokes process) a phonon in the lattice, respectively, occupying the state $|e'\rangle$ of the energy $E_{e'}$. During the transition from the excited state $|e'\rangle$ into the ground state $|0\rangle$, a photon of the energy $\hbar\omega_s$ (scattered) will be emitted. Energy conservation yields:

$$\hbar\omega_s = \hbar\omega_i \pm \hbar\Omega$$

Equation 2-6

In a typical Raman plot (as shown in Figure 2-10 (a)) the intensity of the scattered light is plotted vs. the frequency difference $\omega(cm^{-1}) = \omega_i - \omega_s$ (called *Raman shift*). The successive peaks belong to eigenfrequencies (modes) Ω_j of the elementary excitations and their positions, intensity ratios, and widths contain information about the crystalline quality and the chemical composition of the material. In the process where phonons are created (Stokes process) the frequency difference is positive and in the case of the annihilation of phonons (anti-Stokes process) ω is negative. The eigenfrequencies of both cases, however, are the same, such that the Raman modes are symmetrically arranged around the line of the incident light, as shown in Figure 2-10 (a). Typically, and within this work, only the Stokes case has been looked at since there its maximum intensity is typically larger.

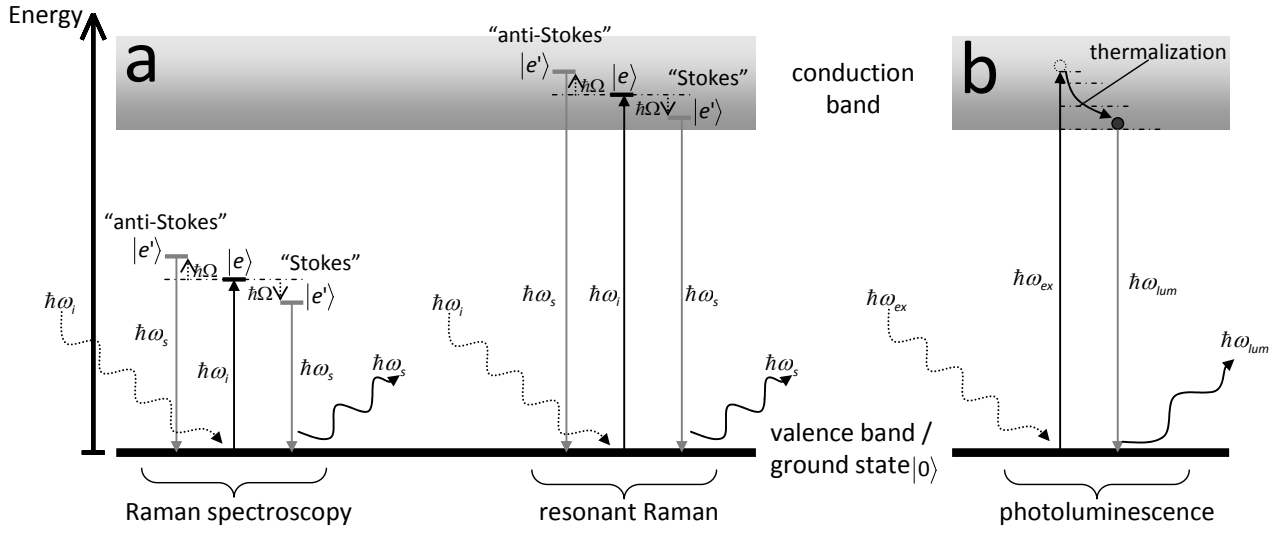

Figure 2-9 (a) Sketch of the inelastic scattering of light on a semiconductor, exciting the electrons into virtual (on the left) and real (on the right) electronic states leading to normal Raman scattering or resonant Raman scattering (left). (b) Sketch of the photoluminescence, where the exciting light $\hbar\omega_{ex}$ lifts an electron from the valence band into the conduction band, which thermalizes to the conduction band minimum, and recombines under the emission of photon of the energy $\hbar\omega_{lum}$ (right).

The intensity of the scattered light I_s can be derived semi-classically, based on the interaction of an oscillating external electric field $\vec{E}(\omega_i)$ with the atoms in the lattice, to be [22, 29, 30]:

$$I_s = I_i \frac{\omega_s^4 V_{vol}}{(4\pi\varepsilon\varepsilon_0)^2 c^4} \left| e_s \tilde{\chi}(\omega_i, \omega_s) e_i \right|^2$$

Equation 2-7

Here, V_{vol} denotes the scattering volume, $I_{s,i}$ and $e_{s,i}$ the intensity and polarization unit vector of scattered and incident light, and $\tilde{\chi}(\omega_i, \omega_s)$ the generalized susceptibility tensor. The last term yields as the dominant term from third-order perturbation theory [29]:

$$\tilde{\chi}_{\alpha,\beta}(\omega_i, \omega_s) \propto \sum_{e,e'} \frac{\langle 0|p_\alpha|e'\rangle\langle e'|H_{E-L}|e\rangle\langle e|p_\beta|0\rangle}{(E_{e'} - \hbar\omega_s)(E_e - \hbar\omega_i)}$$

Equation 2-8

Here, α and β are the directions of the scattered and incident light, $p_{\alpha,\beta}$ the respective vector components of the dipole operator, and $H_{E\text{-}L}$ the electron-phonon interaction Hamiltonian. Furthermore, it shall be noted that $\sum_{e,e'}$ describes the sum over all virtual as well as real electronic states. In the case of a semiconductor, those states within the band gap are virtual states, and those above are real states, as shown in Figure 2-9. Considering the latter two equations it can be seen that the scattering intensity is generally dependent on three parameters:

(1) The incident light intensity I_i,
(2) the interaction volume V, and
(3) the probabilities of electronic transitions.

While the former two can be varied over one or two orders of magnitude only, the probability of electronic transitions can vary up to eight orders of magnitude, depending on whether the transition leads into a virtual (low probability) or a real (high probability) electronic state [30]. In the latter case, one generally speaks of *resonant Raman* (RR). In a semiconductor, this RR case can be achieved by exciting the electrons over the band gap into the conduction band, as sketched in Figure 2-9.

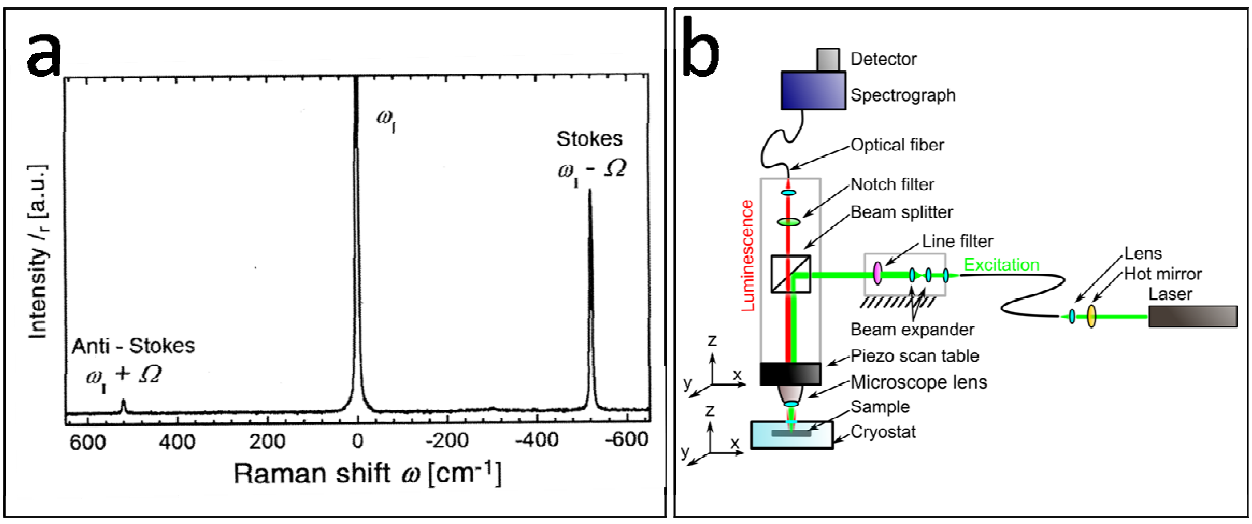

Figure 2-10 (a) Scattering spectrum of crystalline Si showing two inelastic contributions to higher (anti-Stokes) and lower (Stokes) energy [28]. (b) Sketch of the used Raman setup.

In semiconductor science, Raman spectroscopy is typically used to investigate crystalline defects, impurities, or strain, but since the Raman modes are strongly influenced by the crystal structure and the chemical compositions of the material, each Raman spectra of a certain

material acts like a “fingerprint” of this material. This way, it is possible to distinguish different phases.

An advantage of Raman spectroscopy is that it is non-destructive (unless the used laser power is too high). Together with modern technology and confocal optics, it is possible to measure a full Raman spectrum within a very short time frame and lateral resolutions below 1 μm can be achieved [28]. By tuning the energy of the incident light, it is possible to work in resonance mode, making it possible to detect small amounts of a certain material. Besides those advantages, however, it should be noted that Raman spectroscopy is only very surface sensitive with a probing depth of less than 100 nm (depending on the absorption coefficient of the material under investigation and the excitation wavelength used). This makes in-depth investigations difficult.

For further details about Raman spectroscopy in general, the reader is referred to [22, 29, 30].

2.5.2 Used settings

Within the scope of this work, Raman spectroscopy measurements have partly been performed by Rabie Djemour of the University of Luxembourg, and partly in a collaboration with the team of Prof. Perez-Rodriguez from the University of Barcelona. The experimental setup used is shown in Figure 2-10 (b). While in the measurements of Rabie Djemour an excitation wavelength of 514.5 nm and laser intensities between 30 and 50 mW have typically been used, those measurements from the University of Barcelona were performed at 514.5 nm, 532 nm as well as 325 nm excitation wavelengths and a similar intensity range. In the former case, Raman signals from an area of 1 μm^2 have been measured and integrated over an area of 80 x 80 μm^2, while in the latter case the measurement area was circa 1 μm^2 (at 532 and 325 nm) and 100 μm^2 (for measurements at 514.5 nm).

2.6 Photoluminescense (PL)

Photo-induced luminescence (*photoluminescence*, PL) is the emission of photons from a solid caused by the transition of electrons from higher occupied electrical states into lower unoccupied states after a photo-induced excitation, as sketched in Figure 2-9 (b) [31]. For this, electrons are typically excited from the *valence band* (VB) into the *conduction band* (CB) by the use of a light source. After thermalizing to the band egde of the CB or even to defect states within the band gap, electron-hole pairs recombine under the emission of a photon (luminescence). For a measurement at room temperature, the photon flux detected outside the sample can be expressed by

$$Y_{PL}(E) = \frac{1}{4\pi^2\hbar^3c^2}\frac{a(E)E^2}{\exp((E-\Delta\mu)/k_BT)-1},$$

Equation 2-9

where the absorptivity is given by $a(E) = (1-R_f)(1-\exp(-\alpha_{abs}(E)d))$ with the front surface reflectivity R_f, the absorption coefficient α_{abs}, the layer thickness d, the temperature T, the energy E, and where $\Delta\mu$ is the quasi-Fermi level splitting [31].

PL measurements can either be made at room temperature (RT) or temperature dependent at very low temperatures (T). In the former case, a band-to-band transition is typically seen because the thermal energy is sufficiently high such that defects states are already filled,

whereas in the low temperature case defect transitions can be observed in combination with intensity dependent studies. Besides gaining information about defects in the semiconductor, PL measurements can also be used to determine the band gap of a semiconductor, the quasi-Fermi level splitting, and to derive information about the absorptivity and the absorption coefficient, following the procedure published by Gütay et al. [32]. Further details can be found in the following literature [31].

With the target to find a suitable technique to discern secondary phases of CZTS from the actual CZTS phase, RT-PL measurements have been performed (chapter 4). Hereby the focus was set to see whether multiple PL peaks could be seen at once for a sample with different phases of different band gaps (concept of *fingerprints*).

Photoluminescence measurements have been performed by Dr. Katja Hönes and Rabie Djemour on a home-built setup (see Figure 2-10 b) at room temperature with an excitation wavelength of 514.5 nm using an argon ion laser, with an incident power of between 20 and 80 mW, and a spot size of 1 μm. The PL signal has been integrated over an area of 20 x 20 μm^2 under the use of a piezo scan table.

2.7 Auger electron spectroscopy depth profiles

Auger electron spectroscopy (AES) is a powerful tool to conduct chemical surface analyses. Like in EDX, a primary electron beam of typically around 3 to 30 keV is used to interact with the atoms in the sample. By this interaction, an electron from one of the inner shells (e.g. from the K shell as shown in Figure 2-3) of an atom is released (secondary electrons). After that an electron from an energetically higher shell (in this case the L shell) will fall down into the open position, filling the hole while loosing energy. This energy is then either emitted as a photon (X-ray), as in the case of EDX, or it is transferred into a so-called Auger electron, as schematically shown in Figure 2-3. This Auger electron, which comes from an outer atomic shell, will use this energy (a) to escape into the vacuum level (binding energy) and (b) as a kinetic energy. The latter one of the escaping Auger electrons can be measured. By scanning through the kinetic energy range, peaks can be observed at specific energetic positions. These energetic positions correspond via $E_{kin} = (E_{high} - E_{low}) - E_{bind}$ to the energy difference of the inner atomic shells. Since the electronic shells of the different elements have typically slightly different energetic positions, the measured binding energies can be used as a “fingerprint” for the different elements (see tables for energetic positions of the electronic shells for the different elements [33]). By measuring a certain set of peaks (in the E_{kin} plot) it is known which element is present in the sample. The area under such a peak (the integrated intensity) then gives a hint about how much signal comes from a certain element. In samples with different elements, ratios of the integrated peak intensities give an idea of the composition of the sample. Hereby, however, it is important to take the scattering cross-section of the individual elements into account. Doing this, the so-called *relative sensitivity factors* (RSF) have to be used. They can either be looked up in tables or can be determined experimentally. Depending on the energy of the primary electron beam, the information depth for AES varies between 0.4 – 5 nm. This technique is very surface sensitive. For further details, the readier is referred to [33].

Within the scope of this work, AES depth profiles were measured. For this, besides determining the compositional ratios of the different elements, a sputtering step had to be introduced after each AES measurement. By sputtering away atomic layers of the sample, depth information could be acquired step by step.

The Auger analyses for this work were carried out as service measurements at the CRP Gabriel Lippmann on a “Thermo Electron Microlab350” apparatus using a spherical sector analyzer. All

spectra were recorded in direct mode and with a 10 keV and 1 nA primary electron beam. With these analysis conditions, a lateral resolution of 40 nm was achieved. The angle of incidence of the primary electrons beam and of escaping electrons was 30° with respect to the surface normal. The energy resolution of the spectrometer was fixed to 0.5 %. For depth profiles, the samples were sputtered with an Ar^+ ion gun (E = 3 kV, I = 1.5 μA, on a 1 mm^2 area) with an angle of circa 45°. The compositions were obtained using relative sensitivity factors for each element under investigation that were experimentally determined on bulk reference samples analyzed under the same conditions. For each sputtering time t the compositions were determined and plotted against t, which itself corresponds to a point in depth.

2.8 Inductively coupled plasma mass spectroscopy (ICP-MS)

ICP-MS is a highly sensitive analytical tool to quantitatively determine masses of elements in solution at concentrations of the sub-ppb range [34]. Typically used for forensic analyses and in life sciences, ICP-MS also finds its applications, e.g., in the trace analysis of impurities in material compounds or in the quantitative determination of a mass of a certain element. The latter function is the one used within the scope of this work to determine the plating efficiency of the electrodeposition process, described in chapter 3.

To measure the masses of metals that are electrodeposited onto molybdenum substrates, the metallic layers have to be dissolved in aqua regia (ratio 3:1 of HCl : HNO_3) at first, before diluting these solutions such that it fits the requirements and concentration ranges of the used ICP-MS equipment. Then, under the use of a nebulizer, each solution is introduced into the ion-coupled plasma part of the machine where the metallic atoms are ionized. After that, the ions are fed into a mass spectrometer, where the different masses of the expected metals can be detected sequentially. Hereby, the measured counts of a certain mass are correlated to that obtained from a reference solution with known concentration, which is typically measured at the same day. Out of this correlation the overall mass of the originally dissolved metal can be calculated. For a more detailed description, the reader is referred to the following reference [34].

Similar to the AES experiments, the ICP-MS results shown in section 3.7.1 have also been obtained from service measurements performed at the CRP Gabriel Lippmann, the dilutions and the concluding calculations have been performed by the author. The machine that was used is a “Perkin Elmer Sciex ELAN DRC-e” and the reference solution for the individual elements was a multi reference with an error of ± 0.3 %.

To obtain an error to the measured masses, uncertainties of the machine, those of each step of the dilutions, and those of the used reference material have been combined and evaluated using the principles of the Gaussian error propagation. Hereby it shall be noted that the uncertainty of the reference material is the most crucial one which is why the right choice of the reference is important.

2.9 Electro-optical characterization

2.9.1 Current-voltage (IV) characteristics

The figure of merit of a solar cell device is its energy conversion efficiency η_{eff}. To measure this value, current-voltage (IV) characteristics are measured. For this, the sample is illuminated with a known power P_{ill} as well as a known spectral irradiance and while applying different voltages V the output current I is measured, as schematically shown in Figure 2-11 (a). The intercept of the IV curve with the ordinate is hereby called the *short circuit current* I_{sc} and the

intercept of the IV curve with the abscissa is the *open circuit voltage* V_{oc}. Since the output power P_{out} is given via $P_{out} = I \cdot V$, there will be a maximum power point at $P_{max} = I_{max} \cdot V_{max}$ along the line. The power conversion efficiency can now be calculated from

$$\eta_{eff} = \frac{P_{out}}{P_{ill}}.$$

Equation 2-10

The ideal shape of such an IV curve (neglecting the Schockley-Queisser limit) would be rectangular and would deliver a constant current I_{sc} until the open circuit voltage [35]. For such a curve, the maximum power point would have I_{sc} as a current and V_{oc} as a voltage (see Figure 2-11 (a)). A term called the *fill factor* (*FF*) has been invented to indicate how ideal a measured IV curve is and is defined as

$$FF = \frac{I_{max} \cdot V_{max}}{I_{sc} \cdot V_{oc}}.$$

Equation 2-11

Taking the Schockley-Queisser limit into consideration, a value of 87 % for the fill factor is expected for a CIGS solar-based solar cell with a band gap of 1.15 eV assuming an perfect diode (diode factor equals 1) [36].

From IV curve measured in the dark, one can gain information about the *series resistance* R_s and the *shunt resistance* R_{sh} of the device. For this, the inverse slopes of the linear parts of the IV curves in the first and third quadrant are deduced, respectively. In the ideal case, R_{sh} is infinite and R_s is 0 Ω.

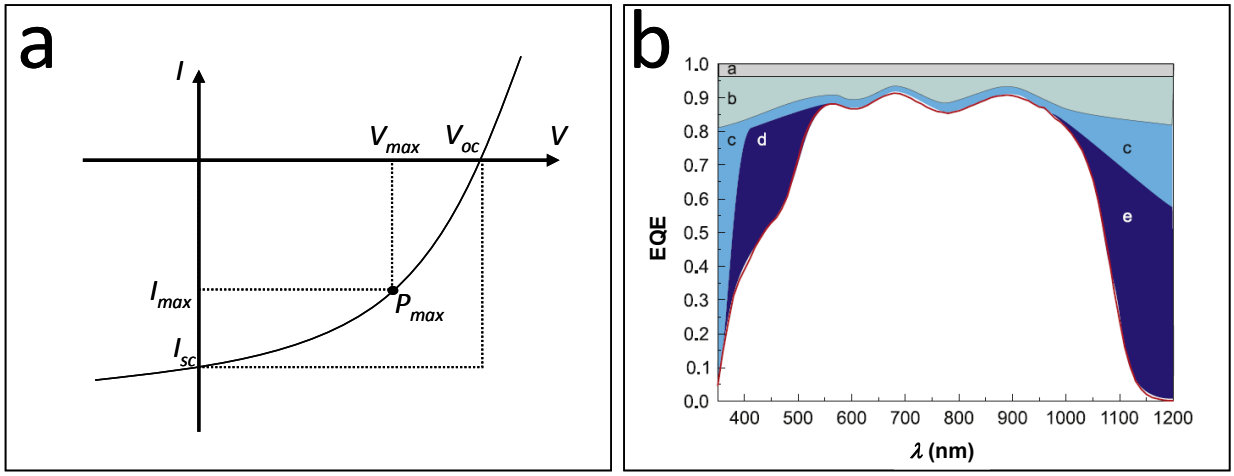

Figure 2-11 Sketch of (a) an IV curve under illumination and (b) of a QE [36]. In the QE, areas of losses from a) grid shading, b) surface reflexion, c) ZnO absorption, d) CdS absorption, and e) insufficient absorption and collection are sketched.

The IV measurements done within the scope of this work were performed on a home-built setup using a halogen lamp (100 mW/cm^2) and a four probe configuration. To calibrate the power of illumination, a silicon calibration cell (WPVS-Cell, RS-ID-3, Serial No. 006-2007, from ISE/S. Brachmann) was used. Figure 2-12 shows the photo current density obtained from the reference cell under the use of the Halogen lamp (yellow line) in comparison with the expected photocurrent by a AM1.5G spectrum. One can see that for low band gap material, the obtained

overall current density for the used case (area under yellow line) is generally underestimated compared to that of the AM1.5G case (area under red line). As a consequence, the given efficiencies that were measured with this setup are generally slightly underestimated.

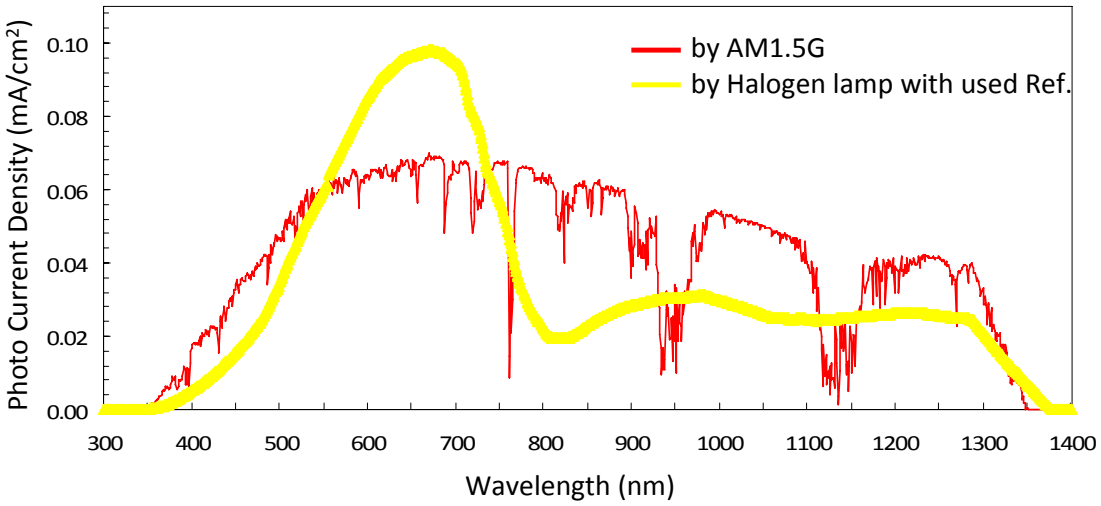

Figure 2-12 Spectrally resolved photo current density as obtained from the used reference cell together with the Halogen lamp in comparison to the photocurrent density as expected from the AM1.5G spectrum.

2.9.2 External quantum efficiency

The *quantum efficiency* (QE) in general is a measure for the photo-sensitivity of a material towards light. It is defined as the percentage of the number of charge carriers collected by the number of photons hitting the photoactive surface. Since the QE is wavelength-dependent, it is typically measured over a certain spectral range, as shown in Figure 2-11 (b).

For complete solar cell device which consist of a stacking of several layers it is typically referred to the *external quantum efficiency* (EQE), which takes the losses of the incident light within the upmost layers into account. Figure 2-11 (b) shows a sketch of a typical EQE of a Cu(In,Ga)Se_2 solar cell with highlighted areas that indicate losses due to a) grid shading, b) surface reflexion, c) ZnO absorption, d) CdS absorption, and e) insufficient absorption and collection [36].

The EQE of a semiconductor photoelectrode can be described by the Gärtner equation [37]:

$$EQE = 1 - \frac{\exp(-\alpha_{abs} W)}{1 + \alpha_{abs} L_n},$$

Equation 2-12

where L_n is the minority charge carrier diffusion length, W the width of the space charge region, and α_{abs} the absorption coefficient. Under the assumption that in a small grained, polycrystalline material, the diffusion length is small, Equation 2-12 can be re-wirtten as

$$EQE = 1 - \exp(-\alpha_{abs} W).$$

Equation 2-13

For a direct band gap material, the absorption coefficient for photon energies near the band gap is expressed by

$$\alpha_{abs} = A(h\nu - E_G)^{\frac{1}{2}}$$

Equation 2-14

with the band gap E_G, and a constant A [38]. Using the latter two equations, a direct correlation of the band gap with the EQE can be derived as follows:

$$-\ln(1 - EQE) = WA(h\nu - E_G)^{\frac{1}{2}}$$

Equation 2-15

Therefore, by plotting $(\ln(1 - EQE))^2$ vs $h\nu$ one obtains a straight line which intersects the x-axis at $h\nu = E_G$. The band gap can be obtained.

The EQE measurements done for this work were performed on a home-built setup. Hereby, the photocurrent measurements were carried out using chopped monochromatic illumination from a xenon and a tungsten lamp (beam area 1 x 1 mm) and a lock-in amplifier was used to measure the photocurrent. The system was calibrated with a silicon and an InGaAs photodiode.

3 Electrodeposition and characterization of precursors

Goal

In this chapter, experimental details are described of how the majority of precursors used for this work were deposited. Furthermore, results of the characterization of the electrodeposited precursors are presented, and improvements in the electrodeposited precursor quality are shown. In addition, suggestions are made in how the ED could be improved further in future experiments.

Background

Electrochemical deposition (electrodeposition, ED) is a commonly used technique to deposit metallic layers, alloys, and compound layers for industrial applications as well as for research purposes. Because of its large scope, the following introduction will primarily focus on the basics of ED and will provide the knowledge necessary to understand experimental results given later in this chapter. Furthermore, a brief summary of published approaches to use electrodeposition to prepare precursors for the Cu_2ZnSnS_4 fabrication will be given. For further details, the reader is referred to the following literature: [39, 40].

3.1 Electrodeposition

3.1.1 Electrochemical cells for electrodeposition

Most generally, electrochemical cells are systems with two conductive electrodes that are separated by at least one conductive electrolyte phase, which contains a reducible or oxidisible component. To understand the processes in such a cell, especially with respect to electrodeposition purposes, one should firstly focus on the (electrical) processes on a half cell (one electrode/electrolyte interface, as sketched in Figure 3-1 (a)) before considering the whole electrochemical cell (see Figure 3-1 (b)) altogether. The important aspects to be considered here are the Fermi level of the electrode (metal M) $E_F = \mu_e(M) - e\varphi_M$ and the redox potential of the solution phase (sol) $E_{F,redox} = (\mu_O(sol) - \mu_R(sol)) - e\varphi(sol)$, where μ_i is the chemical potential of a species *i* (reductant R, oxidant O), and $e\varphi_{sol,M}$ is the inner electrostatic potential. Upon bringing the electrode and the electrolyte in contact, E_F and $E_{F,redox}$ will equalize, as shown in Figure 3-1 (a).

In an electrochemical cell with two metal/electrolyte interfaces (where in the case of Figure 3-1 (b) a salt bridge is dividing two zones), E_F and $E_{F,redox}$ will equalize at each interface. At the same time, the inner electrostatic potential of the solutions are leveled out, even across the salt bridge. Due to this, due to the different work functions Φ_M and hence the Fermi levels of the two different electrodes, and due to the different chemical potentials of the different solutions in the two zones, a potential difference between the two electrodes can be measured. This potential difference is often refered to as *open circuit potential* (OCP).

To be able to deposit or strip ions onto or off an electrode of interest (this electrode is typically called the *working electrode,* WE), an external potential *V* between both electrodes in solution can be applied to shift the position the Fermi level of the one electrode with respect to that of the other electrode, as schematically drawn in Figure 3-1 (c) and (d). Raising the Fermi level of the metal at the WE (making it more negative, see Figure 3-1 (c)), electrons flow from the metal into solution, where they reduce the metal ions which will lead to a deposition.

Taking the example of Cu electrodeposition from an electrolyte containing Cu^{2+}/SO_4^{2-}, the process occurring at the more negative electrode (the cathode) will be a reduction and hence a deposition of Cu^{2+} ions onto the substrate, following:

$$Cu^{2+}_{(aq)} + 2e^- \rightarrow Cu^0_{(s)}$$

Reaction 3-1

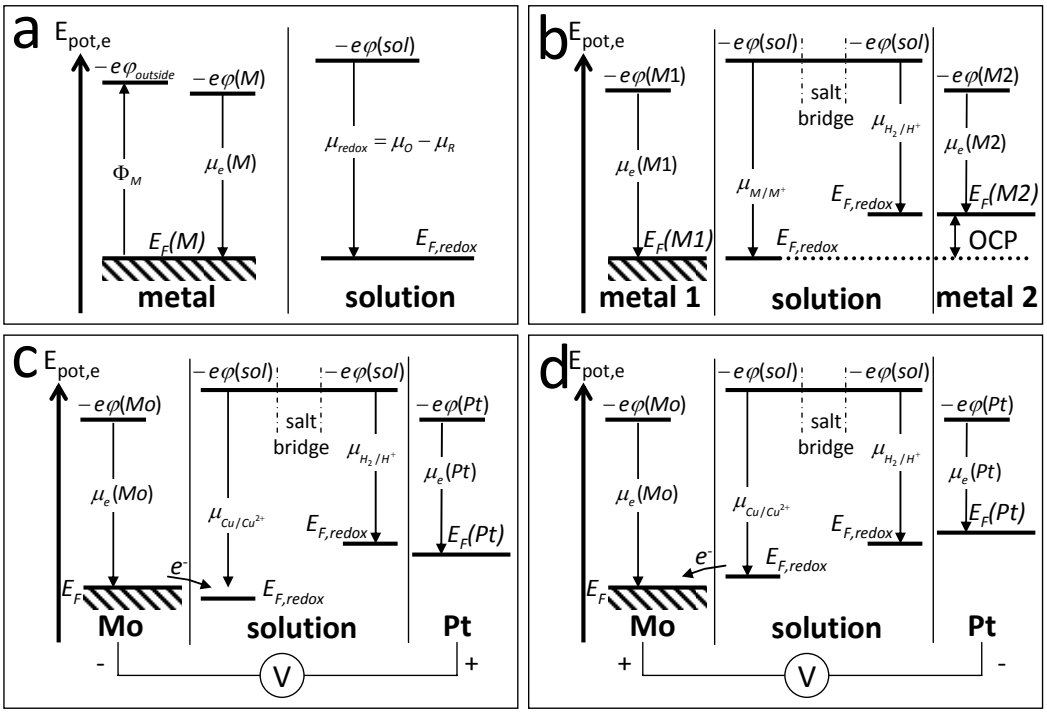

Figure 3-1 (a) Single metal/electrolyte interface. (b) Full electrochemical cell with two metal/electrolyte interfaces. (c) Raising of the Fermi level of the working electrode (left) by applying a more negative voltage *V*, in order to deposit Cu atoms. (d) Lowering of the Fermi level of the working electrode (left) by applying a more positive voltage *V*, in order to strip Cu atoms.

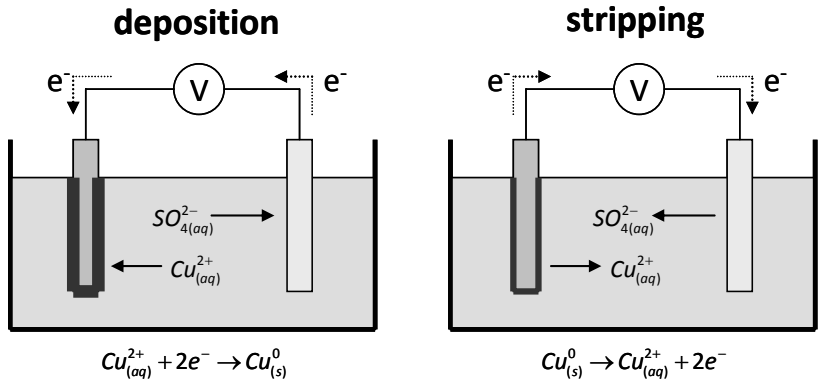

Figure 3-2 Schematic drawing of a two-electrode electrochemical cell undergoing a Cu deposition and Cu stripping in a $CuSO_4$ solution.

Hereby, the concentration of Cu^{2+} ions in the electrolyte will slowly drop. While more Cu^{2+} ions will drift towards the cathode, the SO_4^{2-} ions will drift away towards the anode and hence will contribute to the charge transfer through the electrolyte (see Figure 3-2). Analogously, in a case where $Cu^0_{(s)}$ shall be stripped from the working electrode, a more positive potential has to be applied, lowering the Fermi level of the WE (see Figure 3-1 (d)), such that electrons flow from the solution to the metal, causing an oxidation of $Cu^0_{(s)}$:

$$Cu^{0}_{(s)} \rightarrow Cu^{2+}_{(aq)} + 2e^{-}$$

Reaction 3-2

In both cases, the rate of growth or stripping of the Cu film is proportional to the rate of electron transfer and hence to the current flowing in the system. As a molar quantity, the growth or stripping rate per unit area can be expressed as:

$$\frac{dn}{dt} = \frac{J}{qF},$$

Equation 3-1

where q is the charge on the depositing ion, F is the Faraday constant, and J is the current density.

As mentioned above, the two electrode cell is the most general system usable for electrodeposition but it contains certain drawbacks. Upon immersion of an electrode into an electrolyte, the E_F and $E_{F,redox}$ of the electrode and the electrolyte will equalize, respectively, creating a net charge at the surface of the electrode leading to an electric field. This field will lead to an accumulation of ions from the electrolyte at the interface forming the so-called Helmholtz layer. The potential drop across this layer cannot be measured directly, since any second electrode in the electrolyte would have another Helmholtz layer and thus an unknown potential drop as well. Therefore, only differences in electrode potentials can be measured.

During an electrodeposition process in a two electrodes cell, the formation of such a Helmholtz layer at both electrodes leads to difficulties. While ions from solution are reduced at one electrode, the concentration of those ions in solution will drop leading to a change of the chemical potential $\mu_R(sol)$ of the reductant in the electrolyte and hence to $E_{F,redox}$. This will have an unknown and possibly unequal effect on the two Helmholtz layers making a controllable deposition impossible.

To avoid unknown effects to both Helmholtz layers of the two electrodes, applied potentials should always be quoted with respect to a reference. This implies that one of the two electrode/electrolyte interfaces should be kept constant. This can be achieved by using a so-called *reference electrode* (RE), which is a well-defined system containing a redox couple with a constant potential difference. Such a reference electrode is typically self-contained and electrically only connected with the electrochemical system via a salt bridge. To avoid a change in the redox couple, care has to be taken to avoid high currents to be passed through this reference electrode. Since high currents are quite normal and necessary for electrodepositions, this reference electrode cannot be taken as a replacement for the second electrode in the electrochemical cell, but needs to be introduced as a third electrode. In this three electrode system, which is sketched in Figure 3-3, the deposition potential V will be set and controlled between the *reference electrode* and the *working electrode* while large currents J only flow between the working electrode and the third electrode (the so-called *counter electrode*, CE). Applying all potentials against a reference electrode allows a controlled and repeatable deposition.

Generally, there are different kinds of reference electrodes. Depending on the various possible deposition conditions, their potentials however are all defined with respect to the *normal hydrogen electrode* (NHE).

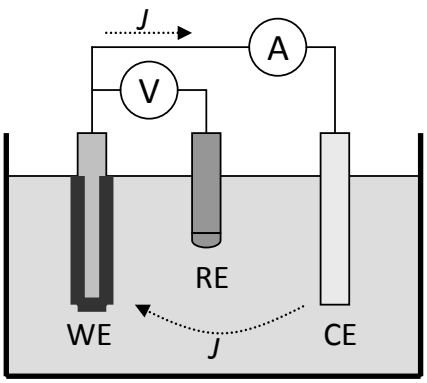

Figure 3-3 Schematic of a three-electrode setup as it was used for the vertical depositions in this work. Typically, a potential *V* is applied between the RE and the WE while the current *J* flows between the CE and the WE.

3.1.2 Cyclic voltammetry

In the previous section, for the case of Cu^{2+} ions, it was briefly discussed that applying a more negative potential than the OCP between the WE and the RE leads to a current of the copper ions from the CE to the WE where they are reduced and hence deposited. Such a current is a good measure for the amount of copper ions deposited in this case. In general, any current flow in the system is a good indicator and measure of an electrochemical reaction taking place. Since such a current is strongly dependent on the applied potential, it is important to measure the current-voltage behavior of the system as a first experiment while investigating a new electrochemical system. The procedure used for this is *cyclic voltammetry*.

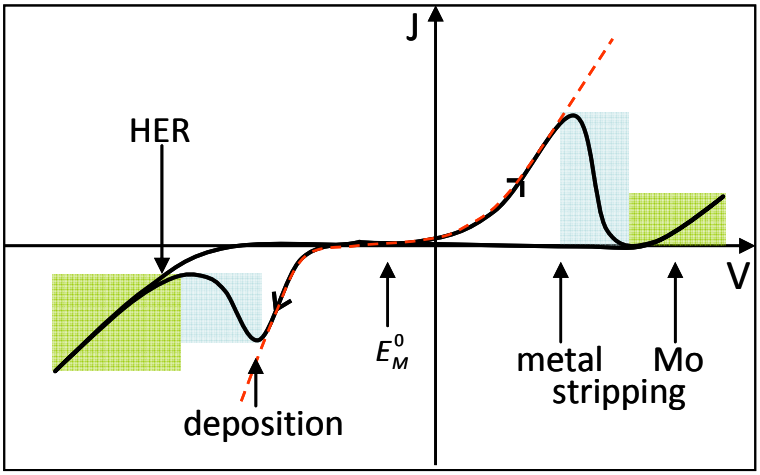

Figure 3-4 Schematic representation of a typical CV for an aqueous electrochemical system showing the various reactions in dependence on the applied potential.

A typical current-voltage behavior (*cyclic voltammogram*, CV) of an aqueous electrochemical system can be seen in Figure 3-4. It contains qualitative as well as quantitative information about the electrochemical system. To obtain such a CV, the potential is swept back and forth while the current is recorded. As a starting point for this scan, the open circuit potential is typically chosen as a point of zero current flow. For the reaction $M^{q+} + 2e^- \rightarrow M^0$ (M^{q+} being positively charged metal ions and M^0 being neutral metal atoms), the potential at which this equilibrium is found is referred to as *standard reduction potential*, E_M^0, and is defined with respect to the NHE under room temperature (25 °C), atmospheric pressure (1 atm), and with a unit activity. For different conditions (different concentrations/activities *a* or temperature T), the actual equilibrium position can be calculated using the *Nernst equation*:

$$E_M = E_M^0 - \frac{RT}{qF}\ln\left(\frac{a_M}{a_{M^{q+}}}\right),$$

Equation 3-2

with R being the molar gas constant, and $a_M = 1$ (for a pure metal). An externally applied electric potential will force the system to shift away from the equilibrium position E_M to a different value E. Such a shift is defined as the *overpotential* η, with

$$\eta = E - E_M,$$

Equation 3-3

and will cause a current flow in the electrochemical system and hence a electrochemical reaction at the electrodes. At the working electrode, a measured net negative current, which is achieved by applying a negative overpotential, will result in a reduction of M^{q+} ions and a net positive current (by a applying a positive overpotential) in their oxidation, respectively. The relation between the overpotential applied and the current density J is described by the *Buttler-Volmer equation*:

$$J = J_0\left[\exp\left(\frac{-qF\alpha\eta}{RT}\right) - \exp\left(\frac{qF(1-\alpha)\eta}{RT}\right)\right],$$

Equation 3-4

where J_0 represents the equal and opposite current at the interface at equilibrium condition and α the reversibility of the electrochemical reaction. In Figure 3-4 the current density described by Equation 3-4 is shown in the red lines and describes the first part of a typical CV (black line) quite well. Walking the lines towards negative overpotentials, a negative current appears which indicates a reduction of metal ions and hence a deposition (following Reaction 3-1). Walking along the line to positive overpotentials, metal ions from the electrode are oxidized and will be stripped from the electrode into the electrolyte (following Reaction 3-2). In a real electrochemical system, however, during deposition or stripping, the concentration of metal ions in solutions or the amount of metal at the electrolyte will decrease, respectively. Since Equation 3-4 is only valid for a constant concentration of metal ions in the electrolyte (in case of deposition) and a constant supply of metal in the electrode (in case of stripping), the current during a real potential scan (black line) drops at some point and cannot be described by this equation any more. In the case of a deposition current, the decrease is due to a depletion of metal ions in the electrolyte in the vicinity of the electrode. Hereby, the current does not reach a zero value since ions from the bulk electrolyte keep on diffusing to the electrode. The deposition is now described as being under diffusion control. In the case of metal stripping, the drop of current is due to a complete depletion of the stripped metal on the electrolyte and will reach a zero value. Both cases are indicated in blue in Figure 3-4. After both currents (in the cases of a negative and of a positive overpotential) have reached their minimum value, they start to increase again, as indicated in green in Figure 3-4. In case of a very negative overpotential, the effect creating this current increase is the *hydrogen evolution reaction* (HER):

$$H^+_{(aq)} + e^- \rightarrow \tfrac{1}{2} H_{2(g)}$$

Reaction 3-3

$$H_2O + e^- \rightarrow \tfrac{1}{2} H_{2(g)} + OH^-_{(aq)}$$

Reaction 3-4

Since typical aqueous electrolytes contain a high concentration of water, the HER can easily take place, causing very high currents in the system and creating large volumes of gas at the electrode. Such evolution of gas will certainly interfere with a deposition process, so that deposition overpotentials should be chosen appropriately so that the HER can be avoided or minimized.

In contrast to this, the current increase at large positive overpotentials can mainly be explained by the oxidation of metal ions from the electrode/substrate used as WE. Both unwanted processes at very negative and very positive overpotentials represent the limits of the voltammogram and hence define the *electrochemical window* for the system studied, within which appropriate potentials for the deposition or stripping have to be chosen. After recording a CV of the system under investigation, suitable potentials used for a deposition process can be chosen. Hereby, care has to be taken that this potential is not near the hydrogen evolution region, such that possible interference of gas evolution and deposition can be avoided. In certain cases, however, the choice of a deposition potential near the hydrogen evolution region is unavoidable. As a result the measured current is not any more fully related to the ions deposited and hence to the growth rate (Equation 3-1) but is a result of both, charge deposited and hydrogen evolution. In this case it is necessary to experimentally determine the fraction of the current that is due to the deposition (also called the *deposition* or *plating efficiency*). This can be done by quantifying the deposited amount and correlating this to the passed charge during deposition.

3.1.3 Constant potential deposition and plating efficiency

Generally, there are two different ways to electrodeposit a layer onto an electrode, one being the deposition under constant current, where a galvanostat (a control unit that controls the voltage across a resistance in series with the electrochemical cell) is being used to automatically vary the potential within a certain range to provide a constant current flow, and the second way being a deposition under constant potential, where a so-called potentiostat (a control unit) applies a potential and measures the current at the same time. In the latter case, the potentiostat is used to apply a fixed potential while the deposition current is measured. For this work, a constant potential deposition has been chosen.

After having determined a suitable deposition potential from a cyclic voltammogram, the next step is to electrodeposit the desired metal onto the substrate. Hereby, at high overpotentials, the deposition current density for the deposition in a static electrolyte is diffusion limited, as briefly mentioned above. The resulting current density can be described by the *Cottrell equation*:

$$J = \frac{nF\left[M^{q+}\right]\sqrt{D}}{\sqrt{\pi t}},$$

Equation 3-5

where D is the diffusion coefficient, t is the time passed , and $[M^{q+}]$ is the initial concentration of the reducible species. In the case where the deposition is performed in a stirred solution or using a *rotating disc electrode* (RDE), the deposition current density is not any more diffusion controlled but mass transport controlled. In the case of the RDE (which has been used in the

depositions conducted for this work) the current density *J* is dependent on the speed of rotation and given by the *Levich equation*:

$$J = 0.62qF\left[M^{q+}\right]\nu^{-\frac{1}{6}}D^{\frac{2}{3}}\omega^{\frac{1}{2}},$$

Equation 3-6

where ω is the angular velocity of the RDE (in rad/s), and ν the kinematic viscosity of the electrolyte (for water at 20 °C, the kinematic viscosity, which is defined as the viscosity of the medium devided by its density, is equal to 10^{-6} m^2s^{-1}). In both, the static and the dynamic case, the current density *J* integrated over the time of deposition gives the total charge Q_{tot} passed. As discussed in the previous subsection, the total charge passed is generally the sum of the charge of the metal deposited Q_M and the charge used for hydrogen evolution Q_{H2}:

$$Q_{tot} = Q_M + Q_{H2}$$

Equation 3-7

Hereby, capacitive charges Q_{cap} are neglected. In order to deposit a film of a certain thickness, the charge passed by the ion deposition needs to be known. To obtain this information from the deposition current densities, the plating efficiency φ_M of the metal deposition needs evaluating. A deposition process can be divided into two stages: (1) The initial deposition of the metal onto the pure substrate; and after having created a layer or the deposited metal, (2) the actual deposition of the metal onto the metal layer. Both processes can have different plating efficiencies, since for both the HER has a different potential. To get a good average of the plating efficiency, various deposition with different Q_{tot} have to be done and their corresponding Q_M have to be measured. Plotting Q_{tot} vs Q_M will give a line and its slope will correspond to the plating efficiency φ_M.

Q_{tot} is known from the current density passed during the deposition, and Q_M can be determined using various techniques, such as: *Atomic absorption spectroscopy* (AAS) – after dissolving the film in an acidic solution – and electrochemical stripping, as shown by J. Scragg [41], but also using *inductively coupled plasma mass spectroscopy* (ICP-MS) – after dissolving the film in an acidic solution – as will be used later in this chapter.

3.2 Electrodeposition approaches for Cu_2ZnSnS_4 precursor fabrication

This section will primarily deal with different approaches that have been published concerning the electrodeposition of precursors for the fabrication of Cu_2ZnSnS_4. The general aim is to homogeneously deposit metallic films of a certain thickness that contain different elements of a certain ratio.

3.2.1 Electrochemical approaches

Up to this point, only a hand full of research groups have been following the route of electrochemical deposition of precursors for Cu_2ZnSnS_4 semiconductor thin film fabrication. Amongst the different strategies of electrodeposition, one can discern betweens those from aqueous solutions [8, 41-50] and those from ionic liquids [51-55]. Since for this work precursors have mainly been electrochemically deposited from aqueous solutions, the focus of this subchapter will be set to this approach. Within this latter approach, however, three main strategies for metallic precursor production have been envisaged by different groups:

(1) Co-deposition of all metallic elements (usually Cu, Zn, and Sn) from one electrolyte [42-44, 46-48].
(2) A stacked elemental layer (SEL) approach, where the metallic elements (usually Cu, Zn, and Sn) were deposited sequentially from different solutions [8, 41, 45, 49, 50].
(3) Electrochemical atomic layer epitaxy (EC-ALE) [56].

The EC-ALE route

Electrochemical atomic layer epitaxy is the electrochemical analogous to atomic layer deposition (ALD) and is based on the alternated underpotential deposition of the desired elements [57, 58]. Since the underpotential deposition is a surface-limited phenomenon, this approach can be used to deposit atomic layer after atomic layer of the desired element. So far only Zhang et al. have used this technique to form a precursor for the formation of a Cu_2ZnSnS_4 thin film [56]. Hereby, they have sequentially deposited sulfur, copper, tin, and zinc in the following order: S/Sn/S/Cu/S/Zn/S/Cu/… . This order has been chosen such that atomic layers of Sn/S, Cu/S, and Zn/S are close together.

An advantage of this deposition route is certainly that all required elements to form CZTS can be deposited such that a subsequent annealing process is only necessary to rearrange/crystallize the thin film and that it does not have to provide sulfur any more. The disadvantage, however, certainly lies in the application of this method, where a large number of layers would have to be deposited one-by-one to achieve a desired film thickness.

So far, there have been no reports on CZTS solar cell that were fabricated using this technique.

The co-deposition route

Amongst the three listed strategies, co-deposition has been the most common approach to electrodeposit precursors for CZTS thin film fabrication. In most of the published results, the electrolyte was typically containing copper sulfate, zinc sulfate, and tin sulfate or tin chloride, besides tri-sodium citrate as a complexing agent [42-44, 46-48]. Up to this point, usually just the metals have been co-deposited to form a Cu-Sn-Zn precursor, however, only one group published results of a deposition of sulfur together with the metals [44]. In their electrolyte, sodium thiosulfate was used as the source for sulfur.

Solar cell devices made from sulfurized co-deposited precursors have shown promising first results with efficiencies up to 3.4 %, achieved by Ennaoui et al, and 3.16 % from Araki et al. [42, 43].

Although a one bath deposition should produce homogeneously mixed (metallic) precursors, leading to homogeneous CZTS films, and although reasonable results have been achieved with this strategy, the approach of co-deposition does have certain drawbacks. First of all, it is difficult and time consuming to adjust the reduction potentials windows of the individual elements by adding a complexing agent such that they overlap. The second challenge is to adjust the concentration of each element and of the complexing agent as well as the pH value (and sometimes also the flow rate of the electrolyte) in a way that a desired composition ratio of those elements could be achieved over a large area. Certainly, the more elements are co-deposited, the more difficult this task will be. Last but not least, having to find compromises between the co-deposition of the individual elements does not necessarily lead to an optimized deposition quality of each element and to an optimized electrolyte lifetime. All of these issues, however, are critical for industrial applications.

The SEL route

In the SEL approach, where the individual elements/metals are deposited one-by-one, it is possible to optimize each individual electrolyte for its purpose. The most important advantage however is its ability to easily vary the precursor composition. For this, one only needs tune the different deposition times, a change of the electrolyte chemistry is not necessary.

Up until the beginning of this PhD project, the stacked elemental layer approach for the fabrication of CZTS thin films has only been followed by Scragg et al. [8, 50]. During this project, there have partly been collaborations with J.J. Scragg [49], leading to CZTS thin film devices with a conversion efficiency of 3.2 % (made from a Mo/Cu/Sn/Cu/Zn stack) from improved electrolytes [49]. This result is in the same range of what has been achieved from co-deposited precursors.

Despite all the positive aspects of the SEL route, it also brings certain drawbacks. Since the different elements/metals are spatially separated in the precursor, certain conditions in a subsequent annealing step have to be met in order to not just introduce sufficient amounts of sulfur but also to intermix all elements homogeneously. Associated with this, the stacking order seems to be relevant for a good result. In the work of Araki et al., the influence of a variation of the stacking order on the properties of Cu_2ZnSnS_4 devices that were produced by E-beam evaporation and a subsequent sulfurization step has been investigated [59]. Their result showed that a Mo/Zn/Sn/Cu stack was the most favorable stacking sequence for CZTS formation, but also that it is important to have Cu and Sn in adjacent layers.

In this work, the SEL approach has been chosen due to its simplicity of varying the precursor composition. In addition, the deposition solutions introduced by Scragg et al have been utilized here [49]. Details to the deposition solutions are listed later, in chapter 3.3.2.

3.2.2 Uniformity of electrodeposited precursors

The uniformity of a precursor can be crucial for the formation of the desired phase, especially if secondary phases can be a problem and would have to be avoided. In the co-deposited route, where a certain elemental ratio can be deposited independently of the lateral position on the sample, thickness variations are not necessarily critical. In the case of the SEL approach, however, macroscopic, lateral thickness variations of individual layers can lead to compositional gradients and hence locally support the formation of secondary phases (as sketched in Figure 3-5).

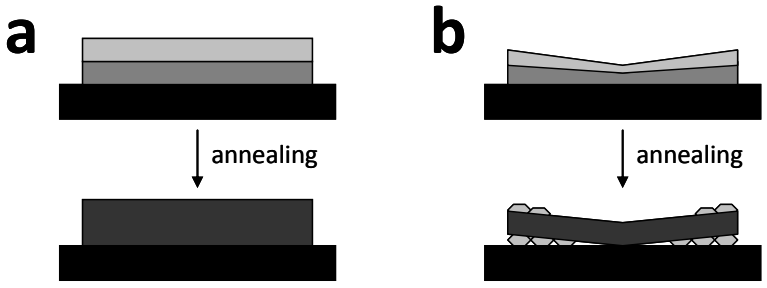

Figure 3-5 Sketch of a cross-section of (a) an ideally uniform precursor stacks (top) which lead to an ideally uniform annealed absorber layer (bottom), and of (b) precursor stack with macroscopic, lateral inhomogeneities (top) which after annealing can lead to secondary phases in the parts where the stoichiometric composition was not met.

At a vertical deposition setup with diffusion controlled ion transport, a gradient of current densities between the bottom to the top of the electrode (as shown in Figure 3-6 (a)) can lead

to such an inhomogeneous deposition and hence to thickness variation of the individual deposits. In order to avoid this, the ion transport has to become mass transport controlled. To achieve this, one can either stir the solution during deposition, one can deposit using a flow controller, or one can use a *rotating disc electrode* (RDE) as the working electrode (see Figure 3-6 (b)). In all of those cases the forced convection of the solution will provide sufficient amounts of ions at the working electrode, leading to a thinner Helmholtz layer, and ensuring that the effect of larger number of electric field lines at the edges of the working electrode does not influence the current density as much – compared to the mass transport of ions – as it does in the diffusion controlled case. In the case of a RDE arrangement, the working electrode is positioned face down, parallel to the counter electrode to minimize the effect a current density gradient between bottom and top. Upon rotation of the rotating disc head – assuming that the WE diameter itself is small compared to the diameter of the rotating disc head, and that the solution extent is large compared to the diameter of the disc – the electrolyte is drawn homogeneously towards the working electrode, providing a uniform current density. In the used setup, this latter issue might not completely be fulfilled.

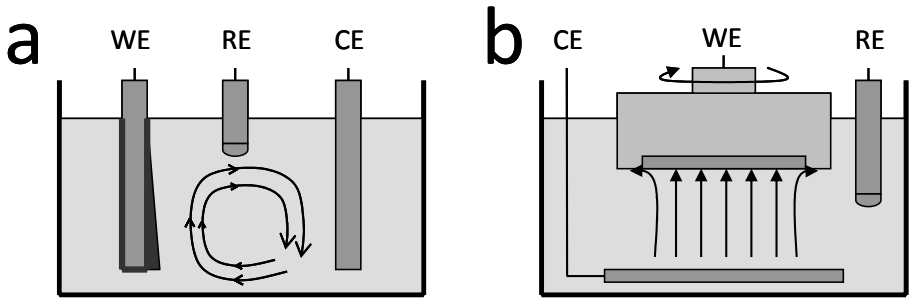

Figure 3-6 Schematic illustration (a) of the natural currents during a deposition using a vertical setup and (b) of the current flow generated by the rotating disc electrode.

3.2.3 Alloying of the precursor

Up to this point, the deposited elemental layers have considered to be discrete. Already at room temperature and upon deposition, however, an interdiffusion of the layers, leading to an alloy formation, is quite significant. Since the reaction pathway to form CZTS depends on the phases present in the precursor, it is important to know the particular conditions of the precursor before the annealing treatment. Furthermore, to be able to compare annealed samples from similar precursors, one needs to make sure that the state of alloy of precursors before an annealing is comparable for the different samples.

As this work focuses on the formation of a CZTS phase and its possible secondary phases, the two main precursor stacks of interest are Cu/Sn and Cu/Zn (please see chapter 4 and 5). In the following, a literature data of room temperature alloy formation of those two stacks is briefly discussed.

The Cu-Sn system

The Cu-Sn system contains a large number of stable phases, which can be seen in its phase diagram, as shown in [60] and in Appendix G. At room temperature, Cu and Sn primarily react to form the hexagonal η-Cu_6Sn_5 phase, as has been reported by K.N. Tu as well as by Carlos et al and J.J. Scragg, but sometimes also to the Cu_5Sn_4 phase, as seen by J.J. Scragg [41, 61, 62]. The investigations of Carlos and Scragg were performed on electrodeposited layers and alongside the Cu-Sn alloys, elemental Cu and Sn have been seen [41, 61]. In the work of Tu it has been reported that within 34 days at room temperature, a 200 nm thick layer of tin on a thick copper

substrate has been entirely consumed to form Cu_6Sn_5 [62]. Hereby, copper primarily diffuses into tin with a diffusion coefficient of $2.0 \cdot 10^{-11}$ m^2s^{-1}, while the diffusion coefficient for the Sn into Cu lies at the order or 10^{-27} m^2s^{-1} [63].

The Cu-Zn system

The phase diagram of the Cu-Zn system (shown in [60] and in Appendix G) reveals a large variety of possible phases of the Cu-Zn. For the case of room temperature alloys from electrodeposited thin Cu-Zn films, several phases, such as β-CuZn, γ-Cu_5Zn_8, and ε-$CuZn_5$ as well as a copper rich $Cu_{0.8}Zn_{0.2}$ have been found [41, 64-66]. Hereby, the intermixing of copper and zinc is primarily due to interdiffusion of Zn atoms into Cu, as Bae has concluded from his voltammetric measurements based on Cu-Zn alloy stripping, that showed a diffusion coefficient of $4.4 \cdot 10^{-19}$ m^2s^{-1} from Zn atoms into bulk copper (as compared to $4.2 \cdot 10^{-28}$ m^2s^{-1} for the diffusion of zinc into copper [63, 67].

Experiment

This section briefly discusses experimental details of the electrodeposition of the precursors as well as of measurements conducted to characterize the precursors.

3.3 Electrodeposition of metal stacks

3.3.1 Substrates

For this investigation molybdenum (Mo) coated soda-lime glass was used as a substrate. The Mo thin films were deposited by magnetron RF sputtering onto commercially available soda-lime glass (dimensions: 25 x 25 x 1 mm^3) using the deposition conditions published in [68]. The molybdenum film had a thickness of ~840 nm [68].

Before using those substrates for deposition, they have been cleaned in an ultra sonic bath for five minutes in, sequentially, detergent (5 vol% decon-90), de-ionized water (DIW), and ethanol, after which they were dried under a flow of nitrogen gas.

3.3.2 Electrolytes

As mentioned in the section "The SEL route" of chapter 3.2.1, the deposition solutions introduced by Scragg et al [41, 49] have been utilized here, only having changed the concentration of the background electrolyte for the Zn bath slightly from 2 M KCl to 3 M KCl. Reasons for this change will be discussed in section 3.6.2. All deposition solutions have been prepared using de-ionized water (resistivity of 18.2 MΩcm), by adding the chemicals in the following order:

1. Background electrolyte and/or pH stabilizer, to provide a pH-stable and highly conductive background electrolyte,
2. complexing agent, to stabilize the dissolved metal ions in solution,
3. metal salt (in case of the Cu salt at elevated temperatures of 55 °C until dissolved), to provide the metals ions for the deposition,
4. other additives, such as surfactants, to improve the morphology of the deposits.

A list of the chemicals used is shown in Table 3-1.

As reported by Scragg, the Cu electrolyte was chosen to be alkaline in order to prevent the Mo from passivation. For more details, the reader is refered to [41].

Table 3-1 Deposition solutions used in this investigation

Electrolyte	Concentration
Copper	3 M NaOH (99.998 % pure, Sigma Aldrich) 0.2 M Sorbitol (99+ %, Sigma Aldrich) 0.1 M $CuSO_4 \cdot 7H_2O$ (99.99 %, Alfa Aeser) 0.932 mM Empigen BB (Sigma Aldrich)
Tin	1 M Methanesulfonic acid (99,5 %, Sigma Aldrich) 50 mM Sn(II) methanefulfonate (50 wt% in water, Sigma Aldrich) 3.6 mM Empigen BB (Sigma Aldrich)
Zinc	3 M KCl (99.995 %, Alfa Aeser) 1 wt.% pH3 Hydrion buffer (Sigma Aldrich) 50 mM $ZnCl_2$ (99.999 %) Alfa Aeser) 0.2 wt% Poly[bis(2-chloroethyl) ether-alt-1,3-bis[3-(dimethylamino)propyl]-urea] (quaternized, solution, Sigma Aldrich)

3.3.3 Electrochemical setup: Deposition and cyclic voltammetry

The general electrochemical setup that was used for this work, consisted (1) of a platinum counter electrode whose surface area was multiple times larger than that of the working electrode, (2) of an Ag/AgCl (3 M KCl: +0.210 V vs. NHE) or a Hg/HgO (1 M KOH: +0.123 V vs. NHE) reference electrode, depending on whether the acidic Sn and Zn or the basic Cu bath was used, respectively, and (3) a Mo substrate as a working electrode. While the potential was applied between the RE and the WE, the current was measured between the WE and the CE. Both, current as well as potential was controlled and monitored by a potentiostat (AUTOLAB, type: PGSTAT302N).

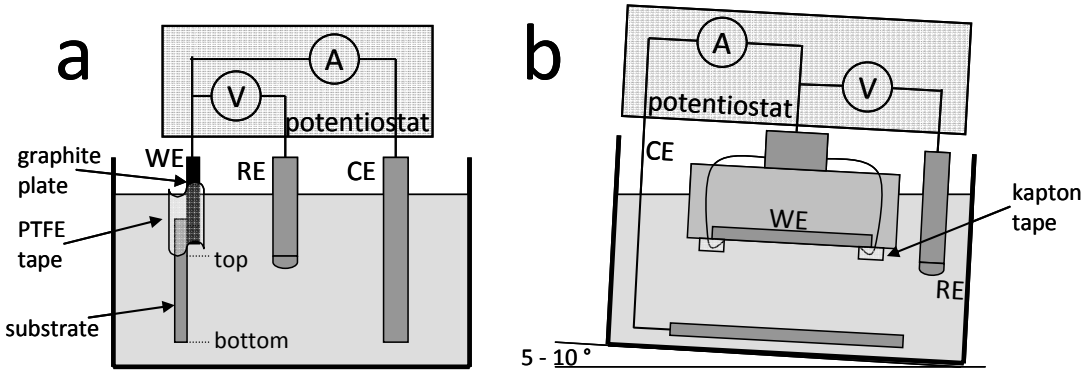

Figure 3-7 The electrochemical setup for the deposition (a) vertically and (b) using the rotating disc electrode.

Vertical deposition

For the experiments that prove an enhancement in lateral homogeneity using the RDE in comparison to a vertical deposition, some Mo substrates had to be mounted vertically. For this, the samples were pressed with the Mo coated side onto a graphite plate using PTFE tape. The graphite plate itself was mounted on a glass rod in which a wire was responsible to electrically connect the graphite (and hence the substrate) to the potentiostat. Upon applying the deposition potential, the samples were lowered into the electrolyte in which the RE and the counter electrode had been placed before (see Figure 3-7 (a)). Care was taken that the surfaces of the CE and the WE were in parallel to avoid a potential gradient caused by the setup geometry. The depositions were carried out until the desired charge had been passed. After the depositions, the samples were removed quickly from the solution, rinsed using DIW, de-mounted from the graphite plate, rinsed thoroughly again (for ca. 1 min), and then dried under a flow of nitrogen.

Deposition using the RDE

For all other electrodepositions, the Mo substrates were mounted on a RDE head that was custom-built for this application. The main body of the head consisted of a cylindrical polyethylene block, in which on the one end a 1 mm deep and 25 x 25 mm^2 wide recess was cut into which the samples were placed. To connect the samples, electrical wires were mounted onto the corners of the samples' surfaces using kapton (polyimide) tape which, furthermore, was responsible to hold the substrates in place. The electrical wires were then put through holes to the backside of the head where they were connected to a cylindrical metallic block that itself was mounted onto the RDE head, which could then be screwed onto the RDE motor. A sketch of the RDE head can be seen in Figure 3-7 (b).

Before each deposition, the electrical path resistance between the metallic block at the back of the RDE head and the Mo substrate at its front was measured to ensure that the applied

potential mainly drops over the substrate and the RE. Typically, only mounted substrates with resistance values of below 1 Ω were used for depositions.

One important difference of the "RDE setup" to the vertical deposition can be found in the fact that the complete "RDE setup" was tilted by 5 to 10 °, to ensure that no gas bubbles (due to hydrogen evolution or due to lowering the RDE head into the solution) are trapped at the WE surface.

Just before lowering the head into the electrolyte, the rotation was set to a certain value that was controlled by a built-in tachometer. Similar to the vertical deposition, the deposition potential here was also applied upon lowering the head into the electrolyte. The rest of the deposition and cleaning procedures used were similar to that described in the previous "vertical deposition" section.

In both cases (the vertical as well as the RDE deposition) the deposition areas of the samples, that were set by either the PTFE or the kapton taping, were measured before the deposition and used to calculate the deposition charge needed for the desired thickness. Here, the plating efficiencies had to be taken into account to achieve a desired composition for stacked samples.

Cyclic voltammetry

The starting potential of a measured cycle was usually chosen to be the open circuit potential (the equilibrium potential). To start a measurement, the substrate was lowered into the electrolye without an applied potential, such that the equilibrium position was set. After a few seconds at this potential, the cycle was started, first into the negative direction. The scan was repeated until a steady state was reached.

3.4 Characterization of precursor films

Besides cyclic voltammetry (discussed in section 3.1.2), the precursor samples have been investigated and characterized by several other techniques. Hereby, ICP-MS and electrochemical stripping were used to investigate the deposition/plating efficiency of the individual metal depositions, SEM images were used to ensure a microscopic homogeneity and EDX line "mapping" (see explanation in Figure 3-8) to measure the macroscopic homogeneity of the deposits, and XRD as well as AES were used to investigate the state of alloy of the metallic layers of the precursor.

Details to all the mentioned techniques, their limitations, and typically used measuring conditions can be found in chapter 2. In the following, a brief description of the conducted experiments will be outlined.

3.4.1 Microscopic and macroscopic homogeneity study: SEM and EDX line "mapping"

SEM images of the individual metallic layers were taken to ensure a microscopic homogeneity. Typically, all SEM images were taken at an accelerating voltage of 7 or 8 keV.

To determine the macroscopic, lateral homogeneity, EDX measurements were taken at different positions along a line on the sample (see Figure 3-8). Hereby, EDX spectra were taken at the same small magnification value (typically 300 x magnification) in a way that compositional information were averaged over a large lateral area. Typically, 20 keV accelerating voltage was used for these measurements to make sure that the EDX information volume extends into the Mo. To withdraw information about the lateral homogeneity, the atomic percentage of the sum of all individual elements without Mo or of Mo only is plotted vs. the lateral position, such that a total percentage variation can be seen. This percentage variation corresponds to a relative thickness variation, since the interaction volume of the

electrons in the sample is roughly the same over the lateral positions, while the signal coming from the Mo substrate varies. The smaller the signal from the Mo becomes, the thicker the layers above must be, hence a relative thickness variation can be observed indirectly.

Further details for both, SEM and EDX measurements can be found in section 2.3.

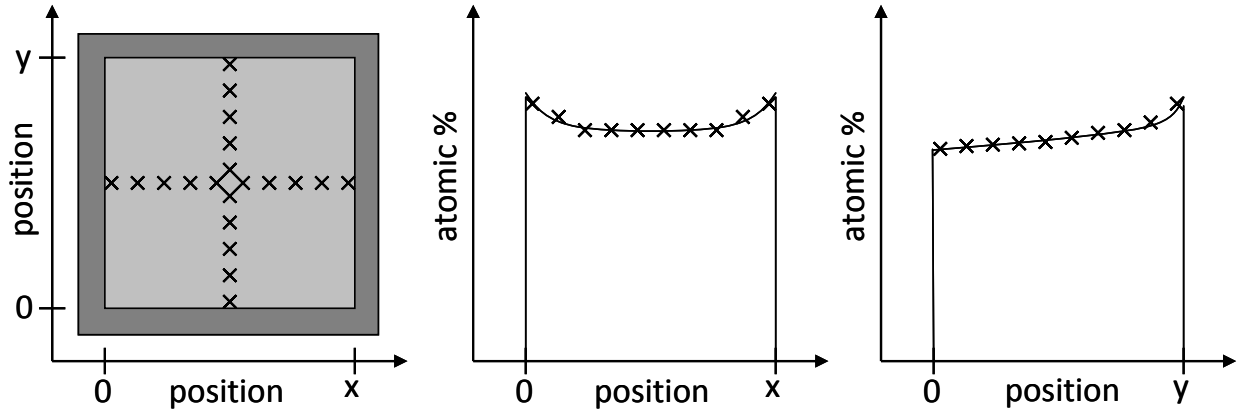

Figure 3-8 Schematic diagrams of an EDX line mapping performed on a x- and y-direction on a sample.

3.4.2 Plating efficiency: ICP-MS measurements and electrochemical stripping

To determine the plating efficiency of the three different metal depositions, a series of samples has been electroplated under standard conditions. Subsequent to their deposition, all samples were dissolved in aqua regia. After this, the different solutions have been diluted in a way that the concentration region of the ICP-MS machine was met (see section 2.8 for details). All sample solutions were measured in the ICP-MS and by comparing the counts per mass of the sample with that of a reference solution, a quantitative number for the metal could be given. A ratio of this experimentally determined total mass per sample and the mass calculated from the total charge passed during deposition has been calculated and gives the value for the plating efficiency. This measurement has been done for a few samples per metallic layer to have some statistical error. Details are given in section 2.8.

To validate those values received from ICP-MS measurements, electrochemical stripping has also been performed. For the stripping, the metal layer (of Sn or Zn) has been deposited at the standard deposition potential taken from the CV (for Sn at -0.49 V, for Zn at -1.22 V, both vs Ag/AgCl), and subsequently this metal layer has been electrochemically stripped again at the stripping potential (-0.2 V for Sn, -0.86 V for Zn, both vs Ag/AgCl), also taken from the CV of the individual metal. The stripped charge was then plotted against the deposited charge and the slope determines the average plating efficiency, assuming a stripping efficiency of 100 %.

3.4.3 Alloying study: X-ray diffraction

To study the state of alloy and its evolution in time of a Mo/Cu/Sn and Mo/Cu/Zn precursor stack, a sample of each stack has been electrodeposited. Right after their depositions, those samples were measured in the XRD to get information about the crystalline phases present. After leaving the samples under vacuum for a certain period of time, the XRD measurement has been repeated and the result was compared to the previous measurement. In the following this step was repeated several times to determine the point in time when the alloying slows down in a way that the precursor stays (basically) unchanged.

All measurements were performed under the typical conditions that are described in section 2.4.4.

3.4.4 AES depth profile

After having determined when the alloying of the stacked layers slows down, it was important to get an idea of how the depth profile of the typically used metallic stack looks like before an annealing step. This information is valuable when investigating the single steps of the phase formation of CZTS from a Mo/Cu/Zn precursor (as discussed in chapter 5). To get this information, a metallic stack was electrodeposited, then the sample was kept under vacuum for more than 1 week until the alloying process slowed down, and then a depth profile has been measured with AES.

Details of the measurement conditions can be found in section 2.7.

Results and Discussion

This part of the chapter deals with the results obtained by the different studies to characterize the precursors used in this work. At first, the electrodeposition of the individual layers as well as their plating efficiencies is envisaged, before the attention is drawn to the improvement of the lateral homogeneity. Finally, to ensure the comparability of the precursors made for this work, its state of alloy is discussed.

3.5 Electrodeposition of the precursors

3.5.1 Cu layer

From Table 3-1 one can see that the Cu deposition was performed from a strong basic solution of a pH of around 14.5, which is why an alkaline-resistive Hg/HgO reference electrode has been used. Whenever a Cu deposition is discussed, all potentials are given with respect to the Hg/HgO reference (1 M KOH), which has a potential of +0.123 V vs. NHE.

Figure 3-10 shows the measured cyclic voltammogram of the Cu deposition onto a Mo substrate. One can see that the reduction peak is situated in a range between -0.98 V and -1.11 V and indicates the optimal deposition range. To the more negative region, however, it is fairly close to the range of the HER, which already gives a hint that the plating efficiency of the Cu deposition might be lower than 100 %. Results of the efficiency investigations are given in section 3.7.

On the reverse scan, there is no clear oxidation peak of Cu. As has been shown by J.J. Scragg, the potential of the Cu oxidations is very close to that of the Mo oxidation, which makes it hard to study the Cu deposition on a Mo substrate [41]. Since this work mainly uses the electrodeposition technique to fabricate CZTS precursor layers, it is of less importance to look into more detail of the oxidation potentials. Important for the following layers to be deposited, however, is the electrochemical window. Its positive end is clearly marked with the Mo oxidation edge. The issue of having similar oxidation potentials for Cu and Mo makes it impossible to determine the plating efficiency of Cu by stripping experiments.

To deposit a Cu layer, a constant potential of -1.085 V has typically been used. The outcome of such a deposit was a bright and smooth Cu layer with a good adhesion. Figure 3-9 (a) shows a typical SEM image of this Cu deposit of a thickness of approximately 170 nm. One can see that the very small copper grains (diameter of 100 nm) sit compactly together. As Scragg mentions in his work, such compactness is mainly due to the surfactant used in the bath recipe, which reduces the surface roughness by increasing the nucleation density while blocking up surface sites during deposition [41].

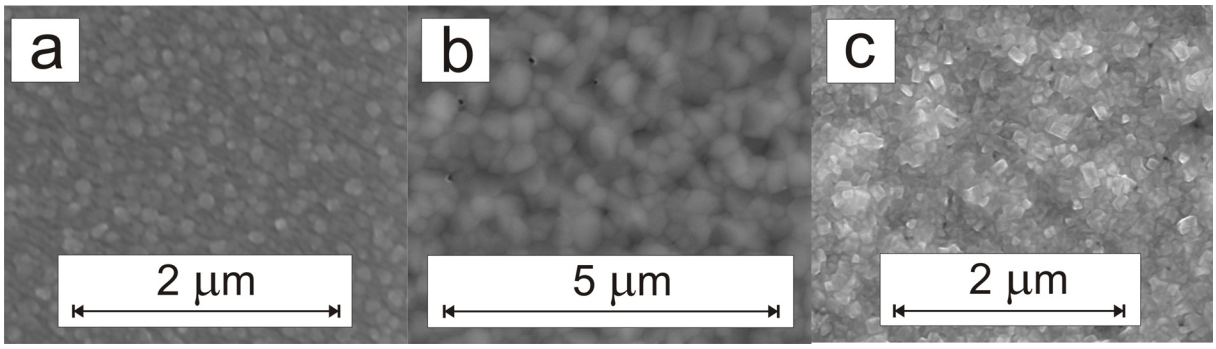

Figure 3-9 SEM top view images of (a) Cu layer deposited on Mo, (b) Sn layer deposited on Cu, and (c) Zn layer deposited on Cu.

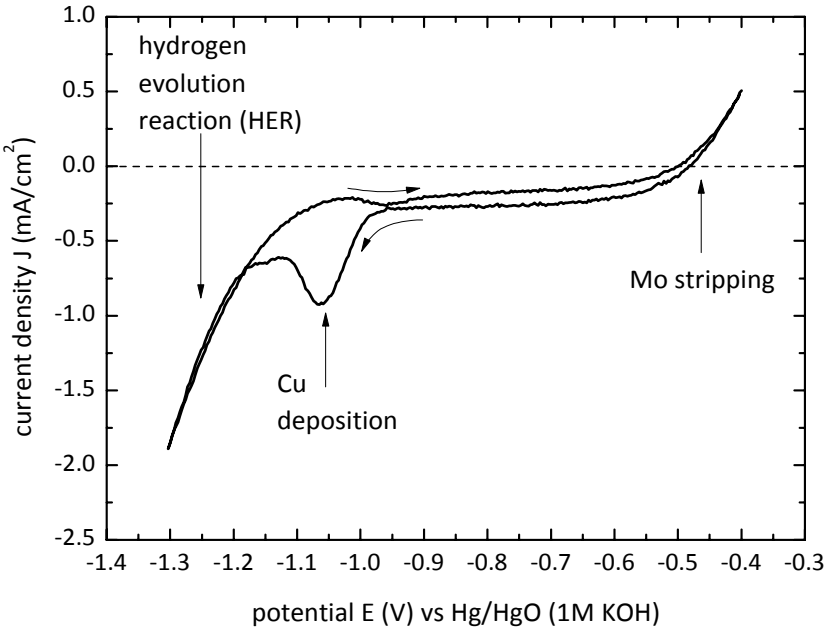

Figure 3-10 Cyclic voltammogram of a static Mo substrate in a Cu^{2+} containing bath. Arrows indicate the direction of the scan, where -0.54 V was the starting point, -1.3 V the first, and -0.4 V the second vortex point. All potentials are given vs a Hg/HgO (1 M KOH) reference electrode. The scan rate was 0.02 V/s.

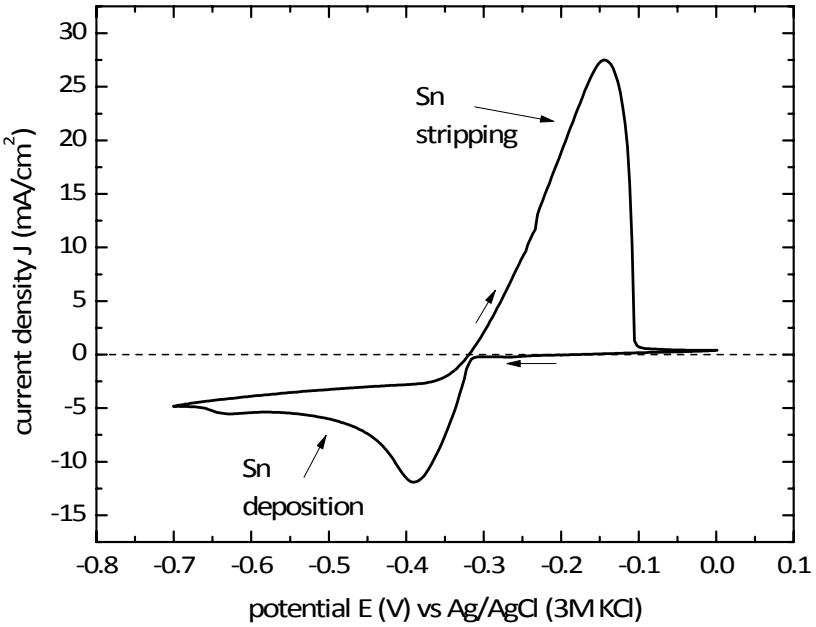

Figure 3-11 Cyclic voltammogram of a static Cu film in a Sn^{2+} containing bath. Arrows indicate the direction of the scan, where -0.21 V was the starting point, -0.7 V the first, and 0.0 V the second vortex point. All potentials are given vs a Ag/AgCl (3 M KCl) reference electrode. The scan rate was 0.02 V/s.

3.5.2 Sn layer

The electrolyte used for the deposition of Sn has a pH of around 1 (see Table 3-1). As a consequence, the reference electrode used for these depositions was a Ag/AgCl reference (3 M KCl), with a potential of +0.210 V vs. NHE. In the following, all potentials discussed with respect to a Sn deposition are given versus the mentioned Ag/AgCl reference.

Figure 3-11 shows the CV of the deposition of Sn on a Cu substrate. The deposition window lies between -0.32 V and -0.65 V and that of the Sn stripping from Cu at values between -0.3 V

and -0.1 V. In the CV shown here, the region of the HER is not shown and starts at even more negative potentials than shown. Similarly to this, the stripping range of Cu and Mo, so the lower end of the electrochemical window, lies at more positive potentials than 0.0 V and is also not shown here. For depositions of Sn on Cu, a potential of -0.49 V was typically chosen. For the stripping experiments shown in section 3.7, a potential of -0.20 V was used.

Figure 3-9 (b) shows the morphology of a Sn deposit (thickness of roughly 200 nm) on Cu. The tin grains have a diameter of up to 500 nm and sit together compactly. The as-deposited Sn layer shows a very high adhesion to the underlying Cu.

3.5.3 Zn layer

Similarly to the Sn deposition, a Ag/AgCl reference electrode has also been used for the deposition of zinc from a pH3 bath.

The cyclic voltammogram of the deposition of Zn onto a Cu layer is presented in Figure 3-12. For this deposition, the range of Zn reduction lies between -1.10 V and -1.30 V and that of the zinc oxidation between -1.00 V and -0.80 V. The electrochemical window in this case lies inbetween -1.40 V cathodically, beyond which the HER is the dominant reaction, and -0.30 V anodically, where the stripping range of Cu and Mo starts. For depositions of Zn on Cu, a potential of -1.22 V was typically chosen. Since this potential is fairly close to that of the HER, a plating efficiency of less than 100 % can be expected. For the stripping experiments shown in section 3.7, a potential of -0.86 V was used.

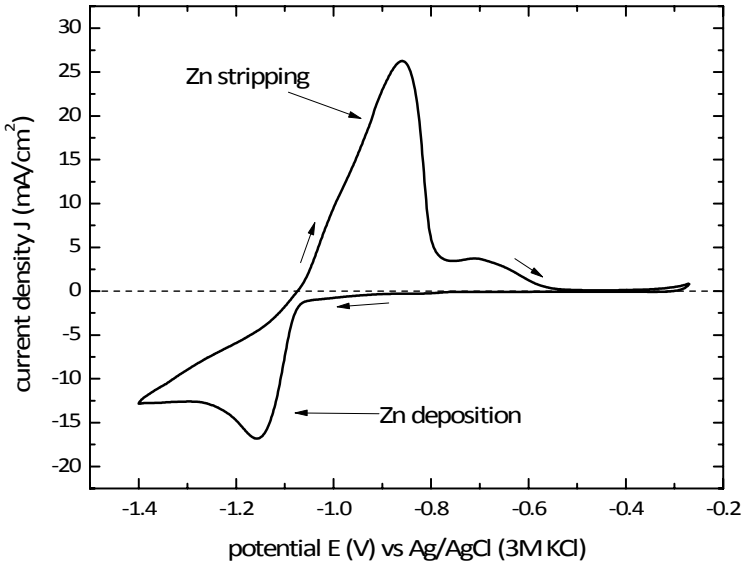

Figure 3-12 Cyclic voltammogram of a static Cu film in a Zn^{2+} containing bath. Arrows indicate the direction of the scan, where -0.27 V was the starting point, -1.40 V the first, and -0.25 V the second vortex point. All potentials are given vs a Ag/AgCl (3 M KCl) reference electrode. The scan rate was 0.05 V/s.

The SEM image in Figure 3-9 (c) shows the morphology of the Zn layer on Cu. The thickness of this layer is typically around 110 nm. This grain size of this very adhesive zinc deposit is fairy small and lies at around 100 nm or less. In the given image, dark spots can be seen, which might indicate holes in the layer. These could be arising from small hydrogen bubbles that might block the deposition of Zn.

3.6 Lateral homogeneity in the precursor

As discussed in section 3.2.2, it is important to deposit precursor layers of uniform thickness to avoid compositional gradients that can lead to regions of secondary phases after annealing.

3.6.1 Vertical deposition vs. deposition under flow control

At the beginning of this project, a vertical electrodeposition setup has been used, as schematically shown in Figure 3-7 (a) [45]. As a measure of the lateral homogeneity of the deposited films, EDX line mappings have been performed, as introduced in the experimental section of this chapter. Figure 3-13 shows a typical EDX line scan (in grey) in both directions, (a) vertical (bottom-top) as well as (b) horizontal (left-right), across a Mo/Cu precursor that was deposited vertically, as indicated in [45]. In the vertical grey line one can see that a larger amount of Cu has been deposited on the bottom of the sample, where on top (at the solution surface near place) there is significantly less Cu. Along the horizontal line, the deposit is fairly flat in the middle, where at the left and right edge the Cu signal gets stronger, indicating a larger Cu thickness. Such a compositional gradient in already one layer does have a strong effect on the overall composition of the annealed sampe. To control the uniformity of the deposit across the whole surface, control of the flux of ions must be achieved at all points across the deposition substrate [45]. For the vertically held substrate in the unstirred deposition bath there is no control of the flux of ions to the substrate [45]. At the sample edges there is a higher flux to the sample surface than in the middle and this explains why the Cu layer is thicker at the edges [45]. Additionally the thickness variation from the top to the bottom is explained by a convection of solution up the surface of the film due to a density difference in the solution near the surface compared to the bulk caused by the solution being depleted in ions near the deposition surface [45]. The depleted solution is less dense than the bulk and rises up allowing fresh solution to arrive at the bottom of the film, and thus the bottom of the film has a relatively higher concentration of ions arriving at its surface than the top leading to a thicker layer at the bottom than the top [45]. In the case of the sample deposited under rotation (see black line in Figure 3-13), where the flux of ions is controlled by the speed of rotation, the Cu signal is homogeneously throughout both measured directions. Small variations lie within the error of the measurement. This result shows that a deposition under mass transport control does improve the lateral uniformity of the deposit. Therefore, the RDE has been used to deposit precursor layers for all further experiments.

It shall be noted that for these measurements an EDX (EDAX Genesis XM 4i) was used which has a fairly large error as seen in section 2.3.2. This large error did probably screen some edge effect that will be discussed in section 3.6.3. In the following, EDX measurements were performed using the Oxford Instruments INCA X-MAX with the error given in section 2.3.2.

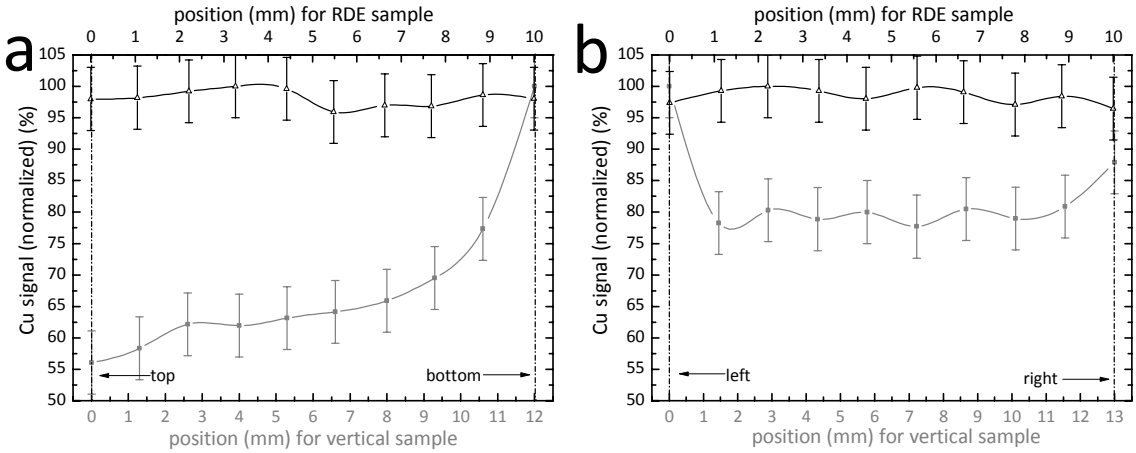

Figure 3-13 EDX line scans measured on a Mo/Cu precursor, showing the relative thickness variation of Cu on Mo across the film along (a) a vertical line (bottom-top), and (b) a horizontal line (left-right) for both, a sample prepared using the vertical setup (grey line with filled symbol) and a sample prepared using the RDE (black line and open symbol). The error bars were determined as described in section 2.3.2.

3.6.2 Lateral homogeneity of a two-stack: Improved Zn deposition

After showing that a mass transport controlled electrochemical system does improve the lateral uniformity of an individual deposit, this section deals with the optimization of the deposited zinc layer on copper by changing the background electrolyte concentration of the zinc bath. Generally, the speed of rotation of the RDE head during deposition was kept at 100 RPM (rotations per minute) as Scragg suggested it to be the optimum [41].

Figure 3-14 shows the EDX line maps of two Mo/Cu/Zn samples, where the Zn layer was deposited using 2 M KCl (in grey) and 3 M KCl (in black) as background electrolyte in zinc bath, respectively. Since both precursors consisted of a couple of layers, the normalized Mo signal is plotted vs. the position across the sample, being inversely related to the thickness variation. One feature that can be taken from this graph is that in both cases, there are still thicker deposits at the edges of the samples than in their central region. This can be explained by the general tendency that electric field lines concentrate at the edges of electrodes, as described in [69]. In the case of the bath with lower background electrolyte concentration, this effect is observed more drastically than in the one with a higher concentration. The standard deviations from the mean values (0.89 for 2 M KCl and 0.99 for 3 M KCl) are 3 % and 1 %, respectively. This can be explained by a higher ionic conductivity in the case of a 3 M KCl solution that lowers the number of electric field lines around the edges and provides a more uniform deposit.

Within the available timeframe of this work, such an investigation has only been performed for the zinc layer since the uniformity of the copper as well as tin deposits were sufficient. In both of the latter cases, the suggested bath concentrations as well as other deposition conditions (see Table 3-2) suggested by Scragg have been used for this work [41]. There have also been no further attempts to optimize the uniformity of the Zn deposit beyond this standard deviation of 1 %.

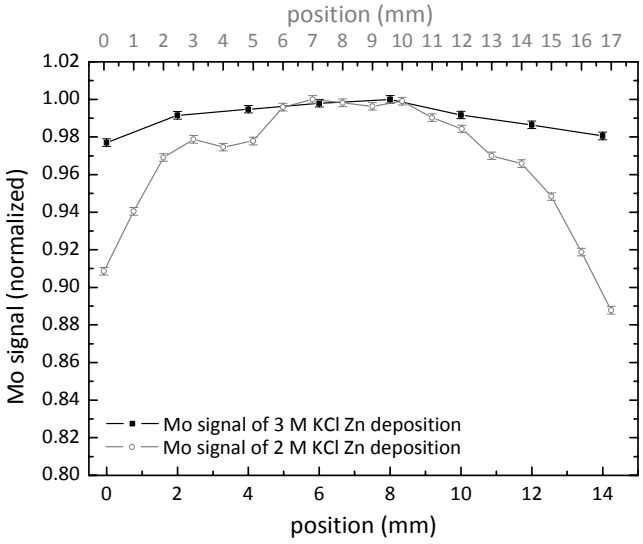

Figure 3-14 Effect of background electrolyte concentration on the uniformity of electrodeposited zinc films on copper. In black, the normalized Mo signal from the EDX line map of the 3 M KCl samples is shown, and in grey that of the 2 M KCl sample. The error bars were determined as described in section 2.3.2.

Table 3-2 Typical electrodeposition conditions for each step in the preparation of Mo/Cu, Mo/Cu/Sn, and Mo/Cu/Zn precursors.

Deposit	Potential (V vs. Ref.)	Speed of rotation (RPM)
Cu on Mo	-1.085 (Hg/HgO)	300
Sn on Cu	-0.49 (Ag/AgCl)	300
Zn on Cu	-1.22 (Ag/AgCl)	100

3.6.3 Lateral homogeneity of an annealed sample

In the previous section it was shown that the lateral thickness variation of a Mo/Cu/Zn precursor could be minimized. Hereby, the main variations could be seen on the edges of the sample. In this section it will be investigated, how such a thickness variation translates into an annealed sample. Therefore, a typical Mo/Cu/Zn stack was annealed using standard conditions (see chapter 5) and matrices of EDX line maps were taken from the sample before and after annealing. Figure 3-15 (a) and (b) shows those line maps matrices.

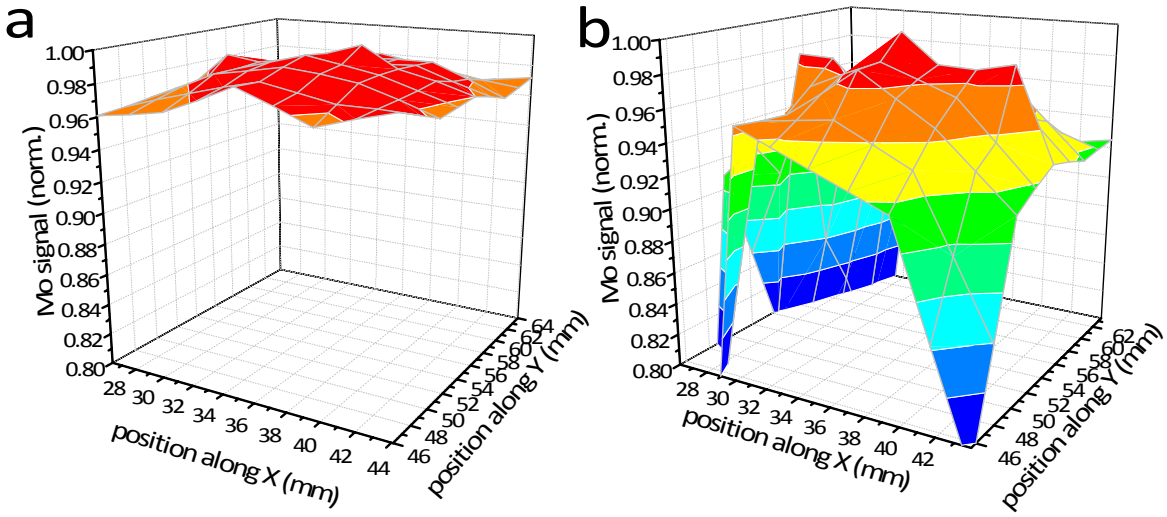

Figure 3-15 Comparison of relative thickness variations of a sample (a) before and (b) after annealing.

Comparing the line maps from Figure 3-15 (a) and (b), one can clearly see that the overall uniformity changes upon annealing to larger lateral inhomogeneities. In the case of the precursor stack, the standard deviation from the mean value (0.982) of the normalized Mo signal is comparable to that measured in the previous section and has a value of 1.1 %. In comparison, the standard deviation from the mean value (0.944) of the annealed sample of 11.6 % is much larger. This is mainly due to the large thickness variations along the edge of the sample's surface. While neglecting the outer 2 mm of the annealed sample, the value for the standard deviation can be decreased to 2.7 %, leaving a relatively flat film of an area of around 14 x 14 mm^2.

From this result it can be seen that it is important to remove the outer 2 mm of a sample after annealing and before its characterization to avoid certain misinterpretations. Furthermore, this result defines the framework in which large scale averaging characterization results (such as X-ray pattern) shall be interpreted.

3.7 Deposition efficiency

So far, it has been looked at determining the deposition conditions of each layer to achieve a good uniformity and compact films. In order to get a precursor stack of a desired thickness and composition, it is necessary to determine the deposition efficiency of each layer. In the following, two approaches have been chosen for its determination: *Inductively coupled plasma mass spectroscopy* (ICP-MS) and *electrochemical stripping*.

3.7.1 Plating efficiency from ICP-MS measurements

As described in section 3.4.2, a few samples have been electrodeposited under standard conditions to be analyzed in the ICP-MS. Table 3-3 lists the results for the masses $m_{ICP\text{-}MS}$ of the

individual metals that were obtained by ICP-MS. Furthermore, it contains the masses $m_{calculated}$ that were calculated from the charge passed during the deposition. The ratio of the given masses gives the plating efficiency $\varphi_{plating\ efficiency}$ of each deposition, leading to an average plating efficiency $\varphi_{average\ efficiency}$ for a certain metal deposition.

For the deposition of Cu on a Mo substrate, an average deposition efficiency of 85 ± 6 %, for that for Sn on Cu an average of 94 ± 3 %, and for that Zn on Cu an average of 78 ± 2 % has been determined. The result of the plating efficiency for tin is in good agreement with that found by J.J. Scragg – who used the same plating bath for Sn and Cu, and a similar one for Zn – however the ones for the copper (100 % in [41]) and zinc (90 % in [41]) deposition are slightly off. The reason for the differences in Zn deposition probably lies in the fact that the plating solution used here had a much higher background electrolyte concentration. One difference made in the deposition of Cu between Scragg's and this work is that here a slightly more negative deposition potential was chosen, which increases the chance of hydrogen evolution. A difference in plating efficiency of 15 %, however, cannot be fully explain by this and might be due to other, yet unknown and unclear reasons.

The calculation of the error is discussed in section 2.8.

Table 3-3 Results of ICP-MS measurements of the different samples, and their plating efficiency

Element	Sample	$m_{ICP\text{-}MS}$ (µg)	$m_{calculated}$ (µg)	$\varphi_{plating\ efficiency}$ (%)	$\varphi_{average\ efficiency}$ (%)
Cu	Cu_01	253 ± 3	278.2 ± 0.3	91 ± 1	**85 ± 6**
	Cu_02	215 ± 3	246.3 ± 0.3	88 ± 1	
	Cu_03	209 ± 3	269.6 ± 0.3	78 ± 1	
	Cu_04	201 ± 3	238.4 ± 0.3	84 ± 1	
Sn	Sn_01	323 ± 8	346.9 ± 0.6	93 ± 2	**94 ± 3**
	Sn_02	323 ± 7	335.2 ± 0.6	96 ± 2	
	Sn_03	320 ± 8	333.4 ± 0.6	96 ± 2	
	Sn_04	319 ± 7	334.6 ± 0.6	96 ± 2	
	Sn_05	344 ± 8	384.4 ± 0.6	90 ± 2	
Zn	Zn_01	162 ± 3	211.1 ± 0.3	77 ± 1	**78 ± 2**
	Zn_02	160 ± 3	205.0 ± 0.3	78 ± 1	
	Zn_03	164 ± 3	203.9 ± 0.3	80 ± 1	
	Zn_04	161 ± 3	204.6 ± 0.3	79 ± 1	
	Zn_05	178 ± 3	229.7 ± 0.3	77 ± 1	

3.7.2 Plating efficiency from electro-chemical stripping

To confirm the data shown in the previous section, a series of depositions, followed by electrochemical stripping, have been performed and the charges deposited and stripped have been recorded. Since the oxidation potential for Cu and Mo are too close to each other such that Cu could not be stripped individually, as discussed in section 3.5.1, it was only possible to conduct these experiments for Sn and Zn depositions on Cu.

In the series of experiments that have been conducted, five different charges have been deposited and subsequently been stripped. For both, tin as well as zinc, the charges deposited have been plotted as a function of the charge stripped, as shown in Figure 3-16 (a) and (b), respectively. Assuming that the total amount of the deposited metals are oxidized as the stripping current reaches a zero value, the ratio of the stripped charge Q_{strip} and the charge passed during deposition Q_{dep} provides the plating efficiency. Since the actual deposition is divided into two parts, (1) one being the metal deposition onto the Cu substrate and (2) one

being the metal deposition onto the same metal (as discussed in section 3.1.3) the plating efficiencies for the different charges deposited are slightly different, as can be seen in Figure 3-16. A good average for the overall efficiency can hence be given by the slope of a straight line, fitting all data points and passing through zero. For the tin deposition, the obtained value is 92.9 ± 0.5 % and matches the result measured in the ICP-MS experiment. The plating efficiency for the zinc deposition of 79.4 ± 1.3 % is also in a very good agreement to the previously discussed value of 78 ± 2 %.

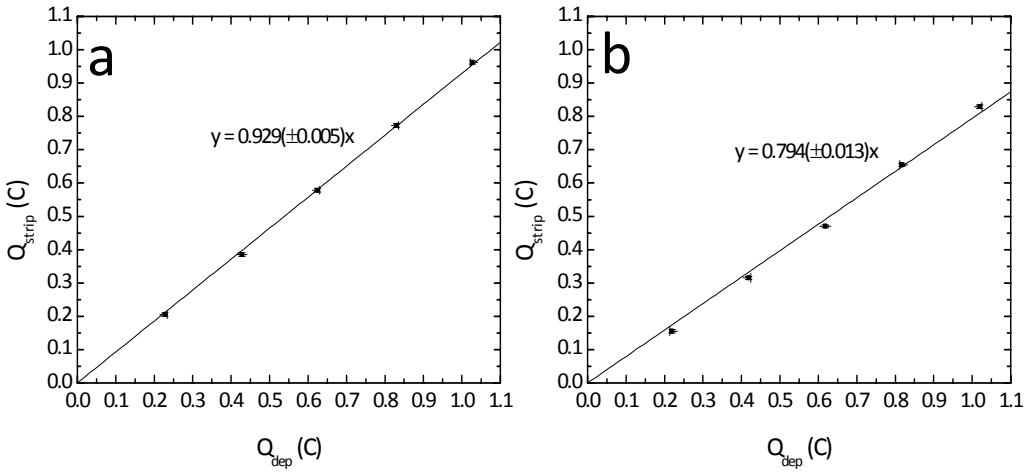

Figure 3-16 Stripped charge as a function of the charge deposited for (a) Sn on Cu and for (b) Zn on Cu.

3.8 Alloy formation in metallic bilayers

After being able to uniformly deposit metallic stacks of a certain thickness and composition ratio, it is now important to make sure that the precursors are roughly the same state of alloy before annealing them. This ensures that the subsequent reactions during the annealing process are comparable. In the following, time resolved *X-ray diffraction* results of both, the Mo/Cu/Zn as well as the Mo/Cu/Sn stack are presented.

3.8.1 Alloy formation in a Mo/Cu/Zn stack

Figure 3-17 shows XRD patterns of a zinc poor (Cu/Zn = 2.7), as-deposited Mo/Cu/Zn stack, one hour, eight hours, one week, and one month after its deposition. Aside from the peaks marked with "*", which belong to a Mo phase (coming from the substrate), the main other peaks belong to Cu, Zn, $CuZn_5$, and Cu_5Zn_8 phases.

In the pattern measured one hour after deposition, certain peaks can already be associated with $CuZn_5$ (37.69°, 42.19°, and 57.56°; green lines) and Cu_5Zn_8 (43.20°, and 50.30°; red lines) alloys. This indicates that already at this very early stage after deposition an alloying process has occurred, as could be expected from the high diffusion coefficient of Zn into Cu at room temperature (see section 3.2.3). Other than these, unique reflections due to a pure zinc phase (36.47° and 38.99°; dark yellow lines) indicate that not all the zinc has alloyed with Cu, yet. Peaks arising from a pure Cu phase (43.35° and 50.49°; blue lines), however, are not unique but match those of Cu_5Zn_8. Therefore, the existence of a pure Cu phase can neither be proven nor disproven by XRD, but its presence can be expected.

The pattern measured eight hours after deposition already shows some strong changes compared to the 1 hour case. While all reflections due to the $CuZn_5$ phase become weaker, the ones from the Cu_5Zn_8 (especially at 34.98°, and 48.03°) get stronger, indicating a more enhanced intermixture of Zn and Cu. This trend continues in the pattern taken one week after deposition, making peaks of the $CuZn_5$ phase disappear and the ones due to Cu_5Zn_8 even

stronger. Hereby, no major changes can be observed for the unique Zn reflections that are still present. After this, however, the alloying process seems to slow down, leaving the pattern, measured one month after deposition, almost unchanged to that measured one week after deposition. A more or less steady state of alloying is reached at around one week. Following this result, the precursor stacks deposited for the samples used in the scope of this work have typically been left under vacuum for around one week after their deposition to ensure a comparable state of alloy before their annealing.

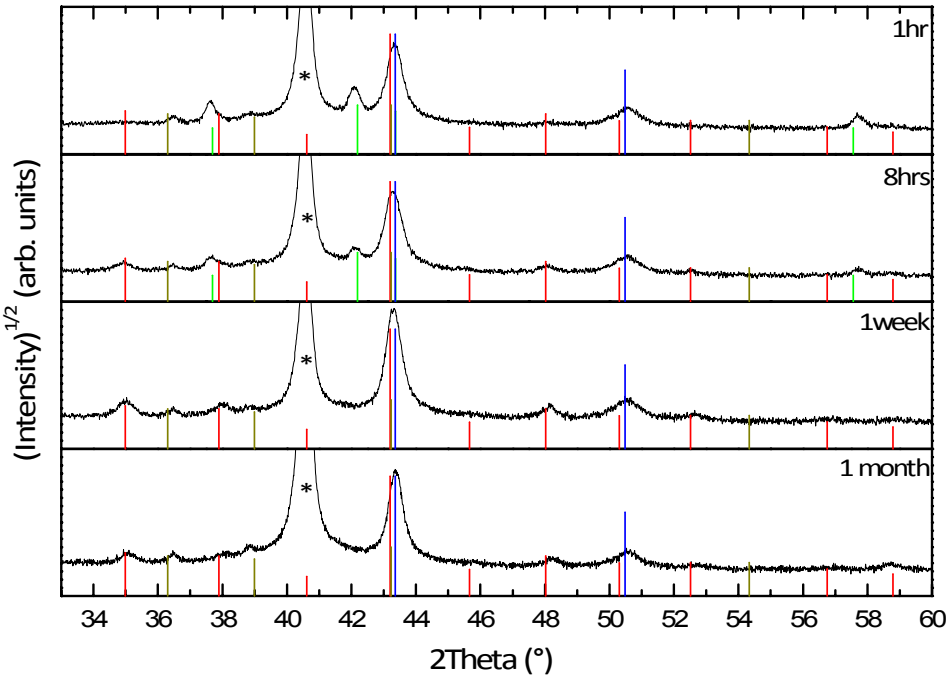

Figure 3-17 XRD pattern of an as-deposited Mo/Cu/Zn stack, 1 hr, 8 hrs, 1 week, and 1 month after deposition. The peaks indicated with "*" represent a Mo phase (JCPDS: 04-001-0059), the red lines indicate the Cu_5Zn_8 phase (JCPDS: 04-007-1117), the green lines a $CuZn_5$ phase (JCPDS: 00-035-1152), the blue ones a Cu (JCPDS: 04-001-2746) and the dark yellow ones a Zn phase (JCPDS: 00-004-0831), respectively.

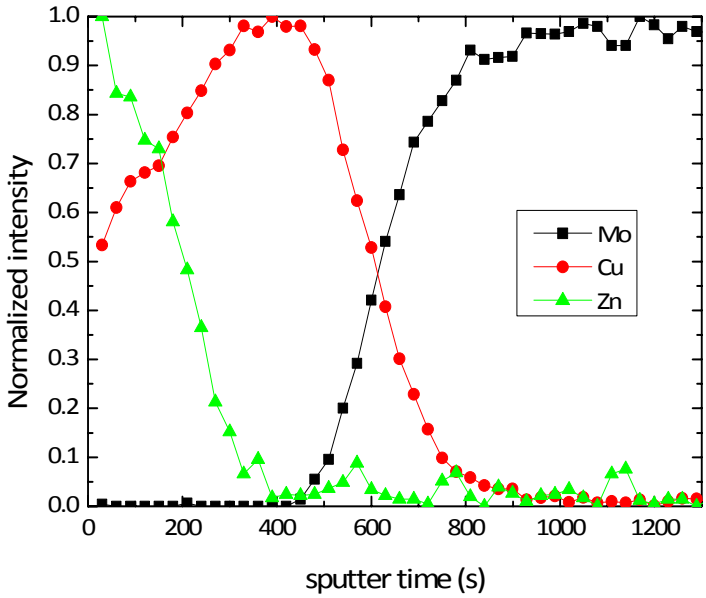

Figure 3-18 Normalized Auger electron spectroscopy depth profile measured on a Mo/Cu/Zn stack older than 1 week. The red signal belongs to Cu, the green one to Zn, and the black one to Mo. Some oxygen has been detected in the Mo which is not shown here.

To know the distribution of Zn and Cu throughout the depth of the film of a typical precursor that has been left under vacuum for one week, an AES depth profile has been measured. Figure 3-18 shows the result. One can see a fairly large amount of Cu at the surface of the film (at low sputter times), underlining the quick alloy formation at room temperature. While the Zn signal gradually decreases to a zero value around three quarters into the film, the signal coming from Cu increases, reaching its maximum. This result indicates that a pure Cu phase is present at the back of the film and that its contribution to the XRD pattern is hidden behind the reflections due to Cu_5Zn_8. This result will be of importance when looking at the formation of CZTS during the annealing process, which will be shown in chapter 5.

3.8.2 Alloy formation in a Mo/Cu/Sn stack

The XRD pattern of an as-deposited Mo/Cu/Sn stack, one hour, one day, one week, and three weeks after its deposition is shown in Figure 3-19. Besides the contribution of the Mo substrate (marked with "*"), reflections due to a pure Sn phase (30.64°, 32.02°, 43.88°, and 44.91°; red lines) and those coming from a Cu-Sn alloy (main reflections of either CuSn, Cu_6Sn_5, or Cu_5Sn_4: 30.17°, 43.06°, and 43.32°; green lines) can be observed already one hour after the deposition of the sample. Similar to the case of a Mo/Cu/Zn stack and as expected (see section 3.2.3), a very fast intermixture of Cu and Sn can be observed.

It shall be noted the main reflections of the given Cu-Sn alloys are all very close and small reflections are not seen, so that a clear distinction is not possible on the basis of those results. Furthermore, the existence of a Cu phase (43.35°; orange lines) can also neither be proven nor disproven, but its presence can be expected.

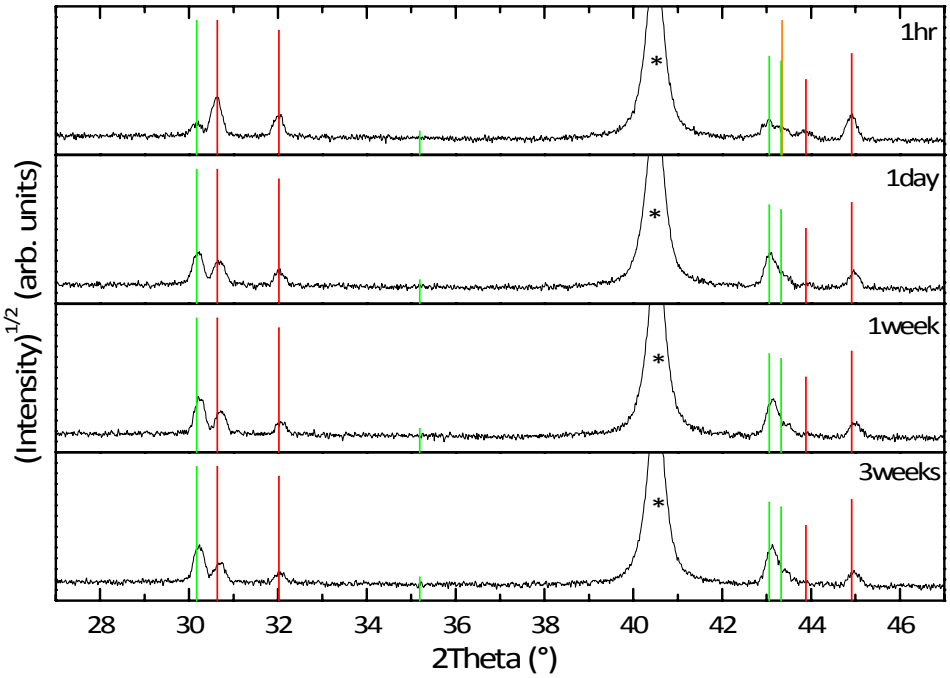

Figure 3-19 XRD pattern of an as-deposited Mo/Cu/Sn stack, 1 hr, 1 day, 1 week, and 3 weeks after deposition. The peaks indicated with "*" represent a Mo phase (JCPDS: 04-001-0059), the red lines indicate the Sn phase (JCPDS: 04-004-7747), the orange ones a Cu (JCPDS: 04-001-2746) phase, and the green lines indicate phases due to a Cu-Sn alloy (CuSn, Cu_6Sn_5, Cu_5Sn_4) which all share their main peaks and which could all be present here (JCPDS: 03-065-3434, 04-007-2658, 04-007-2295).

The pattern measured one day after the deposition already shows certain differences compared to the pattern of the measurement one hour after deposition. While the peaks due to a Sn phase lose in intensity, the ones related to a Cu-Sn alloy become stronger. This trend continues noticeably one week after deposition and seems to slow down after that. No major changes can be seen between the “1 week” and “3 week” measurements. A more or less steady state of alloying is reached at around one week.

This result is very similar to the one from the Mo/Cu/Zn stack. In the same manner as for those Mo/Cu/Zn precursors, the Mo/Cu/Sn precursors (used for the secondary phase study in chapter 4) have also been kept under vacuum for around one week before annealing to ensure a comparable state of alloy.

Conclusion

Electrodeposition is a commonly used technique in industrial applications as well as for research purposes to deposit metals, alloys, and compound layers in a cost-effective way. Within the scope of this work, electrodeposition techniques were used to provide precursors for the study of (1) possible secondary phases of the semiconductor Cu_2ZnSnS_4 (see chapter 4), and (2) of the formation process of Cu_2ZnSnS_4 from a simplified precursor stack (see chapter 5). For this, an existing electrodeposition procedure was used.

In this chapter it could be shown that a macroscopically as well as microscopically uniform deposition of Cu, Zn, or Sn comprising stacks was possible. Hereby, the macroscopically uniformity was achieved by a mass transport controlled deposition using a rotating disc electrode, and their uniformity limits as well as their translation into annealed samples were discussed. The main result was that a relatively flat film (1 % std. deviation in uniformity for a precursor and 2.7 % for an annealed sample) can be produced over an area of 14 x 14 mm^2.

In a further study, the deposition efficiency of Cu onto Mo, Sn onto Cu, as well as Zn onto Cu has been investigated in order to deposit layers of a desired thickness. The results show that none of the depositions are totally efficient (plating efficiencies for Cu: 85 ± 6%, Zn: 78 ±1 %, and Sn: 94 ± 3 %) such that hydrogen evolution has to be considered in each deposition.

Knowing how to deposit uniform metal stacks of a certain thickness and compositional ratios, the alloying of Cu/Sn as well as Cu/Zn stacks was demonstrated. A time-dependent study showed that in both cases the alloy formations slowed down drastically around one week after deposition. This result is of importance when looking at the reaction mechanism of the formation of CZTS from a metallic precursor stack. To ensure comparable conditions of the precursors before annealing, all precursors have been kept under vacuum for around one week before further usage.

4 Secondary phases

Goal

After introducing how the precursors for the different studies have been prepared, this chapter mainly focuses on the possible secondary phases that can be formed during the process of Cu_2ZnSnS_4 formation. In this respect, the first point of interest is to determine which pure phases can be formed at the same conditions typically used to form CZTS. The obtained phases are then characterized by XRD, Raman spectroscopy, SEM, and EDX/WDX measurements and the results are compared to that of the CZTS phase. The main part of this chapter then focuses on the discrimination of secondary phases from the CZTS phase and gives an answer to the question which analytical tool can be used to identify all present phases in a thin film and to qualitatively and quantitatively discern them from the Cu_2ZnSnS_4 phase. In further investigations KCN etching of the different phases will be discussed briefly, and the use of the Cu_2SnS_3 ternary phase as a photovoltaic absorber will be shown.

Background

4.1 The Cu-Zn-Sn-S material system

4.1.1 Phase diagram and crystal structure

Until now, the phase diagram of the quaternary system Cu-Zn-Sn-S has only been studied by Moh and by Olekseyuk and co-workers [15, 70]. In the quasi-ternary phase diagram presented by Moh (not shown here), the Cu_2ZnSnS_4 phase is the only stable phase at 600 °C [70]. In more recent results by Olekseyuk et al., where the pseudo-ternary phase diagram (a two dimensional representation of a four dimensional phase diagram presented with three axis of three phases) is given at 397 °C (see Figure 4-1), an additional quaternary phase $Cu_2ZnSn_3S_8$ has been observed. Similar to Cu_2ZnSnS_4 and according to Olekseyuk et al., this tin rich compound crystallizes also in a tetragonal structure [15]. As outlined in several publications (such as in [41, 71, 72]), the crystal structure of Cu_2ZnSnS_4 derives from that of the ternary chalcopyrite structure $CuIn(S,Se)_2$ (see Figure 4-2) by replacing the trivalent indium ions with equal numbers of divalent Zn and tetravalent Sn ions. Hereby, two different ion arrangements are found. While the Sn and S atoms are unchanged, the ordering of the Zn and Cu atoms can vary, as sketched in Figure 4-2. When the ordering is such that the Zn atoms are in plane with the Sn atoms while the Cu atoms occupy a different plane on its own, this is known as the stannite-type structure (space group $I\bar{4}2m$). In the case where in the one plane Cu and Sn and in the other plane Cu an Zn are mixed, this is known as the kesterite-type structure (space group $I\bar{4}$) [41, 73].

Experimentally, using X-ray diffraction, it is difficult to distinguish between a kesterite- and a stannite-type structure in the case of Cu_2ZnSnS_4. This is due to the fact that the X-rays interact with the electron shell of the atoms which makes the isoelectronic Cu^+ and Zn^{2+} indistinguishable [72]. In neutron scattering, where the neutrons interact with the nuclei, a discrimination of Cu and Zn and hence of kesterite- and stannite-type structures is possible [72].

Several groups have calculated the total energies of the stannite- as well as kesterite-type phase for the Cu_2ZnSnS_4 compound [5, 7, 74, 75]. They have found that the lowest energy configuration for CZTS is the kesterite-type structure, but only by a difference of around 3 meV/atom [5, 7, 74, 75]. This small energy difference can be the reason that a stannite-type phase co-exists with a kesterite-type phase [72]. Such a polymorphism exists in the case of

$Cu(In,Ga)Se_2$ and has been shown to influence the solar cell conversion efficiency in a negative way [76]. Since in the case of CZTS the band gap for stannite-type structures is predicted to be smaller than that of kesterite-type structures (see electro-optical properties), a mixed stannite-kesterite thin film would suffer from the lower V_{OC} [72].

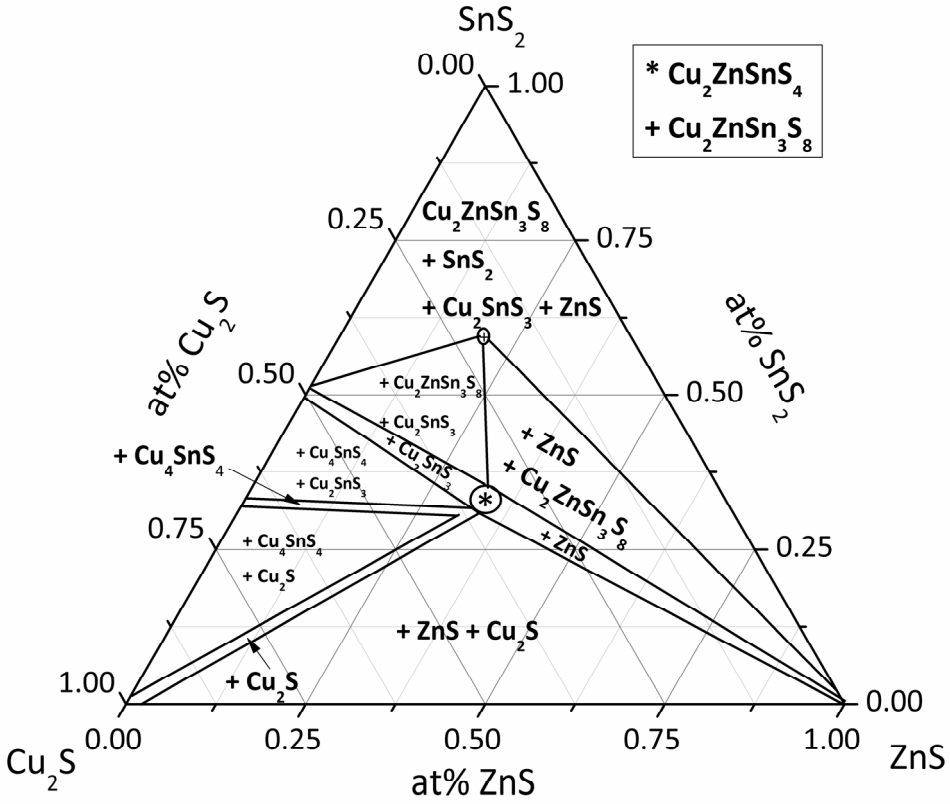

Figure 4-1 Pseudo-ternary phase diagram adapted from [15], showing the two stable quaternary phases Cu_2ZnSnS_4 ("*") and $Cu_2ZnSn_3S_8$ ("+"), and all possible secondary phases at 397 °C according to [15].

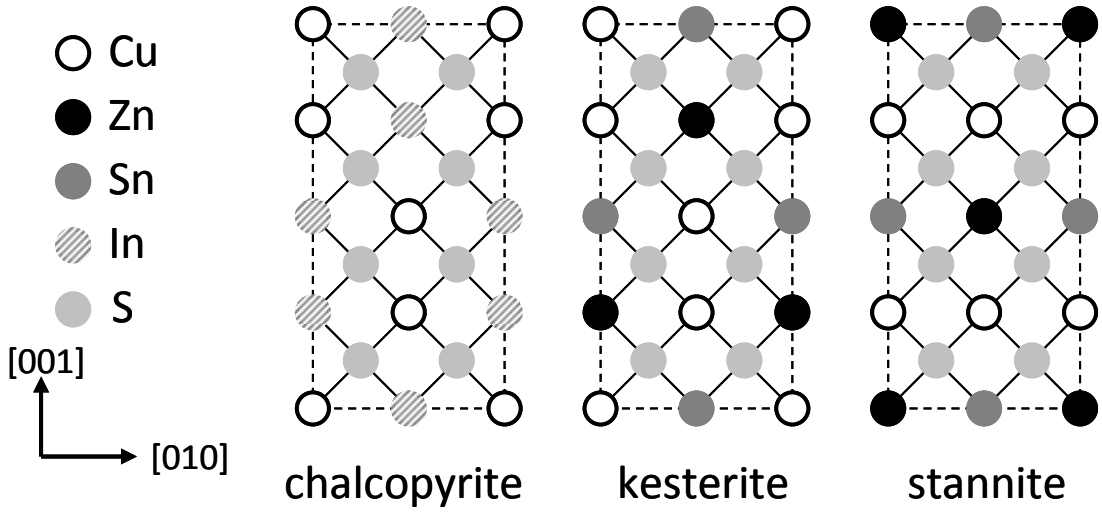

Figure 4-2 Schematic representation of chalcopyrite, kesterite, and stannite structure.

From the pseudo-ternary phase diagram of Olekseyuk, shown in Figure 4-1, it can be seen that the existence region of single phase CZTS is rather small compared to that of CIGS, for example [15, 77]. Outside of this single phase region, the co-existence of one or more secondary phases with a Cu_2ZnSnS_4 phase is very likely. In Table 4-1, a list of all possible secondary phases is given,

and their thermodynamic as well as electro-optical properties are discussed in the sections below.

Within the scope of this work, XRD has been used, which makes it hard to tell stannite- from kesterite-type structures. Since the main focus of this work is to study the discrimination of a Cu_2ZnSnS_4 phase from possible secondary phases, it is *not* distinguished between a stannite- and a kesterite-type structure (especially when using diffraction reference data to match a measured XRD pattern). Furthermore, when talking about Cu_2ZnSnS_4 it sometimes is referred to as "kesterite". This sloppy terminology does not apply to any specific structural phase of the Cu_2ZnSnS_4 compound but has only been used for simplicity reasons.

Lattice constants as well as other crystallographic details about the stannite-type and kesterite-type phases are shown in Table 4-1. Furthermore, the positions of the X-ray diffraction peaks as taken from the database are shown in Figure 4-11 [23].

4.1.2 Electro-optical properties

One of the most fundamental criteria for a semiconductor to be suitable for photovoltaic applications is the absorption of incident photons to create electron-hole pairs. For the absorption of the solar spectrum, the band gap of the absorbing material must be chosen appropriately. The Schockley-Queisser limit, which describes the thermodynamic efficiency limit for photovoltaic solar energy conversion as a function of the band gap of the absorber used in the solar cell device, hereby gives the upper and lower limit for the band gap [78]. For the solar spectrum, a maximum efficiency of around 30 % can be achieved with materials with band gaps between 1.0 and 1.5 eV [78, 79]. In the case of Cu_2ZnSnS_4, theoretical predictions of the band gap have given values between 1.30 and 1.42 eV for the stannite-type material, and values between 1.49 and 1.64 eV for the kesterite-type material [5, 7, 74, 80]. Hereby, it is interesting to see that the stannite-type material typically has a 0.1 to 0.2 eV smaller band gap than the kesterite-type CZTS. Experimentally determined values of the band gap of CZTS range from 1.4 eV to 1.55 eV [4, 6, 8, 9, 11, 13, 46, 81-86], where most results lie at 1.50 eV [41]. The observed differences can either be explained by a mix of the results for stannite- and kesterite-type CZTS or by differences in the extrapolation of the measured data, since in most cases the band gap was determined via optical transmission or by quantum efficiency measurements. Nevertheless, band gap values of around 1.45 to 1.50 eV lie within the range where a maximum of 30 % energy conversion efficiency is possible [78]. The band gap of the CZTS semiconductor was reported to be direct [4].

Besides the suitable band gap, the quaternary Cu_2ZnSnS_4 compound has so far only been reported p-type with a high absorption [4]. The absorption coefficient was determined to be $\alpha > 10^4$ cm^{-1} (at energies right ablve the band gap) and is comparable to that of Cu(In,Ga)Se_2 solar cells. Comparable is also the determined Hall mobilities in polycrystalline film of 6 to 12 cm^2/Vs (3 to 22 cm^2/Vs for Cu(In,Ga)Se_2), only the charge carrier density of the order of 10^{18} cm^{-3}, compared to 10^{16} cm^{-3} for Cu(In,Ga)Se_2, seems too high [4, 9, 11, 87-90].

Altogether, these values show that Cu_2ZnSnS_4 is a suitable semiconductor for the use as an absorber layer in photovoltaic devices. Currently, the record device for pure sulfide CZTS[1] lies at 6.8 %, achieved by IBM and the Katagiri group, and the record for the mixed sulfide-selenide CZTS/Se lies at 10.1 % achieved by IBM [13, 14, 92].

[1] In a recent development, IBM published an 8.4 % efficient solar cell device based on pure sulfide CZTS. In their process, a thermally evaporated Cu, Zn, Sn, and S containing precursor is annealed at 570 °C in a sulfur containing atmosphere for 5 min under atmospheric pressure [91] B. Shin, O. Gunawan, Y. Zhu, N. A. Bojarczuk, S. J. Chey, and S. Guha, Progress in Photovoltaics: Research and Applications (2011)..

Table 4-1 Collection of the most probable phases of the Cu-Zn-Sn-S (sub-) system with their structural details as taken from the crystallographic database [23]. The given PDFs have been selected by their quality (as given by the database) and by their usability to explain measured data as shown in this work.

Phase	Structure	Space group	Lattice parameter (Å)	PDF-No./Ref. [23]
Cu_2ZnSnS_4 (stannite)	tetragonal	$I\bar{4}2m$	a = b = 5.43, c = 10.86 $\alpha=\beta=\gamma=90°$	01-075-4122
Cu_2ZnSnS_4 (kesterite)	tetragonal	$I\bar{4}$	a = b = 5.44, c = 10.88 $\alpha=\beta=\gamma=90°$	00-021-0883
$Cu_2ZnSn_3S_8$	tetragonal	-	-	[15]
Cu_2SnS_3	cubic	$F\bar{4}3m$	a =b = c = 5.43 $\alpha=\beta=\gamma=90°$	01-089-2877
Cu_2SnS_3	tetragonal	$I\bar{4}2m$	a = b = 5.41, c = 10.82 $\alpha=\beta=\gamma=90°$	01-089-4714
Cu_2SnS_3	hexagonal	-	-	[93]
Cu_2SnS_3	monoclinic	Cc	a = 6.66, b = 11.54, c = 6.65 $\alpha=\gamma=90°,\ \beta=109.39°$	04-010-5719
Cu_2SnS_3	triclinic	$P1$	a = 11.51, b = 18.76, c = 6.64 $\alpha=90.29°, \beta=\gamma=90°$	00-027-0198
Cu_3SnS_4	orthorhombic	P	a = 10.73, b = 10.77, c = 10.70 $\alpha=\beta=\gamma=90°$	00-036-0218
Cu_4SnS_4	orthorhombic	$Pnma$	a = 7.69, b = 13.57, c = 6.42 $\alpha=\beta=\gamma=90°$	00-027-0196
$Cu_2Sn_3S_7$	monoclinic	F	a = 12.68, b = 7.35, c = 12.76 $\alpha=\gamma=90°,\ \beta=109.6°$	00-039-0970
α-ZnS (sphalerite)	cubic	$F\bar{4}3m$	a =b = c = 5.4 $\alpha=\beta=\gamma=90°$	04-001-6857
β-ZnS (wurzite)	hexagonal	$P63mc$	a =b = 3.82, c = 6.26 $\alpha=\beta=\gamma=90°$	04-008-7254
Cu_2S (α-chalcocite)	monoclinic	$P21/c$	a = 15.25, b = 11.88, c = 13.49 $\alpha=\gamma=90°,\ \beta=116.35°$	04-007-1284
Cu_2S (β-chalcocite)	hexagonal	$P63/mmc$	a =b = 3.89, c = 6.68 $\alpha=\beta=\gamma=90°$	04-010-5153
$Cu_{2-x}S$ (digenite)	cubic	-	a =b = c = 27.76 $\alpha=\beta=\gamma=90°$	00-023-0960
Cu_7S_4 (anilit)	orthorhombic	$Pnma$	a = 7.90, b = 7.82, c = 11.08 $\alpha=\beta=\gamma=90°$	00-033-0489
$Cu_{31}S_{17}$	monoclinic	$P21/n$	a = 26.90, b = 15.75, c = 13.47 $\alpha=\gamma=90°,\ \beta=90.13°$	00-034-0660
CuS (covellit)	hexagonal	$P63/mmc$	a =b = 3.79, c = 16.34 $\alpha=\beta=\gamma=90°$	00-006-0464
SnS_2	hexagonal	$P\bar{3}m1$	a =b = 3.65, c = 5.90 $\alpha=\beta=\gamma=90°$	00-023-0677
Sn_2S_3	orthorhombic	$Pnam$	a = 8.86, b = 14.02, c = 3.75 $\alpha=\beta=\gamma=90°$	00-014-0619
SnS	orthorhombic	$Cmcm$	a = 4.0, b = 11.15, c = 4.32 $\alpha=\beta=\gamma=90°$	04-002-9907

4.2 Possible secondary phases – the Cu-Zn-Sn-S subsystems

Due to the small existence region of single phase Cu_2ZnSnS_4, there is a high probability to grow undesired secondary phases that co-exist with CZTS. Figure 4-1 shows some of those possible secondary phases according to [15]. This section will summarize their thermodynamic and electro-optical properties in more details.

4.2.1 The Cu-Sn-S system

Thermodynamics and crystal structure

Figure 4-3 (a) gives a survey of all known ternary phases in the Cu-Sn-S system as published by Fiechter et al. and according to findings of Moh, Khanafer, Wang, Hahn, Jaulmes, Chen, De Chalbaud, Onoda and their co-workers, respectively [70, 94-101]. Most of those investigated phases lie either close to or right on a tie line connecting Cu_2S and SnS_2, which means that they also appear in the pseudo-ternary phase diagram in Figure 4-1. Some of the phases from that tie line are the ternary $Cu_2Sn_3S_7$ which crystallizes in a monoclinic structure, the orthorhombic Cu_4SnS_4 phase, and the polymorphic phase Cu_2SnS_3 (CTS), as discussed by Moh, Wang, and Fiechter [70, 96, 101]. Amongst the various publications, the Cu_2SnS_3 phase has been reported to crystallize at high temperatures (above 775 °C) in a cubic structure [70] and at low temperatures (below 775 °C) either in a tetragonal structure [70, 94, 97] or in a monoclinic or triclinic structure [95, 100, 101]. In a more recent publication, Wu and co-workers even synthesized a hexagonal Cu_2SnS_3 phase [93]. In comparison to Figure 4-3 (a), part (b) shows the Cu_2S – SnS_2 tie-line as published by Olekseyuk et al. [15]. In principle, the appearing phases are the same, except that Olekseyuk reports of fewer phases.

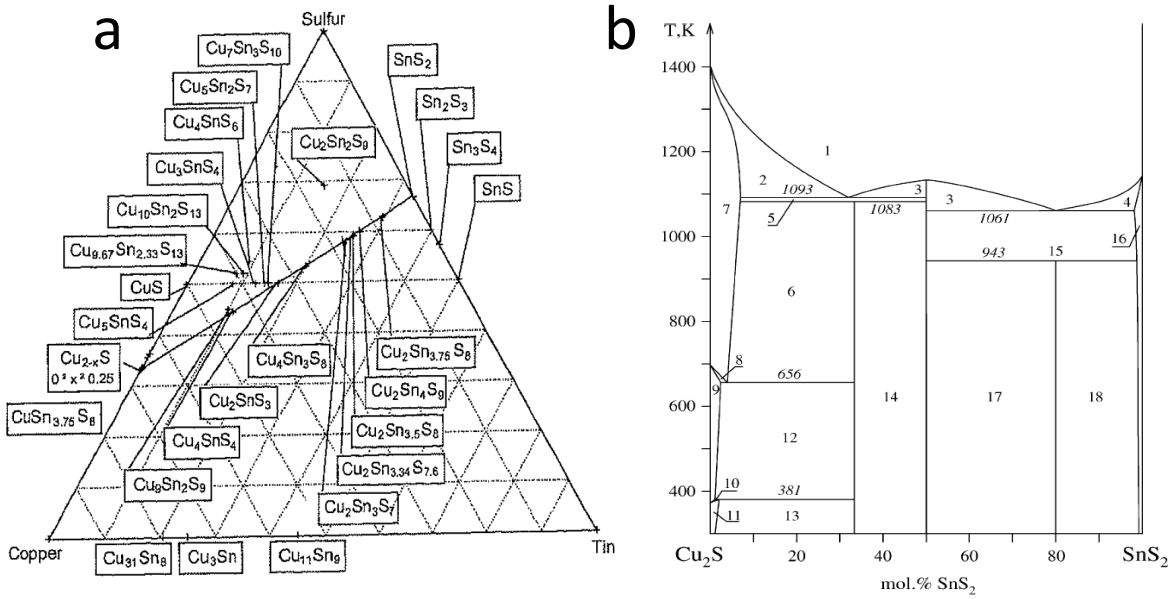

Figure 4-3 (a) Survey of all known phases in the Cu-Sn-S system over all temperatures as published by Fiechter [96]. (b) Phase diagram of the Cu_2S–SnS_2 system as published by Olekseyuk [15]: (1) L, (2) L + α, (3) L + Cu_2SnS_3, (4) L + α, (5) Cu_2SnS_3 + α, (6) Cu_4SnS_4 + α, (7) α, (8) α + α', (9) α', (10) α' + α'', (11) α'', (12) Cu_4SnS_4 + α', (13) Cu_4SnS_4 + α'', (14) Cu_2SnS_3 +Cu_4SnS_4, (15) Cu_2SnS_3 + γ, (16) γ, (17) Cu_2SnS_3 + $Cu_2Sn_4S_9$, (18) $Cu_2Sn_4S_9$ + γ. L – liquid, α, α', α'' – different Cu_2S, γ – SnS_2.

Fernandes et al. published XRD results measured on three different copper, tin, and sulfur containing thin films that were annealed at three different temperatures and which have slightly different compositions [102-104]. At 350 °C they found a tetragonal Cu_2SnS_3 phase, at 520 °C an orthorhombic Cu_3SnS_4 phase, both in agreement to the findings discussed above, but

at 400 °C they found a cubic Cu_2SnS_3 phase, which is in contrast to the findings discussed above [102-104]. It is therefore either possible that their XRD measurement was not detailed enough to see the small peaks that prove the tetragonal, triclinic, or monoclinic structure (see Figure 4-11), or that a cubic Cu_2SnS_3 phase is not just a high temperature phase.

In the work presented here, all samples have been annealed at temperatures just below 600 °C. At this temperature, Moh and Onoda synthesized Cu_2SnS_3 samples with a monoclinic structure [70, 100].

Lattice constants as well as other crystallographic details about the discussed ternary phases are shown in Table 4-1. Furthermore, the positions of the X-ray diffraction peaks as taken from the database are shown in Figure 4-11 [23].

Electro-optical properties

Cu_4SnS_4 has been reported to be a p-type semiconductor with a band gap of 1.2 eV [105]. Furthermore, a hole mobility of 10 $cm^2/(Vs)$ and a hole concentration of 10^{17} cm^{-3} have been measured [105]. For $Cu_2Sn_3S_7$ a band gap of 0.93 eV and an absorption coefficient of above 10^5 cm^{-1} (right above the band gap) have been reported [96].

Similar to the above, Cu_2SnS_3 has been found to be a p-type semiconductor [105]. In 1987, Kuku and Fakolujo reported on the only solar cell device[2], based on a Schottky junction consisting of Cu_2SnS_3 and Indium, with a power conversion efficiency of 0.11 % under a 100 mW/cm^2 incident radiation [106]. Experimentally, an absorption coefficient of $\alpha > 10^4$ cm^{-1} (right above the band gap) [106-108], an electrical conductivity of 10 $\Omega^{-1}cm$, a hole mobility of 80 $cm^2/(Vs)$, and a hole concentration of 10^{18} cm^{-3} has been measured for polycrystalline Cu_2SnS_3 thin films [105]. While the absorption coefficient is in the same order of magnitude as those of CZTS and CIGS solar cells, the hole mobility and electrical conductivity measured by Avellaneda et al. for CTS seem to be a slightly higher than in the case of CZTS and CIGS thin films [71, 88, 89, 105, 109]. A possible explanation for these high values was given due to the presence of $Cu_{2-x}S$ phases in those thin films. Apart from these properties, the band gap of the p-type semiconductor Cu_2SnS_3 has been reported to be between 0.93 and 1.51 eV [96, 103, 105-108], which lies in an optimal region for photovoltaic application. While the band gap value of 1.51 eV measured by Kuku et al. is very high which might be due to a large extrapolation over 0.2 eV, values between 0.93 and 1.35 eV for the band gap seem to be dependent on the crystal structure of the polymorphic compound Cu_2SnS_3, where 0.98 eV was measured for a “cubic” phase (although there are some doubts whether this phase was really cubic as this sample was grown at low temperatures and as the conclusion was drawn from unclear XRD data) and 1.35 eV for a tetragonal phase [103]. In a recent publication, Zhai and co-workers have confirmed a band gap of around 0.8 to 0.9 eV for monoclinic Cu_2SnS_3 from first-principles calculations [110].

4.2.2 The Cu-Zn-S system

Figure 4-4 (a) shows the phase diagram of the Cu_2S-ZnS system. According to the studies of Olekseyuk et al., the solubility of Zn in Cu_2S is less than 5 mol% at around 400 °C [15]. Furthermore, Cu_2S and ZnS rather seem to co-exist than to form a ternary phase. Similar results have been found by Craig at al. who failed to synthesise a Cu-Zn-S containing compound at atmospheric pressures [111]. Only Birther reports on a successful synthesis of a $Zn_yCu_{1-y}S_2$

[2] On first sight, this compound presented by Kuku et al. seems to be very Cu deficient compared to the stoichiometric ratio, however this apparent discrepancy appears to be a labeling error concerning the film composition, meaning that in Table 1 the unit ”at.%” probably meant to be ”wt.%”.

compound, this however, at high pressures of 65 kbar [112]. This concludes that no ternary Cu-Zn-S phase is to be expected at atmospheric conditions.

4.2.3 The Zn-Sn-S system

According to Olekseyuk et al., the solubility of SnS_2 into ZnS and vice versa is less than 1 mol% [15]. Figure 4-4 (b) shows the phase diagram of the ZnS-SnS_2 system and only a coexistence region of ZnS and SnS_2 can be found. This agrees well with the finding of Burk et al. who show the coexistence of ZnS with SnS, Sn_2S_3, as well as SnS_2 at 600 °C [113]. This concludes that also no Zn-Sn-S ternary phase is to be expected at atmospheric pressures and at annealing temperatures used in this work.

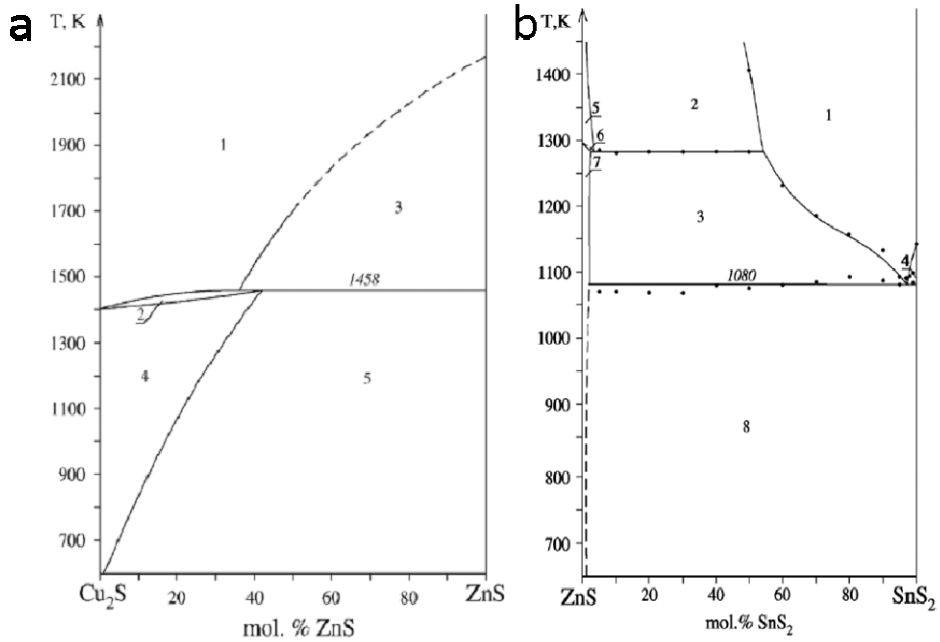

Figure 4-4 Phase diagrams of (a) the Cu_2S-ZnS system and (b) the ZnS-SnS_2 system according to [15]. In (a): (1) melt, (2) melt + Cu_2S, (3) melt + ZnS, (4) Cu_2S, (5) Cu_2S + ZnS. In (b): (1) melt, (2) melt + ZnS (wurzite), (3) melt + ZnS (sphalerite), (4) melt + SnS_2, (5) ZnS (wurzite), (6) ZnS (sphalerite) + ZnS (wurzite), (7) ZnS (sphalerite), (8) ZnS (sphalerite) + SnS_2.

4.2.4 The Cu-S system

Thermodynamics and crystal structure

The phase diagram of the Cu-S system is shown in Figure 4-5. Besides the meta-stable phase $Cu_{1.96}S$ that crystallizes in a tetragonal structure, there are six stable phases of the Cu-S system [114]. The copper rich Cu_2S phase (α-chalcocit) has a monoclinic crystal structure and is present between room temperature and 103.5 °C, at which it transforms into the hexagonal β-chalcocit (Cu_2S) phase. At temperatures above 435 °C, this phase decays into an less Cu rich phase $Cu_{2-x}S$ (Digenite) which has a cubic structure and which is stable down until 72 °C. Typically for $Cu_{2-x}S$, x is smaller than 0.3 and the lattice parameters increase for higher Cu amounts [115]. Below temperatures of 72 °C, $Cu_{2-x}S$ turns into the orthorhombic Anilit phase (Cu_7S_4). At the Cu poor side of Anilit the hexagonal CuS (Covellit) phase is present. This phase is stable up until temperatures of 507 °C, where it decays into Digenite. At the copper rich side of Anilit, the monoclinic $Cu_{31}S_{16}$ phase is present. At temperatures above 72 °C, this phase decays into the Digenite and Chalcocit phase. The structural details of the different phases are collected in Table 4-1 and the respective angular positions of the X-ray diffraction peaks are shown in Figure 4-11, as taken from literature and databases [23, 116].

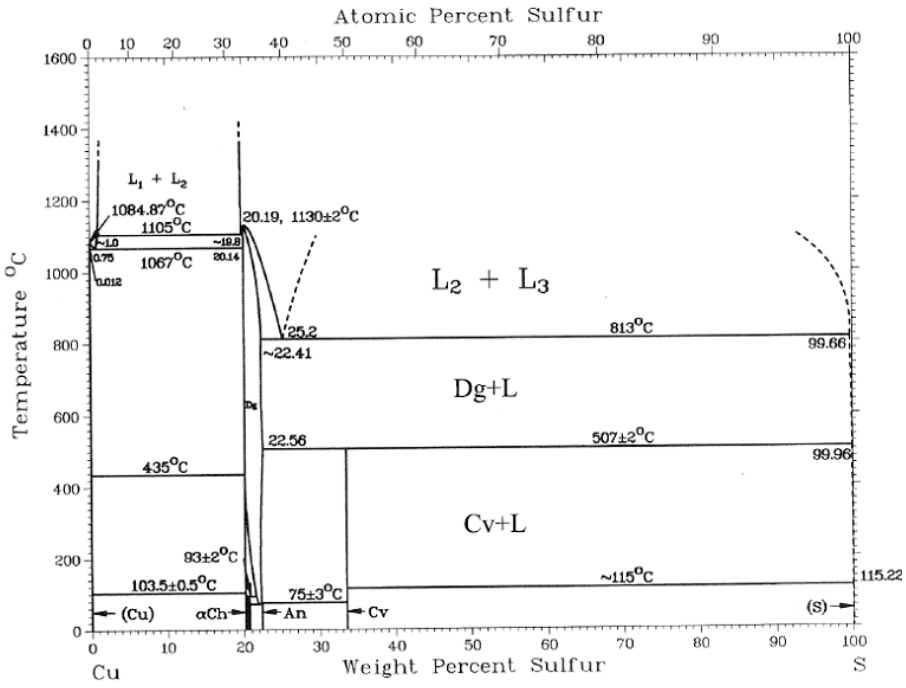

Figure 4-5 Phase diagram of the Cu-S system according to [60].

Electro-optical properties

Copper sulfides are reported to be p-type semiconductors [117, 118]. The copper rich $Cu_{2-x}S$ phases have band gaps ranging between 2.5 and 3.1 eV while the band gap of the Covellit phase was reported to be between 2.2 and 2.8 eV [117-119]. For the latter case, Maji et al. presented RT-PL results where a broad peak at 465 nm (370 nm excitation) was observed [118]. The resistivity of the CuS phase was measured to be around $3 \cdot 10^5 \Omega cm$ and the charge carrier concentration around $5 \cdot 10^{12} cm^{-3}$ [118]. For $Cu_{2-X}S$ a charge carrier concentration of greater than 10^{20} cm^{-3} is assumed.

Cu_yS phases are reported to be of interest as absorbers in 3D solar cells [117].

4.2.5 The Sn-S system

Thermodynamics and crystal structure

In Figure 4-6 the phase diagram of the Sn-S system is shown [60]. For increasing amounts of sulfur, three different phases are present: SnS, Sn_2S_3, and SnS_2, respectively. All of those phases are polymorphic and can be present in a low temperature α-phase as well as in a high temperature β-phase. Restricting to the temperature region that is interesting for the present work (below 600 °C), SnS crystallizes in an orthorhombic structure. The critical temperature is around 602 °C. That of Sn_2S_3, which is also present in an orthorhombic structure, and that of SnS_2, which typically crystallizes in a hexagonal structure, lies around 680 °C. The structural details of the different phases are collected in Table 4-1 and the respective angular positions of the X-ray diffraction peaks are shown in Figure 4-11, as taken from literature and databases [23, 116].

Electro-optical properties

The band gap of tin sulfides strongly depends on the compound. While Sn_2S_3 and SnS_2 compounds have a band gap of 2.0 and 2.2 eV, respectively, that of the Sn rich p-type semiconductor SnS is far lower with reported values between 0.9 and 1.35 eV [120-124]. Such

low values of the band gap make SnS a suitable candidate for photovoltaic applications itself, as reported by Ristov and Subramania, amongst others [122, 124]. The reported charge carrier concentration of SnS is of the order of 10^{15} cm^{-3} [120].

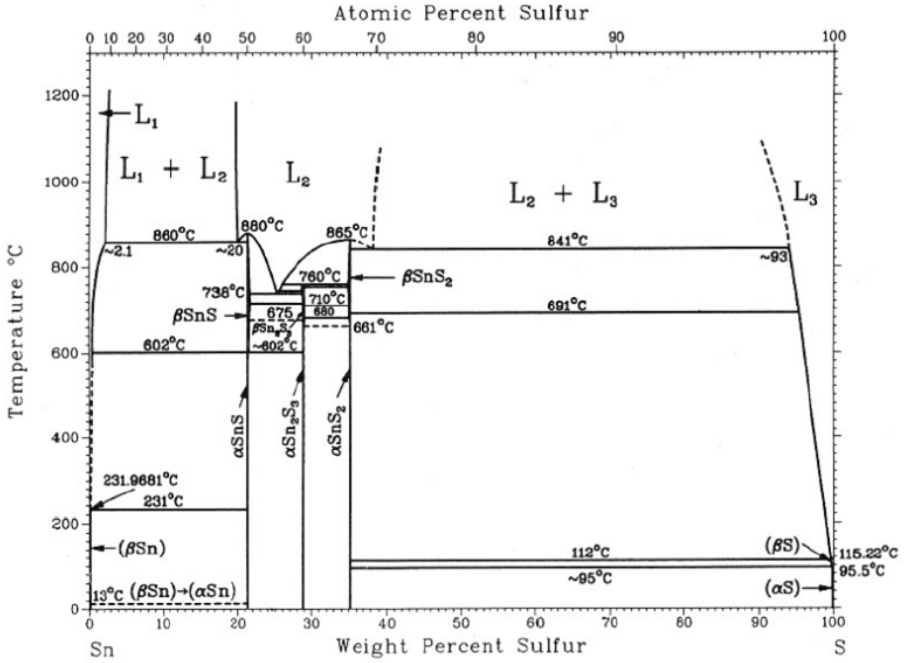

Figure 4-6 Phase diagram of the Sn-S system according to [60].

4.2.6 The Zn-S system

Thermodynamics and crystal structure

Figure 4-7 shows the phase diagram of the Zn-S system according to [60] and it can be seen that ZnS is the only binary phase that can be formed in this system. ZnS, however, is polymorphic and exists as a low temperature phase (α-ZnS, < 1020 °C) and as a high temperature phase (β-ZnS). The former of the two phases (α-ZnS) crystallizes in a cubic sphalerite structure, while β-ZnS crystallizes in a hexagonal wurtzite structure. As reported in [125], the wurtzite structure can however also exist at room temperature. For both ZnS phases, Table 4-1 shows the structural details and Figure 4-11 the angular positions of the X-ray diffraction reflexes, as taken from literature and databases [23, 116].

Electro-optical properties

The two polymorphs of ZnS (non-doped) have different band gaps (E_G) with 3.9 eV in the sphalerite case and 3.7 eV in the wurtzite case [116]. Depending on a dopant, however, this value for E_G can vary. In the case of Cu doping, for example, the band gap can be decreased below values of 1.8 eV, causing a photo induced luminescence peak at 1.77 eV [116]. For undoped and defect free ZnS, one would expect such a room temperature PL peak at the band gap.

Depending on the dopant used, ZnS can have n-type or p-type semiconducting properties. In the case of Cu doping, ZnS:Cu typically has n-type properties [126]. Due to its high band gap and n-type properties, ZnS is a suitable material for a buffer layer in photovoltaic applications, as shown by [127].

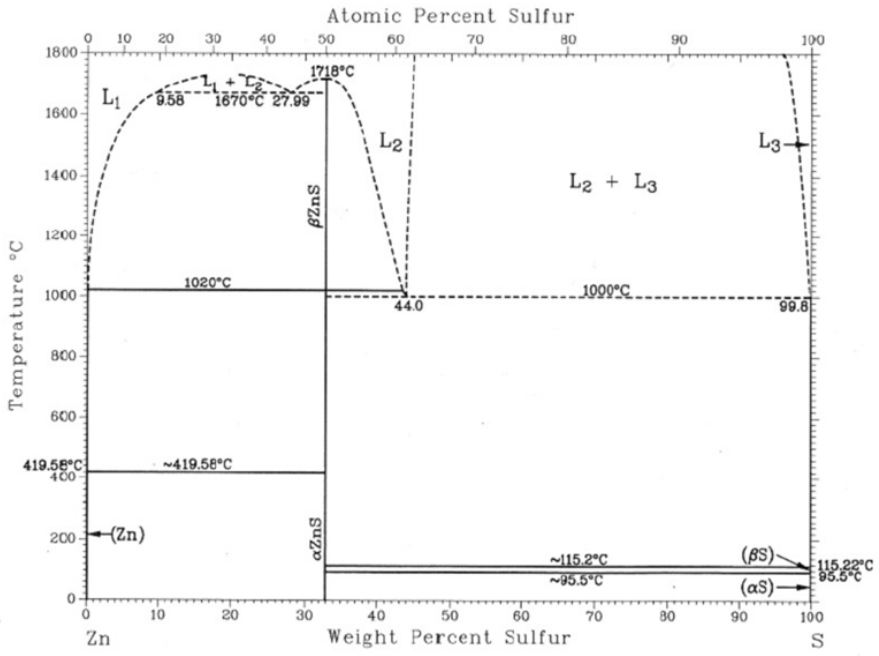

Figure 4-7 Phase diagram of Zn-S system according to [60].

4.3 Thermodynamics of chemical reactions

After sections 4.1 and 4.2 already showed which phases can be expected in the Cu-Zn-Sn-S (sub-) system in a thermodynamic equilibrium, this section focuses on basic thermodynamic principles of chemical reactions. Later in this chapter, this knowledge is used to explain the formation of secondary phases, and estimations of the Gibbs free energy of formation for CTS and CZTS (chapter 5) are given. Furthermore, in chapter 5, thermodynamics are used to explain the findings of the study of CZTS formation from the novel annealing procedure and to forecast more effective fabrication conditions for high quality CZTS material.

In the following, firstly, the basic principles of equilibrium reaction theory are briefly summarized, before the free energies of the various possible formation reactions are shown. Finally, the partial pressures of the most common elements and compounds in this quaternary system are listed and briefly discussed with respect to possible elemental losses.

The following background theory was obtained from the following reference: [128].

4.3.1 Basic equilibrium reaction theory

For a chemical reaction to take place, both, thermodynamic as well as kinetic conditions need to be met. Assuming that in the present case a sufficiently high activation energy and sufficient concentrations of the reactants are given throughout the process, it is thermodynamics that defines whether a chemical reaction is favorable or not. The function that describes the direction of the chemical reaction is the *Gibbs free energy G*, with

$$G = H - TS$$

Equation 4-1

where H is the enthalpy (the energy change of a system at constant pressure), S the entropy, and T the temperature of the system. Furthermore, it can be proven that the change in Gibbs free energy $\Delta G = \Delta H - T\Delta S$ represents the maximum amount of work that a system can do at constant temperature and pressure after any p-V work has been accounted for, where p is the

pressure and *V* is the volume [128]. A *standard Gibbs free energy of formation* $\Delta G^0_{f,298}$ can be defined as the change in Gibbs free energy when 1 mol of a compound is formed at 1 bar and 298 K from its elements in their standard states.

For a reaction to be spontaneous, the change in Gibbs free energy must be negative. During a reaction, however, ΔG constantly changes and will reach a minimum value at some composition. At this minimum, the reaction will have no tendency to change and hence it will stop [128]. A point of equilibrium has been reached. Hereby, as a quantitative measure of the composition of a reaction mixture, the *reaction quotient Q* can be defined by

$$Q = \frac{(a_C)^k (a_D)^l}{(a_A)^i (a_B)^j}$$

Equation 4-2

for a generalized reaction: $i\,A + j\,B = k\,C + l\,D$, with $a_{A,B,C,D}$ is the activity of the respective reactant and product, and *i, j, k, l* represent the amount of each reactant. For a system at equilibrium, Q_{eqm} equals the so called *equilibrium constant* K_{eqm} for the reaction which itself can be related to the standard Gibbs free energy of formation via the following expression:

$$K_{eqm} = \exp\left(\frac{-\Delta G^0}{RT}\right),$$

Equation 4-3

R being the gas constant. The previous two equations can hence be used to calculate ΔG for a reaction under certain conditions, knowing the activities of the reactants and products. The dependence of *G* on the temperature *T*, activity *a*, and pressure *p* is given by the following equations:

$$G = G^0 + nRT\ln(a) = G^0 + nRT\ln(\frac{p}{1bar})$$

Equation 4-4

where for an ideal gas $a = \frac{p}{p^0}$ with p^0 = 1 bar [128]. Furthermore, as the effect of pressure on solids and liquids is negligible and, by definition $G = G^0$ for a pure liquid or solid, it follows that $a_{(solid)} = a_{(liquid)} = 1$ [128].

Further details on the thermodynamics of an equilibrium reaction can be found in any thermodynamics text book such as [128].

It shall be noted that in the present case the Gibbs free energy is considered and not the Helmholtz free energy, since a constant pressure during the annealing is assumed.

4.3.2 Free energy of formation for the possible phases

After the previous section briefly introduced the general background on the thermodynamics of equilibrium reactions, this section focuses on the possible reactions in the quaternary Cu-Zn-Sn-S (sub-) system. Table 4-2 shows the expected reactions that form the binary sulfides as well as the reaction that can lead to Cu_2ZnSnS_4, assuming that S_2 is present in the gas phase.

Together with the respective reactions, the temperature dependence of the Gibbs free energy of formation ΔG_A per mole S_2 for a compound A is given, as taken from literature [129, 130].

In Figure 4-8 (a), ΔG_A (per mole S_2) of the different reactions is plotted with respect to the temperature range of the annealing used in this work. For equilibrium conditions, the required partial pressures of S_2 can also be calculated using Equation 4-2 and Equation 4-3. This dependence is given by:

$$\exp\left(\frac{-\Delta G^0}{RT}\right)=\frac{(a_C)^k_{eqm}(a_D)^l_{eqm}}{(a_A)^i_{eqm}(a_B)^j_{eqm}},$$

Equation 4-5

where for an ideal gas the activity $a=\frac{p}{p^0}$ (p^0 = 1 bar). The dependence of the minimum partial pressure of S_2 necessary to form the respective phases on the temperature is given by Figure 4-8 (b). From this Figure it can be seen that the formation of ZnS requires a much lower partial pressure of S_2, than for example SnS or Cu_2S. In an annealing system, where the temperature of the sample and of the elemental sulfur is heated at the same time with constant rates, the partial pressure of sulfur will build up continuously, hence it can be assumed that to minimize the Gibbs free energy of formation, the gaseous sulfur will react with Zn first (at lower partial pressures), before it reacts with Cu or Sn.

Table 4-2 Temperature dependent free energy of reaction of the expected reactions in the Cu-Zn-Sn-S (sub-) system according to [129, 130].

Reaction	ΔG_A (Jmol^{-1}), T in units of K	Valid T range (°C)
$2Zn+S_2 \leftrightarrow 2ZnS$	$\Delta G_{ZnS}=-537523+191.3T$	25-420
	$\Delta G_{ZnS}=-548501+207T$	420-1200
$4Cu+S_2 \leftrightarrow 2Cu_2S$	$\Delta G_{Cu_2S}=-267546+72T$	103-425
	$\Delta G_{Cu_2S}=-259864+61.2T$	435-1067
$2Sn+S_2 \leftrightarrow 2SnS$	$\Delta G_{SnS}=-343866+173.1T$	25-232
	$\Delta G_{SnS}=-353845+193.4T$	232-600
$4SnS+S_2 \leftrightarrow 2Sn_2S_3$	$\Delta G_{Sn_2S_3}=-234304+199.9T$	25-600
$2Sn_2S_3+S_2 \leftrightarrow 4SnS_2$	$\Delta G_{SnS_2}=-222589+205.3T$	25-760
$Cu_2S+SnS+½\,S_2 \rightarrow Cu_2SnS_3$	$\Delta G_{CTS}=$ unknown	---
$ZnS+Cu_2S+SnS_2 \rightarrow Cu_2ZnSnS_4$	$\Delta G_{CZTS}=$ unknown	---

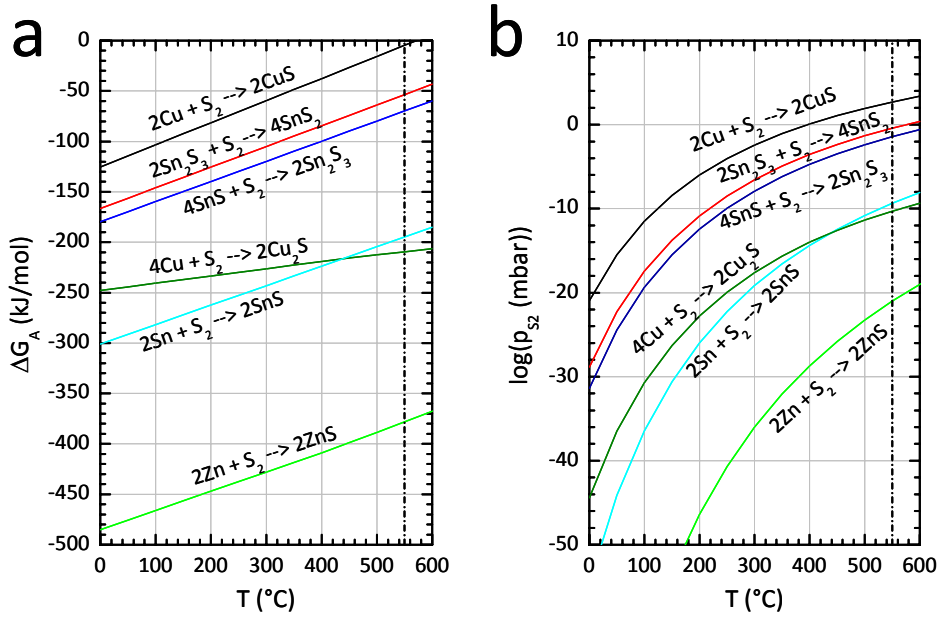

Figure 4-8 (a) Temperature dependence of the Gibbs free energy of reaction ΔG_A (per mole S_2) of the expected reactions in the Cu-Zn-Sn-S (sub-) system according to [129, 130]. (b) Minimum partial pressure of S_2 required to form the respective phases at equilibrium situation. The dotted lines in both graphs indicate the temperature of the standard annealing as used in this work.

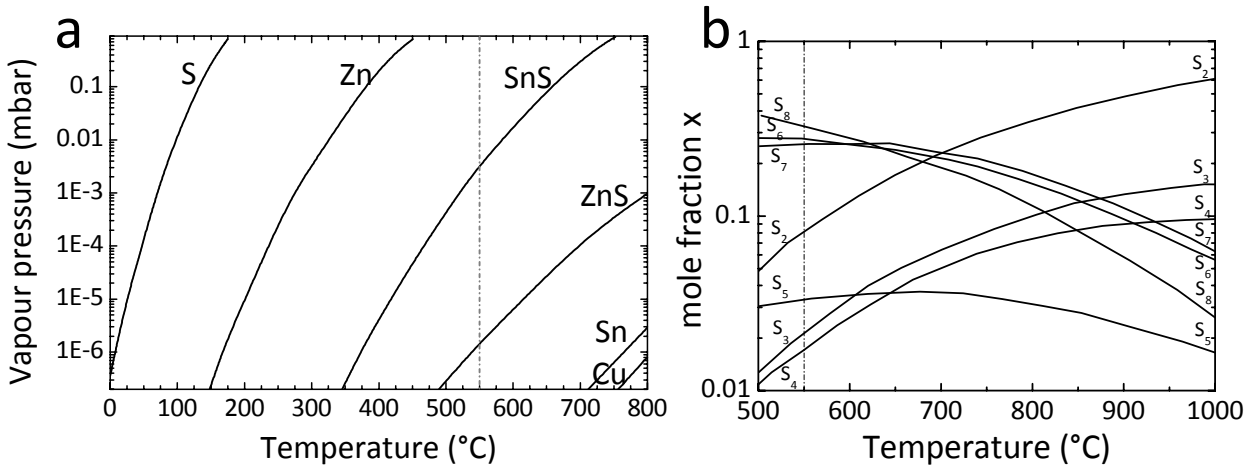

Figure 4-9 (a) Vapour pressures of the elements of the Cu-Zn-Sn-S system as well as of the most volatile sulfides, SnS and ZnS, as taken from the PhD thesis of A. Weber [131] and according to [132-136]. (b) Mole fraction x of the different molecular species in saturated sulfur vapour, according to [137]. The grey dash-dotted line indicates the annealing temperature for the standard annealing conditions. The dash-dotted lines indicate the annealing temperature as used in this work.

4.3.3 Partial pressures of elements and compounds in the Cu-Zn-Sn-S (sub-) system

Within the work of chapter 5, Cu and Zn containing precursors have been annealed together with elemental sulfur and SnS powder. In order to study the reaction pathway of the formation of Cu_2ZnSnS_4, it is important to know which vapour pressure to expect from the different elements and possible compounds. Figure 4-9 (a) shows the vapour pressures of the most volatile elements and compounds with respect to the temperature, as taken from [131] and according to [132-136]. It can be seen that S, Zn, and SnS are the most volatile elements/compounds in this quaternary (sub-) system, whereas ZnS, Sn, and Cu are less volatile. From the dash-dotted line, which indicates the temperature of the standard annealing, one can see that sulfur, Zn, and SnS have sufficiently high partial pressures at the annealing conditions

used. Therefore, when annealing a metallic precursor, one needs to take care to anneal quick enough in order to form ZnS, before Zn can evaporate (from a metal or out of a Cu-Zn alloy), and to suppy sufficient SnS(g) from the gas phase during the annealing (as one of the main outcomes of this work, see chapter 5), in order to prevent SnS from evaporation from the sample.

In Figure 4-9 (b), the mole fraction of the different molecular species in saturated sulfur vapour is given, according to [137]. This graph depicts that in saturated sulfur vapour mainly S_2, S_6, S_7, and S_8 rings are present at temperatures of the standard annealing conditions (see dash-dotted line). One needs to be aware, however, that in the standard annealing, a saturation of the vapour pressure of sulfur might not be reached, which means that one would have more S_2 molecules present during the annealing than one would expect from the saturated case.

4.3.4 Sublimation of tin sulfides

As one of the outcomes of this thesis, a novel annealing annealing strategy is introduced, in which the samples are annealed in the presence of sulfur **and** SnS(g) (see chapter 5). In order to obtain SnS(g), SnS powder was used as a source, which evaporates in an open system as described by Reaction 4-3. During such an annealing, however, it is also possible that parts of the SnS powder might react with sulfur to form Sn_2S_3(s) or SnS_2(s) compounds. In an open system, these latter compounds, however, are also expected to break down at elevated temperatures. Based on the findings by Piacente et al., this breakdown follows the following reactions [135]:

$$SnS_2(s) \rightarrow \frac{1}{2} Sn_2S_3(s) + \frac{1}{4} S_2(g)$$

Reaction 4-1

$$Sn_2S_3(s) \rightarrow 2SnS(S) + \frac{1}{2} S_2(g)$$

Reaction 4-2

$$SnS(s) \rightarrow SnS(g)$$

Reaction 4-3

Based on these considerations, the addition of SnS powder to the annealing process does not just supply SnS(g) to the annealing environment but might also contribute to a prolonged supply of S_2, as its evaporation (from the elemental sulfur) might be delayed by a primary reaction with SnS forming Sn_2S_3 and/or SnS_2.

4.4 Detection of secondary phases and their discrimination from Cu_2ZnSnS_4

In the previous section the thermodynamic and electro-optical properties of possible phases have been discussed that can be formed alongside the desired Cu_2ZnSnS_4 phase and that could co-exist as unwanted secondary phases. Since the sample growth does not necessarily take place under equilibrium conditions, it is therefore possible that actual phases contained in the sample differ from those predicted by the respective phase diagram.

As the general aim is to grow a Cu_2ZnSnS_4 thin film for the use as a solar cell absorber material, it is important to avoid such secondary phases. This makes it even more important to be able to detect them unambiguously. Figure 4-10 shows schematic cross-sections of a typical thin film solar cell together with four possible sites where secondary phases could be expected, according to [138]. In case (a), it is sketched that a secondary phase could sit in between the absorber layer grains as columnar grains. These so-called *shunting phases* enable alternative

current paths through the absorber layer and affect the shunt resistance, and hence the performance of the cell, in a negative way, in case they are conductive (as for $Cu_{2-x}S$ phases). In the second case (b), where secondary phases sit at the back interface of the absorber layer, high resistivity phases can lead to an increase in the series resistance of the device which then decreases the performance of the solar cell. Common examples for such phases are $Mo(S,Se)_2$ and Zn(S,Se), as discussed by Mitzi et al. and Redinger et al. [71, 139, 140]. A low resistivity secondary phase at the back of the absorber material would theoretically not harm the device, but could still form a barrier due to band offsets or due to being doped differently, which could cause a higher resistance. Unwanted secondary phases can also be found at the front of the absorber layer, so in between the pn-junction of the solar cell device, as shown in Figure 4-10 (c). Independent of its resistivity and its band gap, at this position, a secondary phase does definitely influence the band alignment of the solar cell. In the best case, when the secondary phase is p-type semiconducting and its band gap in only slightly lower than that of the absorber layer (e.g. Cu_2SnS_3 as a secondary phase), it will only lead to a decease of the open circuit voltage, but the solar cell will still be functional. However, in other cases when the band alignment is disturbed by for example large band gap semiconductor, such as ZnS phases (as discussed in [18, 141]), it might lead to a too large spike at the pn-junction, which could be a potential barrier for the charge carriers which would have a negative impact in the functionalty of the device. Highly conductive materials (such as $Cu_{2-x}S$) would destroy the band alignment anyway. As illustrated in Figure 4-10 (d), secondary phases can also be dispersed within the absorber layer (as seen by Ennaoui [43]) where they could influence the recombination of the charge carriers and reduce the generation volume.

These four scenarios show how crucial it is to detect and to avoid secondary phases. In the following sections, a brief summary is given about which tools are commonly used to identify the phases present in the absorber layer.

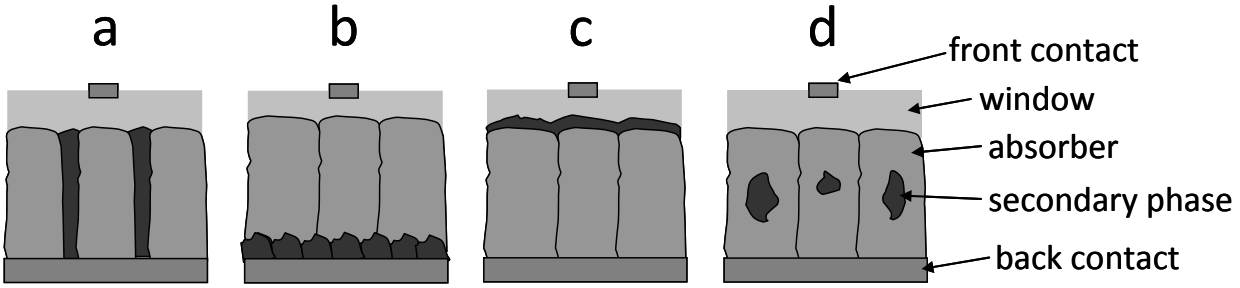

Figure 4-10 Schematic cross-section of a typical thin film solar cell together with four possible sites ((a) as a shunting phase in between grains, (b) at the back contact, (c) at the front contact, and (d) inside the absorber grains) where secondary phases could be expected, according to [138].

4.4.1 X-ray diffraction

In section 2.4 of this work, X-ray diffraction has been introduced as one of the most common techniques used to assign crystallographic phases. Usually, phase assignments are done with confidence unless there happen to be several existing phases with similar symmetry and lattice parameters [41]. Table 4-1 contains a summary of the previously discussed possible secondary phases, and Figure 4-11 shows the angular peak positions of the diffraction pattern of the individual phases as taken from the crystallographic database [23]. As can be seen from this collection, most of the phases have their most intense peaks at unique positions which makes it possible to identify them with confidence. Despite that, however, the most intense peaks of the Cu_2ZnSnS_4, Cu_2SnS_3, and ZnS phases are very close together and even partly overlap, as has also been pointed out on several occasions [8, 41, 49, 50, 71, 104, 141-145]. While the ZnS phase

has only a few diffraction peaks due to its high symmetry, the pattern of the CZTS and CTS phases contain further, minor peaks which make the pattern of CZTS and that of the monoclinic, triclinic, and tetragonal CTS phase unique. This latter fact can hence be used to tell whether e.g. a Cu_2ZnSnS_4 or a monoclinic Cu_2SnS_3 phase is present, the absence of those phases, however, cannot be concluded in case those weaker peaks are not present. In literature, it is often said that is very hard or even impossible to discern ZnS and CTS from a CZTS phase since their main peaks are very close together and overlap (and it is usually referred to the main peak at 28.5 °) [8, 41, 49, 50, 71, 104, 141-145]. So far, however, there has been no qualitative or even quantitative study to prove this statement, even though high resolution XRD measurements together with Rietveld refinement analysis could be helpful to resolve ZnS and CTS from CZTS. Such a study is one of the main objectives of this chapter and the results will be shown later.

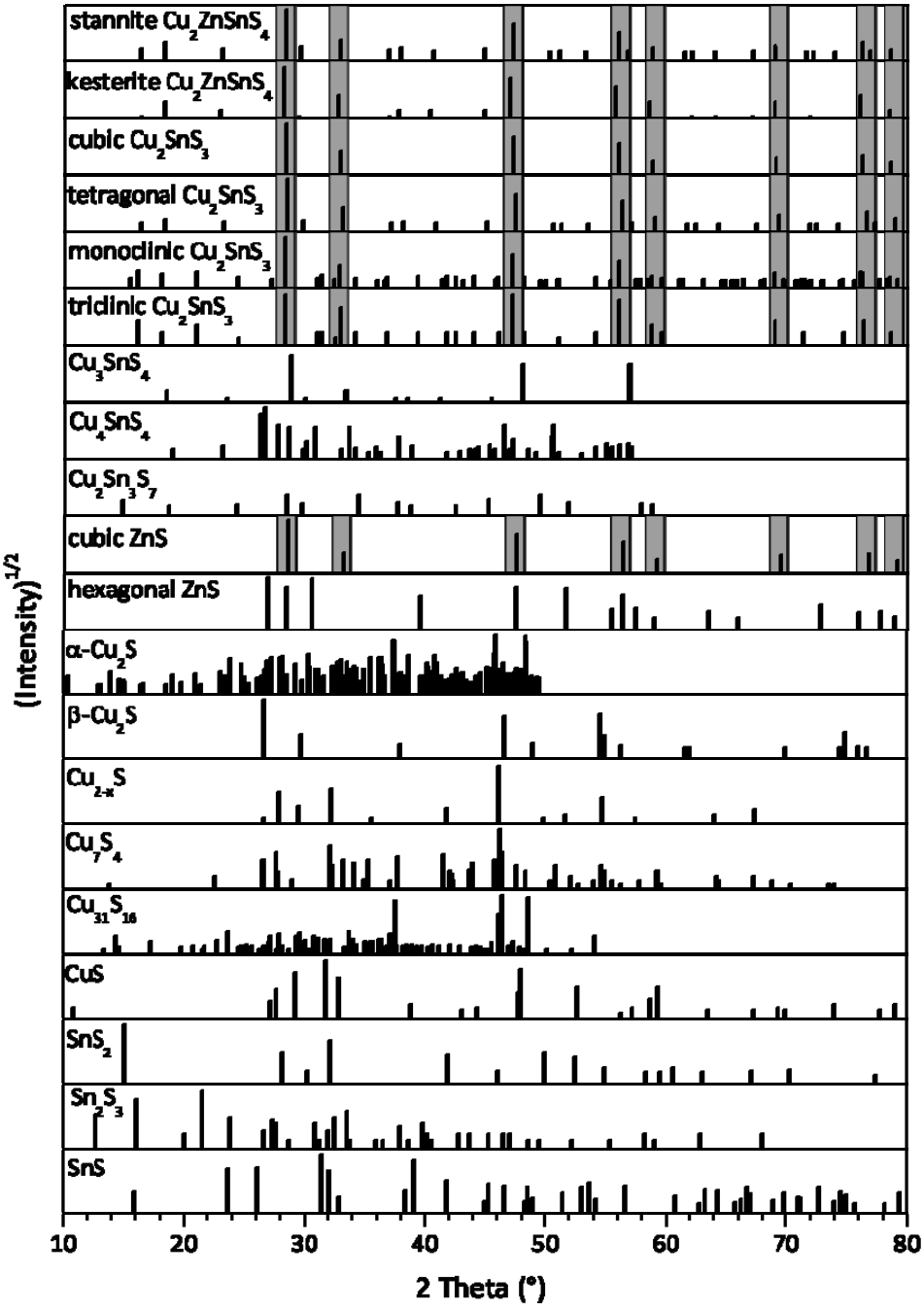

Figure 4-11 XRD pattern of the most common phases of the Cu-Zn-Sn-S (sub-) system according to the crystallographic database [23].

To be able to discern a certain amount of one phase from another main phase, X-ray diffraction, however, has certain weaknesses. Since XRD signals are typically averaged over a larger area of the sample, it will still be hard or even impossible to detect a signal coming from a minority phase that could for example sit at the back of the absorber layer, even if the main peaks of the phases to be discerned are well separated from each other and even if the grazing incident mode is used to mainly probe the thin film, as discussed in section 2.4. The reason for this can be found in the fact that in XRD measurements are mainly optimized to detect the majority phase and not minority phases. This means that not only the angular position of the XRD peaks matter, but also the amount and the position of the minority phases within the film matter. How this applies to the discrimination of CTS and ZnS from CZTS is part of the objective of this work and will be discussed later.

4.4.2 Raman spectroscopy

Raman spectroscopy is an optical, surface sensitive, and typically non-destructive technique which is commonly used to analyze the phononic properties of materials, as introduced in section 2.5. Since the phononic responses of different materials are in the most cases unique, the possibility is given to use the Raman spectra as a “fingerprint” to identify a certain material phase. Raman spectroscopy can hence be used to some extent as an alternative to X-ray diffraction [104].

The phononic responses of the previously discussed phases of the Cu-Zn-Sn-S (sub-) system have been investigated by various groups [102-104, 142, 143, 146-157]. A collection of the typically phononic responses from the various phases is shown in Table 4-3. By comparing the positions of the Raman shifts of the various phases, Fernandes and co-workers concluded that Raman spectroscopy can be used to resolve the different secondary phases from the CZTS phase [104]. This conclusion, however, is based on the individual analysis of pure phases. Based on further studies, they suggest that this technique can furthermore be used to perform depth-resolved analysis by changing the excitation wavelength and thus the penetrations depth of the probing light beam [104]. This strategy, however, might not be feasible since a change in the excitation wavelength would also change the so-called Raman efficiency of the phases to be analyzed. It might lead to misinterpretations of the in-depth analysis or at least would make a de-convolution of the mentioned effects difficult.

A different idea to perform depth-resolved studies with Raman spectroscopy has been suggested by Fontane et al. [143]. It was suggested to use a combined Auger electron and Raman spectroscopy setup, where a sequential Raman measurement and sputtering was performed on a sample, until the sample’s substrate was reached [143]. This way, in-depth information of the present phases could be gained by comparing the measured Raman signals with those from literature and hence could be combined to AES depth profiles. Hereby, the measurement conditions of the Raman setup were kept constant [143]. Furthermore, it was pointed out that a change in the excitation wavelength also changes the individual Raman efficiencies of the different phases. Hereby it was shown that the use of a ultra-violet excitation is a better choice for identifying ZnS than with the green excitation. This result was explained by the much higher Raman efficiency of ZnS using UV excitation. Finally, it was concluded that use of resonant conditions for the Raman spectroscopy is essential for the reliable detection of these secondary phases.

In most of the investigations referenced here, the measurements were performed on individual and mostly pure phases. In these cases, the measured intensities have been optimized to the phase under investigation. So far, there is not yet a quantitative study

performed on a mixed sample where the signal is typically optimized to the most Raman efficient phase. Such a study would determine how much of a minority phase can be detected using Raman spectroscopy when it is mixed with other phases. This issue is part of the objective of this work and results are shown later in this chapter.

A word of caution shall be written here: In Table 4-3, two Cu_2SnS_3 polymorphs are listed and marked with "*". In the publication of Fernandes et al. [104], those measured Raman spectra were assigned to a cubic and a tetragonal Cu_2SnS_3 phase, respectively. This assignment was done by XRD measurements and might be wrong, as firstly, the samples were grown at 300 to 350 °C but the cubic CTS phase is reported to be a high temperature phase (> 775 °C [70], as can be seen in section 4.2.1), and secondly, the assignment was based on a peak shift of 0.1 ° while having a FWHM of these peaks of around 1 °, which makes the classification doubtful. Furthermore, in the case of the tetragonal CTS, none of the "minor tetragonal" only peaks (see Figure 4-11) were observed.

Table 4-3 Raman shifts for the major phases in the Cu-Zn-Sn-S (sub-) system. The most intense peaks are marked in bold. "*" marks Cu_2SnS_3 phases that are published to have a *cubic* and *tetragonal* crystal structure, respectively. This finding, however, needs to be taken with care, since the assumptions were based on XRD pattern in which none of the distinct, tetragonal minor peaks can be seen. Furthermore, the results were based on a peak shift of 0.1 ° while having a FWHM of these peaks of around 1 °, which makes the classification doubtful.

Phase	Raman shift (cm^{-1})	Sources
Cu_2ZnSnS_4	**286**, **337**, 370	[142, 143, 146, 149, 151, 157]
Cu_2SnS_3 (tetragonal* or different phase)	297, **337**, **352**	[104]
Cu_2SnS_3 (cubic* or different phase)	267, **303**, **356**	[104]
Cu_3SnS_4	**318**	[104]
ZnS (cubic)	219, 275, **351**	[148, 155]
ZnS (hexagonal)	72, 158, 177, 219, 273, 286, **351**	[148]
Cu_2S	**472**	[154]
$Cu_{2-x}S$	**264**, **475**	[142, 157]
CuS	**267**, **471**	[154, 158, 159]
SnS_2	202, **317**	[149, 152, 153, 156]
Sn_2S_3	52, 60 ,71, 87, 183 ,234, 251, **307**	[149, 156]
SnS	96, **163**, **189**, **220**, 288	[149, 156, 157]
MoS_2	286, **380**, **408**	[147, 150]

4.4.3 Photoluminescence

As briefly discussed in section 2.6, photoluminescence measurements can be used to discern different phases from each other by looking at the peak position of the luminescence of the respective phases. In her doctoral thesis, Katja Hönes has discussed this possibility for the first time for the CZTS system [160]. In her work, she has measured a variety of individual phases, including Cu_2ZnSnS_4, Cu_2SnS_3, ZnS, and Cu_2S. In low temperature PL measurements (at 10 K) she obtained broad peaks for the CZTS and CTS phase at 1.14 eV and 0.81 eV, respectively. This is in accordance with what has been found by Altosaar et al. [146], and it indicates that a discrimination of those phases should be possible with PL measurements. For the ZnS and Cu_2S phase, however, no peaks were observed. For ZnS, this is due to the fact that the excitation

energy of the laser in the setup is below the band gap of those phases, which makes a luminescence impossible. It has been concluded, however, that in principle and depending on the excitation energy used, a discrimination of different phases should be possible.

Similar to Raman spectroscopy, however, photoluminescence has the disadvantage of being surface sensitive which limits the applicability of the technique. Therefore, depth profiling, similar to that suggested for Raman spectroscopy, would be necessary to investigate secondary phases that are not surface near. Furthermore, PL strongy depends on the quality of the material. Hereby, a defect rich phase, for example, would not be detectable. In addition, it is yet unclear, how the PL yield of multiple phases in a mixed sample will be influenced. Investigations with respect to this issue are part of the objective of this work and will be discussed later.

4.4.4 Other methods

Given the difficulties in distinguishing certain phases with the mentioned techniques, especially considering their disadvantageous properties of surface sensitivity, etc., other techniques must be used to gain additional information. As one possible technique, EDX mapping or line scans have shown their usefulness. They can give a qualitative idea about the lateral or depth-resolved distribution of certain elements for top-view or cross sectional analysis of the sample, respectively [18, 141]. The presence of a majority element can then indicate a certain phase.

Similar to EDX cross-sectional analysis, secondary ion mass spectrometry (SIMS) and Auger electron spectroscopy depth profiling can be used to make quantitative depth-resolved analysis of the elements and hence of possible secondary phases [139, 143]. Hereby, however, a careful calibration of SIMS and AES has to be performed.

A method to eradicate unwanted secondary phases is selective etching. A commonly used etch is that using KCN solution, which is known to remove Cu-S phases, its effect on other possible secondary phases in the Cu-Zn-Sn-S system, however, has not been studied in detail, yet. Section 4.15 will discuss this issue in more detail.

Experiment

This part briefly discusses the experimental procedures that were used to study the possible secondary phases in the Cu-Zn-Sn-S system and how they can be discerned from the Cu_2ZnSnS_4 phase.

4.5 Sample preparation

In order to determine which ternary and binary phases can be formed under the same annealing conditions that have been used for the fabrication of CZTS thin films, various electrodeposited and vapour-deposited precursors have been annealed in a sulfur containing atmosphere in order to obtain individual samples of individual phases (samples A to E). Hereby, only the precursors of sample C were vapour-deposited as the used electrochemical solution for Sn deposition did not allow a direct deposition on Mo. Table 4-4 contains a list of all prepared samples (with their fabrication sequence) that were used for the studies being presented in this chapter. The electrodeposition was performed using a RDE and the settings presented in chapter 3, and the standard annealing conditions are as described in section 2.2.

To determine which phases form and if those phases can potentially be discerned from the Cu_2ZnSnS_4 phase, all samples have been characterized in terms of their composition, morphology, structure, as well as electronic structure, performing EDX/WDX, SEM, XRD, Raman spectroscopy, and PL measurements. Hereby, the Raman spectroscopy measurements were performed by the group of Prof. Perez-Rodriquez from Barcelona and by Rabie Djemour of the University of Luxembourg. The used settings for the respective techniques are shown in chapter 2.

4.6 Gradient samples with intermixed phases

In order to determine which analytical tool can be used to discern a Cu_2SnS_3 or a ZnS phase from a Cu_2ZnSnS_4 phase, two copper, tin, and sulfur containing samples (samples I and J) were prepared that furthermore contain a zinc layer with a thickness gradient from one side of the sample to the other, as shown in Figure 4-12. To prepare those samples, at first a copper layer was electrodeposited onto a Mo substrate using the rotating disc electrode, as sketched in Figure 3-7 (b). In the subsequent step, a zinc layer with a thickness gradient from one side to the other side of the sample was deposited in a vertical setup. Hereby, the thickness variation was achieved by slowly dipping the sample into the solution during the process of deposition, as sketched in Figure 4-12. The part of the sample that has been exposed to the solution for a longer period of time allowed a thicker deposition of the Zn layer. In the next step, the Mo/Cu/Zn precursor was then annealed under standard conditions in a sulfur and tin sulfide containing environment, which allowed a self-controlled introduction of tin sulfide and sulfur from the vapour phase, as introduced in chapter 5.

To determine which phases have formed with respect to the position on the sample and how well (qualitatively as well as quantitatively) they can be discerned from the CZTS phase, spatially resolved EDX (mapping), SEM, XRD, Raman spectroscopy, and PL measurements have been performed. Figure 4-13 schematically shows the positions and areas of the respective measurements. The used machine settings are described in chapter 2.

Table 4-4 Fabrication sequence of all sample investigated. The standard annealing conditions are described in section 2.2.

Sample	Expected phase	Fabrication process
A	MoS_x	- annealing of a cleaned Mo substrate under standard (I) conditions (sulfur only)
B	$Cu_{2-x}S$	- electrodeposition of a Cu layer onto a Mo substrate using RDE - annealing of this precursor under standard (I) conditions (sulfur only)
C	Sn_xS_x	- vapour-deposition of a Sn layer onto Mo substrate - annealing of this precursor under standard (I) conditions (sulfur only)
D	ZnS	- electrodeposition of a very thin Cu layer onto Mo substrate using RDE in order to enable an electrodeposition of a thicker Zn layer - annealing of this precursor under standard (I) conditions (sulfur only) - KCN etching of this sample in order to remove possible Cu-S phases
E	Cu-Sn-S	- electrodeposition of a Mo/Cu/Sn stack using RDE - annealing of this precursor under standard (I) conditions (sulfur only) - KCN etching of this sample in order to remove possible Cu-S phases
F	Cu_2ZnSnS_4	- electrodeposition of a Mo/Cu/Zn stack using RDE - annealing of this precursor under standard (II) conditions (S + SnS) - KCN etching of this sample in order to remove possible Cu-S phases
G	ZnS + $Cu_{2-x}S$	- electrodeposition of a very thin Cu layer onto Mo substrate using RDE in order to enable an electrodeposition of a thicker Zn layer - annealing of this precursor under standard (I) conditions (sulfur only)
H	ZnS + CZTS	- electrodeposition of a very thin Cu layer onto Mo substrate using RDE in order to enable an electrodeposition of a thicker Zn layer - annealing of this precursor under standard (II) conditions (S + SnS)
I	CZTS + CTS gradient	- electrodeposition of a Cu layer onto Mo substrate using RDE - electrodeposition of a Zn layer with a thickness gradient using vertical deposition (section 4.6) - annealing of this precursor under standard (II) conditions (S + SnS)
J	CZTS + ZnS gradient	- electrodeposition of a Cu layer onto Mo substrate using RDE - electrodeposition of a Zn layer with a thickness gradient using vertical deposition (section 4.6) - annealing of this precursor under standard (II) conditions (S + SnS)
K	CZTS, $Cu_{2-x}S$, ZnS	- electrodeposition of a Cu layer onto Mo substrate using RDE - electrodeposition of a Zn layer onto Mo/Cu using RDE - annealing of this precursor under standard (I) conditions (sulfur only) - annealing of this precursor under standard (II) conditions (S + SnS)
L	CZTS	- electrodeposition of a Cu layer onto Mo substrate using RDE - electrodeposition of a Zn layer onto Mo/Cu using RDE - annealing of this precursor under standard (II) conditions (S + SnS)
M	Cu_2SnS_3	- electrodeposition of a Mo/Cu/Sn stack using RDE - annealing of this precursor under standard (I) conditions (sulfur only) - KCN etching of this sample in order to remove possible Cu-S phases
N	Cu_2SnS_3	- electrodeposition of a Mo/Cu/Sn/Cu/Sn stack using RDE - annealing of this precursor under standard (II) conditions (S + SnS) - KCN etching of this sample in order to remove possible Cu-S phases

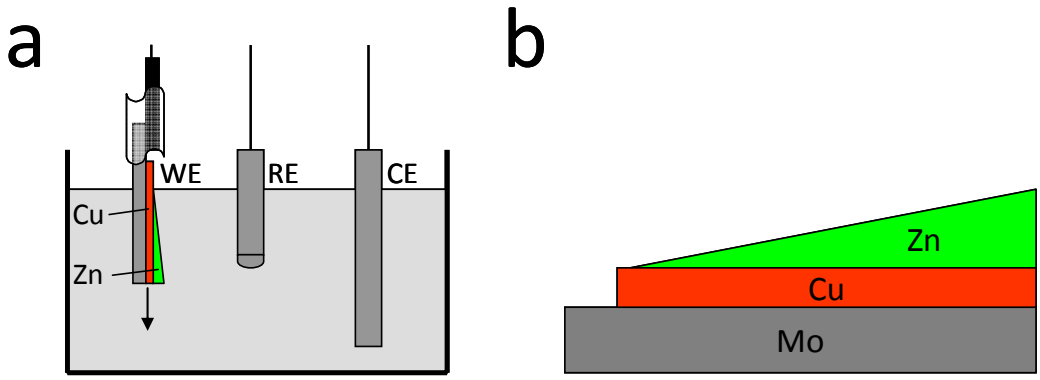

Figure 4-12 (a) Sketch of the vertical deposition setup used to deposit a lateral zinc gradient by slowly dipping the sample into the deposition solution under potential (see arrow). (b) Schematic cross-section of the precursor after electrodeposition.

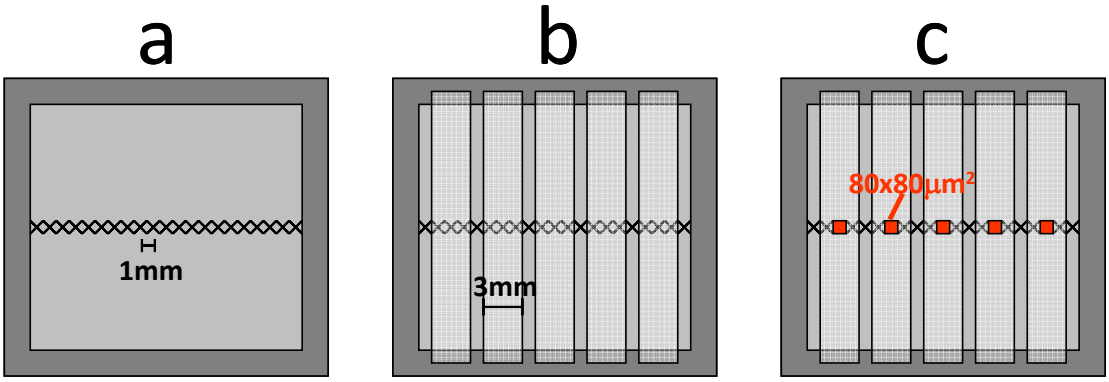

Figure 4-13 Schematic representation of the measurement positions and areas for the sample with zinc gradient. Sketch (a) shows the positions indicated by crosses where the EDX measurements were taken (measurement area ≈ 200 · 300 μm^2), sketch (b) the areas (semi-transparent white boxes) over which the XRD signal was integrated, and sketch (c) the areas (red boxes) at which the EDX mapping, Raman spectroscopy, and PL measurements were performed.

4.7 EDX mapping

To investigate the suitability of EDX mapping for the identification of laterally distributed multiple phases, a Mo/Cu/Zn precursor has been electrodeposited. At first, the sample (K) was annealed in a sulfur containing atmosphere to form $Cu_{2-x}S$ and ZnS phases. Amongst other investigations, this sample was investigated with EDX mapping (see experimental details in section 2.3.2). After annealing of the same sample in a sulfur and tin sulfide containing atmosphere, EDX mapping experiments have been repeated to investigate changes.

4.8 AES depth profiling

As an example to show the suitability of AES depth profiling to identify the depth-resolved position of secondary phases, sample L was chosen. This sample was fabricated by the electrodeposition of a Mo/Cu/Zn stack followed by the annealing in a sulfur and tin sulfide containing atmosphere (see chapter 5) to form CZTS. To investigate whether there is an accumulation of a secondary phase at the form or back of the absorber layer, depth profiles were obtained using Auger electron spectroscopy (see section 2.7 for details).

4.9 KCN-etching experiment

From literature it is known that copper sulfide phases can be removed by etching in an aqueous KCN solution. Due to this, a standard etch in a 5 wt% aqueous KCN solution for 30 s is typically performed for all samples that are subsequently processed to solar cell devices.

In order to find out whether such a standard etch can also be used to remove the ternary Cu_2SnS_3 phase, a CTS sample (sample M) has been prepared (as discussed in Table 4-4) and has been etched for 0 s, 5 s, 60 s, and 360 s. In between each etching step, X-ray diffraction pattern were measured for the same sample area, in order to investigate any changes in peak intensity.

4.10 Solar cell based on the ternary compound Cu_2SnS_3

The fabrication of a solar cell device based on the ternary Cu_2SnS_3 p-type semiconductor has been performed in multiple steps (sample N). At first, Cu and Sn were sequentially electrodeposited onto a Mo substrate in a double sandwich order Mo/Cu/Sn/Cu/Sn. Details of the ED method as well as the bath compositions are given in chapter 3. Following the ED, the precursor was then annealed in a tube furnace at standard conditions (see section 2.2) together with elemental sulfur and SnS powder to convert the metal stack into the desired Cu_2SnS_3 compound. Subsequently, the sample was etched for 30 s in a 5 wt% KCN solution. Photovoltaic devices were formed by the addition of a chemical bath deposited CdS buffer layer (90 nm, see section 5.6), followed by sputtered i-ZnO and Al:ZnO layers, and a Ni:Al front contact grid. The latter two steps were performed by the Helmholtz Zentrum in Berlin.

Compositional and morphological information of the absorber layer have been gained using EDX and SEM, respectively, the phase analysis has been carried out using grazing incidence XRD and Raman spectroscopy, and electro-optical properties were deduced from photoluminescence, current-voltage, as well as external quantum efficiency measurements. The respective measurement details are given in chapter 2.

Results and Discussion

The first part of the chapter deals with the results obtained by the different studies to determine which phases of the Cu-Zn-Sn-S system can be formed individually under the standard annealing conditions and furthermore how such secondary phases can be discerned from a majority Cu_2ZnSnS_4 phase. At first, characterization results of the individual and mostly pure phases are shown and conclusions are drawn of which analytical tool could be useful to qualitatively discern these phases from the CZTS phase. Following this, results of a quantitative analysis are presented in which the issue of the discrimination of minority Cu_2SnS_3 and ZnS phases from a majority Cu_2ZnSnS_4 phase is discussed. This is followed by a brief study of other tools which can be useful to identify secondary phases. Finally, the issue of etching of a Cu_2SnS_3 phase and the potential of this compound as an absorber layer in photovoltaic devices is examined.

4.11 Possible secondary phases and their qualitative discrimination from Cu_2ZnSnS_4

In section 4.2 it has been introduced, which phases of the Cu-Zn-Sn-S system can possibly occur under equilibrium conditions. Since a typical annealing process is not necessarily in equilibrium, the existence of phases at a certain temperature might be different to the expectations drawn from the phase diagrams. Furthermore, the partial pressure of sulfur in the used system is unknown, which makes it difficult to predict (using Figure 4-8) which phases can possibly form. To be able to determine which phases of the various binary and ternary subsystems form under the standard annealing condition for the fabrication of CZTS, as used in this work, and in order to find a way to distinguish and discern those phases from CZTS, individual samples of different phases have been made and characterized structurally as well as compositionally.

After the first subsection introduces which phases can be made, the following subsections discuss which tool could be used to qualitatively discern those phases from the CZTS phase.

4.11.1 Possible secondary phases at standard annealing conditions

Table 4-5 lists the results of the compositional analysis and Figure 4-14 shows the X-ray diffraction pattern obtained from the individual binary and ternary phases, both in comparison to sample F, a majority Cu_2ZnSnS_4 containing sample.

For sample A, where the effect of the substrate with respect to structural analyses was investigated, the main signal in the structural analysis comes from the Mo substrate, as can be seen from the peak at 40.51 °. In addition to this, a very small contribution from the MoS_2 phase can be seen at around 33 °, indicating that the substrate also starts to sulfurize during the annealing process. This finding is in accordance to the compositional investigation using WDX, where sulfur could be found inside the Mo substrate. Hereby, the ratio of Mo/S is much larger than 0.5, as would be expected for a pure MoS_2 phase, which confirms that the sample consists of a thick Mo layer with a small MoS_2 layer.

In the case where a Cu thin film was annealed together with elemental S (sample B), two phases have been formed. According to the XRD analysis, Cu_9S_5 as well as $Cu_{31}S_{16}$ have formed under the standard annealing conditions at 550 °C. According to the crystallographic database, Cu_9S_5 is referenced to be a digenite phase ($Cu_{2-x}S$). This is consistent with the phase diagram (see Figure 4-5) that describes its presence at temperatures above 435 °C. In contrast to this, the $Cu_{31}S_{16}$ phase is a typical low temperature phase (below 72 °C). Therefore, it is assumed

that $Cu_{31}S_{16}$ might have formed during the cool down process. The average compositional ratio of copper to sulfur of this sample has been measured to be 1.74 (using WDX). This value is a little lower than what would be expected for those two phases (Cu_9S_5 and $Cu_{31}S_{16}$) but still within the error of the measurement. Due to the possibility to grow a $Cu_{2-x}S$ phase under the standard annealing conditions, the partial pressure of S_2 must have reached a value of 10^{-10} mbar at some point during the annealing, according to Figure 4-8.

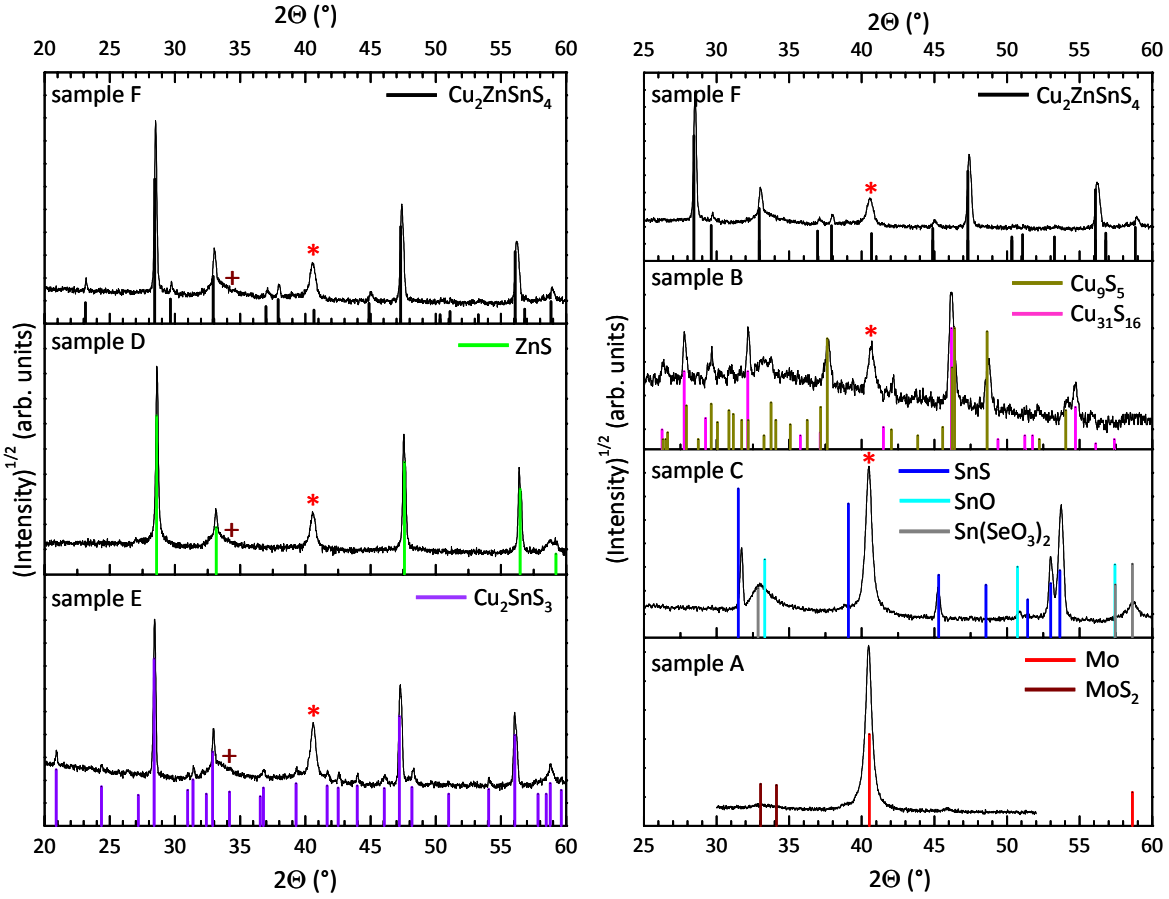

Figure 4-14 XRD pattern of the individual secondary phases that have been prepared under the standard annealing conditions in comparison to that of the Cu_2ZnSnS_4 phase. In addition to the measured pattern, vertical lines are shown that indicate the peak position and intensity ratios of the most probably phases as taken from [23]. Hereby, black indicates a Cu_2ZnSnS_4, green a ZnS, violet indicates a monoclinic Cu_2SnS_3, gold a Cu_9S_5, pink a $Cu_{31}S_{16}$, dark blue a SnS, light blue a SnO, grey a $Sn(SeO_3)_2$, brown and "+" a MoS_2, and red and "*" a Mo phase. The JCPDS numbers are as given in Table 4-1.

Table 4-5 Collection of the compositional and structural results of individual secondary phases that have been prepared under the standard annealing conditions in comparison to those of the Cu_2ZnSnS_4 phase.

Sample	Expected phase	Compositional results (EDX/WDX)	Phases present accord. to XRD
A	MoS_x	Mo/S = 6.94	Mo, MoS_2
B	$Cu_{2-x}S$	Cu/S = 1.74, 40 at% Mo	Mo, Cu_9S_5, $Cu_{31}S_{16}$
C	Sn_xS_y	Sn/S = 1.30, Sn/(S + Se) = 0.93, 60 at% Mo	Mo, SnS, SnO, $Sn(SeO_3)_2$
D	ZnS	Zn/S = 0.97, 0.2 at% of Cu, 8 at% Mo	Mo, MoS_2, cubic ZnS
E	Cu-Sn-S	Cu/Sn = 1.71, S/(Cu + Sn) = 1.09, 13 at% Mo	Mo, MoS_2, monoclinic Cu_2SnS_3
F	Cu_2ZnSnS_4	Zn/Sn = 0.97, Cu/(Zn + Sn) = 0.78, Cu/Sn = 1.53, S/metals = 1.12, 35 at% Mo	Mo, MoS_2, Cu_2ZnSnS_4

The annealing of a Sn containing precursor (sample C) had its difficulties. Out of three attempts, there was only one precursor that showed traces of Sn containing phases residing on the sample. In section 4.3.4 the findings of Piacente et al. have been introduced which describe the decay of SnS_2, Sn_2S_3, and SnS phases at elevated temperatures [135]. Since the vapour pressure of SnS is high at 550 °C (see Figure 4-9 (a)), the evaporation of SnS during a sulfurization step is expected. This explains the difficulties of obtaining a Sn-S phase at the used annealing conditions. The compositional analysis of the residual phases shows a Sn/S ratio of 1.30 (WDX). This result indicates a lack of S even with respect to the S poor SnS phase. Furthermore, the presence of Se has been seen by EDX investigations. Since Se has not been introduced to the annealing process, it is assumed that its existence is due to a contamination of the precursor during the vapour deposition process, as the PVD is typically used with selenium. Looking at results from the X-ray diffraction analysis of this film, SnS, SnO, and $Sn(SeO_3)_2$ phases are found. This result explains the lack of S seen in the WDX analysis however the presence of oxygen also states that either something must have gone wrong with the annealing, or that the sample oxidized significantly during annealing and analysis. This issue is yet unsolved and is connected to the fact that the formation of a Sn-S phase at these annealing conditions is not trivial. For the given results, another consequence arises. As the vapour pressure of Sn is fairly low compared to that of SnS at the given temperature (see Figure 4-9 (a)), and since in two out of three attempts to form a Sn-S phase, nothing was left on the sample, after the annealing, it is assumed that SnS did form under the used conditions and subsequently evaporated off the sample. From this observation and using the Ellignham diagram, one can conclude that the maximum partial pressure of sulfur inside the annealing chamber was at least 10^{-9} mbar. As, however, no sign of a Sn_2S_3 or SnS_2 phase has been observed, it is likely that the partial pressure of S_2 was less than 10^{-2} mbar, unless Sn_2S_3 and SnS_2 were formed and subsequently decomposed again.

As pointed out in Table 4-4, a thin Cu layer had to be deposited first in order to deposit a thicker Zn layer. After sample D had been annealed, the secondary Cu-S phases have been etched away in a KCN solution, leaving only 0.2 at% of Cu behind. The remaining elements were detected to be Zn and S and their average ratio has been determined to be 0.97. This result fits nicely to that of the structural analysis which shows the presence of a cubic ZnS phase, which is in accordance with the phase diagram (see section 4.2.6). Furthermore, the formation of ZnS under the used annealing conditions is in agreement with Figure 4-8, as the partial pressure of S_2 is definitely larger than 10^{-21} mbar.

To determine which of the various ternary Cu-Sn-S phases would form at the standard annealing condition, a Cu and Sn containing precursor has been annealed. After obtaining the XRD pattern, it could be seen that besides the contribution of the Mo substrate, every major as well as minor peak can be explained by the monoclinic Cu_2SnS_3 phase, in peak position as well as in peak intensity ratios as shown in Figure 4-14. This results agrees well with the findings of Moh and Onoda who prepared a monoclinic Cu_2SnS_3 phase at slightly higher temperatures of 600 °C [70, 100]. Since the average composition ratio of Cu/Sn = 1.9 is smaller than expected for this phase, the presence of ternary phases cannot be completely excluded. Due to the presence of all the minor "monoclinic Cu_2SnS_3 only peaks" (at 31 °, 31.5 °, etc), it is however certain that the monoclinic Cu_2SnS_3 phase is the majority ternary phase that forms at the standard annealing conditions. Assuming that Cu_2SnS_3 forms via the following reaction

$$Cu_2S(s) + SnS(s) + \tfrac{1}{2}S_2(g) \rightarrow Cu_2SnS_3(s),$$

Reaction 4-4

knowing that the partial pressure of S_2(g) lies between 10^{-9} and 10^{-2} mbar, and assuming that the formation reaction was in equilibrium, the Gibbs free energy of formation of CTS at 550 °C can be estimated using Equation 4-5 to range between

$$\Delta G_{CTS}(550°C) = -RT \cdot \ln\left(\frac{(a_{CTS})^1}{(a_{Cu_2S})^1 (a_{SnS})^1 (a_{S_2})^{1/2}}\right) = -RT \cdot \ln\left(\frac{1}{1 \cdot 1 \cdot (a_{S_2})^{1/2}}\right) = -RT \cdot \ln\left(\frac{1}{(\frac{p_{S_2}}{1bar})^{1/2}}\right)$$

= -94.5 and -39.4 kJ/mol,

Equation 4-6

respectively. The given range is fairly large, which is mainly due to the un-exact estimation of the partial pressure of sulfur but also dependent on the used reaction mechanism.

From this investigation it can be concluded that aside from the Cu_2ZnSnS_4 phase the following phases are the most probable ones to be expected in the Cu-Zn-Sn-S system and under the standard annealing conditions used in this work: Cu_2SnS_3, ZnS, $Cu_{2-x}S$, and SnS, where SnS typically seems to completely evaporate from the films within the time of annealing.

4.11.2 Qualitative discrimination of individual secondary phases from Cu_2ZnSnS_4

After it has been shown which binary and ternary phases can be expected as a minority phase in a Cu-Zn-Sn-S system under the used annealing conditions, this section will focus on the question which analytical tool can help to discern such secondary phases from a Cu_2ZnSnS_4 phase. In the following, results of X-ray diffraction, Raman spectroscopy, and PL measurements on the individual phases will be discussed.

X-ray diffraction

Figure 4-14 shows the X-ray pattern from the individual samples in comparison to the pattern of a sample with majority CZTS phase. From the pattern on the right hand side of the Figure (samples A, B, C, and F), one can see that the main peaks of the Cu-S, Sn-S, Mo-S, and Mo phases have distinctly different angular positions than the main peaks of the CZTS phase have. From this, it can be concluded that in a mixed sample the mentioned phases should be discernable from CZTS by the presence of non-overlapping peaks, assuming they have a reasonable intensity.

The X-ray pattern of ZnS and the monoclinic CTS (seen on the left side of Figure 4-14), however, are very similar to that of the CZTS phase. The reason for this can be found in the crystal structure of the three phases, as their lattice planes have very similar distances, the peak positions are very similar. Hereby, the cubic ZnS is the phase with the highest symmetry and thusly shows the fewest peaks. Compared to that, the tetragonal CZTS phase has a lower symmetry which explains the presence of some minor, unique peaks. An even lower symmetry is found in the monoclinic ternary phase, which shows an even larger number of minor and unique peaks. Since the common main peaks of the ZnS, CTS, and CZTS phase are very close together, it is the minor peaks that are important in order to identify whether a CZTS or CTS phase is present. The absence of those minor peaks, however, cannot sufficiently exclude the presence of the respective phase, as they can be hidden within the noise.

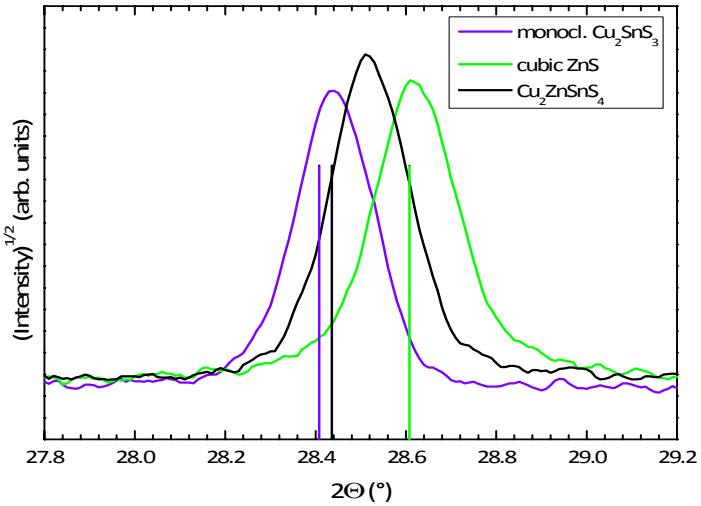

Figure 4-15 Enlarged XRD pattern of samples D (green), E (violet), and F (black) to view the differing peak positions of the (112)-peak (CZTS), (111)-peak (ZnS), and $(\bar{1}31)$-peak (CTS) at around 28.5 °. The vertical lines indicate the position of the respective phases according to the crystallographic database (JCPDS: CZTS: 01-075-4122; ZnS: 04-001-6857; CTS: 04-010-5719) [23].

Figure 4-15 shows an enlarged view of the most prominent peak of the individual ZnS, CTS, and CZTS phase at around 28.5 °, as measured and as given from the crystallographic database (vertical lines) [23]. The position of the measured peaks for the ZnS and CTS fit very nicely to literature values, only the peak position of the CZTS phase is shifted to higher angles. A possible reason for this can be found in the presence of strain in the CZTS layer grown at the annealing conditions used here. Furthermore, it can be seen that the angular position of the peaks of ZnS, CTS, and CZTS are not identical but lie within an angular range of 0.2 °. Assuming that the alignment (especially of the sample height) of the XRD machine is done properly for each measurement, it could potentially be possible to discern an individual CTS or ZnS phase from an individual CZTS phase by the peak position of the main peak (as shown in Figure 4-15). Furthermore, the presence of minor peaks in the pattern should definitely help to say whether CZTS or monoclinic/triclinic/tetragonal CTS is present in the film. This, however, is only true for (mostly) pure and individual phases under the use of optimal measurement conditions. How this translates into mixed samples, where a minority ZnS or CTS shall be discerned from a majority CZTS, is discussed in section 4.12.2.

Raman spectroscopy

Figure 4-16 displays the results of the Raman spectroscopy investigations on the individual samples A, C, D, E and a mixed sample G in comparison with a CZTS Raman spectrum.

In sample A, three narrow and major peaks are found at 286, 382, and 408 cm^{-1}, where the intensity is largest for the peak at highest wavenumber. This fits well to literature data of MoS_2, as has been summarized in Table 4-3 and it supports the findings from the XRD. As Raman spectroscopy is a surface sensitive technique, this result shows that the MoS_2 phase forms at the surface of the film, as can be expected. In addition to those three peaks (286, 382, and 408 cm^{-1}), another two broad and minor peaks were detected at 224 and 458 cm^{-1}. While the latter one is also observed by [147, 150] as a MoS_2 peak, the peak at 224 cm^{-1} is not fully understood but could be due to the measurement setup since it appeared in further Raman spectra, independent on the material (as seen in the spectra of samples A, D, and E).

The spectrum obtained from sample D shows four narrow (286, 351, 382, 408 cm^{-1}) and three broad peaks (219, 452, 467 cm^{-1}). While the peaks at 286, 382, 408, and 467 cm^{-1} can be related to MoS_2, the two at 219 and 351 cm^{-1} can be attributed to the ZnS phase. The observation of the MoS_2 modes in the Raman spectrum is related to the very low absorption of the green excitation light in ZnS, which allows both the excitation and the scattered light to pass through the ZnS layer. The result from this Raman investigation is in good agreement with the XRD results.

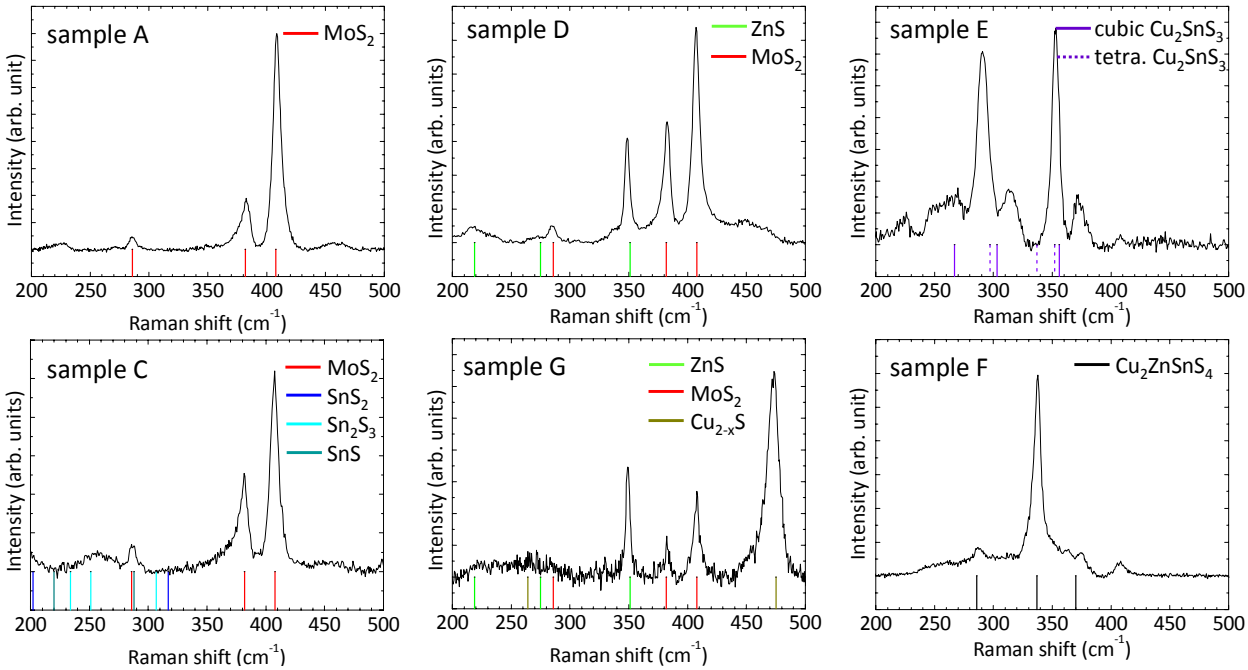

Figure 4-16 Raman spectra of the individual secondary phases that have been prepared under the standard annealing conditions in comparison to that of the Cu_2ZnSnS_4 phase. In addition to the measured pattern, vertical lines are shown that indicate the peak position of the most probable phases as taken from literature (see Table 4-1). Hereby, black indicates a Cu_2ZnSnS_4, green a ZnS, violet indicates a Cu_2SnS_3, gold a $Cu_{2-x}S$, dark blue a SnS_2, light blue a Sn_2S_3, grey a SnS, and red a MoS_2. The measurements of samples C, D, and E were made using a 514.5 nm excitation, and samples A, F, and G using 532 nm excitation.

Unlike the previous cases, the interpretation of the Raman spectrum obtained from sample E is not as simple. In the spectrum shown in Figure 4-16, eight peaks can be assigned altogether: 222, 250, 265, 290, 314, 352, 372, and 408 cm^{-1}. The peak at 408 cm^{-1} can be assigned to the MoS_2 phase, but since its intensity is very weak, the possibility is ruled out to identify any other peak of this spectrum with a MoS_2 mode, since the mode at 408 cm^{-1} is typically the strongest mode, as seen in sample A. The presence of the most dominant mode at 352 cm^{-1} agrees with the dominant mode of Cu_2SnS_3 as measured for the "cubic" and "tetragonal" phase by Fernandes et al. [102-104, 142, 149]. The main contributions at around 265-268 cm^{-1} as well as that at 291 cm^{-1} appear at Raman shifts very close to those to that reported by Fernandes et al. for "cubic" Cu_2SnS_3 (see Table 4-3) [102-104, 142, 149]. The differences in the relative intensity and position of the peaks from the results shown in Figure 4-16 in relation to those reported in literature suggest that in the present case a distorted cubic Cu_2SnS_3 phase is present. The XRD result (Figure 4-14) indicates the presence of a monoclinic Cu_2SnS_3 phase, which in principle can be seen as a distorted cubic structure. As published in [161], polarized Raman measurements, performed on the same sample by the group of Prof. Perez-Rodriguez from Barcelona, allowed the identification of dominant peaks at 290 cm^{-1} and 352 cm^{-1} with the main A' symmetry vibrational modes from the monoclinic Cu_2SnS_3 phase. In addition, the mode at 314 cm^{-1} is

suggested to be related to a third A' symmetry mode of the monoclinic CTS phase as well, while the peaks at 372 cm^{-1} and 222 cm^{-1} could be related to a $Cu_2Sn_3S_7$ phase [161, 162]. These results explain most of the peaks observed here. The origin of the remaining peaks at 250 cm^{-1} and 265 cm^{-1}, however, is yet unclear. Hereby, Sn_2S_3 with a weak mode at 251 cm^{-1} is ruled out as its strong mode at 307 cm^{-1} is missing. Similar to this, the $Cu_{2-x}S$ or CuS phases can be ruled out for the 265 cm^{-1} peak, as their strong phases at 475 and 471 cm^{-1} are also missing, respectively (as seen in Table 4-3).

The spectrum obtained from sample C is also shown in Figure 4-16, together with vertical lines that indicate the position of the SnS_2, SnS, and Sn_2S_3 phase, as published in [149, 152, 153, 156]. The three main peaks at 286, 381, and 407 cm^{-1} can all be attributed to a MoS_2 phase, only the very weak and broad peak at 258 cm^{-1} is yet unclear, since the main modes of the sulfur rich Sn-S phases lie around 310 cm^{-1} and that of the SnS phase is below 220 cm^{-1}, as shown in Table 4-1. Since it was furthermore not possible to relate these findings to the Sn-(Se-O) phases as observed in XRD, no real conclusion can be drawn from this measurement.

Similar to this, the Raman spectrum of sample B (not shown here) did also not show any sign of a Cu-S phase. Therefore, however, a Raman investigation of a mixed sample G (Cu/Zn = 0.9) shows modes from a MoS_2 (382, 408 cm^{-1}), ZnS (351 cm^{-1}) as well as a $Cu_{2-x}S$ (474 cm^{-1}) phase, as shown in Figure 4-16. This indicates that it is possible to discern MoS_2, ZnS, and $Cu_{2-x}S$ from each other.

Comparing the positions of all modes of the possible secondary phases with those of the Cu_2ZnSnS_4 phase (286, 337, 370 cm^{-1}), as shown in Figure 4-16, it can be concluded that the peak positions of the main modes (408 cm^{-1} for MoS_2, 474 cm^{-1} for $Cu_{2-x}S$, 351 cm^{-1} for ZnS, and 352 cm^{-1} for monoclinic CTS) are separated well enough to generally allow a discrimination of all those individual secondary phases from a Cu_2ZnSnS_4 phase (main mode at 337 cm^{-1}). This is in agreement with the findings of Fernandes et al. [149], however, this fact is only true for the comparison of individual and mostly pure binary or ternary phases with an individual and mostly pure CZTS phase. In such individual samples (like sample D), the measurable Raman signal can be optimized individually, whereas in a mixed sample, where the Raman efficiency can vary from one phase to another, the measureable signal is typically optimized to the most Raman efficient phase. This can lead to misinterpretations of the results. To study the discrimination of a ZnS and CTS minority phase from a majority CZTS phase using Raman spectroscopy, a mixed sample has been prepared and the results are presented and discussed in section 4.12.5.

Photoluminescence

Similar to the previous investigations, room temperature PL measurements have been performed on samples A to F in order to determine whether this technique is a possible candidate to be used for discerning possible secondary phases from the CZTS phase.

Since the excitation wavelength for this investigation was 514.5 nm, phases with a larger band gap, such as ZnS and $Cu_{2-x}S$, are not expected to luminese. This also explains that no signal has been obtained (not shown here) by PL measurements from the respective samples. In addition to that, there has also been nothing detected from SnS containing sample C, although the band gap of SnS (0.9 to 1.35 eV) is small enough. An explanation for this is yet unknown.

In contrast to those results, however, RT-PL signals of a monoclinic Cu_2SnS_3 and of a CZTS phase could be obtained and are shown in Figure 4-17. For the ternary Cu_2SnS_3 phase, a broad and asymmetric peak at 0.95 eV was obtained which suits the reported band gap values of around 0.93 eV well [105]. The signal from the CZTS phase was similarly broad and centered

around 1.3 eV. This latter finding is also in good agreement with the RT-PL data for CZTS reported in literature [146].

Comparing the spectral positions of those individual peaks, it should theoretically be possible to discern those phases from one another. This result agrees well with the findings of Katja Hönes, who studied these phases with low temperature PL [160]. Similar to previously mentioned arguments, however, it yet has to be proven whether such a discrimination is still possible in a mixed sample. Results about this are presented and discussed in section 4.12.6.

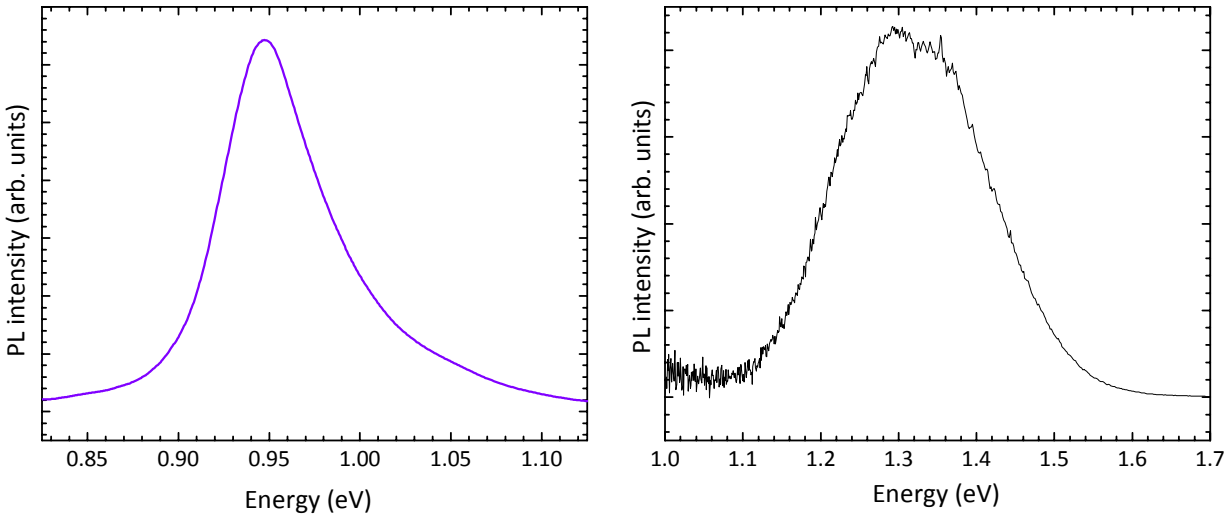

Figure 4-17 Room temperature PL spectra of a monoclinic Cu_2SnS_3 (left) and a Cu_2ZnSnS_4 (right) phase that have been prepared under the standard annealing conditions.

4.12 Quantitative discrimination of a minority Cu_2SnS_3 or ZnS phase from a Cu_2ZnSnS_4 phase

In the previous section it was shown that XRD, Raman spectroscopy, and PL could be useful tools to discern secondary phases from a majority Cu_2ZnSnS_4 phase. The results, however, were obtained from samples that contain individual phases. In such a case, the measured signal is typically optimized to each individual phase seperately. This means that so far, the signals coming from different phases (such as CTS, ZnS, and CZTS), did not have to compete with each other in the same measurement, especially in terms of the individual signal strength obtained from different amounts of the respective phases. When investigating a sample with multiple phases, on the other hand, the measured intensity can only be optimized to one, typically the dominating phase. Furthermore, the measured signal represents a convolution of the individual signals coming from each phase. As each of these individual signals can have different strengths (for example caused by different Raman efficiencies), it is possible that weaker signals (e.g. from phases with a low Raman efficiency) are sceened by stronger ones in the overall measured signal. In such a case, it can be difficult to discern different phases (such as ZnS, CTS, and CZTS) fom one another, although it is suggested by individual measurements.

To study how much of a secondary phase can be discerned from the majority CZTS phase (in a mixed sample) by the mentioned techniques, two samples with Zn gradients have been prepared in order to cover a range from a CTS rich to a ZnS rich side in a sample with a CZTS majority phase. Hereby, the focus was set to determine which tool can sufficiently and quantitatively discern a minority ZnS or CTS phase from a majority CZTS phase.

4.12.1 Composition and morphology of samples with Zn gradient

According to the experimental procedure described in section 4.6, the compositional ratios of the two samples with a deliberate Zn gradient (samples I and J) were obtained by EDX measurements along a line across the two samples. Figure 4-18 shows the obtained values. Hereby, the filled symbols represent the compositional ratios as obtained from the analyzing software, while the open symbols represent the compositional ratios after applying a correction function. The correction function was used to account for the systematic error of the EDX measurement which is caused by the detection of the Mo signal coming from the substrate, and hence for the subsequent mis-calculation of the "real" composition of the film (see section 2.3.2). The correction function is discussed in more detail in Appendix A. In the following, all numbers are given with respect to the corrected compositional ratios (open symbols).

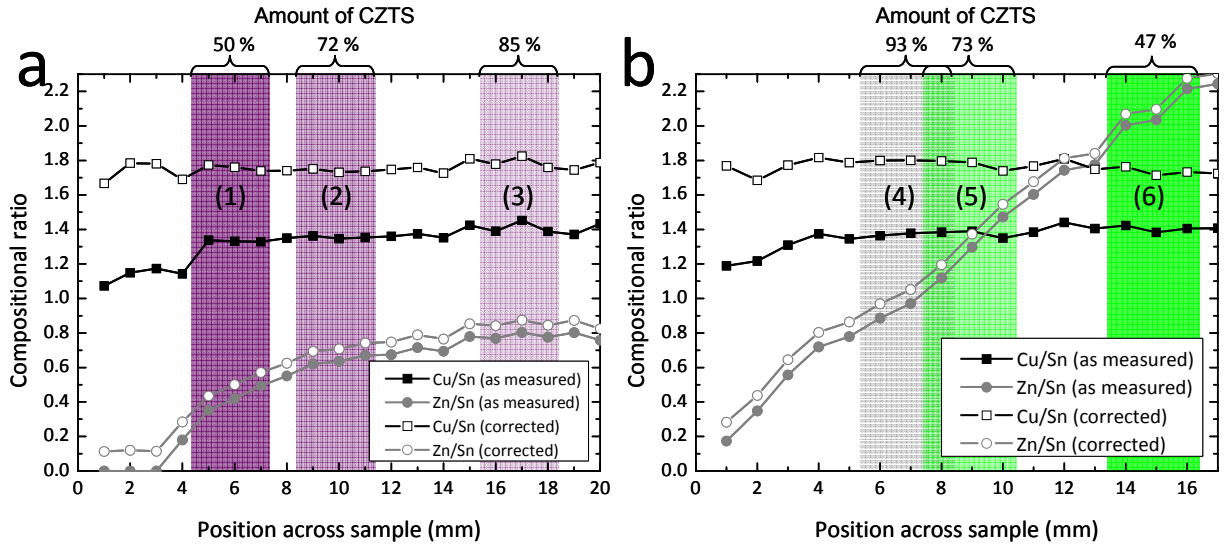

Figure 4-18 Compositional data of (a) sample I and (b) sample J. While the bottom axis shows the position across the sample, the top axis shows the maximum amount of CZTS that can be present at this position range as calculated from the Zn/Sn ratio and averaged over the shaded area. Dark violet indicates larger amounts of a CTS phase and dark green larger amounts of a ZnS phase. The different positions are labeled from (1) to (6). The fillied symbols represent the respective compositional ratio as measured, and the open symbols represent the respective ratios after applying the correction function, introduced in Appendix A.

From the Zn/Sn ratios shown Figure 4-18, the increase in Zn content across both samples is depicted. While this ratio covers a range between 0 and 2.2, that of the Cu/Sn ratio stays mostly constant at values between 1.65 and 1.8. For a stoichiometric Cu_2ZnSnS_4, a Zn/Sn ratio of 1.0 and a Cu/Sn ratio of around 2.0 are expected. In the present case, this latter condition is not completely met, however, it is comparable to the composition of the most efficient CZTS solar cells with Cu/(Zn+Sn) ≈ 0.8 and Zn/Sn ≈ 1.1 (resulting in Cu/Sn ≈ 1.7), as shown in Figure 5-1, indicating that CZTS has formed. Because of the large range of the Zn/Sn ratio, and due to the constant Cu/Sn ratio, a pure CZTS phase can therefore be expected at one point on these samples. In order to study the discrimination of ZnS and CTS from CZTS, six points of interest have been chosen across both samples. In Figure 4-18, these points ((1) to (6)) are marked in violet, gray, and green color such that the pure CZTS phase lies somewhere between points (3) and (4).

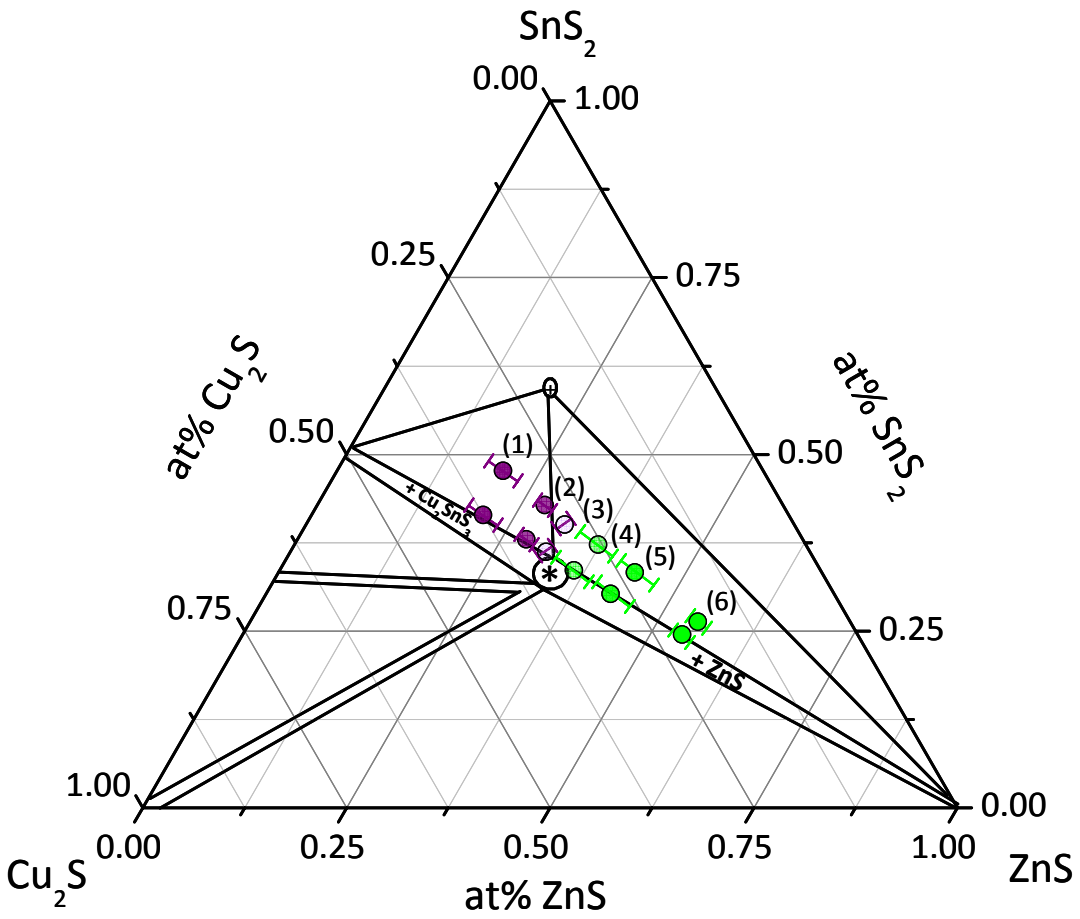

Figure 4-19 Measured (upper points) and corrected (lower point) compositional positions of the areas of interest in the pseudo-ternary phase diagram, as determined from the Zn/Sn and Cu/Sn ratios. The phase regions are according to [15] and were determined at 397 °C, while the present sample was annealed at 550 °C.

This can also be seen in Figure 4-19, which shows the compositional position of the the six differerent areas of interest in the pseudo-ternary phase diagram. While the upper points represent the positions as obtained from the EDX analyzing software, the lower points represent the compositional positions after the correcting function has been applied. One can see, that all the (latter) values lie along a line between the pure ZnS, the pure Cu_2ZnSnS_4 (marked with "*"), and the pure Cu_2SnS_3 phase (at 50 %SnS_2 and 50 %Cu_2S). Furthermore, they all lie on the border line between a two phase and a three phase region. This indicats that a third phase (a tin rich phase, such as SnS, Sn_2S_3, SnS_2, $Cu_2Sn_3S_7$, $Cu_2ZnSn_3S_8$, etc.) might be present at the six different positions, aside the expected CZTS and ZnS/CTS phases. For the present study, however, it is assumed that at each point of interest only two phases (CZTS and ZnS or CTS) are present.

From the position of points (1) to (3) in the phase diagram, it is expected that Cu_2SnS_3 (violet) is present in addition to CZTS, while ZnS (green) is expected to be the secondary phase at points (4) to (6). To calculate the maximum amount of CZTS that can be present with respect to the different positions across both samples, the Zn/Sn ratio was used. For a value of 1.0, a maximum of 100 % of the film can form CZTS. For Zn/Sn < 1.0, it was assumed that CZTS forms as much as possible and the residual Sn is used to form Cu_2SnS_3. Similar to this, for Zn/Sn > 1.0, it was assumed that CZTS forms as much as possible and the residual Zn is used to form ZnS. The respective amounts of Zn or Sn used to make CZTS and that amount used to make ZnS or

CTS finally calculate out the maximal percentage of CZTS in the layer. These numbers for the six points of interest are given in Figure 4-18.

In order to study how much of a secondary phase (ZnS or Cu_2SnS_3) can be detected aside a majority Cu_2ZnSnS_4 phase, XRD, PL & Raman spectroscopy, and EDX mapping investigations were performed at the six points of interest. The results of the mentioned investigations are discussed in the upcoming sections.

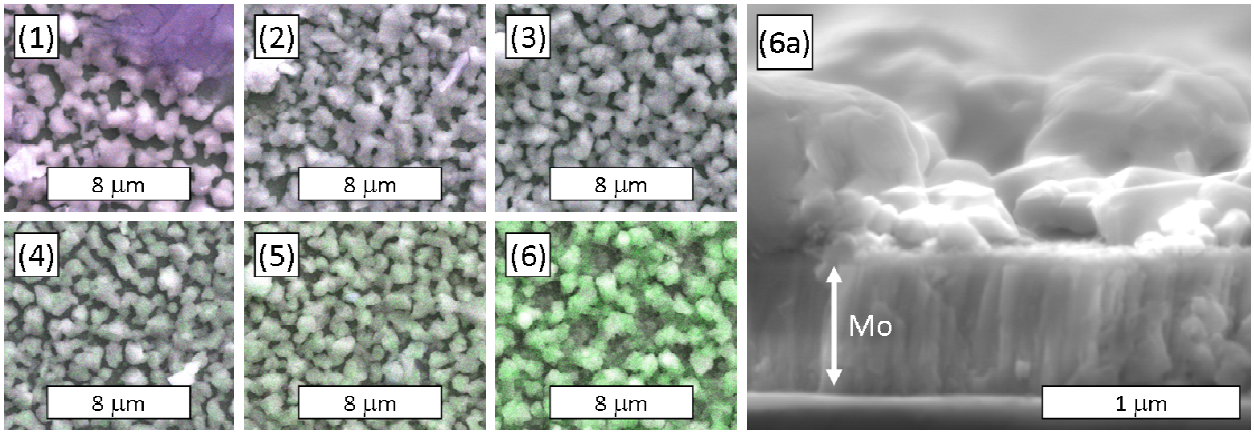

Figure 4-20 Figures (1) to (6) show top view SEM images overlaid with EDX mapping results of the positions (1) to (6) on both gradient samples, respectively. Hereby, red stands for Cu, blue for Sn, and green for Zn. Thusly, a violet color indicates a CTS rich region and green indicates a ZnS rich region. Figure (6a) show a SEM cross-section taken at position (6).

Figure 4-20 (1) to (6) shows SEM top view images overlaid with EDX mapping as obtained from the six areas of interest. The first thing to notice is the different morphologies of the six areas. While in position (1) fewer Zn has been deposited as in at the other positions, there is less material present. A consequence is that not the whole surface is covered with grains, but that there are holes in between the gains. The more Zn was deposited, the smaller ate the pinholes, as can be seen in the Figures (2) to (6). However, even in position (6), where a lot more Zn has been deposited, there are still pinholes in between the grains present (see cross section). This is probably due to the way the sample was fabricated. A detailed analysis of this fabrication method is given in section 5.9. The violet color in Figure (1) displays this lack of Zn (green color) while Cu (red) and Sn (blue) have been measured. The more Zn was inside the layer, the greener the images become. Hereby, Figures (3) and (4) appear fairly grey, indicating their proximity to the stoichiometric point. In most of those EDX maps it can be seen that the majority of grains is similar of color. This indicates that the present phases are in general not laterally distributed. Only Figure (1) shows regions of a darker blue. There an aggregation of Sn can be concluded. Apart from this dark blue spot, one can say that altogether the shape and the size of the typical grains in all six positions look very much alike. This could indicate that similar phases (such as CZTS) have formed everywhere.

Meanwhile, Figure 4-20 (6a) shows a cross-sectional SEM image of sample J at the Zn rich position (6). One can see the fairly open morphology from the side and one discovers small grains surrounded by big grains. Qualitative EDX analyses (not shown here) of the different objects lead to the conclusion that the big grains are CZTS and the small gravel is ZnS.

4.12.2 XRD: Discrimination of phases via peak position of the main XRD peak

In section 4.11.2, it was stated that ZnS and Cu_2SnS_3 could potentially be discerned from Cu_2ZnSnS_4 by looking at the angular position of the main peak of the three phases at around

28.5 °. This assumption was based on X-ray diffraction patterns from three individual samples that contained almost pure ZnS, CTS, and CZTS. In the present case of samples I and J, however, the CZTS phase is side by side with a ZnS or CTS phase. Therefore, it is assumed that diffraction peaks of those phases coexist and that the position of the resulting peak slightly varies depending on the amount of the present phases.

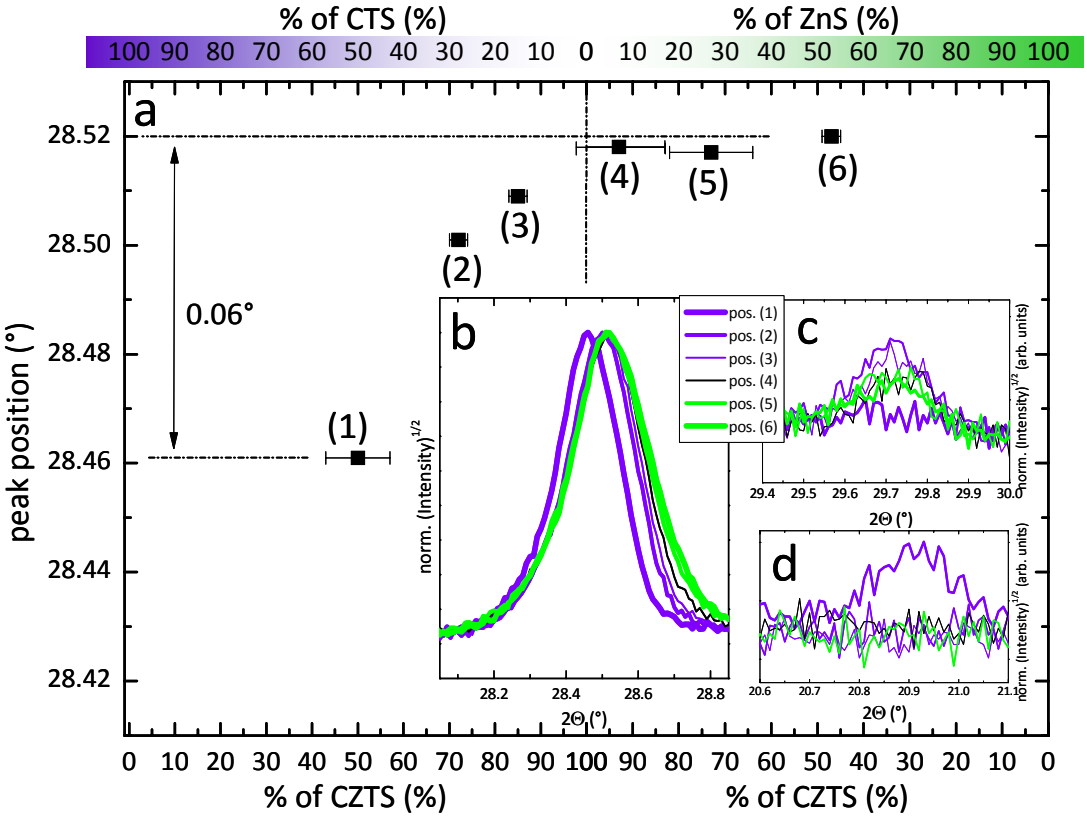

Figure 4-21 (a) (112)-peak position as a function of amount of CZTS. (b) (112)-peak shift as observed in the XRD pattern. (c) Appearance of (103)-peak that proves the existence of Cu_2ZnSnS_4. (d) Disappearance of (021)-peak of the monoclinic Cu_2SnS_3 phase.

Figure 4-21 (a) and (b) show the dependence of the peak position on the amount of CZTS and of the respective secondary phase. In inset (b), one can see that the main peak does shift by increasing the amount of CZTS. In the case of 50 % CZTS (pos. (1)), the measured diffractogram shows the presence of a monoclinic Cu_2SnS_3 phase, with a peak position of 28.46 ° for the main peak. By increasing amounts of CZTS, this peak shifts towards higher values until it reaches a steady state at 28.52 ° for around 93 % of CZTS and 7 % of ZnS (as can be seen in the Figure (a), pos. (4)). This overall peak shift from a 50 % CTS / 50 % CZTS case to an almost pure CZTS phase is with 0.06 ° fairly small. Here, the shift is only detectable due to a series of data points. In a single XRD measurement, however, a peak position of plus or minus 0.06 ° would not be convincing to clearly tell one phase from another, since deviations in this order of magnitude due to strain or due to a not properly aligned setup are certainly possible. The discrimination using only the peak position is hence not sufficient.

A more convincing proof for the presence of a CTS minority phase can be seen in the presence of the distinct and minor CTS peak at 20.9 °. Inset (d) shows the behavior of this peak for increasing amounts of CZTS. One can see that this peak completely disappears going from 50 % CTS to 28 % CTS. While this minor CTS peak disappears, the minor and distinct CZTS peak at 29.7 ° (see inset (c)) simultaneously appears. From this, one can conclude that the “minor peak indicator” does help to discern CTS from CZTS, but only down to 50 % of CTS in a layer. On the

other hand, one should also notice that the minor CZTS peaks also only give an indication of the presence of CZTS on the CTS rich ride if between 50 and 72 % of CZTS is present. On the ZnS rich side, however, the minor CZTS peaks are still detectable for less than 50 % of CZTS.

As commented in section 4.11.2, ZnS does not have a distinct minor peak, which makes it hard to judge whether there is secondary ZnS in the film or not. Looking at the peak position of the (112)-peak for the ZnS rich points on sample J, one can see that there is no obvious shift, although half of the sample consists of ZnS. This also leads to the conclusion that neither ZnS nor CTS can sufficiently be discerned from CZTS simply by looking at the peak position of a single measurement. In literature, this has often been mentioned as a fact but has never been shown.

4.12.3 XRD: Discrimination of phases via peak broadening of the main XRD peak

In inset (b) of Figure 4-21 one can see that aside a peaks shift, there is also a peak broadening caused by the superposition of the main peaks of CZTS and ZnS or CTS, respectively. The reason for this can be found in the fact that the peak positions of those three individual phases do not completely coincide, as visualized in Figure 4-15.

To analyze the dependence of the peak broadening, the measurements as shown in inset (b) of Figure 4-21 have been repeated carefully (see Appendix B for the measured pattern) in order to avoid the slight peak asymmetry that is present in the patterns of Figure 4-21 (b). The obtained symmetric (112)-peaks of the respective positions on the sample were then (single peak) fitted using “WinPlotr” (in the Fullprof software) and the *full width of half maximum* (FWHM) of the peaks were gained. In parallel, the software “PowderCell” was used to simulate the expected change in FWHM as a function of the amount of CZTS together with ZnS or CTS in the layer, respectively.

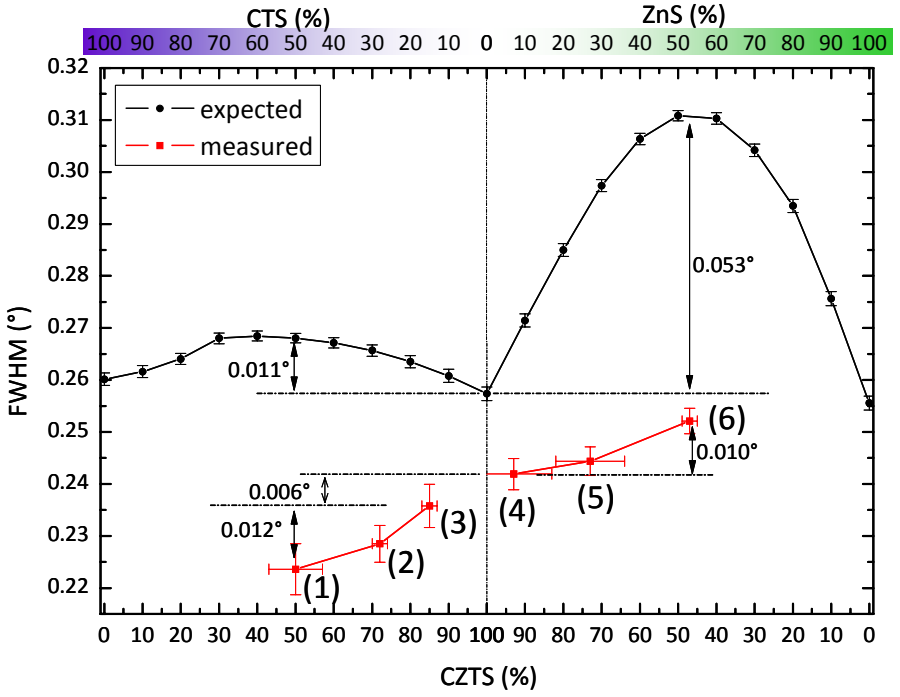

Figure 4-22 FWHM of the (112)-peak as a function of the amount of CZTS in the layer. The black points describe an expected behavior of the FWHM that was obtained by simulation of an XRD pattern of a mixed sample using PowderCell and crystallographic data according to Table 4-1 [23].

Figure 4-22 shows the simulated as well as the measured dependence of FWHM on the amount of CZTS. For 93 % CZTS (pos. (4); closest to pure CZTS), the FWHM has been measured

to be 0.243 °, while that of the simulated peak is around 0.26 °. The discrepancy is fairly small and can be explained by the UVW values that were used for the simulation. While the experiment was performed under a grazing angle of 1 °, the UVW values of the machine (used for the simulation) were obtained under a grazing angle of 5 °. This might lead to slightly wrong simulated peak shapes.

Looking at the ZnS rich region, one can see that the simulated FWHM changes by 0.053 ° to larger values when going from 100 % CZTS to 50 % CZTS and 50 % ZnS. After this the FWHM decreases again until a state of pure ZnS is reached. In the experimentally obtained FWHM, the general behavior stays the same by going from pure CZTS to 50 % CZTS / 50 % ZnS. Hereby, however, the change in FWHM is with 0.010 ° a factor of five smaller than in the simulated case. Another discrepancy of the simulated to the measured situation is that in the former case crystallographic data from a pure ZnS, CTS, and CZTS phase have been used, while in the measured case ZnS might be Sn-doped. As the crystal radius of Sn^{4+} (with a coordination number of IV) is with 0.69 Å larger than that of Zn^{2+} (0.64 Å, with coordination number of IV) [163], Sn-doping of ZnS would increase the lattice constants, which then would cause a peak shift of the ZnS peaks to smaller angles, hence towards the peak position of a pure CZTS peak. A superposition of such closer neighbors then has a smaller effect on the FWHM.

In the CTS rich region, the expected change in FWHM is fairly small with 0.011 °. The reason for this can be found in the fact that the expected peak position of CTS is fairly close to that of CZTS, as can be seen in Figure 4-15. The measured change in FHWM for an almost pure CZTS phase (pos. (4)) to the situation of a half CZTS and a half CTS (pos. (1)) case is also only around 0.018 °. In Figure 4-22, however, one can see that the peak becomes more narrow in a parity situation, unlike expected. Since the errors of the measurements in the CTS rich case are fairly large and of the order of 0.01 ° themselves, the observed change in FHWM is within the error of the measurement. Hence, a convincing peak broadening cannot be observed.

In the case of the presented series, only a small peak broadening can be observed for ZnS as well as CTS rich samples. Since such a change in FWHM is at a similar order of magnitude than that caused by changes in grain size, etc, it is not possible to discern a CTS or ZnS phase from CZTS by looking at the FWHM of a single measurement. In general, each diffractometer has a different machine function that describes the shape of an ideal peak, which makes it even harder to compare peak widths of different origin.

4.12.4 XRD: Discrimination of phases via Rietveld Refinement of XRD pattern

After having shown that it is not possible to sufficiently discern ZnS and CTS from a CZTS phase by considering the peak position and FHWM of the (112)-peak, this section will deal with the question whether a Rietveld refinement analysis of the measured XRD pattern can help to discern ZnS and CTS from CZTS. In Appendix C the refined pattern obtained from the positions (1) to (6) of samples I and J are shown and Table 4-6 contains some values of the refined parameters. Using the same symbols as given in the manual of the used software (FullProf), B_{ov} is the overall and B_{iso} the atom specific temperature coefficient, Pref1 and Pref2 are the texture coefficients, and R_{Bragg} is the quality coefficient, as introduced in section 2.4.3 [25]. As can be seen in Table 4-6, several attempts with different refinement parameters have been made in order to refine the measured pattern. Typically, data of the refinement with the lowest R_{Bragg} value have been used, unless a refinement parameter was not meaningfull. Furthermore, the lattice parameter for the respective phases as obtained from the refinement analysis can be found in Table 4-7.

Table 4-6 Collection of some values of the refined parameters. B_{ov} is the overall and B_{iso} the atom specific temperature coefficient, Pref1 and Pref2 are the texture coefficients, and R_{Bragg} is the quality coefficient, as introduced in section 2.4.3 [25]. Marked in red color are the results with the best quality factor, and in blue the expected amounts of CZTS at the respective position on the samples I and J.

Position on samples	Refined parameters	Temp. value B (Å^2)	Texture factors Pref1/Pref2	Quality coefficient R_{Bragg}	% of phase by refinement	% of CZTS by EDX
(1)	CZTS	B_{ov} = 1.0	1.0/0.0	7.43	CZTS: 100 %	50 ± 7 %
	CZTS + texture	B_{ov} = 1.0	5.5/1.0	8.99	CZTS: 100 %	
	CZTS + B_{ov}	B_{ov} = 2.6	1.0/1.0	5.70	CZTS: 100 %	
	CZTS + texture + CTS	B_{ov} = 1.0	1.18/0.0	7.91	CZTS: 96.0 % CTS: 4.0 %	
	CZTS + texture + CTS + B_{ov}	B_{ov} = 1.7	1.27/0.0	5.93	CZTS: 95.0 % CTS: 5.0 %	
(2)	CZTS	B_{ov} = 1.0	1.0/0.0	4.33	CZTS: 100 %	72 ± 2 %
	CZTS + texture	B_{ov} = 1.0	0.99/0.0	4.33	CZTS: 100 %	
	CZTS + texture + CTS	B_{ov} = 1.0	1.0/0.0	4.93	CZTS:98.8 % CTS: 1.2 %	
	CZTS + texture + CTS + B_{iso}	$B_{iso,S}$ = 1.58 $B_{iso,Sn}$ = 2.75	3.1/1.0	4.41	CZTS: 98.8 % CTS: 1.2 %	
	CZTS + B_{iso}	$B_{iso,S}$ = 2.06 $B_{iso,Sn}$ = 3.6	1.0/0.0	3.73	CZTS: 100 %	
(3)	CZTS	B_{ov} = 1.0	1.0/0.0	6.75	CZTS: 100 %	85 ± 2 %
	CZTS + texture	B_{ov} = 1.0	3.95/0.97	5.42	CZTS: 100 %	
	CZTS + texture + CTS	B_{ov} = 1.0	3.95/0.97	5.43	CZTS: 99.8 % CTS: 0.2 %	
	CZTS + texture + B_{ov}	$B_{iso,S}$ = 2.52 B_{ov} = 1.0	3.92/0.96	5.28	CZTS: 100 %	
(4)	CZTS	B_{ov} = 1.0	1.0/0.0	4.58	CZTS: 100 %	93 ± 10 %
	CZTS + texture	B_{ov} = 1.0	1.8/0.9	4.08	CZTS: 100 %	
	CZTS + texture + ZnS	B_{ov} = 1.0	1.2/0.0	5.23	CZTS: 73.2 % ZnS: 26.8 %	
	CZTS + texture + B_{ov}	B_{ov} < 0	--	--	--	
(5)	CZTS	B_{ov} = 1.0	1.0/0.0	6.63	CZTS: 100 %	73 ± 9 %
	CZTS + texture	B_{ov} = 1.0	1.01/0.01	6.31	CZTS: 100 %	
	CZTS + ZnS + texture	B_{ov} = 1.0	0.7/0.04	2.22	CZTS: 81.9 % ZnS: 18.1 %	
	CZTS + ZnS + texture + B_{ov}	B_{ov} = 2.0	0.7/0.07	2.57	CZTS: 76.3 % ZnS: 23.7 %	
(6)	CZTS	B_{ov} = 1.0	1.0/0.0	8.83	CZTS: 100 %	47 ± 2 %
	CZTS + texture	B_{ov} = 1.0	0.7/0.0	3.72	CZTS: 100 %	
	CZTS + texture + ZnS	B_{ov} = 1.0	0.7/0.0	3.16	CZTS: 66.1 % ZnS: 33.9 %	
	CZTS + texture + ZnS + B_{ov}	B_{ov} = 4.3 (very large)	0.7/0.0	2.33	CZTS: 55.3 % ZnS: 44.7 %	

The values marked in red in Table 4-6 indicate the best refinement results. In case of position (1), where 50 % of CZTS was expected, the best refinement gave a value of 95 % of CZTS and 5 % of CTS. This result shows that a better refinement could be obtained with two co-existing phases, but since the refined values only gave 5 % of CTS, this method might not be favorable

to discern CTS from CZTS either. This conclusion is hardened by the results obtained from the refinement at position (2). Although two attempts to refine the XRD pattern with a 99 % CZTS and a 1 % CTS phase also resulted in reasonable R_{Bragg} values, the best match was found in a refinement with 100 % CZTS. At this position, however, a maximum of 72 % CZTS is expected. Similar results are also obtained for positions (3) and (4) with amount of CZTS of 85 % and 93 %, respectively. In the latter case, 7 % of the phases inside the layer are expected to be ZnS. Attempts to refine this pattern better with a CZTS and a ZnS phase resulted in a worse quality factor. Unlike the results of the CTS rich positions, in position (5), where the composition suggests a presence of around 27 % of ZnS, Rietveld analysis gives the best match under the use of 18 % ZnS. This value is in fact within the error of the expected value and indicates that discrimination of 18 % of ZnS from CZTS is possible. This conclusion is partly supported by the values obtained from position (6). There around half of the sample is expected to be ZnS, and 34 % have been refined. Actually, an even more matching amount of 45 % of ZnS has been refined, as can be seen in Table 4-6, but in this refinement, the overall temperature coefficient was 4.3 $Å^2$, which is a very large value. Due to the few datapoints of this study, a more precise value for the minimum amount of detectable ZnS is difficult to give. As the compositional error of position (4) is fairly large, one can say that more than 7 % of ZnS needs to be present in order to qualitatively discern ZnS from CZTS with XRD measurements.

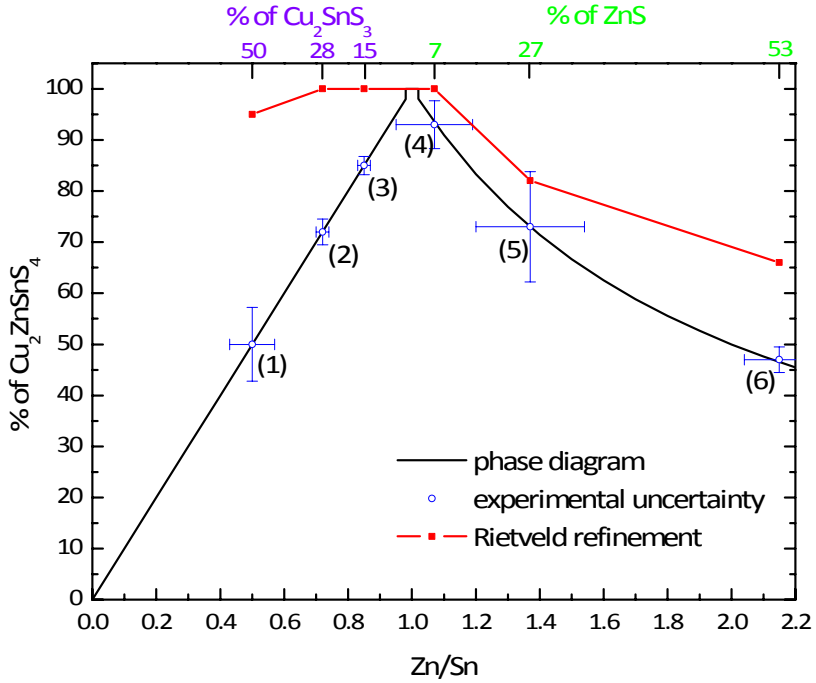

Figure 4-23 Plot of the amount of CZTS vs. the Zn/Sn ratio as obtained from EDX measurements. Hereby, the black line indicates the theoretical curve according to the phase diagram, the blue points given the uncertainty of the XRD measurement area, and red displays the results obtained from Rietveld refinement analyses.

All the described results are also displayed in Figure 4-23, where the predictions of the phase diagram are shown in black, the experimental uncertainty of the composition of the respective positions (1) to (6) are shown in blue, and where the obtained results from the Rietveld analysis are shown in red. From this graph, one can clearly see that even with refinement analyses, it is not possible to reliably discern CTS from CZTS on the basis of X-ray measurements. In the case of ZnS as the secondary phase, the results are slightly better. Taking the error bars of position (4) into account, one can see that a discrimination of more than 7 % of ZnS is possible. For thin film photovoltaic applications, however, even 1 or 2 % of a secondary phase can already be

crucial, dependent on its position within the layer. Therefore, the conclusion is that even with Rietveld analyses, X-ray diffraction measurements are not suitable to tell small amounts of ZnS (≤ 7 %) or also large amounts of Cu_2SnS_3 from Cu_2ZnSnS_4. However, a qualitative discrimination of larger amounts of ZnS (> 7 %) from CZTS is possible with XRD measurements.

Table 4-7 Lattice parameter as obtained from the Rietveld refinement analysis in comparison with data from literature. The following JCPDS data were used: Stannite CZTS: 01-075-4122; kesterite CZTS: 00-021-0883; monoclinic CTS: 04-010-5719; cubic ZnS: 04-001-6857.

Position on samples	Refined phases	Lattice parameter (Å)
(1)	Cu_2ZnSnS_4	a = b = 5.43383, c = 10.8366; $\alpha = \beta = \gamma = 90°$
	Cu_2SnS_3	a = 6.698, b = 11.592, c = 6.726; $\alpha = \gamma = 90°$, $\beta = 109.18°$
(2)	Cu_2ZnSnS_4	a = b = 5.43081, c = 10.8404; $\alpha = \beta = \gamma = 90°$
(3)	Cu_2ZnSnS_4	a = b = 5.43124, c = 10.8255; $\alpha = \beta = \gamma = 90°$
(4)	Cu_2ZnSnS_4	a = b = 5.43047, c = 10.8232; $\alpha = \beta = \gamma = 90°$
(5)	Cu_2ZnSnS_4	a = b = 5.43009, c = 10.8429; $\alpha = \beta = \gamma = 90°$
	ZnS	a = b = c = 5.41382; $\alpha = \beta = \gamma = 90°$
(6)	Cu_2ZnSnS_4	a = b = 5.43135, c = 10.8504; $\alpha = \beta = \gamma = 90°$
	ZnS	a = b = c = 5.41522; $\alpha = \beta = \gamma = 90°$
References (powder samples)	kesterite Cu_2ZnSnS_4	a = b = 5.44, c = 10.88; $\alpha = \beta = \gamma = 90°$
	stannite Cu_2ZnSnS_4	a = b = 5.43, c = 10.86; $\alpha = \beta = \gamma = 90°$
	monoclininc Cu_2SnS_3	a = 6.66, b = 11.54, c = 6.65; $\alpha = \gamma = 90°$, $\beta = 109.4°$
	cubic ZnS	a = b = c = 5.40; $\alpha = \beta = \gamma = 90°$

Table 4-7 shows the lattice parameters of the respective phases as obtained from the Rietveld analysis at the different positions. For CZTS, one can see that independently on the compositional position of the sample, the “a” values fit fairly well to that from the reference (from a powder sample). In contrary to this, the “c” values are around 0.02 to 0.04 Å smaller than what is expected for stannite CZTS (for a powder sample). Hereby, especially the “c” values obtained on positions (3) and (4) vary the most from the literature data, although these positions should be closest to the stoichiometric composition for CZTS. This result is yet unclear. Comparing the obtained lattice parameters (c/2a ≈ 0.9965 to 0.999, for pos. (1) to (6)) to those of other CZTS thin films (c/2a ≈ 0.997 to 0.998), as published by Siebentritt et al. [72], one can see that all values are fairly similar. Hereby, the larger scatter of the values from position (1) to (6) could be connected to the off-stoichiometric composition of the individual points of interest.

The lattice parameters obtained for the CTS phase in position (1) are slightly larger than what is expected for a monoclinic CTS powder sample. Hereby, the small descrepancy might be explainable by the thin film character of sample I.

From positions (5) and (6), the lattice parameters for ZnS could be obtained. With “a” values of around 5.414 Å, they are slightly bigger than what is expected from literature (5.40 Å, from a powder sample). A possible reason for the larger lattice parameters could be a Sn doping of the ZnS phase. Generally, these results confirm the observation made in section 4.12.3, where the observed peak broadening of the superimposing main peaks for CZTS and ZnS was smaller than expected (by simulation). Due to the larger lattice parameters for Sn-doped ZnS, the actual peak position of the ZnS peaks slightly shift to smaller angles, which causes a closer overlap of the ZnS and CZTS peaks, which results in a smaller increase in FWHM than expected (as shown in Figure 4-22).

4.12.5 Raman: Discrimination of phases by Raman spectroscopy

After the previous sections have shown that XRD cannot be used to discern less than 7 % of ZnS (by Refinement) and less than 72 % of CTS (by the presence of minor peaks) from CZTS, the question arises if Raman spectroscopy is more suitable for this application. Considering the results from section 4.11.2, the Raman "fingerprints" of the individual phase are dissimilar enough for that to be possible. To quantitatively answer the questions and in order to see how this applies for a mixed sample, Raman spectra were obtained at the six positions of interest on samples I and J.

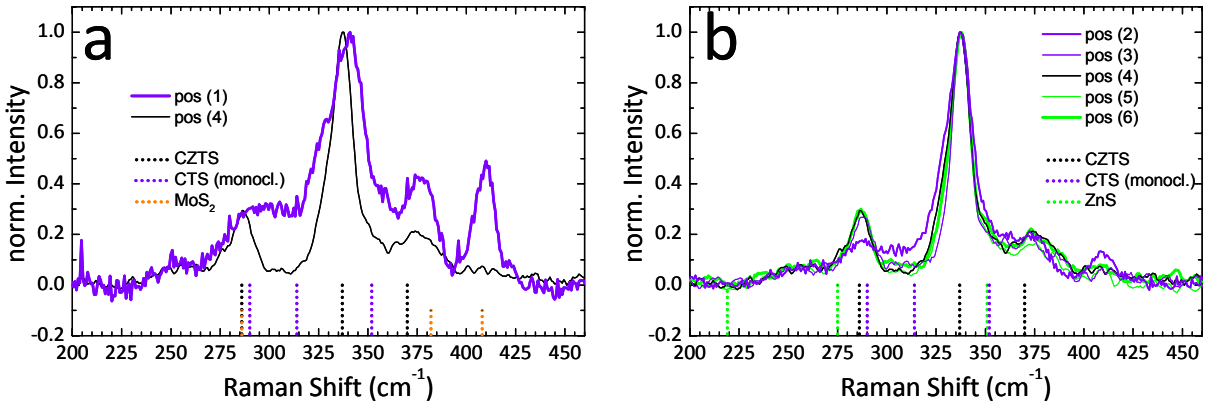

Figure 4-24 Normalized Raman spectra of (a) positions (1), and (4), and of (b) positions (2) to (6), to visualize the change of pattern shape, respectively. The violet, green, and black color represents the majority CTS, ZnS, and CZTS phase, respectively. The vertical lines indicate the positions of the respective Raman modes as taken from literature (see Table 4-3) and as taken from the section 4.11.2 for the monoclinic CTS.

Figure 4-24 (a) and (b) show the Raman spectra obtained from positions (1) to (6). At position (1), a fairly noisy and weak signal was obtained that generally shows the "fingerprint" of a CZTS phase, with a peak broadening of the 337 cm^{-1} mode, indicating the presence of a secondary phase. In addition, the peak at 286 cm^{-1} extends towards higher wavenumbers, which can qualitatively be explained by the presence of a monoclinic CTS phase (see section 4.11.2). The broad peak at 370 cm^{-1} can be explained by the superposition of a CZTS and a MoS_2 peak, which correlates with the presence of the peak at 408 cm^{-1}. Hence, just by looking at the Raman spectrum of position (1), indications of a monoclinic CTS phase can be seen. With an increased amount of Zn in position (2), these indications of a monoclinic CTS phase become so small that by a single measurement one could not tell the presence of a secondary phase together with CZTS. Between position (3) and (6), there are hardly any changes to be observed. Hence, from this very general observation by only looking at the "fingerprints", the presence of a secondary ZnS or CTS phase cannot be discerned from CZTS. The reasons for this can be manifold. At first one needs to consider the surface sensitivity of the technique. Since the information depth of Raman spectroscopy is at the order of 100 nm in CZTS (depending on the excitation wavelength), it is well possible that present secondary phases might hide underneath the CZTS phase. In the case of the ternary Cu_2SnS_3 phase, this issue cannot be excluded here, however, the SEM cross-sectional image of the most Zn rich position (6) in combination with qualitative compositional analyses show that ZnS phases are sitting side by side with grains of the CZTS phase and thus might not be hidden. Looking at the formation process of this layer (see section 5.9.1), however, it is possible that some ZnS could be encapsulated inside the gains, which would make a detection with Raman spectroscopy in the used form impossible. So in principle, small amounts of ZnS (small grains in between the CZTS grains) should be detectable, as in the case of a sample with an individual ZnS phase (see section 4.11.2). Another reason why ZnS

does not contribute (much) to the obtained Raman spectra lies in its Raman efficiency at the used excitation wavelength. Since CTS as well as CZTS have band gaps smaller than the energy of the probing light, the excitation of the electrons are real, hence they are above resonance (see Figure 2-9). The band gap for ZnS, however, is larger than the energy of the excitation light. In this case, electrons are excited into virtual states (below resonance), which is far less probable and hence less efficient. The outcome is that at the given excitation wavelength of 514.5 nm, the Raman efficiency of ZnS is far less than that of CZTS. This leads to the superposition of a small ZnS signal and a large CZTS signal. In the present case, the small signal coming from the ZnS phase seems to be hidden completely within the strong CZTS signal. Since the Raman efficiencies of CTS and CZTS should be roughly at the same order of magnitude, more dominant changes should be observable.

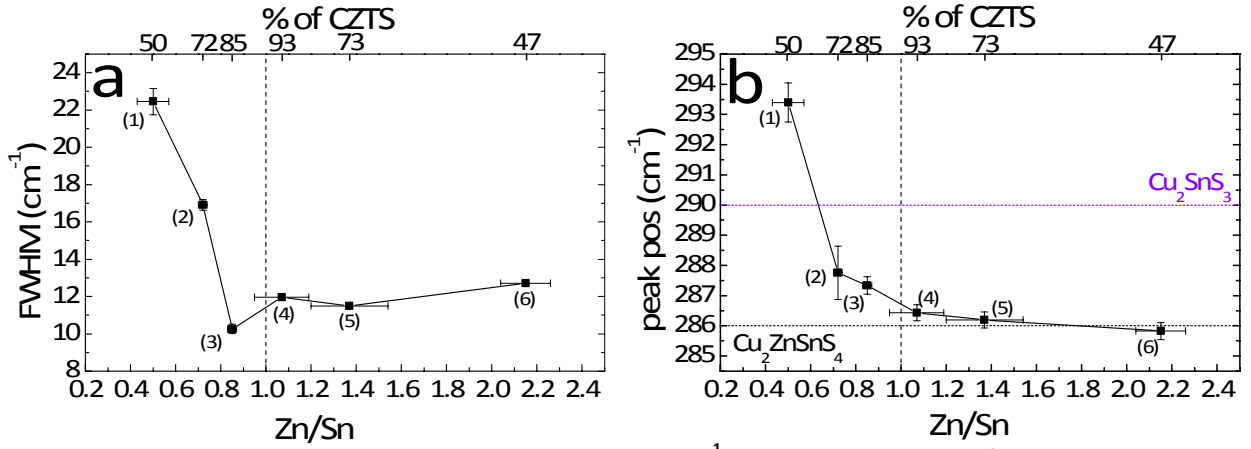

Figure 4-25 (a) Variation of the FWHM of the mode at 337 cm^{-1} with respect to the Zn/Sn ratio. (b) Change in peak position of the ternary 290 cm^{-1} mode to the 286 cm^{-1} mode of CZTS.

Focusing on the detailed changes of the given spectra, there are two worth pointing out:

a) The changes in FWHM of the 337cm^{-1} peak,

b) The changes in peak position of the 290 cm^{-1} and of the 370 cm^{-1} peak.

In Figure 4-25 (a), the change of the FWHM of the mode at 337 cm^{-1} is plotted against the Zn/Sn ratio of the respective positions. This plot has to be divided into two parts: At first the FWHM decreases from position (1) to position (3) by around 12 cm^{-1} due to the decrease of the contribution of the CTS modes at 314 cm^{-1} and 352 cm^{-1}, and then the FWHM slightly increases again by 2 cm^{-1} towards positions with larger ZnS contributions. This latter increase might be attributed to the ZnS mode at 351 cm^{-1}, but contributes only slightly due to the smaller Raman efficiency of this phase. This observation, however, does only help to discern more than 28 % of CTS from 72 % of CZTS, while ZnS is not discernable like this. For further conclusions, a variation of 2 cm^{-1} is too small, especially when comparing literature results from different setups.

Figure 4-25 (b) shows the change in peak position of the 290 cm^{-1} CTS mode towards the 286 cm^{-1} CZTS mode. This mode was chosen for detailed analysis, since the mode at 370 cm^{-1} contains large contributions of a MoS_2 phase, while the contribution of a MoS_2 phase at 290 cm^{-1} is very small, according to Figure 4-16 and literature [147, 150]. From this analysis (Figure 4-25 (b)), a clear shift in peak position from a monoclinic CTS mode to a CZTS mode can be seen. Between position (1) and (2), the peak shifts over 5 cm^{-1}, and between pos. (2) and (4) (the most CZTS rich position) for another 2 cm^{-1}. In this measurement series, a peak shift of 2 cm^{-1} is detectable which hence allows a discrimination of 28 % CTS from 72 % CZTS. In a single measurement, however, only the peak shift of 7 cm^{-1} from position (1) to (4) might be discernable. This might allow a discrimination of 50 % of CTS from CZTS as seen in Figure 4-24

(a). It shall be noted that a shift of only 2 cm^{-1} is not much when comparing a single result from one setup to another single result from different setup. Even 7 cm^{-1} are already difficult to tell. In this case, however, this series of measurements were performed back-to-back on the same setup, from which the given conclusions can be drawn. Between positions (4) and (6), no significant change in peak position is observed which concludes that the discrimination of ZnS from CZTS is not possible via this route.

Generally, it needs to be noted that CTS and ZnS cannot sufficiently (< 50 %) be discerned from CZTS in a single measurement using single wavelength excitation. In a measurement series, at least, it is possible to discern 28 % of CTS from CZTS. Furthermore, it needs to be kept in mind that Raman spectroscopy is very surface sensitive, which makes it hard to discern secondary phases that are not at the surface. To solve this problem Fontane et al. have suggested depth profiled Raman spectroscopy [143]. In their work, they show that the combination of sequential sputtering and Raman spectroscopy can be very suitable in order to detect secondary phases depth resolved.

The error bars of the presented data were calculated from the statistical error of the measurement and that of the peak fits that were necessary to evaluate the FWHM and exact peak position. In order to fit the Raman peaks, the region from 225 cm^{-1} to 450 cm^{-1} was generally selected and a multiple peak fit with a Laurentzian peak shape was applied. Hereby, the number of peaks was chosen such that all theoretically expected CTS and CZTS, or ZnS and CZTS peaks could be accounted for, respectively.

4.12.6 PL: Discrimination of phases by photoluminescence

After it has been shown that XRD and Raman spectroscopy are only partly able to discern ZnS and CTS from CZTS in a mixed sample, this section shall answer the question whether PL is a suitable tool for this task. For this, RT-PL measurements have been performed at the same areas where the Raman spectra were taken at.

Figure 4-26 shows the results of those measurements for positions (1) to (6). At the ZnS rich positions (6) to (5) the same broad peak at around 1.35 eV is seen as it is also observed in the CZTS rich position (4). This results correlates with the fact that the band gap of ZnS is larger that the energy of the excitation light, which makes ZnS invisible for this measurement. Hence, the observed peak can be attributed to CZTS, which fits well to the observed peaks in literature [146]. In position (3), where CZTS coexists with CTS, also only the peak at 1.35 eV is observed, although the band gap of CTS was determined to be 0.93 eV, as shown in section 4.16. The reason, why there is no contribution of the CTS phase in this spectrum is yet unclear but could be correlated to a poor crystal quality of the CTS crystals. At positions (2) and (1), no signal at all has been obtained from the RT-PL measurement. The reason for this is also yet unclear, but might also be due to a poor crystal quality of the CZTS and CTS crystals.

Altogether this investigation has shown that PL spectroscopy is probably not a good tool to discern CTS or ZnS from CZTS.

As a general comment it shall be noted that it was very difficult to obtain a PL signal from these samples at all. The reason for this is yet unresolved.

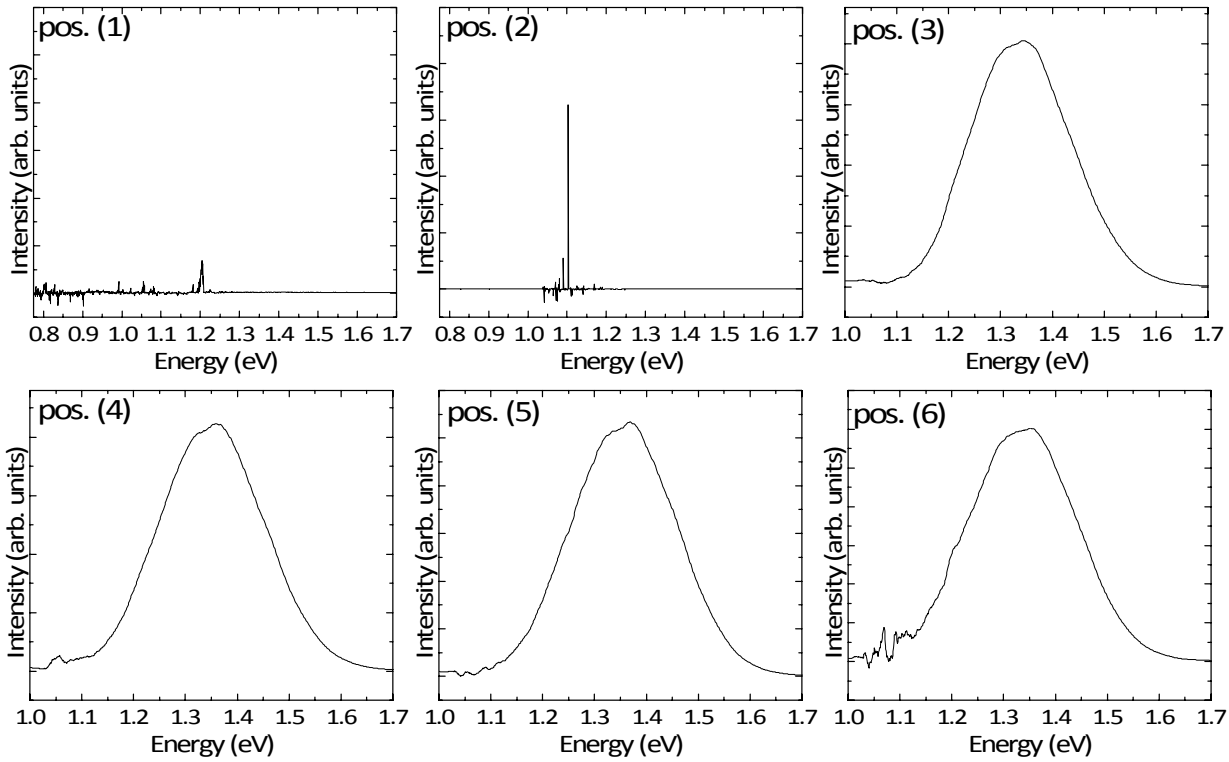

Figure 4-26 Smoothed PL signals obtained at positions (1) to (6) of samples I and J.

4.13 Multiple wavelength Raman spectroscopy

In section 4.12.5 it was pointed out that the Raman efficiency of ZnS is far less than that of CZTS since Raman scattering occurs below resonance for ZnS and above resonance for CZTS, at green light excitation. In this section, the difference in Raman efficiency dependent on the excitation wavelengths shall be demonstrated.

For this purpose, a very Zn rich sample H has been prepared. Compositional analysis found Zn/Sn = 12.16 and Cu/(Zn+Sn) = 0.12, respectively. Assuming that all present Cu and Sn form to CZTS leaving ZnS behind, roughly 90 % of the sample consists of ZnS, and only 10 % of CZTS. SEM top view overlaid with EDX maps and cross-sectional images are shown in Figure 4-27 (d) and (e), respectively. One can see that the few big grains are CZTS (white color in EDX map) whereas the small grains in between mainly consists of ZnS (green color). These data correlate nicely to the findings of position (6) on sample J (section 4.12.1). The presence of the two phases ZnS and CZTS is proven by the XRD pattern, as shown Figure 4-27 (c). Aside the minor and distinct CZTS peak at 29.7 °, a peak broadening of the major peak at 28.5 °, and a peak splitting of the peaks at 69 ° and 77 ° can be seen. This indicates firstly, both phases are present, and secondly that 90 % of ZnS phase can indeed be discerned from 10 % CZTS in XRD by their peak position.

Knowing that sample H contains a majority of ZnS and some CZTS, this sample has been investigated with Raman spectroscopy with excitation wavelengths of 325nm as well as 532 nm. Figure 4-27 (a) and (b) shows the obtained modal distributions, respectively. While the Raman spectrum obtained at 325 nm excitation clearly shows the modes of ZnS, the spectrum taken at 532 nm looks the same as obtained for positions (5) and (6) of sample J (see section 4.12.5), where only a contribution of CZTS (besides some MoS_2) can be seen. Hereby it shall be noted that the ZnS main peak at 349 cm^{-1} (in Figure 4-27 (a)) is already slightly shifted to lower wavenumbers as expected from literature (351 cm^{-1}, as seen in Table 4-3), which makes it even

harder to detect a ZnS phase in the spectrum shown in Figure 4-27 (b), as the CZTS and ZnS signals overlap even more. The very different results for the different excitation wavelengths, however, can be explained with the Raman efficiencies of CZTS and ZnS at the different excitation wavelengths. While the energy of the excitation light is smaller than the band gap of ZnS in the case of 532 nm, the majority of the light passes through the transparent ZnS while only a small part is Raman scattered. At the same time, the probability of Raman scattering on the CZTS grains is orders of magnitude higher and leads to the observed spectrum. In the case where the excitation energy is equal or higher than the band gap of ZnS (in the case of 325 nm excitation), resonant Raman scattering of ZnS occurs. This means that the probability of Raman scattering is increased by the excitation of electrons in real states. For the spectrum shown here, this means that the major signal contribution comes from the ZnS phase. Furthermore, as no sign of CZTS is seen in the spectrum of Figure 4-27 (a), it is assumed that the Raman signal from ZnS in its resonant case is much larger than that coming from the CZTS phase in its above-resonant case, implying that the weaker CZTS signal is hidden within the stong ZnS signal.

To be able to discern small amounts of a secondary phase from a CZTS phase, this implies that single wavelength Raman spectroscopy is insufficient and that multiple wavelength Raman spectroscopy is necessary.

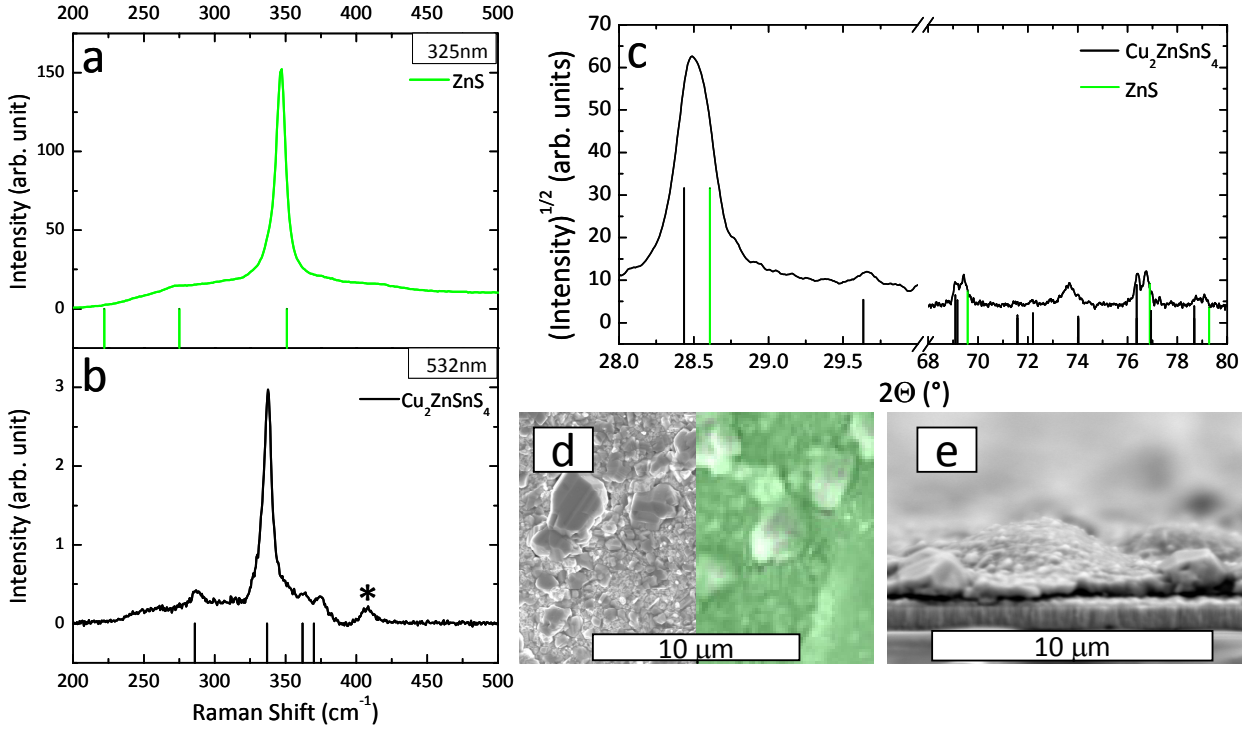

Figure 4-27 Raman spectra of sample H using (a) 325 nm and (b) 532 nm excitation wavelength. "*" represents a contribution of MoS_2. (C) XRD pattern of sample H together. (d) SEM top view image (left) overlaid with EDX maps (right) of sample H of different areas, where green indicates Zn, blue indicates Sn, and red indicates the presence of Cu. Adding Cu, Zn, and Sn will result in white color which represents CZTS. (e) Cross-sectional image of sample H.

4.14 Other techniques that help to find secondary phases

In the previous sections it was shown that XRD and Raman spectroscopy can only be used to discern amounts of several 10 % of ZnS and CTS from the CZTS phase in a mixed sample. Furthermore, it has been discussed that Raman spectroscopy is only then useful if measurements at various excitation wavelengths are performed and if it is combined with Raman depth profiling, as suggested by Fontane et al. [143]. Since not every lab has the

capabilities to do that, other ways have to be found, in order to get the hands on the discrimination of the phases present in a film. Within the scope of this work, EDX mapping and AES depth profiling have partly been used to fulfill this task.

4.14.1 EDX mapping

In section 4.12.1, EDX mapping results of the different positions on samples I and J were used to illustrate whether a sample is generally Zn poor or Zn rich. In those maps (see Figure 4-20), however, only the overall "greenness" changed and there were no regions of distinct phases. In contrast to this, Figure 4-28 shows an SEM images overlaid with EDX mapping results of (a) a Mo/Cu/Zn stack that was annealed in the presence of sulfur and (b) of the same sample additionally annealed in S + SnS (more details and further investigations can be see in section 5.7 of chapter 5). In Figure (a), one can clearly discern two different colors, where red corresponds to copper and green to zinc. This leads to the conclusion that two phases are present, a ZnS and a Cu-S phase. This conclusion is supported by the line scans across this map, where relation of Cu and Zn phases is not seen. In contrast to this example, Figure (b) shows the sample after additional annealing. Since Sn has been introduced during this annealing step (for details see section 5.7), a CZTS phase has formed. Since in a CZTS phase all elements coincide, one can only see the addition of a red, blue, and green color, which equals to white, and leaves the SEM image behind. Looking at the line scan, one can clearly see the correlation of all elements. From this one can conclude that all elements are distributed equally across the whole sample.

The given examples shall demonstrate that EDX mapping is a suitable tool to investigate the lateral distribution of secondary phases. It's weakness, however, is it can only detect larger grains/areas of a certain phase, as the resolution of EDX measurements is of around 1 μm for a acceleration voltage of 20 keV, as used here. Another weakness lies in the fact that EDX only detects the lateral distribution, where the depth-resolved distribution of phases is difficult to obtain.

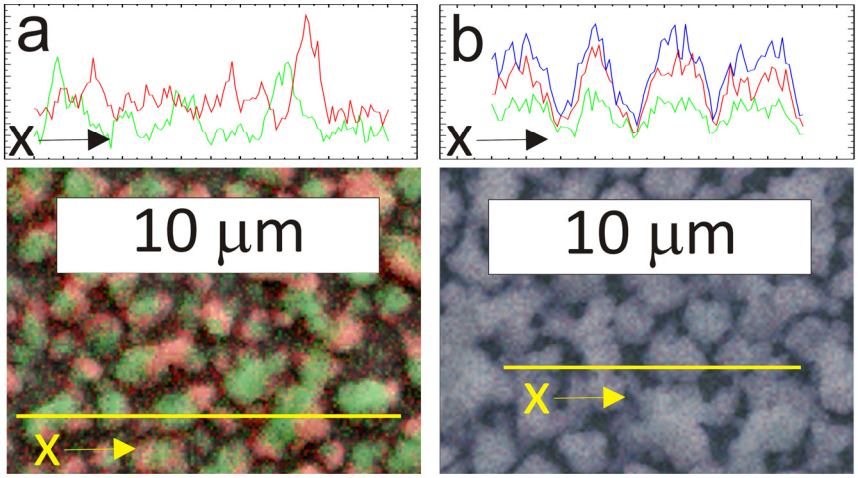

Figure 4-28 EDX mapping overlaying an SEM image of sample K, (a) after annealing in only S and (b) after additional annealing in S + SnS. Red corresponds to Cu, green to Zn, and blue to a contribution of Sn. The yellow line represents the position of the line scans, which themselves are shown above the respective maps.

4.14.2 AES depth profiling

To resolve the in-depth distribution of secondary phases, depth profile techniques, such as AES and SIMS, can be used. Within the scope of this work, AES depth profiles were obtained to investigate the CZTS phase formation processes, as shown in section 5.9. An example that

shows AES depth profiles can resolve secondary phases is shown in Figure 4-29 (a). There, the normalized intensities of the elements in the thin films are plotted with respect to the sputtering time. One can see that at the surface of the film, Cu, Zn, Sn, and S are well alinged, indicating that CZTS is present. Looking at the back interface, however, one can see that the amount of Zn increases, while the amounts of Cu and Sn decrease in parallel. This can be understood by the presence of a ZnS phase at the back in addition to CZTS. Although this interpretation is only of qualitative nature, the comparison to the XRD pattern (Figure 4-29 (b)), which only shows the presence of CZTS, shows the advantage of combining different mesurements.

The conclusion of this example is that depth profile techniques such as AES as well as SIMS depth profiling are suitable tools to investigate the depth-resolved distribution of secondary phases.

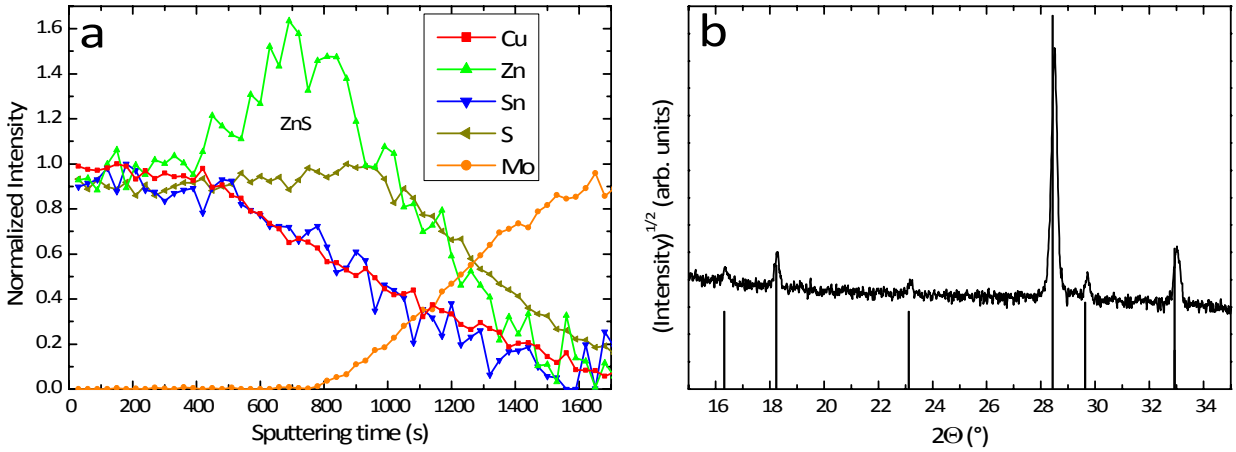

Figure 4-29 Normalized AES depth profile (left) and XRD (right) of sample L. The black vertical lines in the XRD pattern show the positions of the CZTS phase according to literature (see Table 4-1).

4.15 KCN etching of Cu_2SnS_3

After discussing which tools are suitable to discern secondary phases from CZTS, this section focuses on the question whether the ternary Cu_2SnS_3 phase can be etched by KCN in the same way as Cu-S phases can be etched away. To study this, a ternary phase has been fabricated as shown in Table 4-4 (sample M) and XRD patterns have been obtained before etching as well as 5 s, 60 s, and 360 s after KCN etching in a 5 wt% aqueous solution.

Since it has been taken care that always the same area of the sample has been analyzed, a decrease in the CTS peak intensities in parallel to an increase in the Mo signal is expected in case Cu_2SnS_3 is etched off the sample. From the results shown in Appendix F (Figure F-1), however, it can be seen that the intensity of all peaks stays the same, even after 6 min of KCN etching. Since CZTS samples are typically etched for 30 s to remove Cu-S phases before those phases are processed to solar cells devices, such a 6 min etch is a fairly long timeframe. It can be concluded that within this timeframe Cu_2SnS_3 is not etched.

4.16 Applications of Cu_2SnS_3 compound: Absorber layer in photovoltaic device

In the previous sections, it was shown that the quaternary Cu-Zn-Sn-S system is a fairly complicated system in terms of the secondary phases that can form during growth and in terms of their identification and discrimination. One of those secondary phases, Cu_2SnS_3, however, is a p-type semiconductor itself with a suitable band gap for photovoltaic applications, as pointed out in section 4.2.1. Already in 1987, Kuku and Fakolujo reported on a solar cell device based on

a Schottky junction consisting of Cu_2SnS_3 and Indium [106]. Their device showed a power conversion efficiency of 0.11 % under 100 mW/cm^2 incident radiation [106]. In this section, the successful fabrication of a pn-junction based solar cell device based on the ternary compound Cu_2SnS_3 is demonstrated.

4.16.1 Composition and morphology of the absorber layer

Figure 4-30 (a) and (b) show the morphology of the absorber layer after its fabrication (see sample N in Table 4-4). One can see large grains of between 2 and 6 μm in diameter with pinholes of similar horizontal dimensions in between. By comparing the surface area that is covered with grains to the total surface area of a typical and large scale SEM top view image, it can be seen that 67.5 % of the average sample's surface is covered with grains, leaving one third with pinholes. The effect that leads to such an open morphology is yet unclear.

The grains shown in Figure 4-30 (a) and (b) appear to be single phase, however an EDX compositional analysis of a single grain after KCN etching shows a Cu/Sn ratio of 1.9 and a S/(Cu+Sn) ratio of 1.09. These values are slightly S rich and Cu poor with respect to a stoichiometric Cu_2SnS_3, but fit well to what has been observed for sample E. Nevertheless, secondary Sn rich phases cannot be excluded by this investigation.

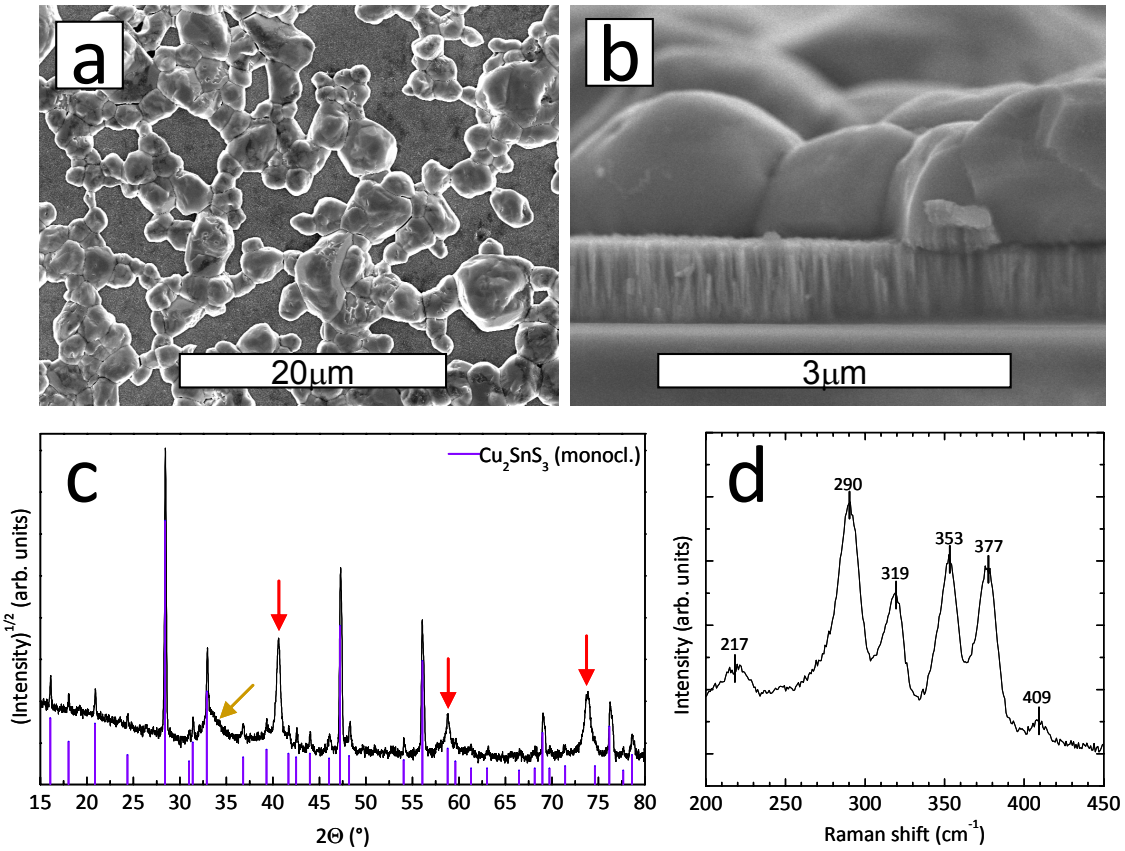

Figure 4-30 (a) SEM image two view image, (b) SEM cross section image, (c) XRD pattern, and (d) Raman spectrum of the ternary absorber layer Cu_2SnS_3. The violet lines in the XRD pattern indicate the positions of the XRD peaks according to literature (see Table 4-1). The red arrows indicate the contribution of the Mo substrate and the orange peak the contribution due to MoS_2.

4.16.2 Structural investigations

Structural investigations of this sample using GI-XRD measurements show that a monoclinic Cu_2SnS_3 has been produced. In Figure 4-30 (c) the diffractogram is displayed. Apart from the peaks marked with a red or orange arrow, all experimental peaks could be assigned to the

monoclinic Cu_2SnS_3 phase. This phase is also the expected one at this temperature, as pointed out in section 4.2.1 [100]. The marked peaks could be assigned to Mo (red arrow) and MoS_2 (orange arrow). The broad peak of MoS_2 at around 34 ° is rather dominant, which is mainly due to the large surface area of pinholes on the sample. The majority phase however can clearly be attributed to a monoclinic Cu_2SnS_3 phase, which correlates to the results of section 4.11.2.

In addition, Raman spectroscopy measurements have been performed and the result is displayed in Figure 4-30 (d). Altogether, four major and two minor peaks can be seen. While the small contribution at 408 cm^{-1} corresponds to a MoS_2 phase, the peaks at 290 cm^{-1} and 352 cm^{-1} support the results of a monoclinic Cu_2SnS_3 phase, as discussed in section 4.11.2. In addition, the peaks at 217 cm^{-1}, 319 cm^{-1}, and 377 cm^{-1} can be explained by a secondary $Cu_2Sn_3S_7$ phase, as discussed in section 4.11.2 and according to [161, 162]. As no sign of this $Cu_2Sn_3S_7$ phase is seen in XRD, it can be conclusion that the majority phase in the film is Cu_2SnS_3. Furthermore, this result also shows again that XRD is not the right tool to identify small amounts of a secondary phase.

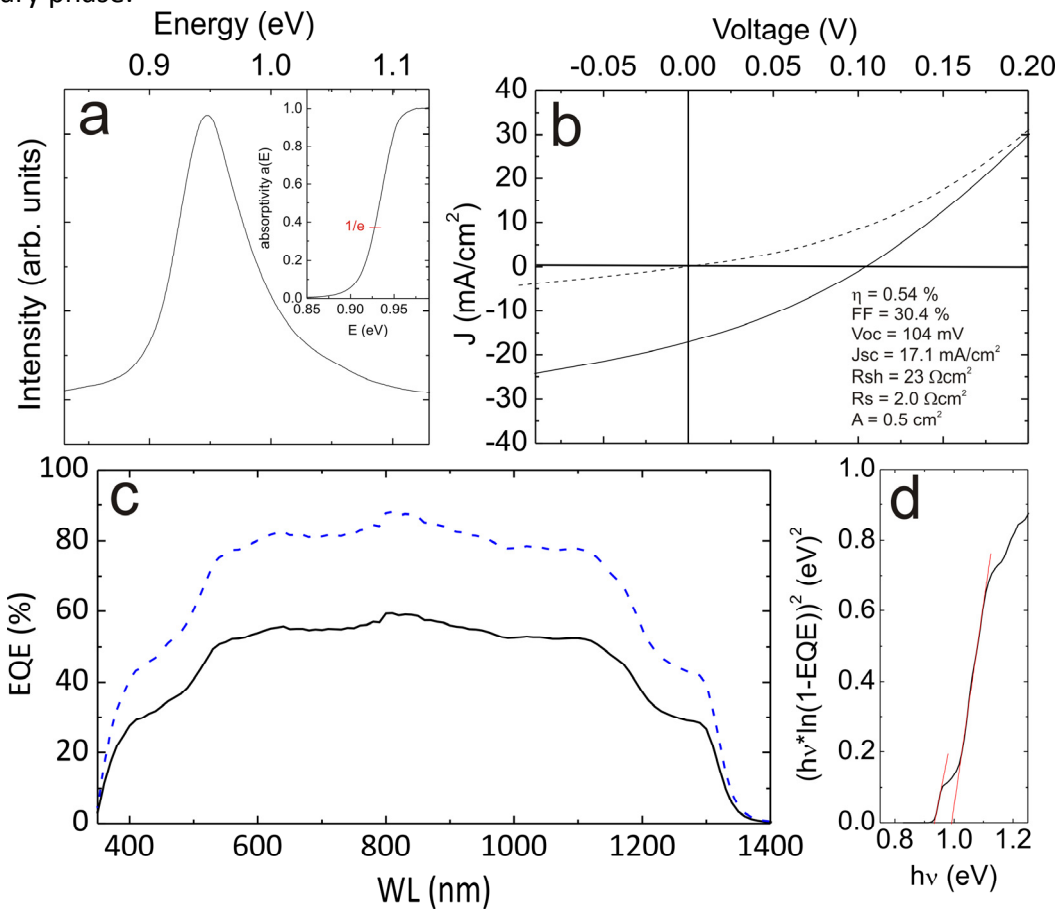

Figure 4-31 (a) PL peak of the absorber layer and the extracted absorptivity a(E). (b) IV curve of the best solar cell device. (c) EQE (black solid line) and effective EQE (blue dashed line) of the device. (d) Band gap extraction from the EQE.

4.16.3 Opto-electronic properties

Figure 4-31 (a) shows a large area PL spectrum recorded at room temperature. There, a fairly broad and asymmetric peak at 0.95 eV can be seen, which is attributed to the band-to-band transition. Following the procedure described in [32] together with Equation 2-9 (see section 2.6), an absorption coefficient of $\alpha > 10^4$ cm^{-1} has been extracted at 0.95 eV (so 0.02 eV higher than the band gap) from the given PL signal. The value of 1 μm for the layer thickness d needed for this evaluation was roughly extracted from SEM cross section (Figure 4-30 (b)),

keeping in mind that around one third of the surface area is not covered with grains. Therefore, this value for *d* shall be seen as an upper estimate and hence a lower estimate for the absorption coefficient. In the inset in Figure 4-31 (a) the spectral absorptivity is shown. From this data one can extract a value for the band gap by intercepting the graph at a(E)=1/e. The obtained value is E_G = 0.927 eV, which along with the value of alpha lie within the range of what has been reported in literature [105, 107].

4.16.4 Photovoltaic device

Figure 4-31 (b) shows the solar cell performance of the best device obtained from this monoclinic ternary compound. The dashed line represents the JV curve in the dark and the solid one the JV curve under illumination. The open circuit voltage (V_{OC}) is 104 mV, the short-circuit current (J_{SC}) is 17.1 mA/cm^2, the fill factor (FF) is 30.4 %, and the power conversion efficiency is 0.54 %. The reason for the small J_{SC} is due to the fact that only two thirds of the sample's surface have been covered with the absorber layer. Therefore, only two thirds of the photons arriving at the surface can be maximally absorbed. Furthermore, such a large area of holes also causes the shunt resistance (R_{sh} = 23 Ω cm^2) to be this small. This latter value has been obtained by fitting the negative voltage side (from -0.1 to 0 V) of the dark JV curve, while the serial resistance (R_S) has been obtained by plotting the positive voltage side (between 0.3 and 0.4 V, not shown here). R_S has been found to be 2.0 Ω cm^2. Further reasons for the small J_{SC} could be the losses due to reflections at the front of the device, unwanted absorption in the window layer, or a bad charge carrier collection. As this device, however, was only a very first attempt to make a solar cell from a Cu_2SnS_3 absorber layer based on a pn-junction, further optimizations has been disregarded so far. Apart from the low J_{SC}, the value for the V_{OC} is also very low, even for such a low band gap (see below) material. Here, one of the problems is the bad shunt and serial resistances, a combination which can cause a bad V_{OC}.

The values presented here belong to the best cell measured, however in total six functional devices, each having a conversion efficiency of larger than 0.27 % have been made so far.

The EQE of the best device is shown in Figure 4-31 (c), along with an area corrected effective EQE_{eff}. The latter value was obtained by dividing the measured EQE with 0.675 (the percentage of the covered area of the film), assuming all photons to arrive on absorber material (and not on holes). Where the measured EQE shows a maximum value of just less than 60 %, that of the effective EQE is just less than 90 % which is within the range of the highly efficient CIGS solar cells. This shows the high potential of the Cu_2SnS_3 based solar cells. Calculating the J_{SC} by integrating the EQE with the AM1.5 solar spectrum gives a value of 25.07 mA/cm^2 which is significantly higher than what has been measured in the JV curve. One reason for this can be found in the front grid of the device. This taken into account would lead to a grid corrected $J_{SC;gridcorrected}$ of 18.23 mA/cm^2. The further discrepancy can be explained by an underestimation of our JV setup (as explained in section 2.9.1) for such a low band gap material. Therefore, one can expect the real efficiency of this device to be even higher than the 0.54 % measured. Calculations of J_{SC} from the effective EQE even lead to a larger value of the short circuit current ($J_{SC;EQEeff}$ = 37.14 mA/cm^2). This effective $J_{SC;EQEeff}$ is high compared to the measured J_{SC} and shall demonstrate the potential of this ternary compound for photovoltaic applications.

Extrapolating the E_G from the EQE, as shown in Figure 4-31 (d) and as introduced in section 2.9.2, one can see that the absorber layer is either not single phase (which would correlate with the findings of the Raman spectroscopy results) or that the monoclinic Cu_2SnS_3 phase has two band gaps at 0.93 and 0.99 eV. The lower of the two values fits also nicely to what has been obtained from the PL measurement and to literature values [102, 103, 105].

Conclusions

The goal of this section was determine which secondary phases can form under the same conditions that are used to produce Cu_2ZnSnS_4 and to determine which analytical tool is useful to discern these secondary phases qualitatively as well as quantitatively. For this study, X-ray diffraction, Raman spectroscopy, photoluminescence, EDX mapping, and Auger electron spectroscopy measurements have been performed and evaluated accordingly.

Initially, XRD, Raman spectroscopy, and PL studies were performed on individually prepared secondary phases, such as MoS_2, Cu-S (Cu_9S_5, $Cu_{31}S_{16}$), Sn-S (SnS, SnO, $Sn(SeO_3)_2$), ZnS, and Cu_2SnS_3. The obtained pattern/spectra were then compared qualitatively to determine how well the individual "fingerprints" differ from that of an individual Cu_2ZnSnS_4 phase. As a result, it was obtained that:

1. Raman spectroscopy should be a suitable tool to discern all secondary phases from CZTS, as the main Raman modes of the possible secondary phases differ well enough from that of CZTS.
2. XRD should be suitable to discern all phases of the Cu-S and Sn-S system from CZTS, and that the presence of Cu_2ZnSnS_4 as well as monoclinic Cu_2SnS_3 should be predictable by the presence of the respective minor peaks, although their major peaks overlap. Since ZnS does not have such minor peaks and since all of its major peaks also overlap with those of CTS and CZTS, its presence in a sample can never be fully excluded with confidence. Due to its slightly different peak position of the major peaks, a discrimination could be possible if the experimental setup is properly aligned.
3. PL spectra should only be suitable to discern CTS from CZTS, since ZnS, SnS, and $Cu_{2-x}S$ phases did not show a PL spectrum using a green light excitation. The monoclinic CTS showed a peak at 0.95 eV and CZTS a peak at 1.3 eV.

All measurements of the first study were performed on individual and almost pure samples, where the signal of each measurement could be optimized to the respective phase under investigation. Since the general idea is to discern small amounts of secondary phases from a CZTS absorber layer it is necessary to be able discern those phases in a mixed sample. In such a case, however, the signal of each measurement can only be optimized to the most dominant phase. Signals from less dominant phases could be hidden. Therefore, a second study was necessary to investigate how much of a ZnS or CTS phase could be discernable from CZTS inside a mixed sample. For this study, two samples with a deliberate Zn gradient were prepared to allow the access to a CTS rich as well as to a ZnS rich region in a sample with CZTS. After studying several points on these samples, the following conclusions are drawn:

1. Using X-ray diffraction, Cu_2SnS_3 can only be discerned by its minor peak from CZTS if it makes up more than 28 % of the sample, while Rietveld refinement analysis, the change in FWHM, and the change in peak position does not help.
2. Using XRD, ZnS can only be discerned by Rietveld refinement analysis from CZTS if it makes up more than 7 % of the sample. The change in peak position helps to discern 90 % of ZnS from CZTS while a change in FWHM is not useful at all.
3. Single wavelength Raman spectroscopy (at green light excitation) is useful to discern more than 28 % of CTS from CZTS by looking at the peak shift of 290 cm^{-1} to 286 cm^{-1}, but it cannot be used to discern ZnS from CZTS. This conclusion, however, is only

valid for a measurement series. A single measurement on a sample would be less clear to interpret due to the small change in the modal shift.

4. PL spectroscopy (at green excitation) is probably not the right tool to discern CTS or any other phase from CZTS, especially when the crystal quality of the secondary phases is poor.

In a further experiment, it was shown that the use of multiple wavelengths in Raman spectroscopy can become a useful tool for the phase discrimination. On a sample with around 90 % ZnS and only 10 % CZTS content, Raman spectra at 532 nm and 325 nm were compared and it could be seen that in the former case only a CZTS signal, and in the latter case only that of ZnS was observed. A reason for this is found in the resonant Raman case for ZnS at 325 nm.

Apart from XRD, PL, and Raman spectroscopy, the usefulness of AES depth profiling and EDX mapping could be pointed out. Experiments show that EDX mapping can be used to resolve lateral distributions of present phases, where AES depth profiling (similar to SIMS depth profiling) can be useful to resolve phase distributions in depth.

Finally, studies on the etching behavior as well as on the usefulness of the monoclinic Cu_2SnS_3 phase have been performed. In the former study it was shown that a 5 wt% aqueous KCN solution cannot be used to etch off monoclinic CTS from a sample. In the latter study, the suitability of the p-type Cu_2SnS_3 semiconductor for photovoltaic applications has been investigated and it was shown that this compound can be used as an absorber layer in a photovoltaic device. Hereby, the power conversion efficiency of the device presented was measured to be 0.54 %, which is a factor of five higher than what had been previously obtained with a Schottky based device. An external quantum efficiency of less than 60 %, a small J_{SC} of 17.1 mA/cm^2, and a tiny R_{sh} of 23 $\Omega\,cm^2$ could be explained by a high number of pinholes in the absorber layer, leaving only 67.5 % of the sample surface to be covered by Cu_2SnS_3 grains. This suggests that a much higher EQE as well as power conversion efficiency should be achievable by a more densely packed absorber layer. Calculations of an effective EQE support this assumption.

5 Kesterite equilibrium reaction and its consequences

Goal

After showing the difficulties of discerning secondary phases from the Cu_2ZnSnS_4 phase, the goal of this chapter is to find a way to grow absorber layers for high quality CZTS thin film solar cells by avoiding secondary phases (at the surface of the absorber). Hereby, the equilibrium reaction of the formation of kesterite thin film is the key point. At first, the equilibrium reaction is introduced and hypotheses for possible consequences are stated. In the following investigations, a few of these consequences are studied in more detail. Thereby, it was focused on two major points:

1. The introduction of a simplified metal deposition and annealing route to form kesterite thin films as a consequence of a novel annealing strategy ([164]) that obeys the equilibrium reaction conditions.
2. The consequence of applying equilibrium reaction conditions during the annealing process on the solar cell device performance.

Hereby, samples made via an electrodeposition and annealing (EDA) route were primarily used to learn more about the process of CZTS formation during the annealing step while samples made via PVD were utilized to display the effect of the novel equilibrium condition annealing strategy on the solar cell device performance.

It shall be mentioned that all of the discussed issues in this chapter are not only valid for the sulfide kesterite (CZTS) but equivalently valid for selenide kesterite (CZTSe) as well (see Appendix D for some Se results and the following reference [139]).

Background

5.1 Cu_2ZnSnS_4 formation

In recent years, research in the formation of single phase CZTS films for photovoltaic applications has encountered a real boom. After Ito et al. examined the electrical and optical properties of CZTS already in 1988 [4], it took until around 2005 until this material, consisting of earth-abundant and relatively non-toxic elements, slowly made its way into the spotlight of thin film photovoltaic research. In the various published studies, different systems and techniques have been used to fabricate CZTS thin films. This section briefly summarizes the achievements using the various techniques and highlights the typical sulfurization conditions as well as the suggested reaction pathways for the formation of CZTS, according to literature. Finally, a small collection of current challenges in CZTS formation studies are pointed out in order to highlight the importance of the presented conclusions of this chapter.

5.1.1 Routes and techniques of CZTS formation

Vacuum-based approaches

From many applications, vacuum-based techniques are known to provide deposits of very high uniformity and with a very good capability of reproduction. For kesterite deposition, these vacuum-based techniques can be divided into two categories, sputtering- and evaporation-based techniques.

The most successful sputtering results for CZTS have been shown by Katagiri and co-workers [165]. In their RF co-sputtering approach, elemental Cu as well as ZnS and SnS materials were deposited onto a rotating substrate in order to provide a homogeneous deposition. After a long

annealing step (details see section 5.1.2), a CZTS layer could be finalized into a 6.8 % efficient device, currently being the record[3] for a pure sulfur CZTS device (together with a co-evaporated precursor from IBM [92], see below) [13]. The compositional ratios for the best devices made by the group of Katagiri are Zn/Sn ≈ 1.2 and Cu/(Zn+Sn) ≈ 0.9, as shown in Figure 5-1 as taken from [165]. The best selenide CZTSe device from a sputtered precursor was prepared of sequentially sputtering Cu, Zn, and Sn followed by an annealing step with elemental Se inside the vacuum chamber as the selenium source [166]. A power conversion efficiency of 3.2 % was reported.

The most successful[3] evaporation result was reported by Wang and co-workers, also with a 6.8 % efficient pure sulfide CZTS device [92]. In this approach, elemental Cu, Zn, Sn, and S were co-evaporated onto a slighthly heated substrate (100 °C), followed by a reactive annealing at 540 °C on a hot plate. In a study of various sequentially deposited precursor stacks, followed by a subsequent annealing, Araki and co-workers have pointed out the importance of adjacent elemental layers for the formation of CZTS [59]. From their morphological as well as performance results, they concluded the optimal precursor stacking order to be Mo/Zn/Cu/Sn. Furthermore, the importance of neighboring Cu and Sn layers was pointed out. Both of those routes, however, include a sulfurization/annealing step. A simpler approach in terms of the number of steps has been introduced by Schubert et al.[4] [168]. In their approach, copper, tin, and zinc sulfide materials as well as elemental sulfur was co-evaporated onto a heated substrate (500 °C) in order to avoid a second annealing step. Devices with a power conversion efficiency of around 4.1 % have been reported of [168].

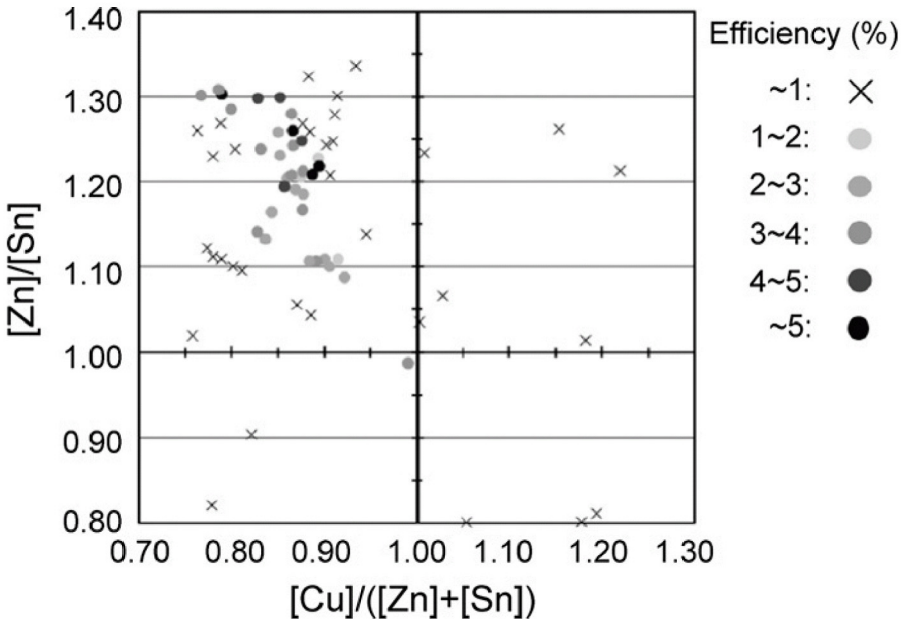

Figure 5-1 Conversion efficiency of CZTS-based thin-film solar cells vs. [Cu]/([Zn]+[Sn]) and [Zn]/[Sn] ratios as taken from [165].

[3] In a recent development, IBM published an 8.4 % efficient solar cell device based on pure sulfide CZTS. In their process, a thermally evaporated Cu, Zn, Sn, and S containing precursor is annealed at 570 °C in a sulfur containing atmosphere for 5 min under atmospheric pressure [91] B. Shin, O. Gunawan, Y. Zhu, N. A. Bojarczuk, S. J. Chey, and S. Guha, Progress in Photovoltaics: Research and Applications (2011)..

[4] Recently, NREL demonstrated a 8.4%-efficient CZTSe solar cell produced using a one step co-evaporation process [167] NREL, http://www.nrel.gov/science_technology/pdfs/52659.pdf, 2011..

Electrodeposition

Electrodeposition is a well established and attractive industrial approach for a low cost and large scale deposition. The currently best[5] CZTS device made from an electrodeposition and annealing approach has been published by Ennaoui and co-workers in 2009 [43]. In their fabrication route Cu, Sn, and Zn were co-deposited from one bath, followed by an annealing step with H_2S as the sulfur source (see Table 5-1). A power conversion efficiency of 3.4 % was obtained.

Almost as efficient has been the device reported by Scragg and co-workers with 3.2 % [49]. Their fabrication route was based on a stacked metallic layer approach, where a Mo/Cu/Sn/Cu/Zn stack has been electrodeposited sequentially followed by an annealing step in which elemental sulfur was used as the source of sulfur. To achieve a homogeneous deposition, a rotating disc electrode has been used. In further studies of Scragg, the use of H_2S gas during the annealing was studied [50].

Other solution-based techniques

Similar to the electrodeposition, direct liquid deposition approaches are very attractive for large scale-manufacturing due to their compatibility with ultra-high throughput deposition techniques [71]. In recent publications of researchers of the IBM T.J. Watson Research Center, solution-based techniques have been used to produce mixed sulfur-selenide CZTSSe devices of power conversion efficiencies larger than 10 % [14]. In their process, a hydrazine solution containing Zn, Cu_2S, and SnS(Se) has been spin coated onto a Mo substrate which subsequently has been heated on a hot plate for 5 min and under the presence of sulfur in order to dry and crystallize the deposit [10, 170]. This result shows the potential of CZTSSe absorber layers for photovoltaic applications.

In another liquid-based approach, Guo et al. produced CZTSSe nanocrystals which they deposited onto Mo substrate, followed by an annealing step [171]. Their approach leads to 7.2 % efficient devices.

5.1.2 Sulfurization condition in literature

In the previous section, a brief summary of the most common techniques to form CZTS / CZTSSe / CZTSe has been shown. Except the approach of Schubert and co-workers (see footnote 4 on page 104), all other fabrication processes include two important steps: Firstly, the deposition of Cu, Sn, Zn, and sometimes S/Se, and secondly the annealing/ sulfurization/sintering step. Latter step is mainly performed in order to form the desired $Cu_2ZnSn(S,Se)_4$ phase.

Table 5-1 contains the annealing conditions of the previously reported approaches. All of them have in common that the samples are heated above 500 °C and that some sort of sulfur source (elemental sulfur or H_2S) was present. H_2S of around 5 wt% to 20 wt% was typically accompanied by nitrogen gas, whereas elemental sulfur was typically evaporated in nitrogen or argon atmosphere. In some of the mentioned annealing systems, the background gas was refreshed in a constant flow, whereas in other systems, the background gas was kept static with pressures up to atmospheric pressures. All of this indicates that there is not yet a general consensus of which annealing conditions are favorable in order to form single phase CZTS. A

[5] In a recent development, IBM published a 7.3 % efficient solar cell device based on pure sulfide CZTS. In their process, the electrodeposition of metal stacks were followed by an annealing of a CuZnSn precursor in a sulfur atmosphere [169] S. Ahmed, K. B. Reuter, O. Gunawan, L. Guo, L. T. Romankiw, and H. Deligianni, Advanced Energy Materials:n/a..

possible reason for this can be found in the fact that various different apparatuses are used to anneal in. While the absorber layer of the most efficient co-evaporated pure sufur CZTS device (6.8 % [92]) was annealed on a hot plate at 550 °C under atmospheric pressures for only 5 min, the best sputtered pure sulfur CZTS device (also 6.8 % [13]) was annealed for 3 hrs at 580 °C under a gas flow of 10 sccm N_2 + 20 wt% H_2S in a glass ampoule in an electric furnace. This indicates that various different annealing conditions can lead to good results, but also that optimal conditions are strongly dependent on the respective annealing apparatus. However, there are also certain annealing conditions that are universal.

As this chapter focuses on the formation of CZTS during the annealing step, one of the outcomes of this work is a universial condition that improves annealing of CZTS.

Table 5-1 Sulfurization conditions of the annealings performed for the formation processes of CZTS/Se as given in section 5.1.2. S/Se_x indicates elemental sulfur/selenium. RTP stands for rapid thermal processor.

Reference	Annealing apparatus	Temp. (°C)	Time (min)	Process gas	Pressure (mbar)	S/Se source	Efficiency (%)
Katagiri [13]	Furnace	580	180	N_2 + 20 wt% H_2S	Gas flow	H_2S	6.8
Zoppi [166]	Tube furnace	500	30	Ar	Not given	Se_x	3.2
Wang [92]	Hot plate	540	5	N_2	atmosph.	S_x	6.8
Araki [59]	Furnace	560	120	N_2	Gas flow	S_x	1.8
Ennaoui [43]	Furnace	550	120	Ar + 5 wt% H_2S	atmosph.	H_2S	3.4
Scragg [49]	Tube furnace	560	120	N_2 + 10 wt% H_2	500	S_x	3.2
Scragg [50]	RTP	550	120	N_2 + 5 wt% H_2	500	H_2S	---
Barkhouse [14]	Hot plate	540	5	N_2	atmosph.	S_x	10.1
Guo [171]	Graphite box	500	20	Not given	Not given	Se_x	7.2

5.1.3 Formation reactions of Cu_2ZnSnS_4 as reported in literature

Hergert and Hock predicted two pathways that could run in parallel for the formation of CZTS from binary sulfides [172]. In the first pathway, Cu-S reacts with Sn-S to form Cu_2SnS_3 before reacting with ZnS to finally form CZTS, as shown in Reaction 5-1. The second pathway is more direct and Cu-S, Sn-S, and ZnS react immediately to form Cu_2ZnSnS_4, as shown in Reaction 5-2:

$$CuS/Cu_2S + SnS/SnS_2 + ZnS \ (+\text{sulfur}) \rightarrow Cu_2SnS_3 + ZnS \rightarrow Cu_2ZnSnS_4$$

Reaction 5-1

$$CuS/Cu_2S + SnS/SnS_2 + ZnS \ (+\text{sulfur}) \rightarrow Cu_2ZnSnS_4$$

Reaction 5-2

The formation of CZTS from binary compounds has been observed to take place quickly, as investigated by Weber et al. [173]. From their temperature dependent in-situ XRD experiments, it was concluded that the formation of CZTS should be completed within 70 seconds (at a temperature of 500 °C) [173]. A second order rate constant of $2 \cdot 10^{-9}$ to $3 \cdot 10^{-10} cm^2 s^{-1}$ has been calculated for an assumed diffusion limited process of CZTS formation from stacked binary sulfides (Mo/SnS/CuS/ZnS).

In another in-situ XRD experiment performed on a co-electrodeposited Cu-Zn-Sn precursor coated with a sulfur layer, temperature resolved investigations on the phase formation were performed by Schurr et al. [48]. Hereby, precursors were heated at a rate of 0.8 °C/s to around 630 °C while diffractograms were recorded. As a result, the following reaction sequence was observed:

$$2Cu_6Sn_5 + 19S \rightarrow 8SnS_2 + 3Cu_{2-x}S + 2Cu_3Sn \quad \text{(up to 300 °C)}$$

Reaction 5-3

$$2Cu_2S + SnS_2 + 2S \rightarrow Cu_4SnS_6 \quad \text{(up to 570 °C)}$$

Reaction 5-4

$$2CuZn + 3S \rightarrow Cu_{2-x}S + 2ZnS \quad \text{(510 °C)}$$

Reaction 5-5

$$Cu_4SnS_6 \rightarrow 2Cu_{2-x}S + SnS_2\,(melt) + 2S \quad \text{(570 °C)}$$

Reaction 5-6

$$Cu_{2-x}S + SnS_2\,(melt) \rightarrow Cu_2SnS_3 \quad \text{(> 570 °C)}$$

Reaction 5-7

$$Cu_2SnS_3 + ZnS \rightarrow Cu_2ZnSnS_4 \quad \text{(575 °C)}$$

Reaction 5-8

In his PhD thesis, Scragg reports on a similar but ex-situ XRD investigation performed on an electrodeposited stacked elemental layer (Mo/Cu/Sn/Cu/Zn) [41]. In his study, Scragg uses a rapid thermal processing oven in order to heat up (10 °/s) similar precursors in several runs to 550 °C in the presence of sulfur. At certain temperatures and annealing times, different samples are “freeze-cooled” in order to resolve the following reaction sequence:

$$Cu_5Zn_8 + S_2(g) \rightarrow Cu_2S + ZnS$$

Reaction 5-9

$$½\,S_2(g) + Cu_2S(s) \rightarrow 2Cu_2S(s) + 2V_{Cu}$$

Reaction 5-10

$$Cu_6Sn_5(s) + 3V_{Cu} \rightarrow Cu_3Sn(s) + 4Sn(I)$$

Reaction 5-11

$$Cu_3Sn(s) + 3V_{Cu} \rightarrow Sn(I)$$

Reaction 5-12

$$Cu_6Sn_5(s) + 1.5S_2(g) \rightarrow 3Cu_2S(s) + 5Sn(I)$$

Reaction 5-13

$$Cu_2S + Sn + 2S + ZnS \rightarrow Cu_2ZnSnS_4, Cu_2SnS_3$$

Reaction 5-14

The different results of Scragg and Schurr et al. for the formation sequence of CZTS might originate from the different heat ramps used. While the in-situ XRD analysis performed by Schurr et al. required a fairly slow heating process of 0.8 °/s, Scragg’s ex-situ experiments could be performed with a much higher heating rate of 10 °/s. This difference leads to the fact that in

Scragg's case Sn did not form SnS, but immediately reacted with sulfur, ZnS, and $Cu_{2-x}S$ to CZTS and/or CTS.

The study from Scragg is the closest to the investigations done within the scope of this chapter, where a Mo/Cu/Zn stack is annealed in a sulfur and tin sulfide containing environment.

5.1.4 Challenges in CZTS formation related to this work

Despite all the good results that have been obtained for CZTSSe based solar cell devices, there are still various challenges related with the optimization of such devices that are discussed in literature. Amongst others, the choice of the right buffer layer in terms of band alignment, the undesired fabrication of $Mo(S,Se)_2$ at the back contact [71, 139, 140], the loss of tin during deposition or an annealing step [141], the growth of single phase CZTS, and the identification of secondary phases are only some of the most common challenges [174]. This section briefly points out two challenges that are in the focus of this work.

Growth of single phase CZTS and identification of secondary phases

After section 4.1 has pointed out that the existence region of single phase Cu_2ZnSnS_4 is relatively small, it is not a big surprise that a major challenge is to find the best strategy to grow single phase CZTS in order to avoid harmful secondary phases. In the previous sections, a brief summary of the commonly used strategies was given. Part of this work is to study the effectiveness of a novel ED and annealing route in order to make single phase CZTS.

Connected to the problem of single phase CZTS as discussed in chapter 4, another challenge is the identification of secondary phases and their discrimination from CZTS. This is especially important when considering the results of Katagiri displayed in Figure 5-1 [165]. There, one can see that the most efficient CZTS devices have a Cu-poor and Zn-rich composition while the device efficiency results of stoichiometric samples were rather poor. One possible explanation could be the presence of Cu vacancies, another one, however is the presence of secondary phases. Therefore, to study the role of secondary phases in CZTS absorber layers with regards to the power conversion efficiency, it is important to be able to discern small amounts of a phase from CZTS. Results of studies concerning the discrimination of secondary phases were shown is chapter 4.

Tin loss during fabrication process

In the growth of CZTS, there have been many reports on the issue of Sn loss [6, 9, 131, 140, 141]. As the vapour pressure of Sn is far too low to evaporate from the film in its elemental form at the typical temperatures [132] (see Figure 4-9) it is more probable that tin loss occurs via the evaporation of the more volatile SnS molecules [135]. Based on the decomposition reaction of solid $SnS_2(s)$ (see Reaction 5-15), as studied by Piacente et al., Weber et al. studied the decomposition reaction of Cu_2ZnSnS_4, Cu_2SnS_3, as well as of Cu_4SnS_4 thin films, made by annealing of multilayers of binary sulfides [141].

$$2SnS_2(s) \rightarrow Sn_2S_3(s) + \tfrac{1}{2}S_2(g) \rightarrow 2SnS(s) + S_2(g) \rightarrow 2SnS(g) + S_2(g)$$

Reaction 5-15

In his detailed studies using X-ray diffraction and X-ray fluorescence measurements, Weber could obtain the rates of Sn loss for the different compounds. Hereby, it was concluded, that for a fixed temperature, the rate of Sn loss decreases in the following order: $SnS \rightarrow Cu_2SnS_3 \rightarrow Cu_4SnS_4 \rightarrow Cu_2ZnSnS_4$ [131, 141]. Furthermore, it could be concluded that

aside from the direct evaporation of SnS, there is a decomposition pathway for CZTS as follows [141]:

$$Cu_2ZnSnS_4(s) \rightarrow Cu_2S(s) + ZnS(s) + SnS(g) + \tfrac{1}{2}S_2(g)$$

Reaction 5-16

and for the ternary Cu-Sn-S phases as shown here:

$$2Cu_2SnS_3(s) \rightarrow Cu_4SnS_4(s) + SnS(g) + \tfrac{1}{2}S_2(g)$$

Reaction 5-17

$$Cu_4SnS_4(s) \rightarrow 2Cu_2S(s) + SnS(g) + \tfrac{1}{2}S_2(g)$$

Reaction 5-18

Depending on the annealing conditions, a loss of tin can either be negligible (at temperatures below 500 °C as suggested by Weber for his annealing conditions [131]) or it can lead to a complete Sn depletion of the layer, as shown by Redinger et al. for their conditions, respectively [140]. From Reaction 5-16, however, it can be foreseen that already a very small loss of tin can potentially cause severe problems for a photovoltaic device. In the given reaction it is shown that solid $Cu_{2-x}S$ and ZnS phases remain on the sample after the evaporation of SnS and S_2 (as sketched in Figure 5-2 (b)). Since SnS and S_2 are assumed to evaporate from the sample's surface, it is hypothesized that already a small amount of the residual $Cu_{2-x}S$ and ZnS phases has a negative influence on the band alignment at the pn-junction and potentially destroy it, as they form an additional layer in between the absorber and window layers, as shown in Figure 5-2 (c).

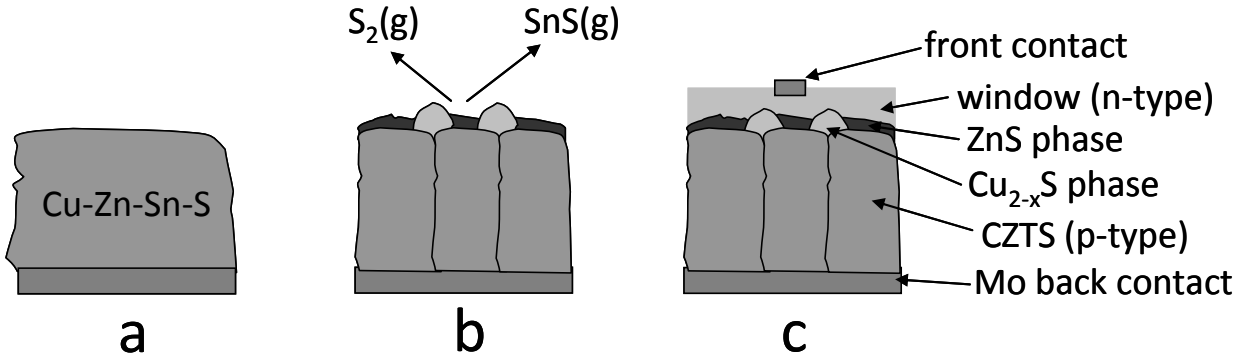

Figure 5-2 (a) Cu, Zn, Sn, and S containing precursor before heat treatment. (b) Evaporation of SnS and S_2 from the layer during the annealing, as proposed by Weber et al. [141]. (c) Finalized solar cell with $Cu_{2-x}S$ and ZnS phases between the absorber and window layers.

In the present chapter, a novel annealing strategy will be introduced that solves the problem of tin loss. In addition, the negative influence of secondary phases at the pn-junction will be shown.

5.2 CZTS thin film solar cell configuration

The basic solar cell configuration for CZTS solar cells was taken over from that of CIGS based devices. On its left, Figure 5-3 shows a SEM cross-sectional image, and on its right a schematic of the layered structure of a typical CZTS based solar cell. As a substrate, soda lime glass is usually chosen. Its primary advantages for CIGS samples were the lower costs and the fact that

its thermal expansion coefficient matched that of $CuInSe_2$ quite well [175]. Furthermore, it was found out that an in-diffusion of sodium from the glass substrate into the CIGS absorber layer increased the device performance [176]. The electrical back contact typically consists of a thin layer of molybdenum (around 500 – 800 nm), on top of which the Cu_2ZnSnS_4 absorber layer (around 2 μm) is fabricated. In this layer, the incident light is absorbed. In order to form a pn-junction at which the photovoltaic effect occurs, an n-type layer needs to be deposited. In CZTS as well as CIGS based devices, this n-type layer consists of three individual layers: A thin buffer layer, an intrinsic ZnO layer (both around 50 nm thick), and a transparent conducting oxide layer (typically Al:ZnO) of around 500 nm. To form an electrical front contact, a metal contact grid is deposited [175].

Since the research on CZTS based solar cells is fairly new, there have been no big changes to this configuration in order to optimize efficiencies, yet. In CIGS research, in contrary, there have been studies on the exchange of the CdS buffer layers by other n-type semiconductors. Within these studies, the best results were obtained for cells with a ZnS buffer layer [177]. Altogether, however, the best efficiencies are yet obtained with a CdS buffer layer.

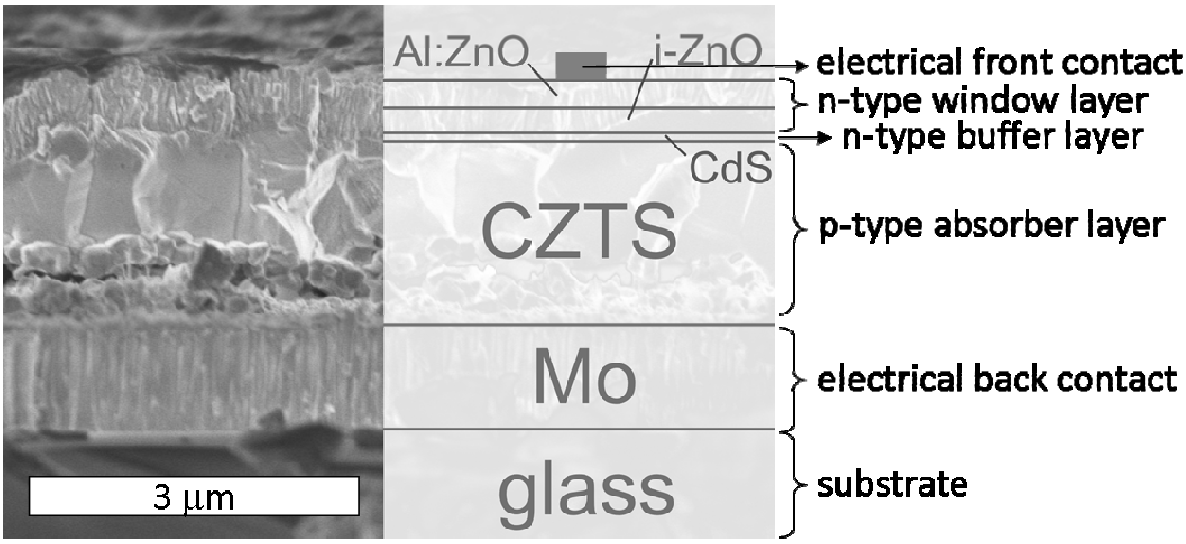

Figure 5-3 SEM cross-sectional image of the layered structure of a typical CZTS based solar cell.

Experiment

This part briefly discusses the experimental procedures that were used to study the equilibrium formation reaction of CZTS and that were used to prove some of its consequences, such as a novel route to form CZTS from a simplified precursor, or the stabilization of the absorber layer's surface by avoiding un-desired secondary phases.

5.3 Study of equilibrium formation reaction of CZTS

In the previous sections it was shown that in most of the cases an annealing step is required in order to form CZTS absorber layers for solar cells. As Table 5-1 shows, a typical annealing comprises the heat up of a samples in the presence of a sulfur source (either elemental sulfur or H_2S) in a certain process gas. At such common conditions, but very low background pressures, Weber et al. observed the decomposition of CZTS leaving behind solid $Cu_{2-x}S$(s) and ZnS(s) [141]. Hereby, the decomposition process was suggested to proceed via the evaporation of gaseous S_2(g) and SnS(g), as Reaction 5-16 shows. As this behavior can be thought of as a universal issue, the question arises whether this decomposition reaction is irreversible or not. In the upcoming section 5.7 the hypothesis is stated that Reaction 5-16 can in fact be seen as a reversible reaction where tin sulfide can be pushed back into the film, leading to the formation of CZTS again. To achieve this, the novelty of annealing the sample in a sulfur **and** SnS(g) environment is proposed.

In order to prove the hypothesis, a sample (sample K, see Table 5-2) containing $Cu_{2-x}S$(s) and ZnS(s) had to be fabricated. For this, a Mo/Cu/Zn stack was electrodeposited (see section 3.3 for details) and annealed under standard conditions (see section 2.2) in a "sulfur only" environment. To prove the presence of the $Cu_{2-x}S$(s) and ZnS(s) phases, EDX mapping as well as GIXRD measurements were performed. In the next step, this sample was annealed under standard conditions together with elemental S **and** SnS powder. SnS(s) has a high enough vapour pressure (see Figure 4-9) to evaporate at the standard annealing temperatures (550 °C), so that the desired annealing in a sulfur **and** SnS(g) environment is achieved. After the annealing, the sample was again investigated with EDX mapping and XRD measurements in order to prove that CZTS could be formed.

As a last step, it needed to be shown that the absence of SnS(g) and sulfur would lead to a tin loss, turning back the equilibrium point of the reaction to the $Cu_{2-x}S$(s) and ZnS(s) side. For this, sample K was heated to 550 °C under vacuum for 360 min. Subsequently, the samples were again characterized with EDX mapping and XRD measurements.

A brief summary of the different steps is also given in Table 5-2, together with the different fabrication conditions of other samples used for this work.

5.4 Sn incorporation via the gas phase

As a consequence of annealing the samples in a sulfur and SnS(g) environment, a novel strategy to form CZTS from a simplified precursor (Mo/Cu/Zn metal stack) is suggested (see section 5.8). In the following subsections, experiments are described that show a proof of principle of this suggested strategy, that study the tin incorporation into a metal stack precursor, and that investigate the reaction pathway of the CZTS formation of this novel strategy by ex-situ annealing and XRD experiments. A summary of the formation and investigation processes of the respective samples are given in Table 5-2.

Table 5-2 Fabrication sequence of all sample investigated. The standard annealing conditions ((I) and (II)) are described in section 2.2.

Sample	Study	Fabrication and investigation processes
K	Equilibrium reaction	- electrodeposition of a Cu layer onto Mo substrate - electrodeposition of a Zn layer onto Mo/Cu - annealing of this precursor under standard conditions (I) ("sulfur only") - investigations with EDX, EDX mapping, and GIXRD - annealing of this sample under standard conditions (II) (S + SnS) - investigations with EDX, EDX mapping, and GIXRD - heating the sample at 550 °C under vacuum for 360 min - investigations with EDX, EDX mapping, and GIXRD
O	Novel strategy to form CZTS	- electrodeposition of a Cu layer onto Mo substrate - electrodeposition of a Zn layer onto Mo/Cu - annealing of this sample under standard conditions (II) (550 °C, 500 mbar N_2/H_2 (90/10), 100 mg S, 12 mg SnS) - investigations with EDX, SEM, XRD, and AES depth profiling
P	Sn incorporation	- electrodeposition of a Cu layer onto Mo substrate - electrodeposition of a Zn layer onto Mo/Cu - annealing of (i) ¼ of the sample (P1) in 100 mg S and 0 mg SnS powder (ii) ¼ of the sample (P2) in 100 mg S and 0.04 mg SnS powder (iii) ¼ of the sample (P3) in 100 mg S and 0.08 mg SnS powder (iv) ¼ of the sample (P4) in 100 mg S and 0.20 mg SnS powder - investigations of all quarters with EDX, EDX mapping, and GIXRD - P5: electrodeposition of a Mo/Cu/Zn stack and annealing under standard conditions (II) in 100 mg S and 11 mg SnS - P6: electrodeposition of a Mo/Cu/Zn stack and annealing under standard conditions (II) in 100 mg S and 20 mg SnS
Q	Formation reaction (500 mbar) (use of self-made as well as IBM precursor)	- electrodeposition of a Cu layer onto Mo substrate - electrodeposition of a Zn layer onto Mo/Cu - annealing of samples Q2 to Q7 at 100 °C, 200 °C, 300 °C, 400 °C, 500 °C, and 550 °C for 0 min with 100 mg S and 20 mg SnS powder, respectively - annealing of samples Q8 to Q15 at 550 °C for 1 min, 2 min, 5 min, 10 min, 15 min, 30 min, 60 min, and 120 min with 100 mg S and 20 mg SnS powder - XRD, EDX, SEM, AES depth profile investigations
R	Formation reaction (1 mbar) (use of self-made as well as IBM precursor)	- electrodeposition of a Cu layer onto Mo substrate - electrodeposition of a Zn layer onto Mo/Cu - annealing of samples R1 and R2 at 500 °C and 550 °C for 0 min with 100 mg S and 20 mg SnS powder, respectively - annealing of samples R3 to R8 at 550 °C for 2 min, 5 min, 15 min, 30 min, 60 min, and 120 min with 100 mg S and 20 mg SnS powder - XRD, EDX, SEM, AES depth profile investigations
S	PVD approach	-co-deposition of Cu, Zn, Sn, and Se on two samples using PVD ($T_{subst.}$ = 330 °C) -annealing sample S1 under standard conditions (I) (but 1 mbar) together with elemental sulfur (process A: commonly used process in literature) -annealing sample S2 under standard conditions (II) (but 1 mbar) together with elemental sulfur and an elemental Sn source to form SnS(g) (process B) -SEM/EDX investigations and processing of samples to solar cells
T	ED approach (IBM precursors)	-electrodeposition of Cu, Zn, and Sn, (Mo/Cu/Zn/Sn) on two identical samples followed by an alloying step -annealing sample T1 under standard conditions (I) together with elemental sulfur (process A: commonly used process in literature) -annealing sample T2 under standard conditions (II) together with elemental sulfur and SnS powder as source of SnS(g) (process B) -SEM/EDX investigations and processing of samples to solar cells

5.4.1 Novel strategy to form CZTS from a Mo/Cu/Zn stack

In order to prove that CZTS can be formed via the annealing of a Mo/Cu/Zn precursor (sample O) in a sulfur **and** tin sulfide containing atmosphere, a Zn and Cu stack has been electrodeposited, as introduced in chapter 3. Processing this metallic stack to a CZTS thin film, sample O was annealed in a tube furnace together with 100 mg elemental sulfur and 12 mg SnS powder. To prove that the kesterite phase could successfully be made, standard XRD measurements (see section 2.4.4) were conducted and attention was drawn to the distinct CZTS peaks at around 23.2 ° and 29.6 °. Furthermore, the composition of the sample was obtained from global EDX measurements and SEM top view and cross-sectional images were used to study the morphology of the sample. Finally, AES depth profiles could provide information about the in-depth distribution of possible secondary phases.

5.4.2 Study of Sn incorporation

To study the Sn incorporation from the gas phase into a metal stack precursor, a Mo/Cu/Zn stack has been electrodeposited and cut into quarters. Each quarter has been annealed separately under the same standard conditions together with 100 mg elemental S, only varying the amount of SnS powder from one annealing to the other. Hereby, sample P1 was annealed without SnS powder, sample P2 with 0.04 mg SnS (which corresponds to half a stoichiometric amount necessary for the formation of CZTS), sample P3 with 0.08 mg SnS (which corresponds to the stoichiometric amount necessary for the formation of CZTS), and sample P4 with 0.20 mg SnS (which corresponds to 2.5 times the stoichiometric amount) for two hours under the standard conditions. To facilitate the handling of such small amounts of the SnS, the powder has been “diluted” with graphite powder of similar grain size. In order to support the findings, the obtained results were furthermore compared to those of samples (P5 and P6), that were annealed with around 140 and 250 times the shoichiometric amount of Sn necessary to form CZTS.

After annealing the respective samples, EDX, EDX mapping, and GIXRD measurements have been performed in a standard way (see chapter 2 for details).

5.4.3 Ex-situ investigations of the reaction pathway to form CZTS

To investigate the reaction pathway of the formation of CZTS during the annealing of a Mo/Cu/Zn stack precursor in a sulfur and tin sulfide containing environment and to deduce a formation model, ex-situ XRD measurements were performed on precursors of the same composition.

After cutting a large and homogeneous precursor in pieces (sample Q1 to Q15), each of the pieces was annealed individually under standard conditions (500 mbar of N_2/H_2) together with 100 mg of elemental sulfur and around 20 mg of SnS powder. Figure 5-4 shows the temperature profiles of the respective annealings. Hereby, the precursor (sample Q1) stayed un-annealed, sample Q2 was heated up to 100 °C, sample Q3 to 200 °C, sample Q4 to 300 °C, sample Q5 to 400 °C, sample Q6 to 500 °C, and sample Q7 to 550 °C, each followed by an immediate cool down by quickly removing the graphite box from the hot zone (please refer to Figure 2-1 for visualization). Samples Q8 to Q15 were all heated up to 550 °C, and annealed at that temperature for 1, 2, 5, 10, 15, 30, 60, and 120 min before removing quickly from the hot zone, respectively.

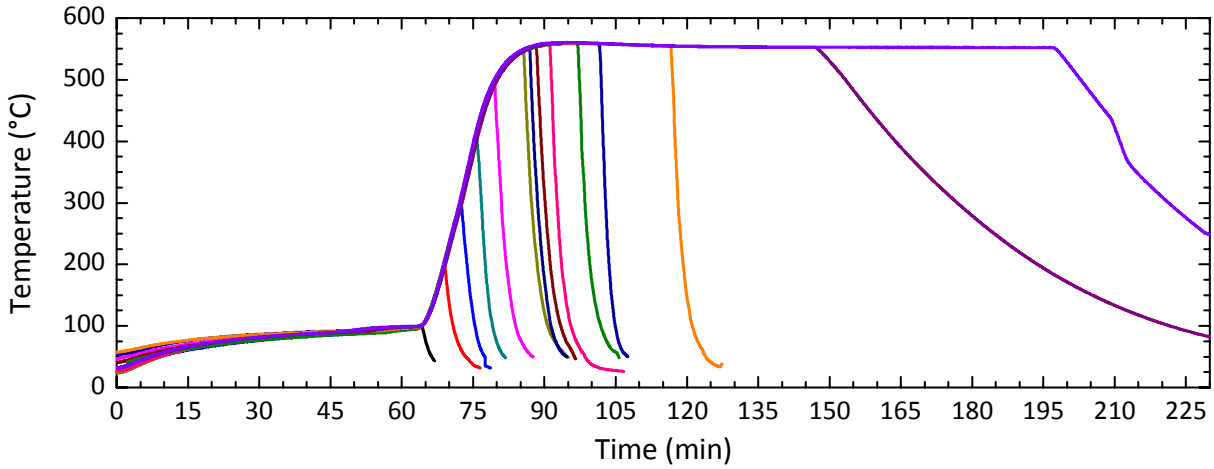

Figure 5-4 Temperature profile (as measured by a thermocouple connected to the graphite box) of the annealing runs performed on samples Q and R.

In a similar way, this annealing was repeated for samples R1 to R8 (pieces from the same precursor) at 1 mbar of forming gas. Hereby, sample R1 was heated to 500 °C, and sample R2 to 550 °C, each followed by an immediate removal/cool down, and samples R3 to R8 were heated to 550 °C for 2, 5, 15, 30, 60, and 120 min, followed by an immediate pullout, respectively. In each annealing, 100 mg of elemental sulfur and around 20 mg of SnS powder were present.

After each annealing, the respective samples were investigated with XRD, EDX, SEM, and AES depth profile measurements in order to obtain temperature and time resolved information about the formation of CZTS. The EDX measurements were performed on three positions of the sample. Figure 5-5 shows a schematic of the sample inside the annealing oven and its orientation with respect to the sulfur and SnS sources. The marked positions on the sample represent the three points where EDX measurements were performed in order to spatially resolve the incorporation of tin.

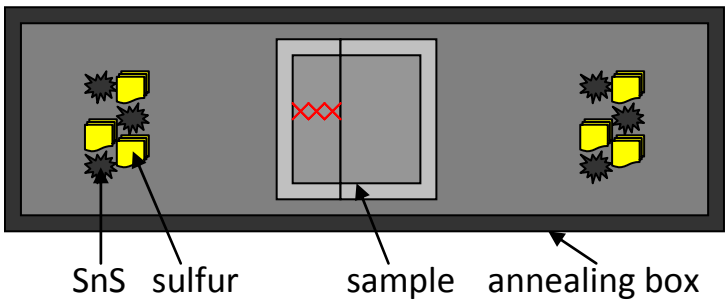

Figure 5-5 Schematic representation of the position of the sample, the elemental sulfur, and SnS powder in the annealing box. The red crosses represent the positions at which EDX measurements have been performed.

5.5 Stabilization of absorber surface

As another consequence of the equilibrium of the formation reaction of CZTS by annealing in a sulfur and tin sulfide environment, it is hypothesized that the surface of the absorber layer (thus the interface to the buffer layer) can be improved/stabilized by keeping the point of equilibrium at or very close to the CZTS side of the reaction, and hence by avoiding the loss of tin. To prove that the introduced annealing strategy generally leads to an enhancement of the power conversion efficiencies of the obtained solar cells, high quality precursors have been prepared using physical vapour deposition (sample S) as well as electrodeposition (sample T) and have been annealed with and without SnS(g).

In order to show the generality of the findings, two different kinds of precursors from two different deposition techniques have been prepared.

Precursors of sample S were prepared via the co-evaporation of Cu, Zn, Sn, and Se, as explained in section 2.1. Care has been taken that all precursors had the same uniform composition.

The precursor of sample T, in contrary, was deposited by the group of Dr. Lili Deligianni from the IBM T.J. Watson Research Center in Yorktown Heights, NY, USA. Hereby, layers of Cu, Zn, and Sn were deposited sequentially from acidic electrolytes and were intentionally alloyed subsequently. Before annealing, the uniform sample was cut in order to obtain two pieces with identical composition.

In either case of sample S and T, one precursor piece was annealed under standard conditions in the presence of only sulfur (process A: comparable to the common annealing strategy in literature, see Table 5-1), whereas the other piece was annealed under the same conditions but in the presence of sulfur **and** SnS(g) (process B). This comparison was done in order to directly compare the influence of the novel annealing strategy (with SnS(g)) with the commonly used annealing.

To investigate the influence of the addition of gaseous SnS(g) on the absorber layer as well as on the power conversion efficiency, the absorber layers from both annealing strategies and both samples (S and T) were investigated using SEM/EDX, and JV curves were measured on the obtained devices.

5.6 Deposition of buffer and window layers as well as front contacts

Within the scope of this work, a few solar cell results are shown in order to provide evidence whether a novel strategy is useful or not in terms of optimizing the solar cell device efficiency. The fabrication of such solar cells involves the deposition of several layers (as shown in Figure 5-3):

(1) Electrical back contact (Mo),
(2) p-type absorber layer (CZTS),
(3) n-type buffer layer (CdS),
(4) n-type window layers (i-ZnO, Al:ZnO), and
(5) electrical front contacts (Ni:Al).

In the present case, the Mo back contact was sputtered onto soda-lime glass by Guillaume Zoppi at the University of Northumbria. Details can be found in [68]. The absorber layer, as focus of this work, was fabricated according to Table 5-2. A CdS buffer layer was deposited in house from a chemical bath deposition (9 min in 2 mM $CdSO_4$, 1.5 M NH_4OH, and 50 mM $(NH_2)_2CS$), subsequently to a 30 s KCN etch in an aqueous 5 wt% KCN solution. Photovoltaic devices were finalized by the addition of intrinsic and alumina doped ZnO layers as well as a Ni:Al front contact grid. The latter two steps were performed by the Helmholtz Zentrum in Berlin.

Results and Discussion

In this part of the chapter, the results obtained from studying the equilibrium reaction of CZTS formation are presented and discussed. In addition, consequences of this equilibrium reaction in terms of a novel strategy to form CZTS from a simplified precursor and in terms of an enhanced stabilization of the absorber/buffer layer interface are experimentally demonstrated and discussed. Hereby, the thermodynamic pathway of CZTS formation is evaluated using ex-situ XRD investigations and an estimation of the Gibbs free energy of formation for the reaction of CZTS is given. In the end, the presented results (of the consequences of the equilibrium reaction) are related to the formation processes that were used to obtain high efficient CZTSSe solar cells, as pusblished in literature.

5.7 Tin incorporation via the gas phase

In section 5.1, literature references are given which discuss the loss of tin from a CZTS thin film during an annealing/heat treatment step. In the main, it is the work of A. Weber that suggests the decomposition reaction of CZTS to follow this pathway [141]:

$$Cu_2ZnSnS_4(s) \rightarrow Cu_2S(s) + ZnS(s) + SnS(g) + \tfrac{1}{2}S_2(g)$$

Reaction 5-19

The main argument used to explain the loss of tin is the fairly high vapour pressure of SnS at the typical annealing temperatures, as shown in Figure 4-9 (a). This reaction, however, is in fact not a truly irreversible decomposition reaction. The hypothesis stated in this work is that this reaction can certainly be thought of as reversible. Therefore, the actual reaction must be re-written as

$$Cu_2ZnSnS_4(s) \leftrightarrow Cu_2S(s) + ZnS(s) + SnS(g) + \tfrac{1}{2}S_2(g)$$

Reaction 5-20

in which an equilibrium position can be reached between either of the two sides (indicated by "$\leftrightarrow$"). Hereby, the equilibrium position is mainly dependent on the partial pressure of SnS(g) **and** S_2(g) in the vicinity of the sample. To tune this equilibrium position to the CZTS side, it is suggested to provide SnS(g) **and** reactive sulfur (S_2(g) or H_2S) with a high enough partial pressure during the annealing procedure. Therefore, in addition to elemental sulfur, which will cause the presence of many different molecular species of sulfur (such as S_X, with X = 2…8, see Figure 4-9 (b)) inside the chamber, SnS powder is used during the annealing step, as it evaporates as SnS(g) under the standard annealing conditions.

In the following, results are shown which prove that one can tune Reaction 5-20 in between both extremes by providing or omitting SnS(g) **and** sulfur during an annealing step. In a further discussion, direct consequences of this equilibrium reaction with respect to the formation of CZTS are listed.

5.7.1 Equilibrium reaction

To prove the reversibility of Reaction 5-20 three annealing experiments (described in section 5.3) were performed in series on a single sample (sample K). A first annealing (denoted as (I)) is performed with a Mo/Cu/Zn stacked metallic precursor in a sulfur atmosphere at a temperature of 550 °C for 120 min to form $Cu_{2-x}S$ and ZnS. Consequently, annealing (I) yields a

sample equivalent to the right-hand side of Reaction 5-20 except for the absent gas-phase species, SnS(g) and S_2(g). The second heat treatment denoted as (II) is performed in a sulfur and SnS atmosphere at a temperature of 550 °C for 120 min to form CZTS and to drive the reaction to the left-hand side of Reaction 5-20. In this case the supply of SnS(g) is realized by introducing SnS powder into the box. In the third experiment (labeled (III)) the Cu_2ZnSnS_4 thin film is annealed in vacuum at a temperature of 550 °C for 6 hrs. According to Reaction 5-20 the thin film should decompose into $Cu_{2-x}S$ and ZnS.

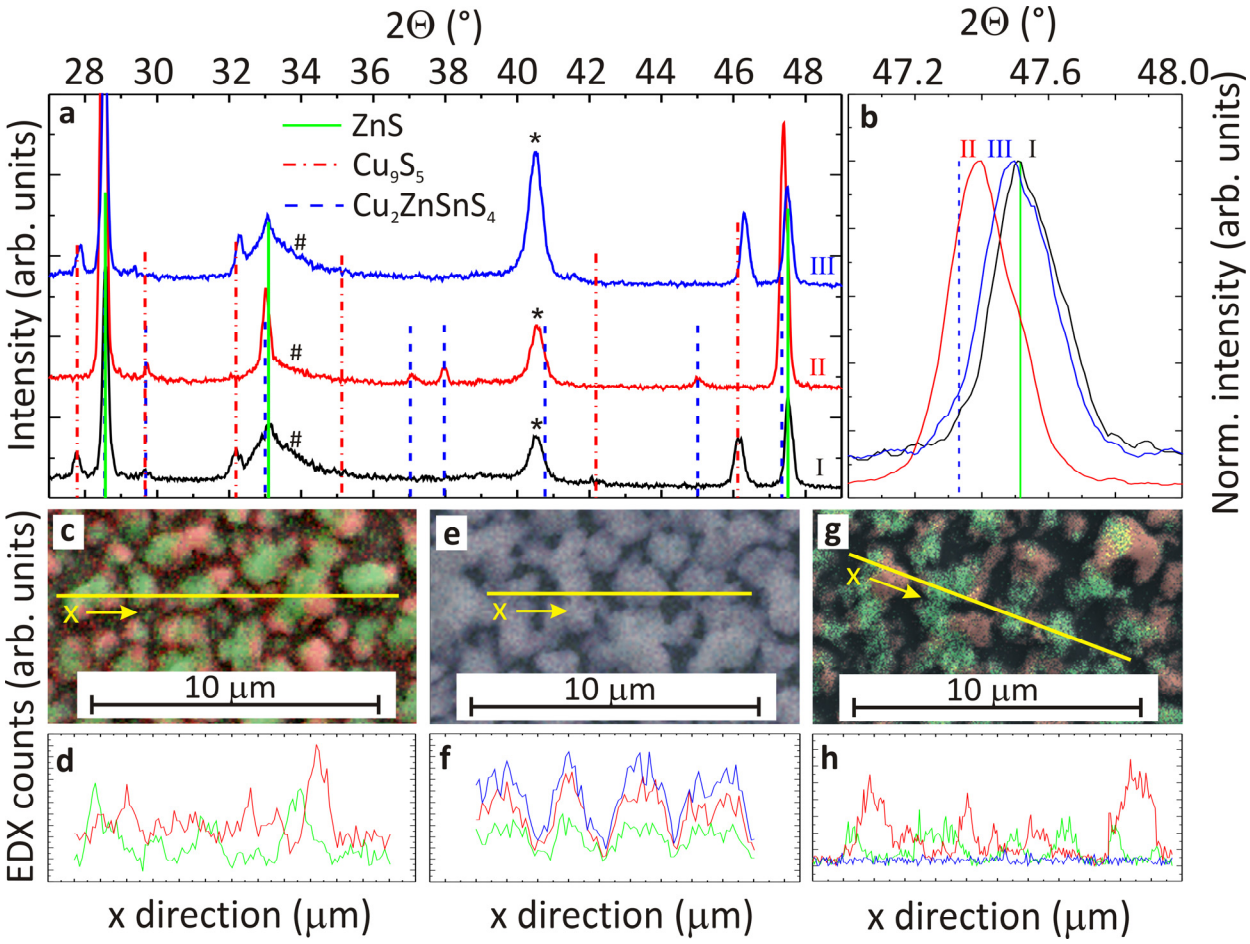

Figure 5-6 (a) Grazing incidence X-ray diffraction pattern of three different annealing experiments which elucidate the equilibrium proposed in Reaction 5-20. I: After annealing of a Cu/Zn stack in sulfur. II: After annealing of a mixed Cu_9S_5 and ZnS film in sulfur and SnS(g). III: After annealing CZTS in vacuum. Identified phases: ZnS (green; 04-001-6857), Cu_9S_5 (red; JCPDS: 00-047-1748), Cu_2ZnSnS_4 (blue; JCPDS: 01-075-4122), Mo substrate (*;JCPDS: 04-001-0059), MoS_2 (#;JCPDS: 04-004-4330) [23]. (b) Enlarged view of 47.2 - 48 ° to demonstrate clear differentiation of CZTS and ZnS. (c, e, g) EDX topview mappings: red Cu, green Zn, blue Sn; details, see text. (c) Corresponds to process (I), (e) corresponds to process (II), (g) corresponds to process (III). (d) Linescan indicated in c, (f) linescan indicated in e, (h) linescan, indicated in g.

Figure 5-6 (a), (b) depicts the XRD analysis after the different heating steps, while EDX mapping results are shown in Figure 5-6 (c)-(h). In the first annealing (I) reflections originating from ZnS and Cu_9S_5, i.e. a Cu-poor Cu_2S, are identified. Moreover, the Mo substrate (denoted by "*") and a small contribution of MoS_2 (labeled by #) are found. WDX analysis yields a Cu/Zn composition of 1.6. EDX mapping of the surface shown in Figure 5-6 (c) enables to analyze the lateral distribution of the $Cu_{2-x}S$ and ZnS grains. The X-rays originating from Cu are color-coded in red, whereas those from Zn are colored in green. No intermixing of the Cu and Zn signal occurs since only red and green are visible after addition of the two EDX images. This is

confirmed in Figure 5-6 (d) where an EDX linescan is shown. It is clearly visible that the Cu and Zn signals are not correlated which means that Cu_9S_5 and ZnS do not intermix. In the XRD analysis of annealing (II), where SnS was present during the heat treatment, no indication of a $Cu_{2-x}S$ is visible anymore as shown in Figure 5-6 (a). Moreover, additional reflections corroborate that CZTS has been formed (see 2θ = 29.7 °, 37 °, 38 °, 45 °). Since the main reflexes of ZnS and CZTS are very close (see 2θ = 28.5 ° and 47.3 °), one cannot exclude remaining ZnS that has not been transformed into CZTS. However, the small shift toward lower angles shown in Figure 5-6 (b) indicates that the majority of the ZnS has been consumed. This is also apparent in Figure 5-6 (e) and (f) where the EDX signals of Cu, Zn, and Sn show a strong correlation in complete contrast to Figure 5-6 (c) where Cu and Zn showed an anti-correlation. Even more interesting is that the resulting WDX elemental ratios, Cu/(Zn + Sn) = 0.78 and Zn/Sn = 0.97, are very close to the optimum values for high-performance solar cell absorbers, as shown in Figure 5-1. This shows that the incorporation of Sn via SnS(g) does not proceed in a random way but seems to be self-limiting. As long as enough $Cu_{2-x}S$ and ZnS are present, SnS(g) and sulfur from the gas phase are incorporated into the film to form CZTS. This model experiment shows that Reaction 5-20 can be used to form CZTS by controlling the partial pressures of the volatile species. In the presented case, the presence of a tin source drives the reaction towards the CZTS side and avoids the loss of tin. Of course the situation can be reversed by taking the finished CZTS absorber and repeating the annealing step for a third time without additional S or SnS. The heating (III) has been performed under vacuum to reduce the sulfur and SnS(g) partial pressures to a minimum in the direct vicinity of the sample by enlarging the mean free path of the sulfur and SnS(g) molecules that evaporate from the film. After 6 hrs of heating the CZTS has been transformed back into $Cu_{2-x}S$ and ZnS as shown by the XRD analysis (Figure 5-6 (a)). A Sn concentration of only 0.2 at% is identified by WDX analysis, and the mapping depicted in Figure 5-6 (g) and (h) shows again anti-correlated Cu and Zn signals.

To conclude, Reaction 5-20 is indeed a reversible equilibrium reaction. By the choice of the partial pressures of S_2(g) and SnS(g), one can tune the equilibrium position of the reaction in between the two extremes. By the right choice, tin loss, and hence the formation of ZnS and $Cu_{2-x}S$, can be avoided.

5.7.2 Consequences of equilibrium reaction

Figure 5-7 (a) and (c) show schematics of an annealing chamber, where a sample is annealed in (a) a S only environment or in (c) a sulfur **and** SnS(g) environment. In case (a), the sample will continuously loose tin via the evaporation of SnS(g) and S_2(g), as suggested by Weber [141], until eventually, the partial pressure of S_2(g) and SnS(g) in the vicinity of the sample is high enough to compensate for the loss and to form an equilibrium reaction. Hereby, it can be assumed that a high background gas pressure, a small annealing chamber (with maybe even heated walls), and a short annealing time can help to keep the equilibrium position closer to the CZTS side of the reaction, as the mean free path is reduced and the molecules reflected on the hot walls. That way, evaporated SnS(g) and S_2(g) will stay in the vicinity of the sample, helping to push back SnS(g) and S_2(g) coming from the sample and hence avoiding large amounts of Sn loss. In the opposite case, where a sample is annealed for a long time in a large chamber (e.g. vacuum chambers) with cold walls under a low background pressure, a fast evaporation of SnS(g) and S_2(g) can be assumed due to the larger mean free path of the evaporated molecules. These might get adsorbed on the cold walls making it hard to raise the partial pressure of these molecules in the vicinity of the sample to create an equilibrium

reaction. Typically, as shown in the results of annealing III of the previously described experiment, this can lead to a complete loss of tin from the sample.

The solution presented in the work is the use of an additional tin source in combination with sulfur during the annealing (as schematically shown in Figure 5-7 (c)), in order to provide a high enough vapour pressure of SnS(g) aside some reactive sulfur (S_2 or H_2S) to push the equilibrium point towards the CZTS side of the reaction (as shown in Figure (d)). In the previously described experiment, SnS powder has been used as a source of SnS(g). This, however, is certainly not the only way to provide a SnS(g) rich environment. In the experiment described in section 5.10.1, elemental Sn together with elemental sulfur was used in the annealing such that Sn and sulfur react to SnS(g) which evaporates at elevated temperatures to provide the partial pressure necessary to stop the decomposition of CZTS.

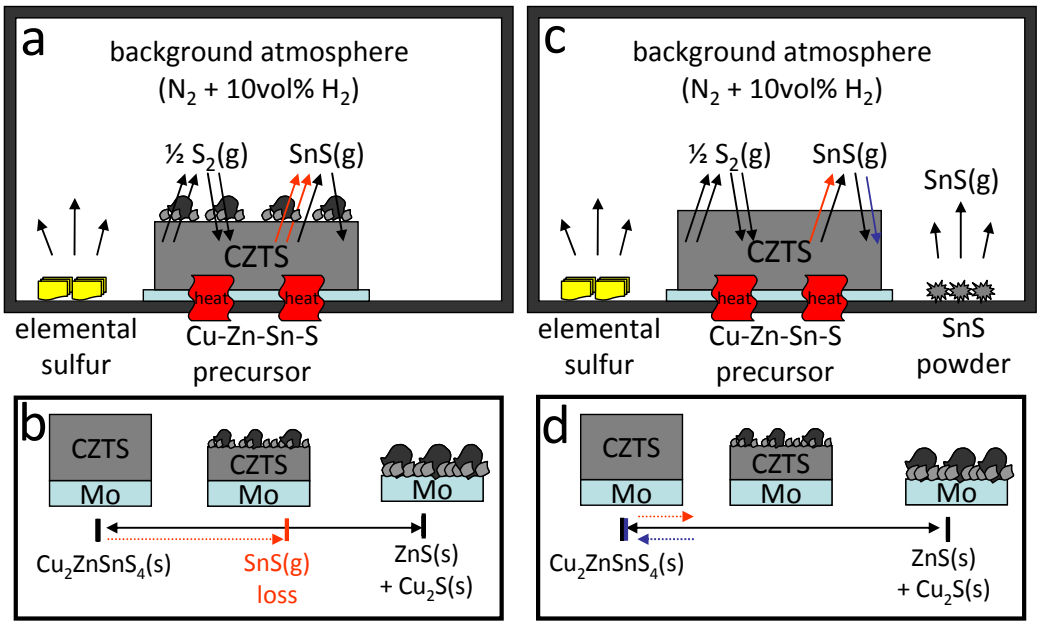

Figure 5-7 Schematic presentation of the tin loss. (a,c) Schematic presentation of an annealing chamber. (b,d) Schematic drawing of the equilibrium position of Reaction 5-20 for the respective annealing chamber. (a,b) show the case of annealing in only sulfur, while (c,d) show that of the annealing in sulfur and SnS(g).

Concluding the experiment, the following general consequences can be stated:

1. Annealing under sufficient partial pressures of sulfur **and** SnS(g) environment keeps the equilibrium of Reaction 5-20 on the side of CZTS and stabilizes the CZTS phase at the absorber's surface, avoiding un-desired secondary phases at the absorber/buffer interface which might have a negative effect on the performance of a solar cell.
2. It is possible to incorporate sufficient amounts of Sn into a $Cu_{2-x}S + ZnS$ containing sample via the gas phase by the evaporation of $SnS(g) + S_2$ in order to form CZTS. Hereby, the incorporation of Sn seems to be self-limiting, as it has been observed in the experiment discussed in section 5.7.1, that not more than the required amount of Sn to form CZTS was incorporated.
3. Having shown that it is possible to form Cu_2ZnSnS_4 by annealing a $Cu_{2-x}S + ZnS$ containing sample in a SnS(g) and sulfur rich environment, it should further be possible to incorporate Sn via the gas phase into a simplified, only Cu and Zn containing precursor in order to form CZTS.
4. Annealing (without additional SnS(g)) in a chamber with a large volume, cold walls, and under low background gas pressures should lead to more drastic loss of tin than

in a chamber with small volume, hot walls, and under a high background pressure, as the evaporated SnS(g) will not contribute as much to raising the partial pressure of SnS(g) in the vicinity of the sample.

5. Annealing (without additional SnS(g)) in an environment of a high partial pressure of reactive sulfur (such as S_2 or H_2S) could minimize or even hinder the decomposition of CZTS as suggested in Reaction 5-20, as the presence of one of the two evaporating molecules should suffice to prevent the decomposition in the first place.

The given consequences are very general and should apply to any annealing system. Furthermore, this reaction is not restricted to the sulfide CZTS case but also applies for selenide CZTSe and mixed sulfur-selenide CZTSSe, providing SnSe(g) in addition to Se_2. As a proof, the formation of a mixed sulfur-selenide CZTSSe from the annealing of a Mo/Cu/Zn precursor in sulfur and SnS(g) environment is shown in the Appendix D.

In the following, consequences “1” and “3” will be investigated in more detail, while consequence “2” has already been proven. Due to the limited time frame of this work, consequences “4” to “6” could not be envisaged in more detail.

5.8 Consequence: Fabrication of CZTS from a simplified precursor

As shown in the previous section, the novel annealing strategy (annealing in a sulfur **and** SnS(g) containing environment) offers the possibility to incorporate tin into a ZnS and $Cu_{2-x}S$ containing sample leading to the formation of CZTS. In this context, it has been stated that under the given conditions the tin incorporation might even be self-limiting. The limit seems to be the formation of CZTS, avoiding any tin rich binary or ternary phases. As another consequence of the novel annealing strategy, the formation of CZTS via a simplified precursor (containing only copper and zinc) was suggested. Within this section, both statements are investigated.

5.8.1 Proof of principle of CZTS formation from a simplified Mo/Cu/Zn stack

To prove that CZTS can be formed by annealing a copper and zinc containing precursor in a sulfur and SnS(g) containing environment, a sample (sample O) has been prepared electrochemically, as described in section 5.4. In the following, this precursor was annealed under the standard conditions together with elemental sulfur and tin sulfide powder. The obtained sample was characterized by various methods as listed in section 5.4.

The left picture in Figure 5-8 (a) shows a representative SEM top view image and Figure 5-8 (b) a cross-sectional image of the annealed sample (un-etched). One can see that the overall morphology does not appear to be very compact, with 2 to 3 μm large grains together with around 1 μm small grains in between. In addition, small grains of around 0.4 μm can be seen. From those two images, it is yet unclear whether one or more phases have been formed. The back-scattered image shown on the right side of Figure 5-8 (a), however, suggests the presence of two phases as darker and brighter areas sit side by side.

The X-ray diffraction pattern (shown in Figure 5-9) suggests the presence of CuS and Cu_9S_5 phases, which might correspond to the small grains observed in the SEM cross section. The main phase observed in this sample however can clearly be attributed to Cu_2ZnSnS_4, as the unique CZTS peaks at for example 23 ° and 29.6 ° are present. From chapter 4 it is known that this does not completely exclude the presence of ZnS or Cu_2SnS_3. Apart from two peaks originating from the underlying Mo substrate, no further peaks are seen.

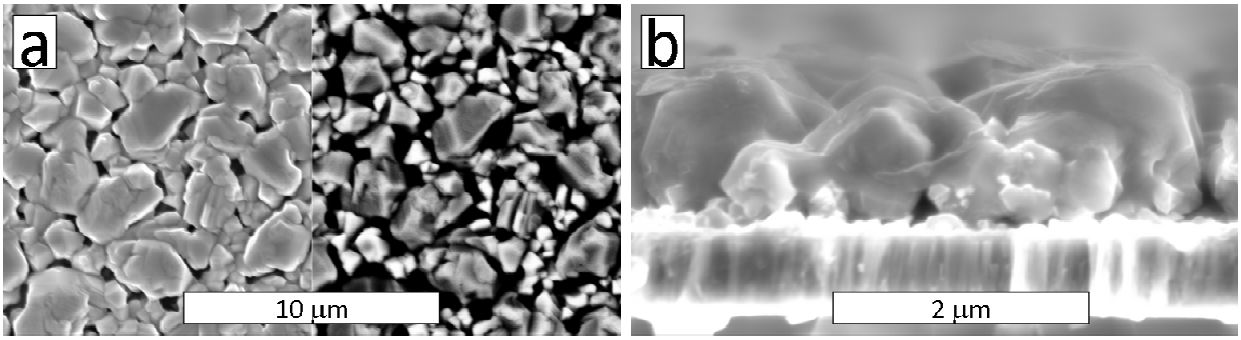

Figure 5-8 (a) SEM top view image (left) and back-scattered electron image (right) of sample O, as obtained from the same area. (b) SEM cross-sectional image of sample O.

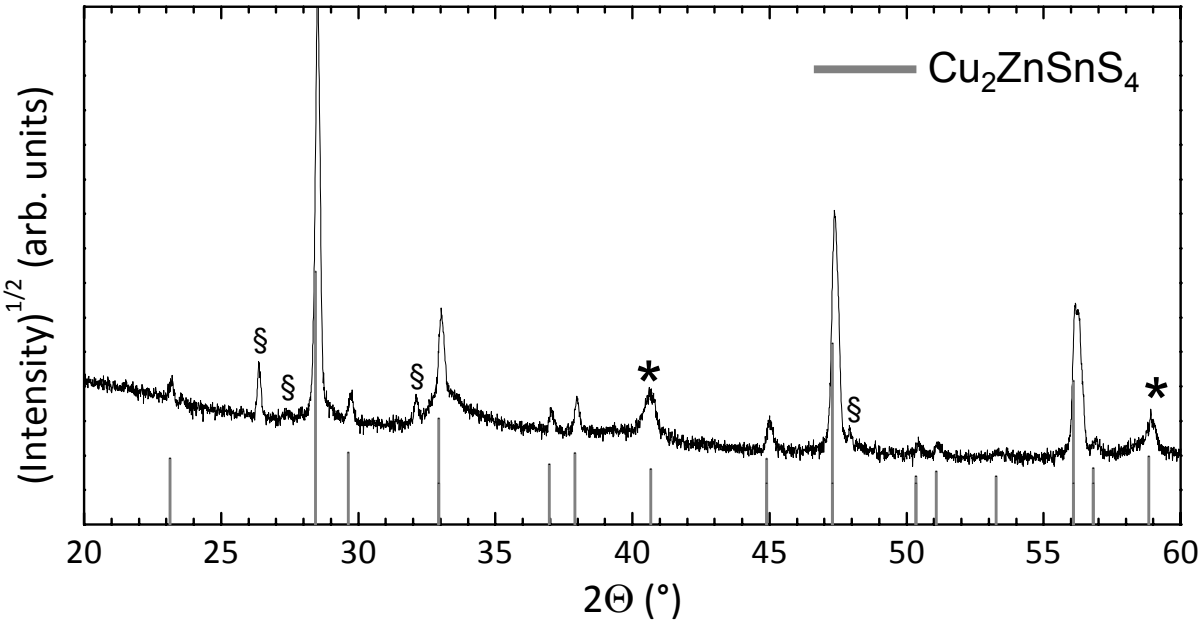

Figure 5-9 XRD pattern of sample O. The grey lines represent the CZTS phase, "*" marks the Mo contribution and "§" indicates Cu-S phases, in accordance with the following JCPDS reference data: CuS: 03-065-3561, Cu_9S_5: 00-047-1748), Mo: 04-001-0059, and CZTS: 01-075-4122 [23].

To study the possible presence of CTS or ZnS in more detail, an AES depth profile was measured. In Figure 5-10 (a), the relative compositions are plotted versus the sputtering time, whereas in part (b) the normalized intensities are shown. Hereby, the intensities of Cu, Zn, Sn, and S were normalized with respect to the values at the surface, as here the Cu/(Zn+Sn) ≈ 1 and Zn/Sn ≈ 1. The the Mo signal was normalized with respect to its maximum value. From Figure 5-10 (a) one can see that right below the surface region the Sn signal slightly decreases into the bulk such that the Zn/Sn ratio reaches a value of around 1.1. At the same time, the signals for Zn and Cu stay fairly constant such that in the bulk, the overall composition (25:13:12:49.5) corresponds well to the stoichiometric composition of Cu_2ZnSnS_4. This suggests that CZTS is the dominant phase present in this film, which is in good correlation with the CZTS results. In the following, while the Mo signal starts to appear, the signals of Cu and Sn decrease while that of Zn stays high. From Figure 5-10 (b), it can be seen that the Cu and Sn signal decrease in parallel, while the zinc signal decreases around 100 s of sputtering later. This suggests the presence of a ZnS phase at the back of the layer. In accordance with the results of chapter 4, such a small amount of ZnS would not be detectable with XRD. It is assumed that the small grains shown in Figure 5-8 (b) does not consist of ZnS as it would contribute to the "surface near region" of the AES depth profile. Therefore, it is concluded that ZnS sits inside the large grains, being

"encapsulated" by CZTS. The reaction path of the formation of ZnS inside the CZTS grains is given in section 5.9.1.

In correlation to the compositional ratios obtained from AES, EDX investigations give compositional ratios of Cu/(Zn + Sn) = 0.83 and Zn/Sn = 1.07 as an average over the whole film depth. These values are in fact very close to the optimum values for high-performance solar cell absorbers, as shown in Figure 5-1. Furthermore, they also show that the average composition is Zn rich and Cu poor, which suggests the presence of an additional ZnS phase. In terms of the incorporation of tin via the gas phase (via SnS(g)), this result supports the hypothesis that the tin in-corporation is self-limited under the used annealing conditions, as again not more than the necessary amount of Sn to form CZTS has been introduced into the layer (see Zn/Sn > 1). A more detailed study on this issue is shown in the next section.

Overall, the experimental data show that CZTS can be formed via the annealing of a simple precursor (containing only Cu and Zn) in a sulfur and SnS(g) containing environment. In section 5.9.1, results of the investigation of the reaction pathway to form CZTS via this novel route are shown and a formation model is deduced. Furthermore, a rough estimate of the Gibbs free energy of formation will be given.

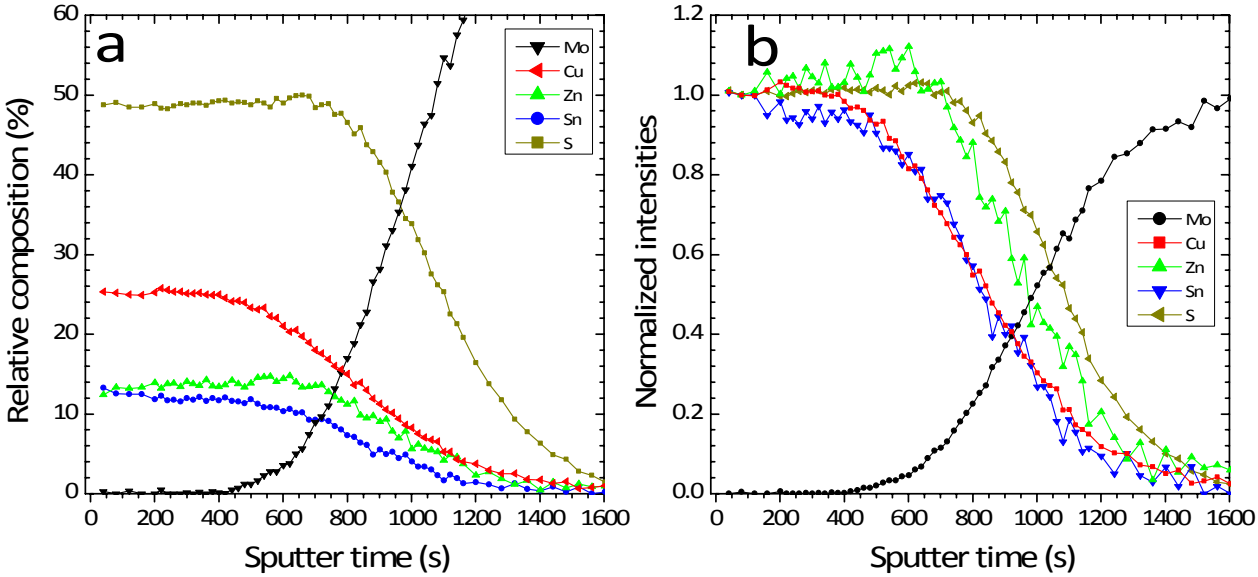

Figure 5-10 (a) AES depth profile as obtained from a representative area of sample O. (b) Normalized AES depth profile, after normalizing the data of each element to the respective value at 100 s of sputtering time. The Mo signal was normalized to its maximum value. Dark yellow lines represent sulfur, red represents copper, blue represents tin, and green represents zinc.

5.8.2 Sn incorporation

On several occasions in the previous sections, the hypothesis was stated that during an annealing with SnS(g), tin incorporates into a tin deficient sample in a self-limiting manner. Hereby, the limit of incorporation appears to be the stoichiometric amount necessary to form CZTS, respectively.

To investigate this issue, a metal stack precursor (Mo/Cu/Zn) was electrodeposited and cut into quarters before annealing, as described in section 5.4.2 (sample P). Each quarter was then annealed under the standard conditions together with (i) 0 times, (ii) 0.5 times, (iii) 1 time, and (iv) 2.5 times the stoichiometric amount of Sn (in the form of SnS powder) to form Cu_2ZnSnS_4.

Figure 5-11 shows EDX mappings overlaying SEM top view images obtained from the four quarters of the sample after the respective annealing. In Figure part (a), one can see a similar result as previously observed for a ZnS and $Cu_{2-x}S$ containing sample (sample K), as shown in

Figure 5-6. There are well separated green and red areas, indicating the presence of ZnS and $Cu_{2-x}S$ phases. In part (b) of the Figure, some of the green and the red areas seem to have slightly disappeared and turned into white areas. This indicates the incorporation of Sn, as the overlap of green, red, and blue color due to zinc, copper, and tin would result in white, respectively. As only 0.5 times of the stoichiometric amount of Sn was used in this annealing process, it is expected that CZTS forms while ZnS and $Cu_{2-x}S$ phases partly remain. Figure part (b) supports this expectation. In part (c) of the same Figure, where exactly the stoichiometric amount of Sn was used in the annealing process, less green and even no red areas can be seen. In fact, only very few areas appear still to be Zn rich, while Cu rich areas are not visible. This leads to the conclusion that the use of the stoichiometric amount of Sn during the annealing lead to the formation of a CZTS majority phase. Figure 5-11 (d) shows a similar result to (c), leaving some green, zinc rich areas behind, together with a majority CZTS phase. Although an increased amount of 2.5 times the stoichiometric amount of Sn was provided, there is no sign of blue and hence tin rich areas. It appears that the incorporated amount of tin in samples P (iii) and P (iv) is of the same order, as Figure 5-13 shows.

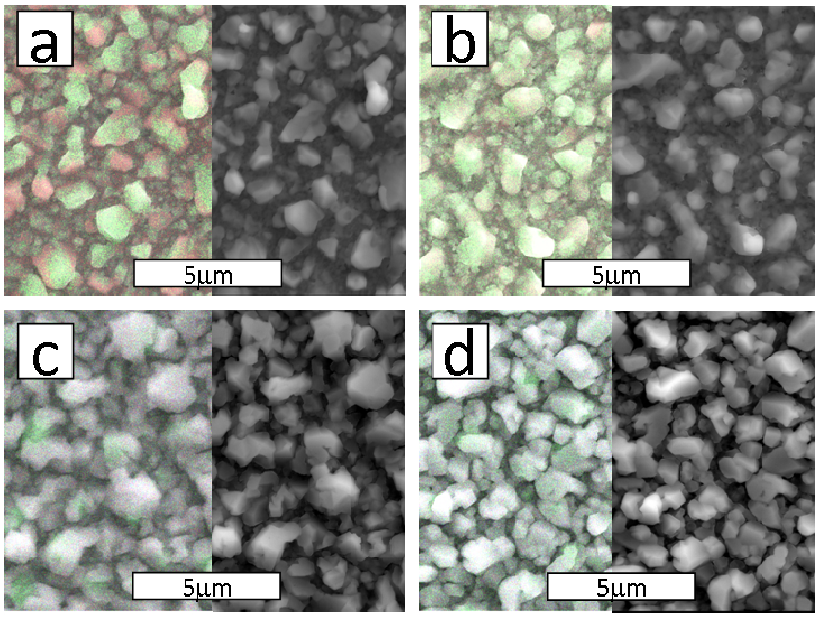

Figure 5-11 EDX mapping (left part) of the different quarters after annealing under standard conditions with (a) 0 times (i), (b) 0.5 times (ii), (c) 1 time (iii), and (d) 2.5 times (iv) the amount of Sn for a stoichiometric Cu_2ZnSnS_4 phase, overlaying SEM top view images (bottom). Red color indicates Cu, green indicates Zn, and blue indicates Sn. The right part of each image shows the SEM top view image of the same area by itself.

All these findings are supported by XRD results obtained from the respective sample quarters. Figure 5-12, shows the interesting sections of the measured XRD patterns obtained from the four sample pieces (please see Appendix E for the whole diffractograms). One can clearly see that in sample P (i) (black line) only reflections due to ZnS and $Cu_{1.765}S$ can be seen. In the sample annealed with 0.5 times the stoichiometric amount of Sn (red line), the peak at 28.6 ° seem to have shifted slightly towards 28.5 °, indicating an overlap of CZTS and ZnS phase. In addition, the peak at 46.3 ° (related to $Cu_{1.765}S$) decreases in intensity while a CZTS peak at 76.4 ° starts to rise. For the samples annealed with 1 and 2.5 time(s) the stoichiometric amount of Sn, the distinct $Cu_{1.765}S$ peak at 46.3 ° has disappeared while the peaks at 28.5 ° and 76.4 ° have clearly moved from the ZnS to the CZTS position. Regarding chapter 4, however, this does not completely exclude the presence of a minority ZnS or CTS phase, especially since Cu_2ZnSnS_4 as well as Cu_2SnS_3 have the same Cu/Sn ratio. Since there have not been additional peaks due

to a Sn-rich phase (e.g. $Cu_2Sn_3S_7$, SnS, Sn_2S_3, or SnS_2, etc), one can conclude that for the XRD results tin has incorporated itself just as much as it needed to form stoichiometric CZTS or CTS, respectively.

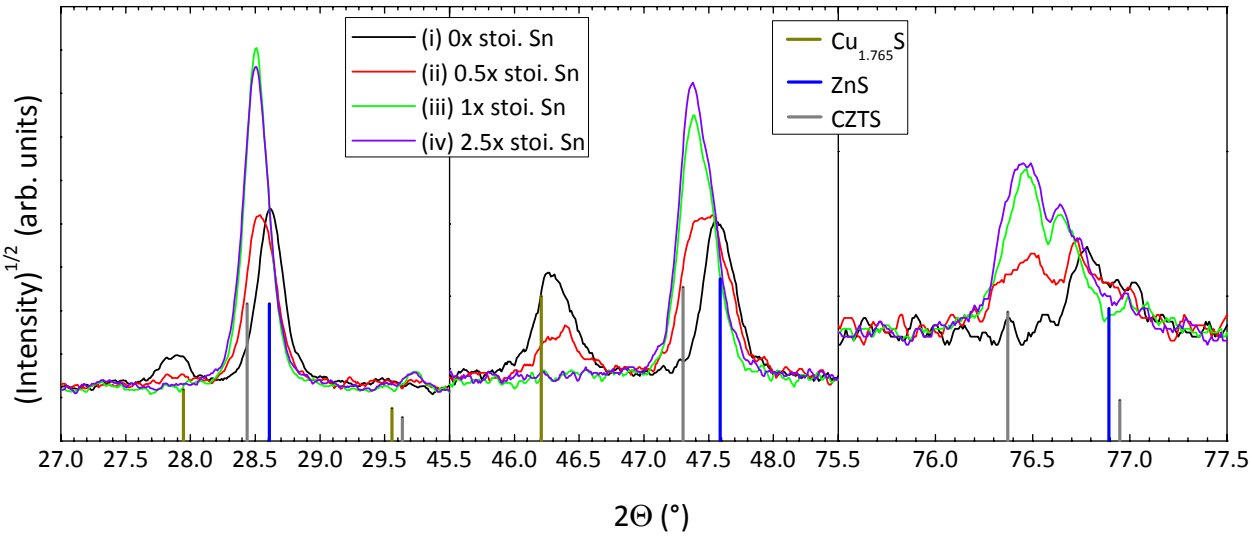

Figure 5-12 XRD patterns obtained from the samples annealed with (i) 0 times (black data), (ii) 0.5 times (red data), (iii) 1 time (green data), and (iv) 2.5 times (violet data) the stoichiometric amount of Sn necessary to form CZTS. The vertical lines in blue correspond to ZnS (JCPDS: 04-001-6857), those in grey to CZTS (JCPDS: 01-075-4122), and the dark yellow ones to $Cu_{1.765}S$ (JCPDS: 00-023-0960) [23].

Since this conclusion is mainly based on qualitative investigations, it is yet an insufficient proof. Therefore, compositional analyses using EDX were obtained in order to provide quantitative results. In Figure 5-13, the obtained compositions are displayed in terms of (a) the pseudo-ternary phase diagram, and (b) in terms of the Sn/(Zn + Cu) ratio vs. the amount of Sn used in the annealing. To provide harder evidence for the self-limiting tin incorporation, the data of two additional samples (P5, P6) were added, while sample P5 was annealed together with around 140 times the stoichiometric amount of Sn, and sample P6 with around 250 times the stoichiometric amount. From Figure 5-13 (b), one can clearly see no additional incorporation of Sn into the sample for annealings with more than the stoichiometric amount of tin. Visualizing this in Figure part (a), it is observed that the positions of the respective samples with more than 1 time the stoichiometric amount only shifts within the error of the measurement (see red circles). Hereby it shall be noted that point (ii) appears to have less copper than the others do. However, as all four pieces ((i) to (iv)) are quarters of the same precursor, it is unlikely that less copper was deposited on this section. Therefore, this deviation of the copper content might be related to a measurement effect coming from the EDX.

After the annealing of samples P5 and P6 (and many other annealings performed for this work) with together with 11 and 20 mg SnS powder (around 140 and 250 times the stoichiometric amount of tin, respectively), it was observed by weighing the remaining powder inside the annealing box that typically only 3 mg of the SnS powder has been used up. This result suggests that during the annealing, the SnS(g) saturated vapour pressure of around $3 \cdot 10^{-3}$ mbar (see Figure 4-9) is reached. Assuming an ideal gas for SnS(g) and a volume of 20 cm^3 for the annealing box, one can calculate (using the ideal gas law) that 0.13 μg of SnS(g) are required to saturated the vapour phase at 550 °C. These values are very small compared to the amount required to form stoichiometric CZTS (0.31 mg of SnS). Furthermore, it leads to the conclusion that not the amount of SnS powder which is put into the annealing box effects the tin incorporation into the sample, but rather it is the low saturated vapour pressure of SnS(g)

which limits the incorporation of tin. In addition, as 3 mg of SnS powder were used up, although only 0.31 mg was required to form a stoichiometric Cu_2ZnSnS_4 film, it can be concluded that the used annealing setup was not completely tight.

All those results lead to the conclusion that no matter how much SnS powder is provided during the annealing, the saturation of the SnS(g) vapour pressure is reached, which limits the tin incorporation with respect to the amount necessary to form CZTS.

As a consequence of this result, in annealings of further studies within this work, around 10 to 20 mg of SnS powder was typically used, which corresponds to 125 to 250 times the stoichiometric amount of Sn necessary, as it facilitated the handling of the powder.

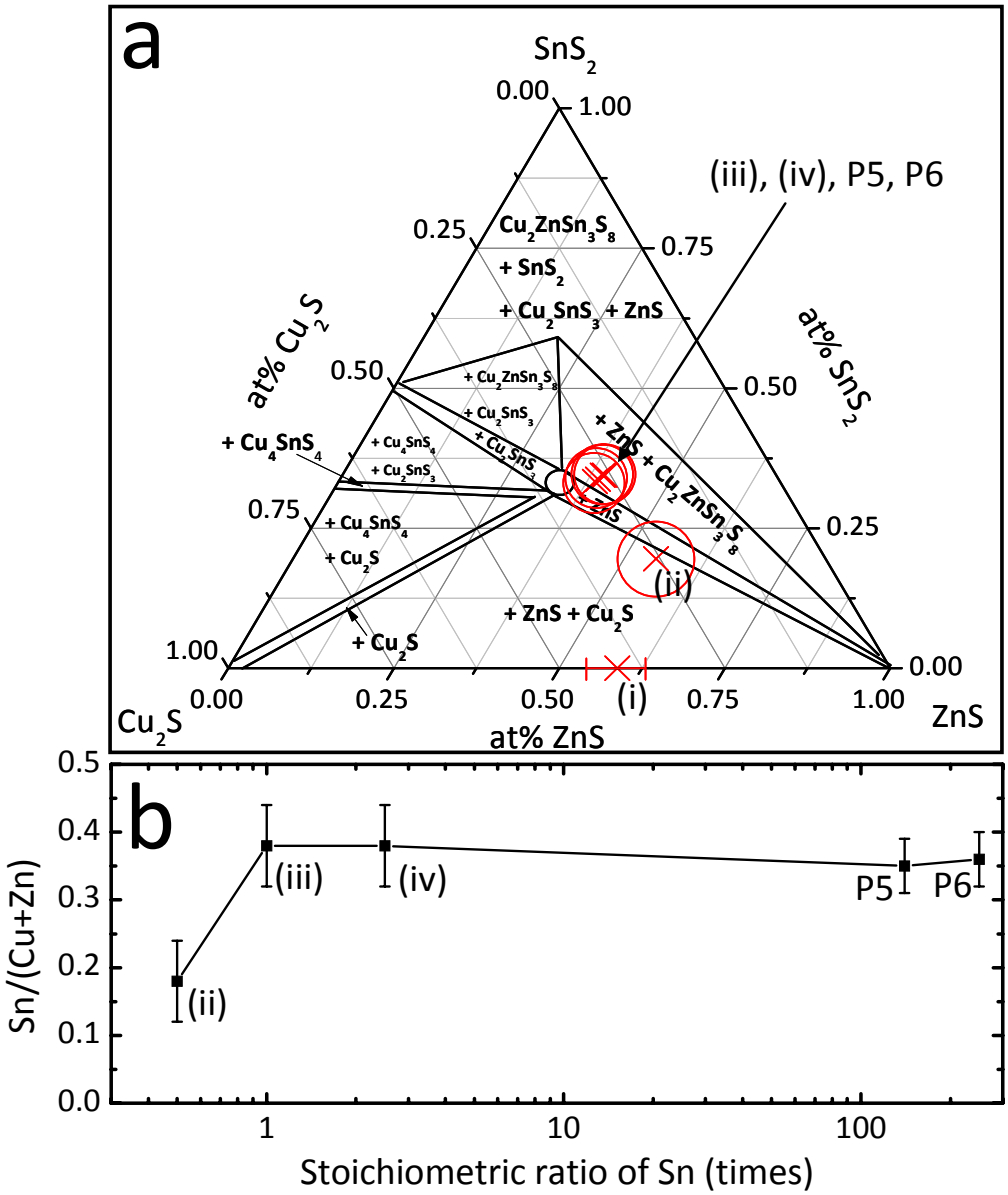

Figure 5-13 (a) Compositional position in pseudo-ternary phase diagram and (b) Sn/(Cu + Zn) ratio of samples P1 to P6 annealed under standard conditions with (ii) 0.5 times, (iii) 1 time, (iv) 2.5 times, as well as 140 and 250 times the amount of Sn for a stoichiometric Cu_2ZnSnS_4 phase. The red circle indicates the maximum uncertainty of the EDX measurement, according to section 2.3.2.

5.9 Model of CZTS formation from the annealing of a Mo/Cu/Zn stack

After the previous sections introduced a novel route to form CZTS from the annealing of a simplified precursor in a sulfur and tin sulfide containing environment, this section focuses on deducing the reaction pathway of the CZTS formation of this strategy, using ex-situ XRD, EDX, SEM, and AES depth profiling techniques. From this, a model is proposed that describes the formation of the thin films absorber layer (and hence the typical grain structure such as that seen in Figure 5-8), and an estimate for the Gibbs free energy of formation of CZTS is given. These investigations were mainly performed for an annealing in 500 mbar of forming gas, but they were partly repeated for an annealing in 1 mbar of forming gas. In the end of this section, power conversion efficiencies of solar cells obtained from different annealing times are presented which help to suggest optimal annealing conditions.

5.9.1 Annealing in 500 mbar forming gas

As described in more detail in section 5.4.3, pieces of the same electrodeposited precursor (Mo/Cu/Zn) have been annealed at different temperatures and for different times (see temperature profile in Figure 5-4) in order to resolve the phase formation process occurring during a standard annealing of a Mo/Cu/Zn sample together with elemental sulfur and tin sulfide powder at 500 mbar forming gas. Hereby, care was taken that the samples were cooled down as quickly as possible after the respective temperature and time was reached, in order to avoid a continuation in phase formation during the cool down step (see Figure 5-4).

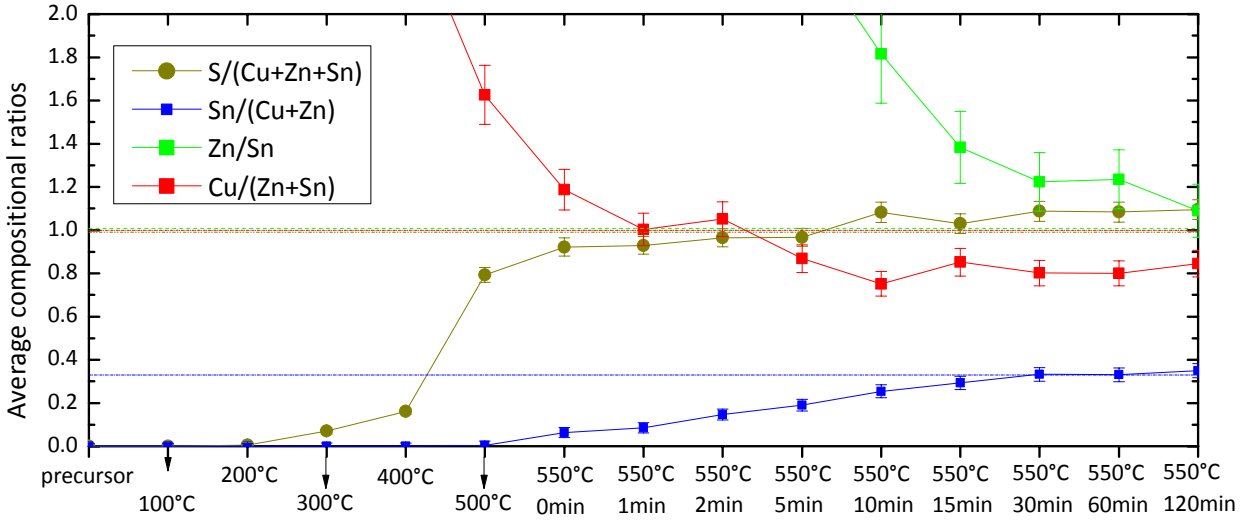

Figure 5-14 Average compositional ratio of samples Q1 to Q15. The dash-dotted horizontal lines represent the expected values of the respective ratios for stoichiometric Cu_2ZnSnS_4.

Composition

After annealing, the compositions of the samples were determined using EDX. Hereby, three positions on each sample were measured, with the position at 0 mm being closer to the sulfur and tin sulfide source than positions 2.5 mm and 5 mm (as schematically drawn in Figure 5-5). Figure 5-14 shows the average compositional ratios obtained from the different samples. The dark yellow data points represent the values of the respective S/(Cu + Zn + Sn) ratios. From this, one can see that the sulfur incorporation starts at a temperature of around 200 °C and it increases dramatically at 500 °C. At 30 min of annealing time, a steady state seems to be reached just above its expected value, indicating that no major inclusion of sulfur into the sample is happening any more. In general, one can say that the sulfur incorporation is complete

after around 10 min already. Relating these data to the literature data shown in Figure 4-8, it is assumed that ZnS is the first sulfide phase to have formed at 200 °C.

The blue data points in Figure 5-14 represent the amount of tin inside the layer, with respect to copper and zinc. From those data it can be seen that tin starts to be incorporated via the gas phase above 500 °C. Similar to the sulfur line, a steady state seems to be reached after 30 min of annealing right at the expected value of Sn/(Cu+Zn) = 0.33. Similar to the before, it can be assumed that after 30 min of annealing at 550 °C, no major changes in phase formation occur any more.

The red data points show the behaviour of the Cu/(Zn+Sn) ratio throughout the annealing. Due to the initial lack of tin inside the film, the values start off to be very high and equilibrate once the tin inclusion finds a steady state. After 30 min of annealing, this steady state is reached at a value of around 0.8, which is lower than the expected value of 1.0 but in the range of what is reported in literature for high efficient devices (see Figure 5-1).

The Zn/Sn ratio (shown in green) behaves very similar to the Cu/(Zn+Sn) ratio, by starting off at very high values for a low Sn content and equilibrating at around 30 min of annealing time. Hereby, a steady state is reached for Zn/Sn = 1.1 to 1.2, which is larger than the expected value of 1.0 but within the range of what is reported in literature for high efficient devices (see Figure 5-1).

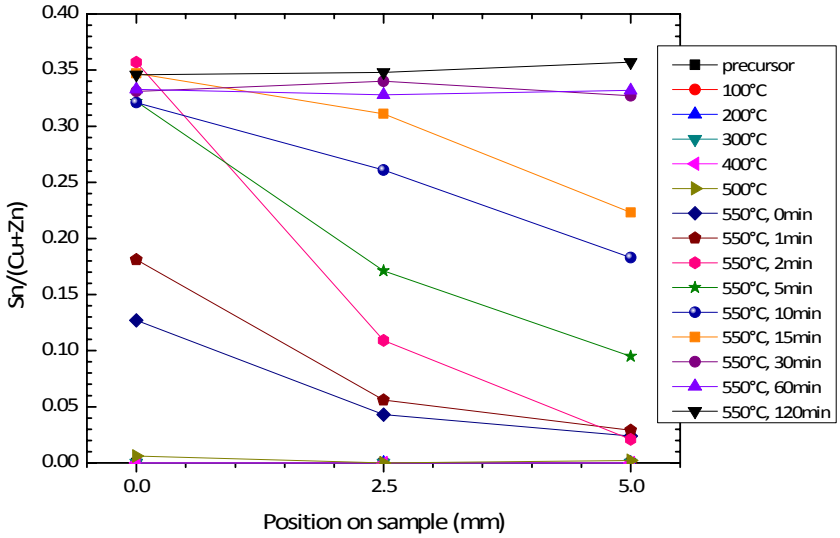

Figure 5-15 Spatially resolved compositional ratio of the samples Q1 to 15. The error bars for Sn/(Cu + Zn) were deliberately excluded from the graph. Its value is Δ Sn/(Cu+Zn) = 0.05.

Figure 5-15 shows the Sn/(Cu + Zn) ratio spatially resolved on the sample (as explained in section 5.4.3). One can see that up until 400 °C, there is no change in the signal, indicating that tin is not incorporated until then. At 500 °C, however, the tin signal slightly starts to increase at position 0 mm, so what is closer to the sulfur and tin sulfide source, while there is yet no tin signal at the other two positions. Heating up the sample to 550 °C, the overall tin content inside the layer starts to rise and a tin gradient is observed. For longer annealing times of up to 2 min at 550 °C, this gradient becomes steeper with a maximum value for Sn/(Cu + Zn) of 0.35 at position 0 mm and very low tin content at 5 mm. This can be explained by the relatively long diffusion time of SnS(g) inside the chamber at 500 mbar, cause by the relatively small mean free path (compared to the 1 mbar annealing case, see section 5.9.2). Furthermore, it seems that the SnS incorporation is much quicker than its diffusion across the sample, as the steepness of the gradient implies. After 5 min of annealing, the Sn content in position 5 mm finally starts to increase also, and it takes up until 30 min until no tin gradient is observed any more, with a

Sn/(Cu + Zn) ratio of around 0.34. This result correlates well with the findings of Figure 5-14 and it suggests that at 500 mbar the annealing time should at least be 30 min, in order to incorporate tin homogeneously and stoichiometrically. As mentioned, the reason for this is due to the slow diffusion (the short mean free path) of SnS(g) at 500 mbar.

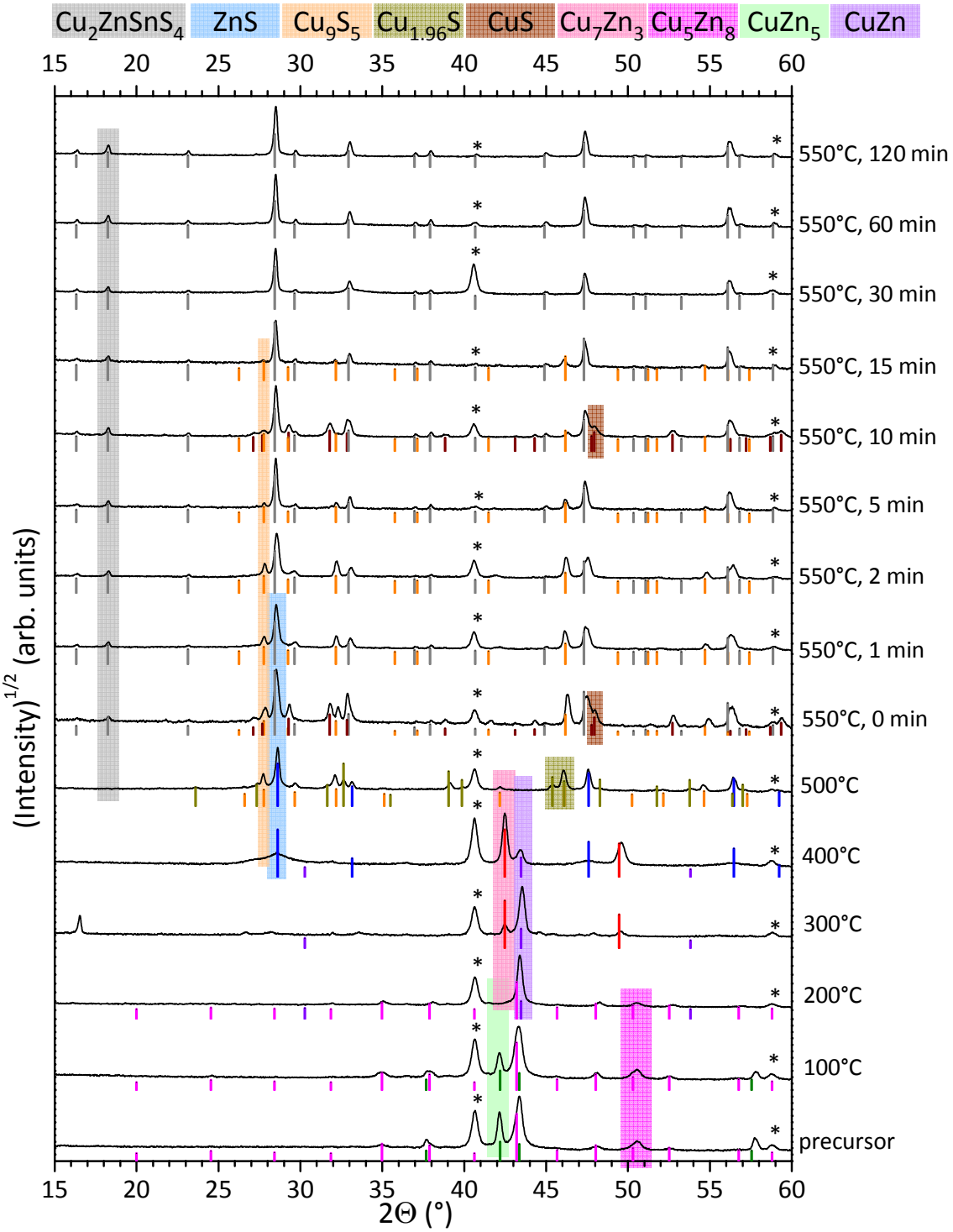

Figure 5-16 GIXRD patterns obtained from samples Q1 to Q15 (bottom to top). The short vertical lines indicate the peak positions of phases present in the respective sample, where grey stands for CZTS (JCPDS: 01-075-4122), blue for ZnS (JCPDS: 04-001-6857), brown for CuS (JCPDS: 00-006-0464), orange for Cu_9S_5 (JCPDS: 00-047-1748, 00-023-0962), dark yellow for $Cu_{1.96}S$ (JCPDS: 04-007-1751), violet for CuZn (JCPDS: 00-002-1231), red for Cu_7Zn_3 (JCPDS: 04-006-262), pink for Cu_5Zn_8 (JCPDS: 00-025-1228) and green for $CuZn_5$ (JCPDS: 00-035-1152) [23]. The peaks marked with "*" indicate a Mo phase (JCPDS: 04-001-0059). The color-coded areas represent the areas of interest of unique peaks of a respective phase. Hereby, the color code is the same as for the vertical lines.

Phase analysis

Figure 5-16 contains the GIXRD patterns obtained from the respective samples Q1 to Q15 (bottom to top). The small vertical lines indicate the presence of certain phases (see Figure caption for color-code) and the rectangular colored regions indicate a change in the amount of a certain phase in the sample. Hereby, care was taken that only unique peaks (not necessarily the strongest ones) of a given phase were considered. In order to facilitate to follow the consecutive phase change, a bar chart is given in Figure 5-17 which shows the presence of the individual phases with respect to annealing temperature and time. The color code of the respective phases corresponds to that of the rectangular areas shown in Figure 5-16. It shall be noted that the given bars start and end in between temperature and time steps, which indicates that these phases start to appear or disappear at some point between the respective steps.

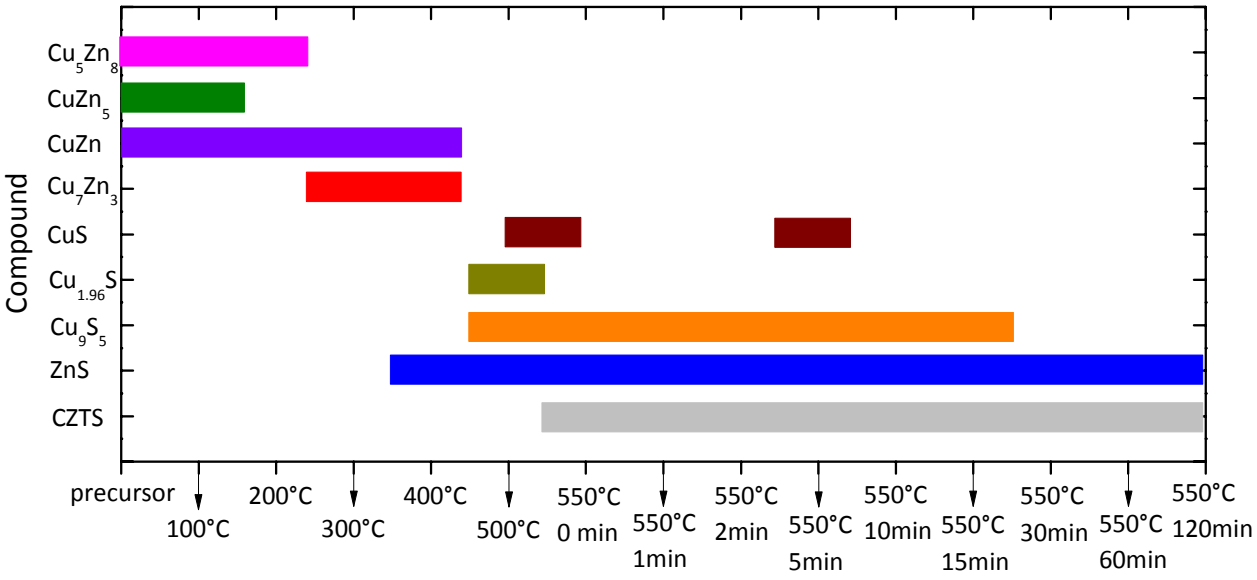

Figure 5-17 The presence of the individual phases with respect to the annealing temperature and time. The color code of the respective phases corresponds to that of the rectangular areas shown in Figure 5-16. It shall be noted that the given bars start and end in between temperature and time steps, which indicates that these phases start to appear or disappear at some point between the respective steps.

From both of the Figures, one can see that below 300 °C only phases are present that correspond to some sort of Cu-Zn alloy. At first, this might slightly contradict the finding of the EDX measurements, where the sulfur incorporation started around 200 °C, however, the amount of sulfur incorporated at 200 °C is so small that the amount of a corresponding phase might not be detectable with XRD, yet. While at 300 °C zinc rich phases of the Cu-Zn alloys have disappeared, copper rich phases of the Cu-Zn alloy have appeared, initiating the formation of ZnS. Between 400 and 500°C, the $Cu_{2-x}S$ formation starts with the formation of Cu_9S_5 and $Cu_{1.96}S$. The order of formation of the sulfide phases (ZnS before $Cu_{2-x}S$) is well in accordance with what is expected from the Ellignham diagram, shown in Figure 4-8. At 500 °C, there is no sign of a Cu-Zn alloy phase left, while the signal of ZnS clearly stands out. At the same time, diffraction peaks from Cu_9S_5 and $Cu_{1.96}S$ phases are also present. This behavior is in good agreement with the steep increase in sulfur content between 400 and 500 °C, as seen in Figure 5-14. At 550 °C and 0 min annealing time, the first appearance of the unique CZTS peak at around 18 ° is observed. Since the main peaks of ZnS overlap with those of CZTS, no conclusion on the presence of ZnS can be drawn with confidence only based on the XRD results. The presence of ZnS, however, is fairly likely at this point, as the composition reveals that not much tin is

incorporated at this point yet. Furthermore, the presence of Cu-S phases gives an indirect indication that the formation of CZTS has not yet used up all ZnS and Cu-S yet. This assumption also holds for the samples that were annealed between 1 min and 15 min, as Cu-S phases are present side by side with CZTS. At 30 min of annealing (and for longer annealing times), there are finally no peaks left that can be attributed to a Cu-S phase. In addition, compositional analysis reveals a steady state for the compositional ratios, indicating that the incorporation of sulfur and tin sulfide is finished. Hence, one could conclude that there might not be additional ZnS left, however according to chapter 4, the presence of minor amounts of ZnS is still possible. Similar to this, the presence of minor Cu-S phases which are not detectable by XRD any more is also still possible. Between 30 min and 120 min of annealing, the XRD patterns do not show any significant changes any more. This is in good agreement with the average compositional analysis of the samples, which showed a steady state of the amounts of sulfur and tin from 30 min of annealing onwards. It also relates nicely to the spatially resolved EDX measurement. Altogether, the XRD results support the conclusions that a Mo/Cu/Zn precursor has to be annealed at least for 30 min at 500 mbar forming gas, in order to homogeneously and stoichiometrically form CZTS.

In order to study the phase formation processes in more detail, AES depth profiles were obtained between the measuring points 2.5 and 5 mm (see Figure 5-15). Figure 5-18 shows the normalized profiles of relevant samples. In profile (a) it can be seen that already at 200 °C, sulfur is introduced to the surface of the sample. This agrees with the EDX result, where a slight increase in the sulfur content has been observed already at 200 °C. It also shows the problem of detecting small amounts of minority phases with XRD. Furthermore, one can see that at the surface of the sample, where the sulfur is located, the signal of copper drops while that of zinc is slightly increasing. This indicates that ZnS is formed at the surface of the layer, leaving the copper back in the bulk. This is in accordance with Figure 4-8 that suggests the formation reaction of ZnS to take place at far lower partial pressures of S_2, than necessary for $Cu_{2-x}S$. At 400 °C (profile (b)), where even more sulfur has been incorporated; only Zn and S are detected at the surface while Cu is at the back of the film without any S. This is an even clearer sign for the formation of ZnS at the front before $Cu_{2-x}S$ forms. All these results are in accordance with the results from EDX and XRD measurements. At 500 °C (profile (c)), where XRD showed the first sign of a $Cu_{2-x}S$ phase, the sulfur content is finally distributed over the whole depth of the layer. At 550 °C and 0 min (profile (d)), AES also detects the first traces of Sn inside the film, as previously seen from the EDX and XRD results. At that temperature and time, the ZnS phase has been pushed to the back of the film, while $Cu_{2-x}S$ is distributed throughout the whole depth of the film. This order begins to change again for an increasing amount of Sn being incorporated after 5 or 10 min of annealing (profiles (e), (f)). From those depth profiles, it can be seen that at the surface of the layer, the Sn signal begins to follow that of Cu, indicating that either Cu_2SnS_3 or CZTS has been formed. Since however, no sign what so ever of the CTS phase has been found in this entire study, it is assumed that CZTS is formed. Bearing the results of chapter 4 in mind, this is however not an easy task to prove this. At the same time, where the Sn signal mostly follows that of Cu after 10 min of annealing, a fairly big bump in the zinc signal is observed at the back of the layer, indicating that there might be a ZnS phase at the back. Furthermore, the lack of Sn at the back, while having a Cu signal indicates the presence of a $Cu_{2-x}S$ phase at the back, too. After 30 min of annealing (profile (g)), where EDX results started to show a steady state, and where XRD did not show the presence of a Cu-S phase any more, the signals of Cu, Zn, Sn, and S are distributed more or less evenly down until two-thirds into the film, leaving slightly Sn and Zn rich signals at the back. This leads to the conclusion that until two-thirds down into

the film mainly CZTS is present. At the back of the film, the increase of the Zn signal indicates the presence of a ZnS phase. The increase of the Sn content at the back is not completely understood yet. The very late decrease of the sulfur signal, however, indicates the presence of a MoS_2 phase at the back contact. After 120 min of annealing (profile (h)), the overall distribution of the elements down until two thirds of the film is fairly even, indicating a majority CZTS phase. Behind this phase, a minority ZnS phase can be observed at the back. Again, the presence of the Sn signal at the back of the film is not completely understood at this point, but the late decrease of the sulfur signal indicates the presence of a MoS_2 phase at the back contact.

It shall be noted that the presence of CTS can neither be proven nor disproven with confidence at this point. Therefore, it was left out of the discussion.

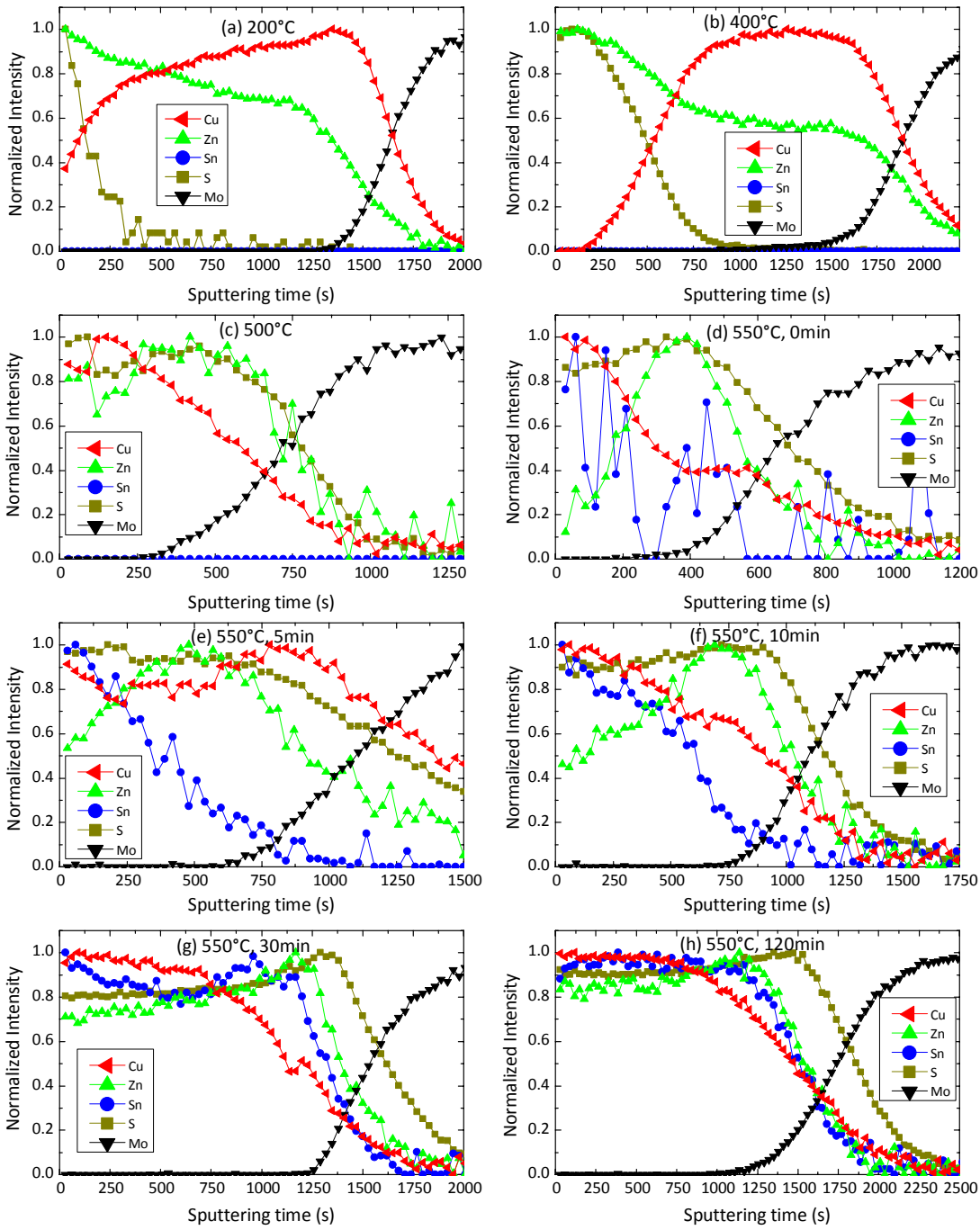

Figure 5-18 Normalized AES depth profiles of a selection of samples Q. The signal of each element was typically normalized to its maximum value. The various different sputtering times are related to different sputter conditions used.

In conclusion, all the results from XRD, EDX, and AES depth profiling correlate well. After 30 min of annealing, the tin has been incorporated uniformly over the whole area and thickness of the film and the averaged composition reaches a steady state. At the same point in time, XRD does not show a sign of a Cu-S phase any more, indicating that all available copper has reacted to form CZTS. Together with the results from the depth profiles, one can conclude that at 500 mbar, a Mo/Cu/Zn precursor must be annealed for at least 30 min in order to avoid many secondary phases. These results allow the description of a reaction pathway and of a formation model, as will be shown later in this section.

Morphology

Figure 5-19 shows SEM top view images of some relevant samples obtained from the measurement position at 5 mm. Figure part (a) shows the typical morphology for a Cu-Zn alloy. On this image, there is yet no sign for the incorporation of sulfur. On the image of the 400 °C step, one can clearly see the formation of a different phase. Relating this to the results of XRD, AES, and EDX, the forming phase can be related to ZnS. Figure part (c) shows the morphology of the mixed $Cu_{2-x}S$ and ZnS film, which looks very different than that of the Cu-Zn alloy. In this SEM image, micrometer large grains can be observed. The general shape of these grains do not change much in the case of the 550 °C (0 min) annealing, only the size becomes smaller. At this point during the annealing, the tin incorporation via the gas phase was observed. In the following process, the morphology changes severely at 5 min, 10 min, until 30 min of annealing at 550 °C. This transformation in morphology displays the growth of CZTS via the consumption of the ZnS(s) and Cu-S(s) under the incorporation of SnS(g) and sulfur from the gas phase. At 30 min of annealing, the morphology looks fairly compact with grains up to 3 μm in size. Between 30 and 120 min of annealing, no major changes in the morphology can be seen, only the overall grain size seems to increase slightly. This result correlates with the XRD, AES, and EDX results, indicating that the process of CZTS formation is completed after 30 min of annealing at 550 °C.

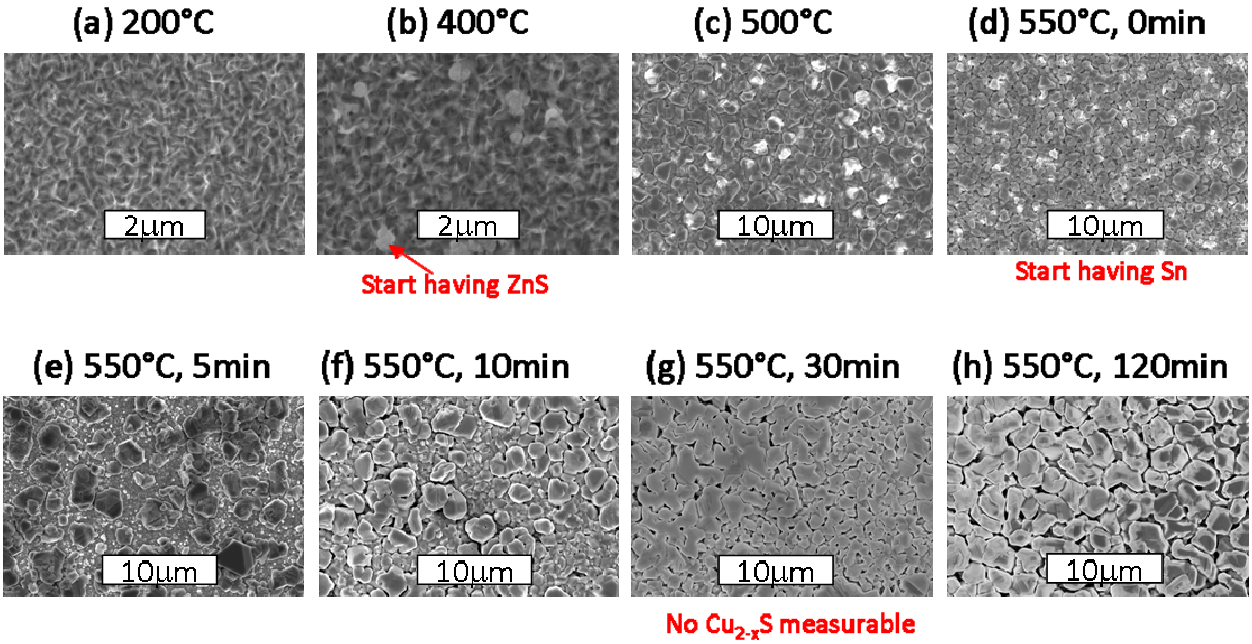

Figure 5-19 SEM top view images obtained on the respective measurement points at 5 mm.

Reaction pathway

From the previously discussed data, it is possible to formulate a reaction pathway for the formation of CZTS from a copper and zinc containing precursor during the annealing in a sulfur and tin sulfide environment.

For temperatures below 200 °C, the main occurring process is an alloy formation of the deposited Cu and Zn layers. This reaction can generally be formulated in the following way:

$$Cu(s) + Zn(s) \rightarrow Cu_x Zn_y(s)$$

Reaction 5-21

In the heat up from 200 to 400 °C, the first sulfur is incorporated, leading to the formation of ZnS, while the Cu-Zn alloy changes from Zn rich to Cu rich:

$$Cu_x Zn_y(s) + \tfrac{1}{2} S_2(g) \rightarrow Cu_x Zn_{y-1}(s) + ZnS(s)$$

Reaction 5-22

Between 400 and 500 °C, the Cu-Zn alloys completely decay, by the formation of ZnS and copper sulfides under the ongoing incorporation of sulfur from the gas phase:

$$2Cu_x Zn_y(s) + \tfrac{3}{2} S_2(g) \rightarrow Cu_{2-x} S(s) + 2ZnS(s)$$

Reaction 5-23

Above 500 °C, tin is incorporated into the film via the gas phase. In parallel, CZTS starts to form, using up ZnS(s) and $Cu_{2-x}S$(s) from the films and sulfur as well as tin sulfide from the gas phase. This process continues until 30 min of annealing at 550 °C, at which no evidence for a $Cu_{2-x}S$ phase in the film can be found any more. This leads to the following reaction pathway of the formation of CZTS during the annealing at 550 °C and 30 min:

$$2ZnS(s) + Cu_{2-x} S(s) + SnS(g) + \tfrac{1}{2} S_2(g) \rightarrow Cu_2 ZnSnS_4(s) + ZnS(s)$$

Reaction 5-24

It shall be noted that AES depth profiles revealed the presence of a Zn rich phase at the back of the films. This suggests that not all the ZnS has been used up, as indicated in Reaction 5-24 by the remaining ZnS on the right hand side. Altogether, the given reactions show that for this precursor type and at the given annealing conditions, a direct reaction from the binary sulfides to the CZTS phase seems to occur.

Figure 5-20 shows a schematic representation of the formation of CZTS from the Mo/Cu/Zn metallic precursor (see AES depth profile of precursor in Figure 3-18), as taken from the previously shown data. It is shown that between 200 and 400 °C, a ZnS phase starts to grow from the surface of the film into the bulk. While copper starts to react with sulfur until 500 °C, a columnar distribution of ZnS and $Cu_{2-x}S$ is assumed. Such an anti-correlated behavior has been observed from EDX mappings on pure ZnS and $Cu_{2-x}S$ samples, as shown in Figure 5-6 (c). While at 550 °C (0 min) AES depth profiles suggest the copper sulfides to be at the sample's surface, the first tin incorporation is seen, leading to the first CZTS phases which start to nucleate at the "quadruple point" of ZnS, Cu-S, and SnS(g) + S_2(g) at the surface. As mentioned previously, the presence of CTS can neither be proven nor disproven and is therefore not taken into account here. After longer annealing times at 550 °C, the CZTS phase grows down into the layer,

consuming the ZnS from below and $Cu_{2-x}S$ from the side. 30 min and longer into the annealing, the obtained data suggest the complete consumption of $Cu_{2-x}S$, leaving behind a CZTS grain with a ZnS core and small pinholes in between the individual grains, as shown in Figure 5-20 (h) and (i). The schematic representation of the formed grains in Figure 5-20 (i) look very much alike that observed from sample O, as the cross-sectional image in Figure 5-8 has shown. Unfortunately, it needs yet to be proven whether the grains of Figure 5-8 contain a ZnS core or not, as has been suggested in the presented model. A possible experiment to solve this question could be a TEM analysis.

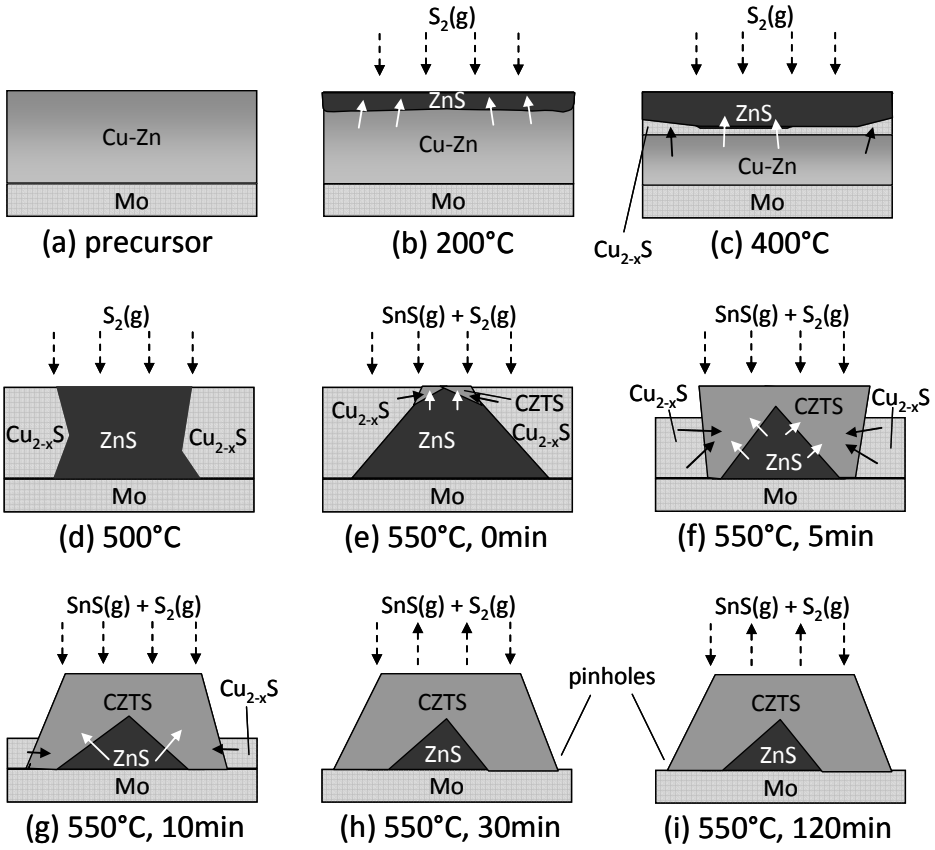

Figure 5-20 Schematic representation of the formation of CZTS grains by annealing a Mo/Cu/Zn metal stack in a sulfur and tin sulfide rich environment. The white arrows indicate the movement of Zn, the black ones that of Cu.

Free energy of formation

From the presented reaction pathway to form CZTS, it could be seen that the general reaction can be simplified to:

$$Cu_2S(s) + ZnS(s) + SnS(g) + \tfrac{1}{2}S_2(g) \leftrightarrow Cu_2ZnSnS_4$$

Reaction 5-25

This reaction is assumed to be in equilibrium. A rough estimate of the Gibbs free energy of formation of CZTS ΔG_{CZTS} at 550 °C can be made, in a similar manner as it was done in section 4.11 for the Cu_2SnS_3 phase. According to section 4.3.2, the equilibrium constant K_{eqm}^{CZTS} for this reaction is given by:

$$K_{eqm}^{CZTS} = \frac{(a_{CZTS})}{(a_{Cu_2S})(a_{ZnS})(a_{SnS})\sqrt{a_{S_2}}} = \frac{1}{(a_{SnS})\sqrt{a_{S_2}}} = \frac{1}{(\frac{p_{SnS}}{p^0})\sqrt{\frac{p_{S_2}}{p^0}}},$$

Equation 5-1

with $p^0 = 1$ bar. As discussed in section 4.11, the partial pressure of sulfur in a standard annealing has been estimated to be between 10^{-2} and 10^{-9} mbar, assuming that SnS_2 and Sn_2S_3 did not form initially. As discussed in section 5.8.2, the vapour pressure of SnS(g) during the annealing is saturated and lies around $3 \cdot 10^{-3}$ mbar. Assuming the partial pressure of SnS(g) to equal this value, the equilibrium constants can be estimated to lie between $1.1 \cdot 10^{8}$ to $3.3 \cdot 10^{11}$. Using the following equation, one can calculate ΔG_{CZTS} for both cases:

$$\Delta G_{CZTS} = -R \cdot T \cdot \ln(K_{eqm}^{CZTS})$$

Equation 5-2

with the gas constant R and the temperature T. For the reaction at 823 K (550 °C), $\Delta G_{CZTS}(550°C)$ is estimated to lie between -126 and -182 kJ/mol. Comparing these numbers to the ones obtained for CTS (-39 to -94 kJ/mol), it seems that CZTS is more likely to form than CTS under the used conditions.

5.9.2 Annealing in 1 mbar forming gas

In order to study the formation of CZTS under standard conditions but at 1 mbar of forming gas pressure, a similar study has been performed on samples R1 to R8 of the same precursor, as explained in section 5.4.2.

Composition

In the compositional study, summarized in Figure 5-21 (a) and (b), it can be seen that sulfur has been incorporated significantly up until 500 °C already, while the incorporation of significant amounts of tin into the layer occurs between 500 and 550 °C. Reaching 550 °C, it appears that the incorporation of sulfur and tin is clearly completed and has already reached a steady state. This result is different to the 500 mbar annealing where a steady state was reached after 30 min. An explanation for this can be found in the greater mean free path of SnS(g) and sulfur at 1 mbar and hence the much quicker diffusion.

The compositional results suggest the actual CZTS formation to be very quick. At 1 mbar background pressure, a long annealing seems un-necessary.

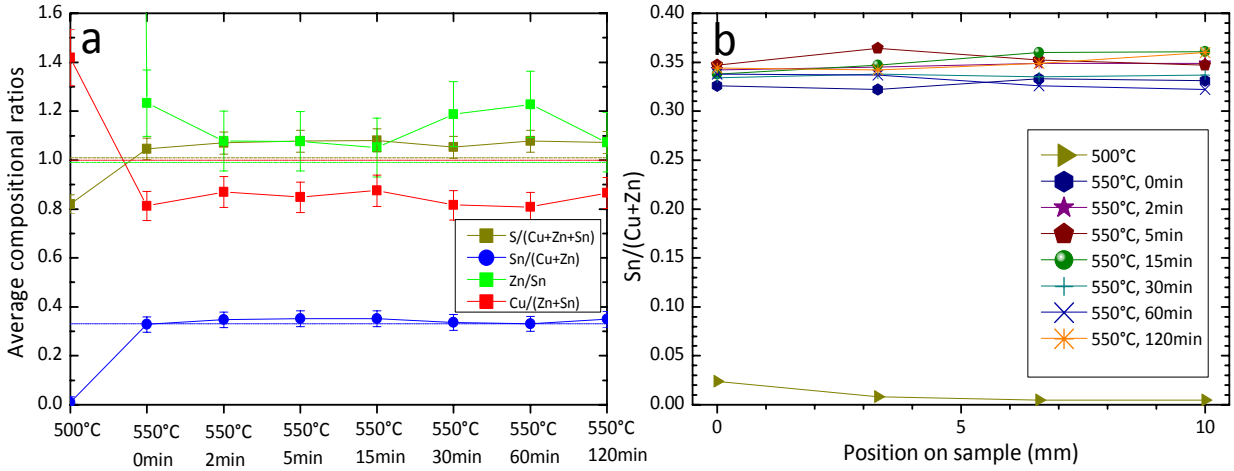

Figure 5-21 (a) Average compositional ratio of the samples R1 to R8. The dash-dotted horizontal lines represent the expected values of the respective ratios for stoichiometric Cu_2ZnSnS_4. (b) Spatially resolved compositional ratio of the samples R1 to R8. The error bars for Sn/(Cu + Zn) were deliberately excluded from the graph. Its value is Δ Sn/(Cu+Zn) = 0.05.

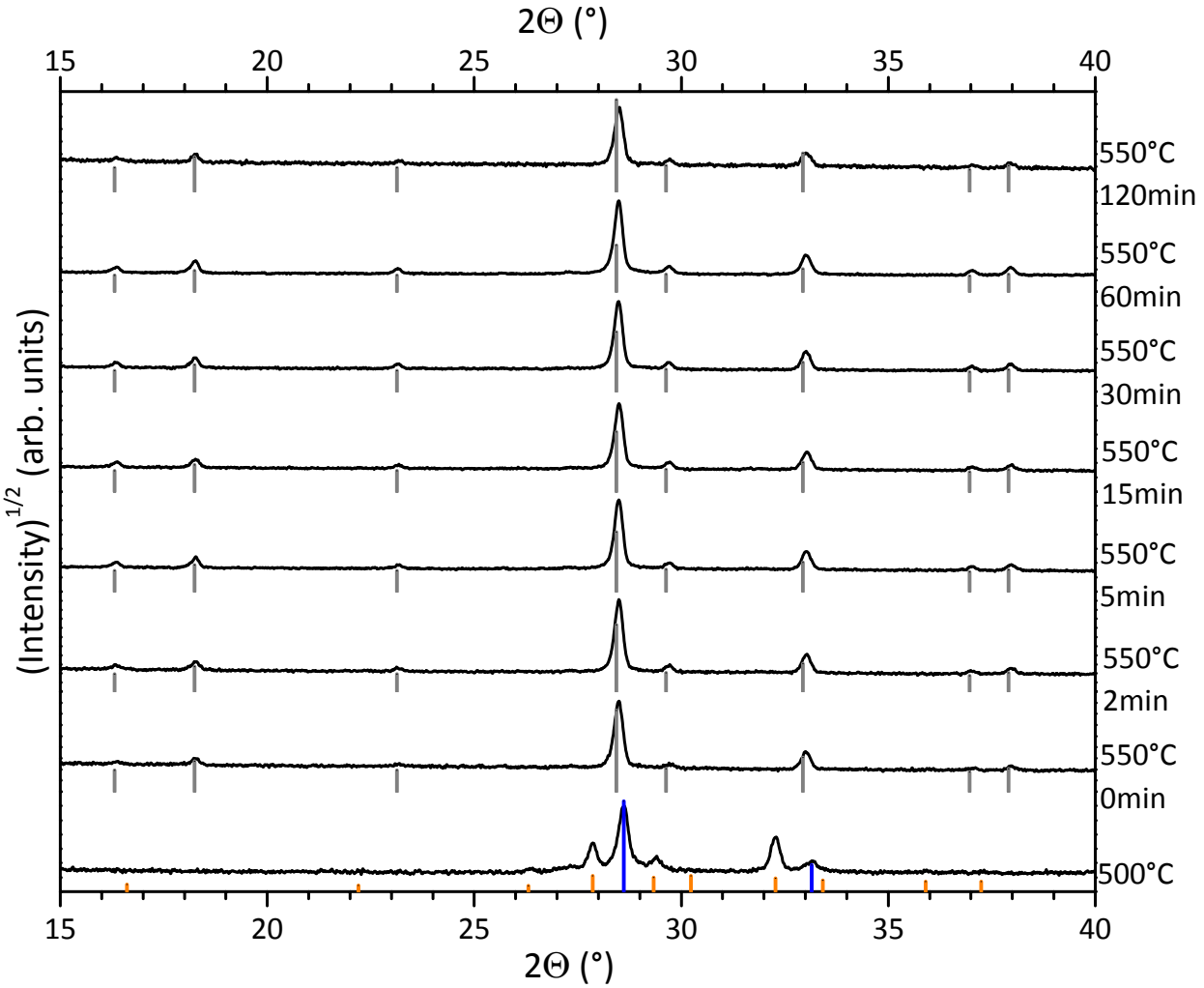

Figure 5-22 XRD patterns obtained from samples R1 to R8 (bottom to top). The short vertical lines indicate the peak positions of phases present in the respective sample, where grey stands for CZTS (JCPDS: 01-075-4122), blue for ZnS (JCPDS: 04-001-6857), and orange for Cu_9S_5 (JCPDS: 00-047-1748, 00-023-0962) [23].

Phase analysis and formation reaction

Figure 5-22 shows the measured XRD patterns from the different samples with respect to the annealing temperature and time. The sample annealed to 500 °C shows the presence of ZnS (blue vertical lines) and Cu_9S_5 (orange vertical lines) phases. Similar to the case at 500 mbar, there is not yet a sign of CZTS, suggesting that the phase formation up until this temperature is comparable to that obtained at 500 mbar. Between 500 and 550 °C (0 min), it appears that Cu_9S_5 is completely consumed together with solid ZnS and SnS(g) + S_2(g) to form CZTS. This can be seen in a small peak shift of the ZnS main peak at 28.6° to 28.5°. The complete reaction occurs much quicker than in the 500 mbar case, which suggests that at 500 mbar, the reaction was mainly controlled by the rate of arrival of SnS(g) and S_2(g), while at 1 mbar, both, the diffusion of S_2(g) and SnS(g), and the formation reaction itself are very quick. As a consequence, it is impossible to obtain a detailed reaction pathway from the presented results at 1 mbar. Due to the close relation of both presented systems, however, it can be assumed that the reaction pathway at 1 mbar is similar to that at 500 mbar. Therefore, the direct formation of CZTS from the binary sulfides is assumed.

Between zero and 120 min of annealing at 550 °C, no major changes in the XRD patterns can be observed. The peak position of the main CZTS peak remains at 28.5°. At the same time, the absence of minor ZnS or CTS phases cannot completely be assured (according to chapter 4). On the one hand, unchanged patterns imply that sufficient SnS(g) and S_2(g) has been present throughout the complete annealing time in order to avoid major loss of tin, on the other hand, the question arises whether a prolonged annealing time is necessary or harmful to form an optimal CZTS absorber layer for solar cells. This question will be dealt with in the upcoming section.

5.9.3 Influence of annealing conditions on solar cell efficiencies

After investigating the reaction pathway to form CZTS from a simplified precursor, the open question remains which annealing conditions lead to the most efficient solar cell devices. As some of the absorber layers partly peeled, either during the annealing or during a KCN etching, not all absorber layers could be processed to full devices. Unfortunately, except samples Q7 (500 °C), Q12 (550 °C, 15 min), and Q15 (550 °C, 120 min), all other samples of the 500 mbar annealing (partly) peeled. This made it difficult to form functional solar cells. In the case of the 1 mbar annealing, it was only samples R1 (500 °C), R2 (550 °C, 0 min), and R3 (550 °C, 2 min) that did peel during the KCN etching. All other ones could be processed to full devices.

Figure 5-23 shows the plot of the power conversion efficiency versus the annealing time at 1 mbar, as obtained from the standard IV measurement on cells of around 0.5 cm^2 active area (see section 2.9.1). One can see that the device efficiencies for absorbers annealed for 30 min and less gave values of around 1 %. The absorbers that were annealed for longer than 30 min, lead to power conversion efficiencies of basically 0 %. These results show that at 1 mbar, shorter annealing times are generally required to obtain good results.

From the few data shown in Figure 5-23, it is, however, hard to judge which annealing time is optimal at 1 mbar background pressure since at such low efficiencies the error is fairly large and not purely correlated to the annealing time and temperature. As the diffusion and incorporation of S_2(g) and SnS(g) is fairly quick, a long annealing, especially longer than 30 min, is not suggested. To determine the optimal annealing time, a further study would be necessary.

At 500 mbar, only three samples did not peel during the annealing or during KCN etching. The remaining samples were also processed to solar cells, and 0 % device efficiencies were obtained for all of them. The conclusion of this experiment is that at 500 mbar of background pressure,

the in-diffusion of SnS(g) is too slow which might cause stresses due to the Sn gradient and lead to peeling. In sample Q12, XRD measurements suggest the presence of copper sulfide phases, indicating that the reaction of CZTS is not complete at this point. At 120 min, the reaction seems complete, but the annealing time might have been too long, in terms of the possible formation of MoS_2 at the back contact, or other things. The real mechanism that makes a long annealing bad in the used system is yet not understood.

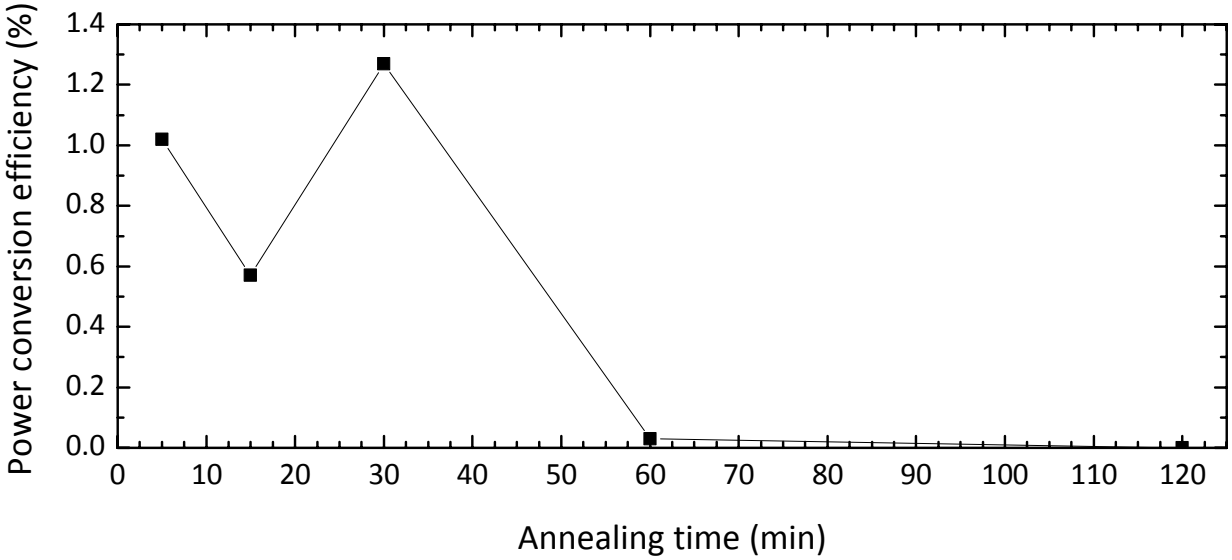

Figure 5-23 Power conversion efficiency of best solar cells obtained from absorber layers fabricated under 1 mbar forming gas at 550 °C with respect to the annealing time (samples R4 to R8).

Altogether, one must say that this novel strategy to form CZTS thin films from annealing a copper and zinc containing precursor in a sulfur and SnS(g) containing environment is probably not the best technique to obtain highly efficient solar cells, as the maximal obtained efficiency was 1.3 % only. The reason for this can be found in the reaction itself. As presented in the model, CZTS seems to grow from the top of the film down to the bottom, as SnS(g) is provided from the gas phase. Such a growth direction opens the possibility that certain un-desired phases might become "encapsulated" at the back of the film (see Figure 5-20). Furthermore, the reaction occurs such that empty spaces arise in between the large grains (see cross-section in Figure 5-8). Those holes are possible pathways for shunting currents.

Although this strategy is un-successful in terms of growing CZTS absorbers for high efficient solar cells, studying the reaction pathway of this novel approach was very useful to understand which requirements need to be met in order to form high efficient solar cells. A more detailed discussion on this topic can be found later in section 5.12.

5.10 Consequence: Stabilization of CZTS at the absorber/buffer interface

In section 5.7.2, possible consequences of the equilibrium reaction to form CZTS were listed. After consequence "3" has been studied in more detail, as shown previously, the attention shall now be drawn to consequence "1". There, it is hypothesized, that an annealing in the presence of sulfur and tin sulfide helps to stabilize the CZTS phase at the surface of the absorber. Furthermore, it is stated that by this novel annealing procedure, un-desired secondary phases (predominantly ZnS and $Cu_{2-x}S$) could be avoided by pushing the equilibrium point of the reaction (close) to the CZTS side. To prove this hypothesis, two identical precursors have been made and subsequently annealed in (a) only sulfur containing environment (process A), and (b) in the novel, sulfur **and** SnS(g) containing environment (process B). Furthermore, the respective

samples were analyzed with SEM/EDX, and were processed into solar cells. In order to prove the generality of the result, this experiment has been performed for PVD-based (section 5.10.1) as well as for ED-based (section 5.10.2) precursors. The reader is referred to section 5.5 for details of the fabrication and annealing for the samples S and T.

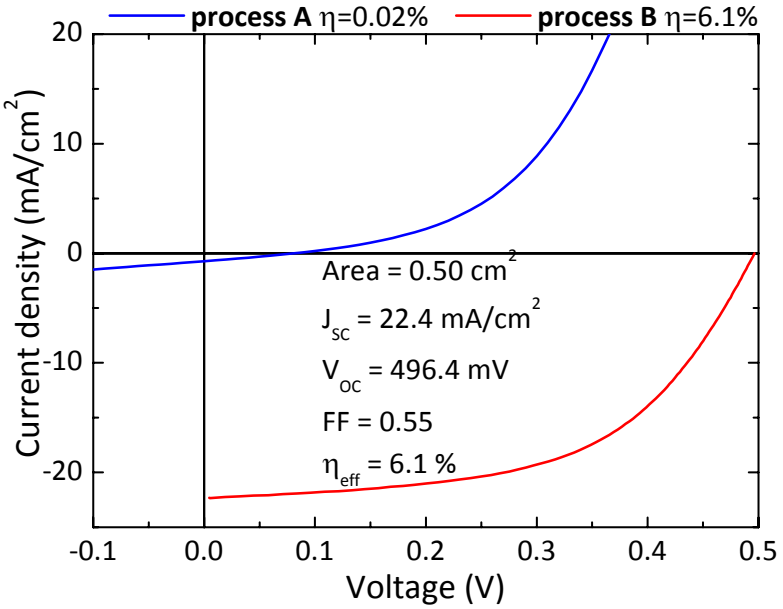

Figure 5-24 Current-voltage characteristics of samples S1 (process A) and S2 (process B) under illumination. Process A (blue): Annealing in sulfur only; Process B (red): Annealing in sulfur and SnS(g). The red curve was certified by Fraunhofer ISE.

5.10.1 Experiment with a PVD-based precursor

In order to demonstrate that it is crucial for the performance of a solar cell to stabilize the CZTS phase at the absorber/buffer interface, possibly by avoiding even small amounts of secondary phases, two precursors were formed alike by co-evaporating Cu, Zn, Sn, and Se onto a Mo substrate. One sample (S1) was annealed in the presence of only sulfur (process A), and the other one was annealed in a sulfur **and** SnS(g) containing environment (process B).

Figure 5-24 shows the JV curves under illumination for both samples (0.5 cm^2 active area). While the sample of process A shows a power conversion efficiency of 0.02 % (J_{SC} = 0.72 mA/cm^2, V_{OC} = 80 mV), the one annealed in process B was much more efficient with 6.1 %, as certified by Fraunhofer ISE (J_{SC} = -22.4 mA/cm^2, V_{OC} = 497 mV), at that time the European record.

The physicochemical reason for this difference can be found in the equilibrium reaction, discussed in section 5.7. While in process A, the desorption of S_2(g) and SnS(g) shifts the equilibrium point of the reaction further towards the ZnS + $Cu_{2-x}S$ side of the reaction, more and more ZnS and $Cu_{2-x}S$ phases might accumulate at the surface of the absorber layer. Although, KCN etching could remove the Cu-S phases before the window layers were deposited, the ZnS phases would still remain at the absorber/buffer interface, influencing the pn-junction in a negative way, for example by the creation a a too large spike. Figure 5-25 (a) shows an SEM image of the surface of the absorber layer as taken after the annealing step and before KCN etching. One can see that at least two different morphologies are present; area with large, dark grains of several micrometer in diameter, and areas with small and brighter grains. In contrast to this result stands that of the sample obtained from process B. While in process B, the sample is annealed in a sulfur **and** SnS(g) containing environment, the equilibrium point of Reaction 5-20 is being pushed towards the CZTS side. As a consequence, less or even no ZnS and Cu-S

phases might be present on the surface. In this case, the pn-junction is not influenced by undesired phases, leading to a better solar cell performance. Looking at Figure 5-25 (b), one can see that the morphology of the CZTS absorber layer is far more homogeneous than in Figure (a), with only large grains remaining, indicating that small amounts of secondary ZnS or Cu-S phases might haven been avoided. Another explanation for the difference in efficiency for these two processes could be, that the evaporation of SnS(g) causes Sn vacancies in the surface near region of CZTS which could influence the band alignment. For this hypothesis, however, there is yet no evidence.

The average compositional ratios of sample S2 (process B) was measured to be Cu/(Zn + Sn) = 0.9 and Zn/Sn = 1.1, which lies in the high performance region for CZTSSe devices, as shown in Figure 5-1.

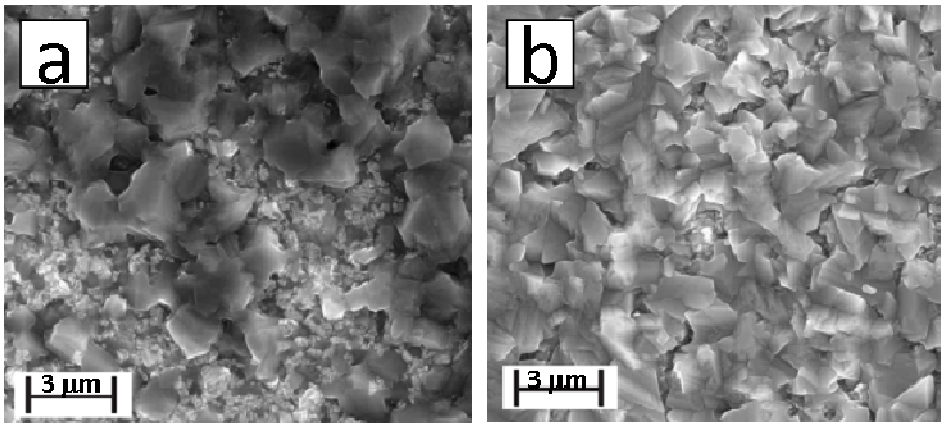

Figure 5-25 SEM top view images of samples (a) S1 (process A), and (b) S2 (process B) after annealing.

5.10.2 Experiment with an ED-based precursor

To show the generality of the result discussed for the PVD-based samples, two identical precursors have been fabricated by the electrodeposition of copper, tin, and zinc metal layers. Like in the previous case, one sample was annealed at standard conditions in only sulfur (process A), and the other one in a sulfur **and** SnS(g) containing environment (process B).

Figure 5-26 shows the current-voltage characteristics under illumination as measured for both samples (0.5 cm^2 total area). Like in the previous case, the sample from process A has a conversion efficiency of 0 %, while that of process B was far more efficient with 3.4 % (J_{SC} = -14.9 mA/cm^2, V_{OC} = 564 mV). It is assumed that the same reason applies as in the previous case, namely the insufficient SnS(g) vapour pressure in process A, that results in a decomposition of CZTS, shifting the equilibrium point of the equation further to the ZnS + $Cu_{2-x}S$ side of the reaction. The remaining secondary phases thus influence the pn-junction and hence the performance of the device. The SEM top view images of samples T1 (process A) and T2 (process B), shown in Figure 5-27 (a) and (b), respectively, again show a two-fold morphology of the sample of process A, while the morphology obtained from process B looks very uniform. Overall, the morphology obtained in the ED-based route, with small very small grains, looks very different to that obtained from the PVD-based precursor. This difference might have been cause be the difference in formation of the CZTS layer by the two formation pathways. While in the PVD case, the annealing step was mainly used to re-crystallize the elements, in the ED-based route, the annealing step was also meant to incorporate sulfur into the film. This can cause a difference in the CZTS formation reaction and might also be a reason for the difference in power conversion efficiency of the PVD-based solar cell compared to the ED-based device. In this context, it shall be noted furthermore that the power conversion efficiency of ED-based

devices might generally be limited by a typically higher number of impurities in the absorber film as compared to PVD-based absorbers.

From EDX analysis of the respective (etched) absorber layers, a Cu/(Zn + Sn) and a Zn/Sn ratio of 0.8 and 1.2 for sample T2 (process B), and of 0.7 and 1.4 for sample T1 (process A), were obtained, respectively. These values indicate a lack of tin of sample T1 (process A) in comparison to sample T2 (process B), supporting the theory of a promoted decomposition of CZTS via the loss of tin in process A. Furthermore, the composition of sample T2 (process B) is similar to those those the high efficient devices, as shown in Figure 5-1.

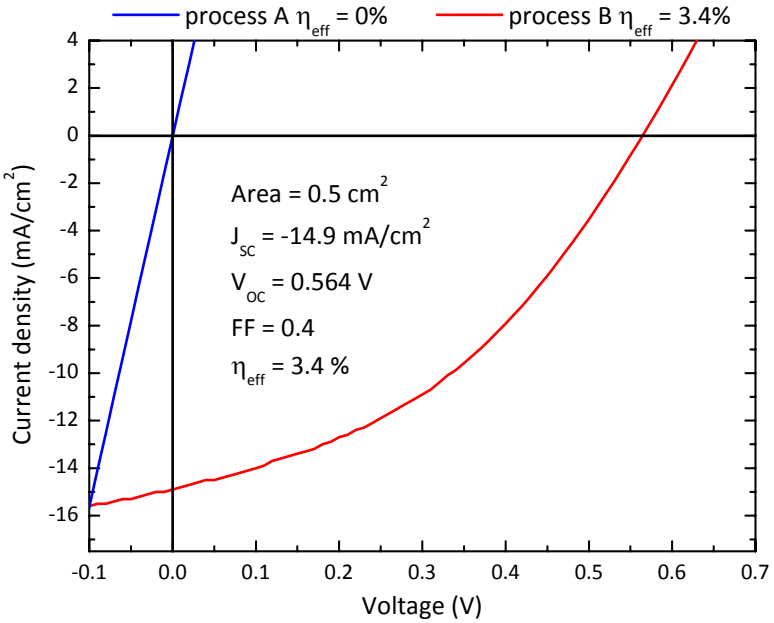

Figure 5-26 Current-voltage characteristics of samples T1 (process A) and T2 (process B) under illumination. Process A (blue): Annealing in sulfur only; Process B (red): Annealing in sulfur and SnS(g).

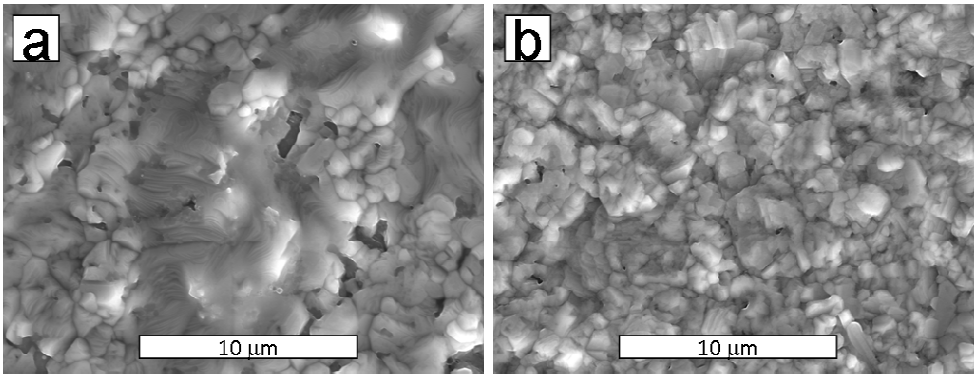

Figure 5-27 SEM top view images of samples (a) T1 (process A), and (b) T2 (process B) after annealing.

5.10.3 Conclusion

Independent of the primary techniques used to fabricate the precursors, independent on the configuration of both precursors (in terms of the present elements), and independent on a pure sulfur or mixed sulfur-selenide system, these experiments have proven that the novel strategy of annealing in the vicinity of sulfur **and** tin sulfide is a successful method to keep the equilibrium point of the CZTS formation and decomposition reaction (Reaction 5-20) on the CZTS side. As a direct consequence of this, tin loss can be reduced or even prevented, which stabilizes the CZTS phase at the absorber's surface. This seems to be one key to produce high efficient CZTS based solar cells.

5.11 Relation of these findings with respect to results from literature – A discussion

5.11.1 Possible explanations for the high efficiencies obtained by various techniques

In the studies shown in section 5.10, it could be seen that it is of high importance for the performance of a solar cell to push the equilibrium point of the formation reaction of CZTS (see Reaction 5-26) to the CZTS side.

$$Cu_2ZnSn(S,Se)_4(s) \leftrightarrow Cu_2(S,Se)(s) + Zn(S,Se)(s) + Sn(S,Se)(g) + \tfrac{1}{2}(S,Se)_2(g)$$

Reaction 5-26

In the presented cases, this adjustment of the equilibrium position was performed by providing sulfur (in the form of S_8, S_7, S_6, S_2 (see Figure 4-9 (b)), and some H_2 (due to the forming gas)) together with SnS(g) during the annealing process. The best CZTSSe-based solar cell obtained from this strategy showed an efficiency of 6.1 %, which was the highest value obtained within Europe at that time. Similar to this, the best performing ED-based sulfide CZTS showed efficiencies of 3.4 % which is just as well performing as the overall record device for electrodeposited CZTS solar cells, according to Ennaoui et al. [43]. In this work, the addition of SnS(g) to the annealing atmosphere was the key to keep the equilibrium at the CZTSSe side. The question arising is whether one can explain the good results that other groups obtained (without using SnS(g) in their annealing step) with the argument of tuning the point of equilibrium towards the CZTS side. Furthermore, the question is: Why did they not observe tin loss?

The record device fabricated by IBM is a mixed sulfur-selenide CZTSSe with 10.1 % efficiency [14]. Precursor layers including all elements (Cu, Zn, Sn, S, and Se) are spin coated from a hydrazine solution onto the substrate and subsequently annealed for a short time of 5 min on a hot plate under atmospheric pressure in the presence of sulfur. As all elements are already in the layer, the material only needs to be dried and re-crystallized. The key to prevent tin loss and to keep the equilibrium point at the CZTSSe side in their process is manifold: First of all, a high excess of chalcogen is already inside the precursor layer which desorbs upon annealing before CZTS is decomposed; a second reason can be found in the short annealing time of 5 min, which does not allow much tin loss; and thirdly, the annealing occurs at atmospheric pressure which also hinders evaporating species from travelling far, which keeps the partial pressure of the desorbing species in the vicinity of the sample high.

The record efficiency of pure sulfide CZTS of Katagiri et al. is produced from a vacuum deposited precursor via the annealing in a flow of 20 vol% H_2S (see Table 5-1) [13]. Although long annealing times of several hours were applied, loss of tin has not been reported. In this case, the key mechanism is assumed to be the presence of H_2S gas. Due to the constant supply of this highly reactive gas, the partial pressure of sulfur was probably high enough in order to significantly slow down or even stop the decomposition reaction of CZTS.

In the work of Gou et al. (7.2 % efficient CZTSSe device), CZTSSe nano-crystals are being sintered in a selenium environment [171]. In their approach, an excess of tin is introduced into the CZTSSe nano-crystals. Upon sintering, SnSe is lost and that way the equilibrium point of the reaction moves via the CZTSSe side in the direction of $Cu_{2-x}S + ZnS$. Annealing for the right period of time lets the equilibrium point stop at or near the CZTSSe side of the reaction.

A similar approach is used by Schubert et al. (4.1 % efficient CZTS device) [168]. A fast co-evaporation is used to limit the losses of SnS, and hence to keep the equilibrium point close to

CZTS. In their case, the rate of decomposition is mainly determined by the surface temperature. Increasing the metal fluxes at a constant rate limits the losses and the occurrence of secondary phases.

A fast post annealing routine at atmospheric pressures seems also the key for Wang et al. in order to avoid tin loss from their co-evaporated precursors (6.8 % efficient CZTS device) [92].

Ennaoui et al. obtained their 3.4 % efficient device from an annealing in reactive H_2S gas [43]. Although the overall annealing time with 2 hours is fairly long, the reactive gas at atmospheric pressure was probably the key to keep the equilibrium point close to the CZTS side of the reaction.

The conclusion of this comparison to literature is that the key principle to avoid tin loss and to obtain highly efficient solar cells is to make sure that the point of equilibrium of the reaction formation is at or close to the CZT(S,Se) side of the reaction. From the results of the present work, it is probably easiest to provide high enough vapour pressures of chalcogen together with that of Sn(S,Se) during the annealing step, as proposed in this work.

5.11.2 Addendum of a recent publication with respect to the decomposition reaction

Close to submission of the present thesis, Scragg et al. published new thoughts and results on the decomposition reaction of CZTS [129], which was founded on the results presented in this thesis [18]. In their work, they have a more detailed look into the reaction pathway of tin loss, suggesting a two stage decomposition reaction as follows:

(1) $$Cu_2ZnSn^{IV}S_4(s) \leftrightarrow Cu_2S(s) + ZnS(s) + Sn^{II}S(s) + \tfrac{1}{2}S_2(g)$$

Reaction 5-27

(2) $$Sn^{II}S(s) \leftrightarrow Sn^{II}S(g)$$

Reaction 5-28

At first, CZTS decomposes into solid binary sulfide, under the evaporation of $S_2(g)$, before the evaporation of SnS(g) occurs. From this two step model, it appears to be possible to keep the equilibrium point of Reaction 5-27 at the left side by providing high enough vapour pressures of S_2. However, as the equilibrium is “dynamic”, meaning that forward and back reactions still proceed continually, decomposition events are always occurring at a certain rate. As a consequence, SnS(s) molecules adsorbed to the CZTS surface are constantly being created and consumed again, hence their lifetime at the surface is nonzero, which allows an evaporation of SnS(g) to take place. If the evaporated SnS(g) molecules are not replaced (e.g. when only annealing with sulfur), then the decomposition of CZTS can never be completely reversed. Therefore, using their more detailed model, Scragg et al. come to the same conclusion as already suggested from the results of this thesis, that the decomposition of CZTS via the evaporation of sulfur and SnS(g) can only be reversed by supplying sulfur and SnS(g) during the annealing step.

Furthermore, Scragg et al. performed decomposition studies as a function of $S_2(g)$ and SnS(g) partial pressures during the annealing step. From their results and under the use of their suggested model, they conclude that the following two criteria must be fulfilled in order to achieve stable CZTS surfaces during an annealing step:

(a) The sulfur partial pressure should be greater than $(2.3 \pm 0.7) \cdot 10^{-4}$ mbar.

(b) The product of partial pressures $p_{SnS}\sqrt{p_{S_2}}$ should be greater than $(3.8 \pm 1.2) \cdot 10^{-5}$ $mbar^{3/2}$.

Using their experimental data, they also estimated $\Delta G_{CZTS}(550°C)$ to be around -22 kJ/mol. This number is far less negative than that obtained in this work (between -126 and -182 kJ/mol).

5.12 The way towards absorbers for high efficient CZTSSe-based solar cells – A general discussion

Looking at the various approaches that were leading to high efficient CZTSSe-based solar cells a few of requirements can be extracted that are necessary to produce absorbers for well performing devices.

The first thing to mention is the appropriate choice of the annealing conditions, as being the main outcome of this work. Within this chapter, especially in the previous section, several issues and "consequences" related to the annealing conditions have been proposed to point out the importance of keeping the equilibrium position of the formation/decomposition reaction (Reaction 5-26) on the CZTS side. In order to achieve this, the annealing conditions, such as the temperature, pressure, S/Se and SnS/Se sources, etc. have to be chosen appropriately. In each case, such appropriate conditions strongy depend on the used annealing equipment/setup, such as the annealing chamber size, cold/heated walls, etc. and can differ from one system to another. Generally, however, one needs to tune the annealing system in a way to make sure that the equilibrium of the formation reaction stay on the CZTS side.

There are, however, other requirements that should be fulfilled as well. By looking at the formation process that lead to record devices (see section 5.1), it is obvious that in all cases, the precursor layers already contained all elements, **including** the chalcogen. For such a precursor, the annealing is mainly necessary in order to re-crystallize/organize the elements, forming CZTSSe. As an example, the 6.1 % device obtained in this work through the annealing of a Cu-Zn-Sn-Se containing precursor can be named. Looking at studies, where fewer elements were present in the precursor [43, 49], such as also the 3.4 % device obtained in this work through the annealing of a Cu-Zn-Sn containing precursor, or for example the 1.3 % device obtained in this work through the annealing of an only Cu-Zn containing precursor, one can see that a general trend to lower efficiencies is observed the fewer elements were originally present in the precursor. Of course, this comparison is not completely valid, as samples from electrodeposited and vapour-deposited precursors, as well as pure sulfide and mixed sulfur-selenide CZTSSe samples are directly compared, but looking at this trend from a more thermodynamic and kinetic point of view, it must be kept in mind that a subsequent introduction of an element, such as sulfur or selenium, typically follows the laws of thermodynamics and kinetics which typically suggest a more complex reaction pathway via the binary sulfides, as ZnS, for example, forms much earlier than $Cu_{2-x}S$, according to Figure 4-8. As a consequence, phase segregation is possible. In the contrary, annealing a precursor that already contains all elements might lead to a direct formation of CZTSSe without the detour via the binaries or even the ternary phases, possibly avoiding the separation of phases. That way, short annealing times would theoretically also be possible which minimize a potential decomposition of CZTSSe and also the time for un-desired secondary phases to from.

Another requirement seems to be necessary in order to fabricate highly efficient solar cells. By looking at Figure 5-1, published by Katagiri et al. [165], one can see that the composition of the absorber layers with the highest efficiencies lie in a sector of Zn/Sn ≈ 1.2 and Cu/(Zn + Sn) ≈ 0.9,

i.e. zinc rich and slightly copper poor. Plotting this composition into the pseudo-ternary phase diagram suggested by Olekseyuk et al. [15], as shown in Figure 5-28, in can be seen that ZnS must be expected, unless the zinc rich and slightly copper poor behavior comes from Zn-doped CZTSSe film, where additional Zn atoms sit on Cu vacant positions. This latter case would imply that the existence region of CZTS is in fact larger than shown by Olekseyuk et al. [15]. Since the presence of secondary phases (e.g. ZnS) are generally assumed to have a negative influence of the performance of a device (independent on their position), it is imagined that such a Zn-doped CZTSSe could be favorable for high efficiencies. Investigating this issue would be very interesting. Due to the similar iso-electronic behaviour of Cu and Zn, neutron scattering experiments would be necessary.

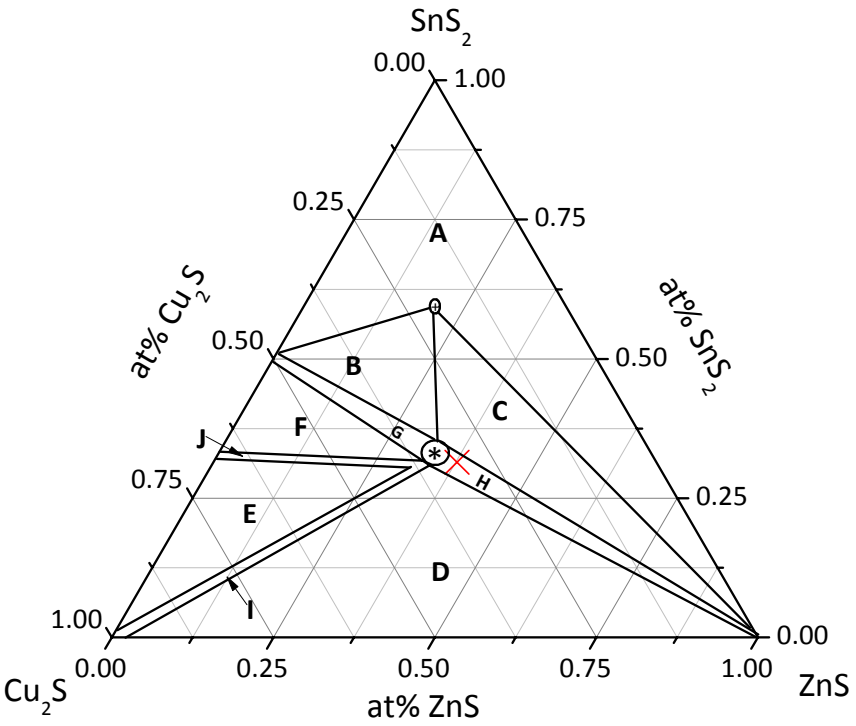

Figure 5-28 Pseudo-ternary phase diagram of the Cu-Zn-Sn-S system at 400 °C according to [15]. The indicated regions contain the following phases: "*" Cu_2ZnSnS_4 (α); "+" $Cu_2ZnSn_3S_8$ (β); "A" β+SnS_2+Cu_2SnS_3+ZnS; "B" α+Cu_2SnS_3+β; "C" α+ZnS+β; "D" α+Cu_2S+ZnS; "E" α+Cu_4SnS_4+Cu_2S; "F" α+Cu_4SnS_4+Cu_2SnS_3; "G" α+Cu_2SnS_3; "H" α+ZnS; "I" α+Cu_2S; "J" α+Cu_4SnS_4. The red cross indicates the position of the "optimal" compositional ratio of Zn/Sn = 1.2, and Cu/(Zn + Sn) = 0.9.

Conclusions

$$Cu_2ZnSn(S,Se)_4(s) \leftrightarrow Cu_2(S,Se)(s) + Zn(S,Se)(s) + Sn(S,Se)(g) + \tfrac{1}{2}(S,Se)_2(g)$$

Reaction 5-29

The goal of this section was to find a way to grow absorber layers for high quality CZTS thin film solar cells by avoiding secondary phases (at the surface of the absorber). Hereby, the attention was drawn to the decomposition reaction of CZTS, as introduced by Weber et al. [141]. In the present work, it could be proven that this reaction is in fact a reversible reaction (as shown in Reaction 5-29) and that it reaches a certain point of equilibrium depending on the applied annealing conditions. In a first experiment, it was shown that this point of equilibrium can be tuned between both extremes by either supplying or denying sufficient SnS(g) **and** S_2(g) in the presence of the sample.

As a first consequence of this finding, a novel strategy to fabricate CZTS from a simplified precursor has been introduced. In an initial experiment, it was shown that a CZTS containing thin film could successfully be grown from a tin free metal stack (Mo/Cu/Zn) by the annealing in a SnS(g) and sulfur rich environment. Hereby, it was found that SnS(g) incorporates itself via the gas phase and in a self-limiting manner, with the composition of Cu_2ZnSnS_4 being the limit for Cu poor samples. To investigate the reaction pathway, and to model the CZTS formation via this novel route, ex-situ XRD analysis in combination with AES depth profiling has been performed on samples annealed under 1 and 500 mbar of background pressure. For the 500 mbar annealing, the formed film appears to be in a steady state after around 30 min of annealing, while for a 1 mbar annealing, this steady is already reached after around 5 min. This difference has been explained by the difference in diffusion of SnS(g) and S_2(g) from their source to the sample. The actual incorporation of tin and sulfur into the film and hence the formation of CZTS, however, appear to be fairly quick. From samples annealed at 500 mbar, no measurable power conversion efficiency could be obtained, mostly due to partial peeling of the absorber layer after annealing or etching. In the case of 1 mbar annealing, fewer samples peeled and solar cell efficiencies of 0.6 to 1.3 % were obtained for samples annealed for 30 min and less. This indicates that longer annealing times might not be favorable, as the growth of MoS_2 phases might be supported in long annealing times. From the obtained XRD and AES data, a CZTS formation model has been suggested which explains the observed morphology as well as the formation of a ZnS phase at the back of the film. Additionally, it shows the weakness of this novel approach, as the kesterite phase is assumed to grow from top to bottom of the thin film, causing secondary phases to be present. This temperature and time resolved study showed furthermore, that CZTS principally forms via the reaction of the binary sulfides via this novel strategy.

A second consequence of the reversibility of Reaction 5-29 is the fact that supplying sufficient SnS(g) and S_2(g) during the annealing helps to push the equilibrium point of the reaction towards the CZTS side. This is especially important in terms of fabricating high efficient solar cell. Annealing experiments performed on PVD as well as ED based precursor layers have proven that providing sufficient SnS(g) and sulfur during the annealing step prevents the loss of tin. As a result, the surface of the absorber is stabilized, possibly because fewer (or even no) ZnS and $Cu_{2-x}S$ phases are present or by avoiding highly defective CZTS, and higher power conversion efficiencies could be achieved. For electrodeposited precursors it was shown that the novelty of annealing in a tin rich environment improved solar cell efficiencies from 0 to

3.4 % (for sulfide CZTS), and in the case of PVD based precursors the improvement was even larger from 0 to 6.1 % efficient cells (for sulfur-selenide CZTSSe).

In a general discussion, the relevance of the equilibrium position of Reaction 5-29 with respect to the highly efficient solar cell results from literature was discussed. In this context, hypotheses were stated that give possible explanations for the good results of other groups. Hereby, three main annealing conditions were pointed out that might be responsible for keeping the equilibrium point of the reaction of the CZTS side:

1. The presence of highly reactive sulfur (S_2 or H_2S).
2. Short annealing times.
3. An overstoichiometric amount of Sn inside the precursor.

As suggested in this work, the annealing in the presence of sulfur **and** tin sulfide should be as a fourth point.

Finally, another discussion was initiated which deals with the requirements that ought to be given in order to obtain high efficient CZTS based solar cells. By the comparison of literature data and experimental results of this thesis, three main requirements appear to be important in order to reach high efficiencies. It appears to be important to provide all elements in a mixed form already in the precursor layer. Furthermore, the growth of Zn rich absorbers with a Zn/Sn ratio of 1.2 seems to be a second requirement, and as the outcome out this chapter, a third requirements appears to be the right choice of the annealing conditions, in order to keep the equilibrium point of Reaction 5-29 on the CZTS side.

6 Conclusions and future recommendations

6.1 Conclusions

The principle aim of this project was twofold: One focus was set to finding the right tool that can be used to identify secondary phases of the Cu-Zn-Sn-S system and to discern them from Cu_2ZnSnS_4 (chapter 4), and the second focus was set to find a way to grow absorber layers for high quality CZTS thin film solar cells by avoiding secondary phases (at the surface of the absorber) (chapter 5).

In order to study both parts of the project appropriately, at first, it was necessary to optimize the precursor electrodeposition in such a way that homogeneous and laterally uniform precursors of a desired elemental ratio could be deposited (chapter 3). In chapter 3, it was shown that the use of a rotating disc electrode enabled the deposition of macroscopically uniform Cu, Zn, and Sn layers by a mass transport controlled deposition. Hereby, relatively flat precursors of only 1 % standard deviation in uniformity over an area of 14 x 14 mm^2 could be produced which lead to annealed samples of similar uniformity (2.7 % standard deviation in uniformity). To be able to deposit desired elemental ratios, the deposition efficiencies of Cu on Mo, Sn on Cu, and Zn on Cu have been investigated. The results show that none of the depositions are perfect such that hydrogen evolution has to be considered in each deposition. Overall, the following deposition efficiencies have been found: 85 ± 6 % for Cu on Mo, 94 ± 3 % for Sn on Cu, 78 ± 1 % for Zn on Cu. In a further study, the time-dependent alloy formation of Cu/Zn and Cu/Sn stacks were investigated. XRD measurements have shown that around one week after deposition, the alloy formation slowed down drastically. This result is of importance when looking at the reaction mechanism of the formation of CZTS from a metallic precursor stack. To ensure comparable conditions of the precursors before annealing, all precursors have typically been kept under vacuum for around one week before further usage.

Chapter 4 dealt with the question which analytical tool is most optimal in order to identify secondary phases of the Cu-Zn-Sn-S system and in order to discern them from Cu_2ZnSnS_4 qualitatively and quantitatively. This study was separated into two parts: Firstly to answer the question whether XRD, Raman spectroscopy, and photoluminsecense would generally be able to identify and discern secondary phases from CZTS qualitatively and on the basis of individually grown samples; and secondly, to answer the question how well those tools are in discerning phases from a mixed sample qualitatively as well as quantitatively.

For the first study, individual samples of possible secondary phases (such as MoS_2, Cu-S (Cu_9S_5, $Cu_{31}S_{16}$), Sn-S (SnS, SnO, $Sn(SeO_3)_2$), ZnS, and monoclinic Cu_2SnS_3) were grown and compared in terms of their respective peak postion and intensity ratio (“fingerprints”) obtained from XRD, Raman spectroscopy, and photoluminescence. The following results were obtained:

1. Raman spectroscopy should be a suitable tool to discern all secondary phases from CZTS, as the main Raman modes of the possible secondary phases differ well enough from that of CZTS.
2. XRD should be suitable to discern all phases of the Cu-S and Sn-S system from CZTS, and that the presence of Cu_2ZnSnS_4 as well as monoclinic Cu_2SnS_3 should be predictable by the presence of the respective minor peaks, although their major peaks overlap. Since ZnS does not have such minor peaks and since all of its major

peaks also overlap with those of CTS and CZTS, its presence in a sample can never be excluded with confidence. Due to its slightly different peak position of the major peaks, a discrimination could be possible in a measurement series if the machine was properly aligned and if a monochromator was used.

3. PL spectra should only be suitable to discern CTS from CZTS, since ZnS, SnS, and $Cu_{2-x}S$ phases did not show a PL spectrum using a green excitation. The monoclinic CTS showed a peak at 0.95 eV and CZTS a peak at 1.3 eV.

These results have shown that especially Raman spectroscopy should be able to discern all secondary phases from CZTS, but also that XRD and PL can be helpful tools.

Since all measurements of the first study were performed on individual samples, where the respective measured signal was optimized to the respective phase, a second study was necessary in order to tell which of these tools can still discern the respective phases from CZTS when the measured signal of different phases overlap and hence directly compete. For this purpose, two samples with a deliberate Zn gradient were prepared to allow the access to CZTS and CTS rich as well as to CZTS and ZnS rich regions, in order to determine how much of a secondary CTS/ZnS phase can be discerned from CZTS by XRD, Raman spectroscopy, and PL, while both phases are present on the same sample. Studying several points on these samples, the following conclusions are drawn:

1. Using X-ray diffraction, Cu_2SnS_3 can only be discerned by its minor peak from CZTS if it makes up more than 28 % of the sample, while Rietveld refinement analysis, the change in FWHM, and the change in peak position does not help.
2. Using XRD, ZnS can only be discerned by Rietveld refinement analysis from CZTS if it makes up more than 7 % of the sample. The change in peak position helps to discern 90 % of ZnS from CZTS while a change in FWHM is not useful at all.
3. Single wavelength Raman spectroscopy (at green light excitation) is useful to discern more than 28 % of CTS from CZTS by looking at the peak shift of 290 cm^{-1} to 286 cm^{-1}, but it cannot be used to discern ZnS from CZTS. This conclusion, however, is only valid for a measurement series. A single measurement on a sample would be less clear to interpret due to the small change in the modal shift.
4. PL spectroscopy (at green excitation) is probably not the right tool to discern CTS or any other phase from CZTS, especially when the crystal quality of the secondary phases is poor.

In general, these results show that by the comparison of a single measurement with other (literature) data, it is impossible to detect small amounts of secondary phases by these techniques. Only when performing measurements in a compositional series, it is qualitatively possible to tell whether a phase is present, but only within the given limits. These results account for all three measurement techniques similarly.

In further experiments, it was shown that the use of multiple-wavelength Raman spectroscopy analysis could be helpful in terms of secondary phase identification. Hereby, it was pointed out that the sequential use of multiple excitation wavelengths which corresponds to the resonant Raman case of the respective phase could be applied in order to identify the presence of a phase. In a different study, the usefulness of AES depth profiling and EDX mapping could be pointed out. In experiments it was shown that EDX mapping can be used to resolve lateral

distributions of present phases, where AES depth profiling (similar to SIMS depth profiling) can be useful to resolve phases in-depth.

Finally, studies on the etching behavior as well as on the usefulness of the monoclinic Cu_2SnS_3 phase have been performed. In the former study it was shown that a 5 wt% aqueous KCN solution cannot be used to etch off monoclinic CTS from a sample. In the latter study, the suitability of the p-type Cu_2SnS_3 semiconductor for photovoltaic applications has been investigated and it was shown that this compound can be used as an absorber layer in a photovoltaic device. Hereby, the power conversion efficiency of the device presented was measured to be 0.54 %, which is a factor of five higher than what had been obtained with a Schottky based device before. An external quantum efficiency of less than 60 %, a small J_{SC} of 17.1 mA/cm^2, and a tiny R_{sh} of 23 $\Omega\,cm^2$ could be explained by a high number of pinholes in the absorber layer, leaving only 67.5 % of the sample surface to be covered by Cu_2SnS_3 grains. This suggests that a much higher EQE as well as power conversion efficiency should be achievable by a more densely packed absorber layer. Calculations of an effective EQE support this assumption.

Chapter 5 finally dealt with the questions of how to grow absorber layers for high quality CZTS thin film solar cells by avoiding secondary phases (at the surface of the absorber). As a key proint of this work, it could be proven that the following reaction is in fact reversible and not a purely decomposition reaction, as stated elsewhere [141]:

$$Cu_2ZnSn(S,Se)_4(s) \leftrightarrow Cu_2(S,Se)(s) + Zn(S,Se)(s) + Sn(S,Se)(g) + \tfrac{1}{2}(S,Se)_2(g)$$

Reaction 6-1

In two independent studies, with differently grown precursors, it could be shown that one requirement to obtain high efficient devices lies in the principle of keeping the equilibrium point of Reaction 6-1 on the CZTS side during the annealing of the precursor. In this work, it was suggested to anneal the precursors in a sulfur/selenium **and** Sn(S,Se)(g) rich environment, and not just in the vicinity of sulfur/selenium. This novel annealing strategy helped to obtain a 6.1 % efficient device (CZTSSe) from PVD-based precursors and a 3.4 % efficient device (CZTS) from electrodeposited precursors. In a comparative study, the annealing of equivalent precursors in the presence of only sulfur resulted in 0 % efficient devices, independent on the precursor's origin. An explanation for the difference of both annealing strategies lies in the different point of equilibrium of Reaction 6-1. While a sulfur **and** SnS(g) rich environment pushed the equilibrium point towards the left side of the reaction, avoiding the formation of secondary phases, the presence of only sulfur lead to a equilibrium point that was a bit further to the right, resulting in the presence of some secondary phases (ZnS and $Cu_{2-x}S$) or highly defective CZTS at the absorber/buffer interface. This has caused the difference in performance.

Apart from this requirement to obtain high efficient solar cell devices, two other requirements were stated by comparing the results from this work with pusblished results. In a discussion section, it was hypothesized that the annealing of Zn rich layers is necessary for good performance. As another requirement, it was stated that all elements should already be inside the precursor before annealing, in order to obtain good efficiencies. Both of the mentioned requirements were only based on some observations and were not proven.

Based on the novel annealing strategy, a novel route to the formation of CZTS has been suggested and investigated. As a consequence of being able to incorporate tin into the absorber layer by providing SnS(g) in the gas phase, it was suggested that the annealing of a copper and zinc containing precursor would lead to the formation of CZTS. As for the investigation of this

approach, it was found that under the used annealing consitions, tin incorporates itself into the film in a self-limiting manner, where the compositional amount of tin in Cu_2ZnSnS_4 appears to be the limit. In a temperature and time resolved ex-situ XRD and AES depth profile study, the formation reaction of a Mo/Cu/Zn precursor in the standard annealing at 500 mbar has been investigated. As a general result, it was shown that sulfur starts to be incorporated above temperatures of 300 °C, forming ZnS from the Cu-Zn alloys. A little later, at 400 °C, the partial pressure of sulfur is high enough for the formation of $Cu_{2-x}S$ to start. At 500 °C, the first sign of CZTS has been detected, in parallel to the first tin incorporation. As the presence of Cu_2SnS_3 could neither be proven nor disproven, it was assumed that CZTS forms directly by the reaction of the solid ZnS(s) and $Cu_{2-x}S$(s) with the gaseous SnS(g) and S_2(g). At a temperature of 550 °C and after 30 min of annealing, the reaction of CZTS seems to have come to completion, as no other binary phases could be detected. This result was also backed up with compositional measurements and AES depth profiles. From all XRD, EDX, SEM, and AES results, a model of CZTS formation has been suggested. In a comparative study of annealing at 1 mbar background pressure, it was seen that the formation of CZTS is mainly diffusion controlled in the 500 mbar case, as the in-diffusion of S_2(g) and SnS(g) at 1 mbar was observed to be much quicker. While from the 500 mbar annealed samples, none could be processed into a solar cell with a measurable efficiency. The samples obtained from the 1 mbar annealing resulted in devices with up to 1.3 % power conversion efficiency. Hereby, it was found that a longer annealing than 30 min was not favorable. Furthermore, the low efficiency of 1.3 %, compared to the 3.4 % and 6.1 % devices helps the hypothesis that as many elements as possible should be present in the precursor before the annealing step, in order to obtain high performance devices.

At this point, it shall be noted again, that all the findings in chapter 5 count for the pure sulfur case as well as for a mixed sulfur-selenide or a pure selenium case.

6.2 Future recommendations

In this section, suggestions are given that might help to facilitate future work of a similar kind. At first, ideas to scale up and enhance the electrodeposition process are proposed. In the next section, recommendations are given in order to identify possible phases and to discern them from CZTS, and in the last section an advice is given on how to grow high efficient CZTS absorbers.

6.2.1 Ideas to scale up and enhance the electrodeposition process

Within chapter 3.6, it was shown how laterally uniform precursors have been deposited onto square inch wide Mo-coated substrates. Within the timeframe of this work, this way of deposition has been the optimum achievable. For future experiments, which might also include up-scaling of the samples, however, this way of deposition might not be preferred. Besides the electrochemical engineering to optimize the deposition solutions, one could also think about enhancements in the equipment that is used to electrodeposit.

To improve the lateral uniformity of the precursor, a so-called *auxiliar thief electrode* (situated around the working electrode in an RDE head) can be used. Typically, the potential of the additional thief electrode around the WE is controlled separately to the one of the WE by a second potentiostat. That way, one can control the field lines between the CE and the WE, especially with regards to getting a homogeneous field line distribution across the substrate and its edges. More details can be found in the given references [178].

In order to scale up the deposition area, large electrochemical cells with a controllable flow of the electrolyte are suggested. Herefore, the use of jets that create a certain electrolyte flow towards the working electrode can be thought of. Furthermore, the use of a large scale *vertical paddle plating cell* is suggested for a homogeneous large scale deposition [179].

6.2.2 Recommendations for secondary phase identification and discrimination

From the results of chapter 4, it can be seen that the identification of secondary phases, especially their discrimination from the CZTS phase, is a non-trivial task. In fact, with GIXRD, and single wavelength Raman spectroscopy, it was not possible to tell small amounts of one phase from CZTS. As already pointed out within chapter 4, multiple wavelength Raman spectroscopy could already be helpful, at least in order to identify small amounts of a phase. This, however, could only be possible if the excitation wavelength is chosen in a way that it promotes resonant Raman of only one of the present phases. Of course, this measurement would have to be repeated with excitations that suit the other expected secondary phases. That way, at least a qualitative identification can be performed.

Another helpful strategy is most certainly to analyze the sample with several techniques that have complementary properties. In this respect, the analysis with EDX mapping and depth profiling techniques (AES or SIMS) would be an example. Furthermore, it is most certainly helpful to measure the same exact area of an absorber layer with several techniques that offer a micrometer resolution or better. Hereby, however, one should try to combine all of these techniques to one system. An example for a combined system is the Raman spectroscopy setup, which is combined with an AES setup, as presented by Fontane et al. [143]. If dreaming is allowed, one system combining SEM, EDX/WDX, micro-Raman (multiple wavelength), micro-PL, AES with sputtering capabilities, and EBSD or XRD (with tunable X-ray energy), where grains of the same area can be analyzed by all techniques, would be nice. Such a system, however, would probably not only be fairly fragile, but it would also be very time consuming to analyze a small area of a sample and to obtain general information about your film. To have a tunable X-ray energy source, a synchrotron might even be necessary. With respect to this, neutron scattering might also be an option, but certainly not on lab scale, especially in industrial terms.

One thing is clear: The identification of secondary phases in the Cu-Zn-Sn-S/Se system is not trivial. It might even be best to find a way to preferentially etch off un-desired phases.

6.2.3 Recommendations for the fabrication of high efficient CZTS solar cells

As pointed out in section 5.12, it seems as if there are three requirements that need to be fulfilled in order to obtain absorber for high performance solar cells based on CZTS/Se. Hereby, it has been pointed out in literature, that the sample should grow slightly Zn rich, as shown in Figure 5-1. As a result of this work, the second requirement is that the annealing conditions should be chosen in a way that the equilibrium point of the formation reaction stays close to the CZTS/Se ride. As a third requirement, results of the present work in combination with published results imply that a precursor should already contain all elements in a uniformly distributed manner, before the annealing step.

These requirments can be achieved in various ways which strongly depend on the used method.

Appendix

A. Correction function to correct for systematic error in EDX

In section 2.3.2 the systematic error of EDX measurements was briefly discussed. In this context, it was explained that the analyzing software typically calculates the relative compositional ratios under the assumption that all detected elements are distributed homogeneously thoughout the probed film. In the present case, however, the analyzed films were either fairly thin or had a fairly open morphology such that at 20 keV acceleration potential the underlying Mo substrate was probed in addition to the actual film. This leads to a systematic error in the evaluated relative elemental composition of the film which is bigger the larger the amount of Mo detected in the measurement is.

In order to get a rough estimate for the systematic error of the compositional ratios (in this case Cu/Sn and Zn/Sn) dependent on the Mo signal, a first order correction function has been deduced experimentally. For this, large area EDX (with 300 times magnification) and point EDX (on a representative single grain) measurements have been performed on seven different points on samples I and J (see Figure A-1 (a) and (b), respectively) and the compositional ratios have been compared with respect to the observed Mo content (see Figure A-2). Hereby, EDX measurements on a single grain revealed much lower Mo signals, as the Mo contribution due to the fairly open morphology is much larger in the large area measurements. All of those measurement pairs (same color is graph) have been plotted together and a first order approximation of the general trend has been deduced. Hereby, the black lines in the given graphs represent the obtained linear fits with the following slopes: -0.010 ± 0.001 for Cu/Sn vs Mo, and -0.0019 ± 0.0316 for Zn/Sn vs Mo.

Using these slopes, one can get a rough estimation of the “real” composition ratios of the film by extrapolating a measured Cu/Sn or Zn/Sn ratio (with a given Mo signal) to 0 at% Mo (intercept with y-axis).

Figure 4-19 displays the systematic error of the experimentally determined compositions with a Mo contribution for the measurements points on samples I and J (points on upper line) and the estimated “real” compositions of the films (points on lower line) after extrapolation of the Cu/Sn and Zn/Sn ratios to 0 at% of Mo. One can see that such a systematic error is significant.

The correction function used for this estimation is fairly rough, as can also be seen from the large error of the slope for the Zn/Sn case. The reason for this can be found in the fact that the measurements were performed on positions with different Zn/Sn ratios, which causes the scatter of the data points in y-direction. On the other hand, this large error indicates the difficulty of the determination of the “real” film compositions with EDX, when information about the substrate composition is intermixed with that of the film, or when the film itself is inhomogeneous. Therefore, in the general case, where substrate information is detected, it is suggested to use proper simulation software such as “INCA Thin Film ID”, as provided by Oxford Instruments together with the evaluation software for the EDX spectra (“INCA”), in order to propperly estimate the “real” composition. Within the timeframe of this work, such a simulation was not possible any more but it is recommended for future investigations.

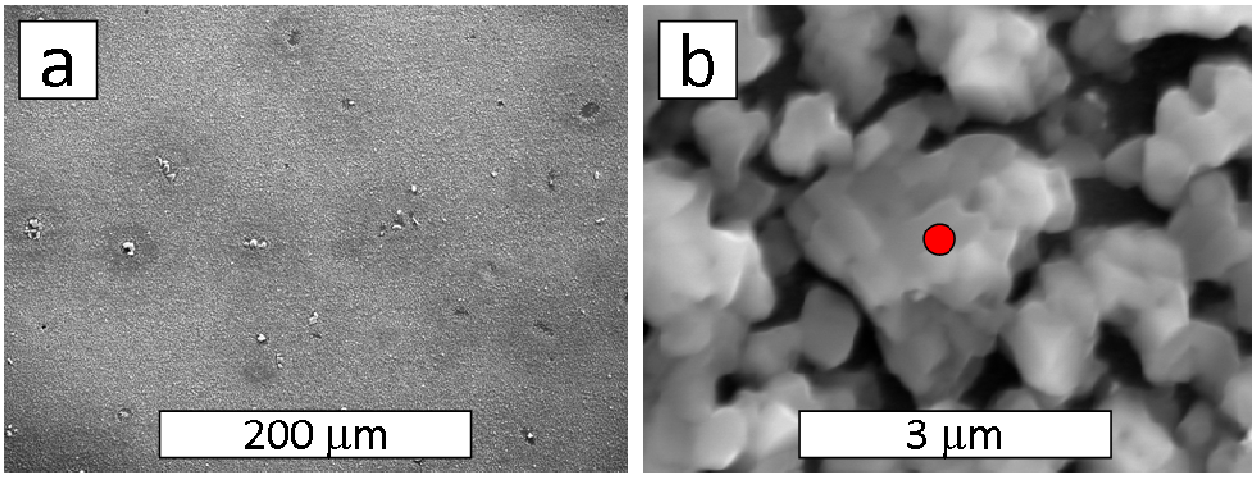

Figure A-1 SEM top view images of (a) the 300 times magnified large area of EDX measurent, and (b) the point of EDX measurement on an average grain. The red dot indicated the center of the measurement point. In (a) the EDX singal was averaged over the whole area as shown here.

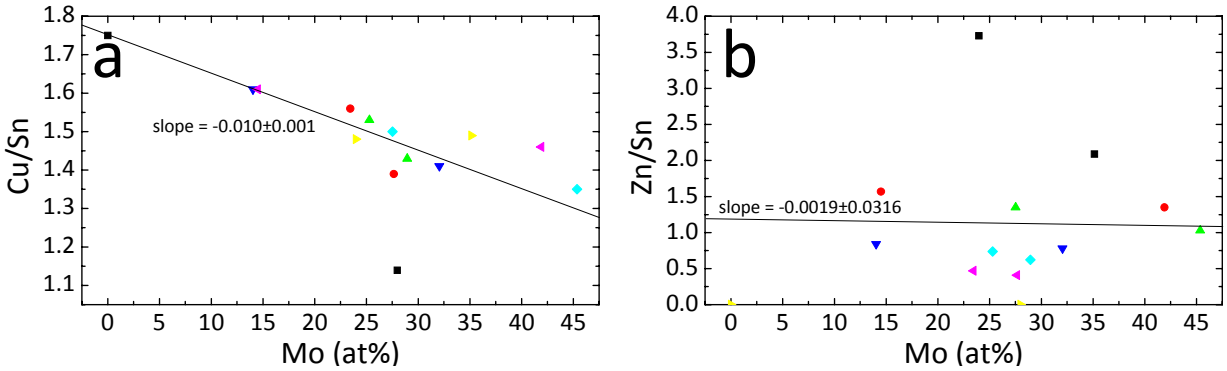

Figure A-2 Compositional ratios depending on the observed Mo signal. The black lines represent linear fits over all data with the given slopes. The different colors represent large area and point measurements performed on the same position on samples I and J. Graph (a) shows the Cu/Sn , graph (b) the Zn/Sn ratio.

B. XRD patterns obtained from different positions on samples I and J

Figure B-1 shows the whole GIXRD pattern as measured on the positions (1) to (6) on samples I and J. The evaluation of the peak broadening as discussed in section 4.12.3 were performed on the (112)-peak at around 28.3 °. In the patterns from position (2) to (6), one can clearly see the unique CZTS peak at 29.5 °, indicating its presence.

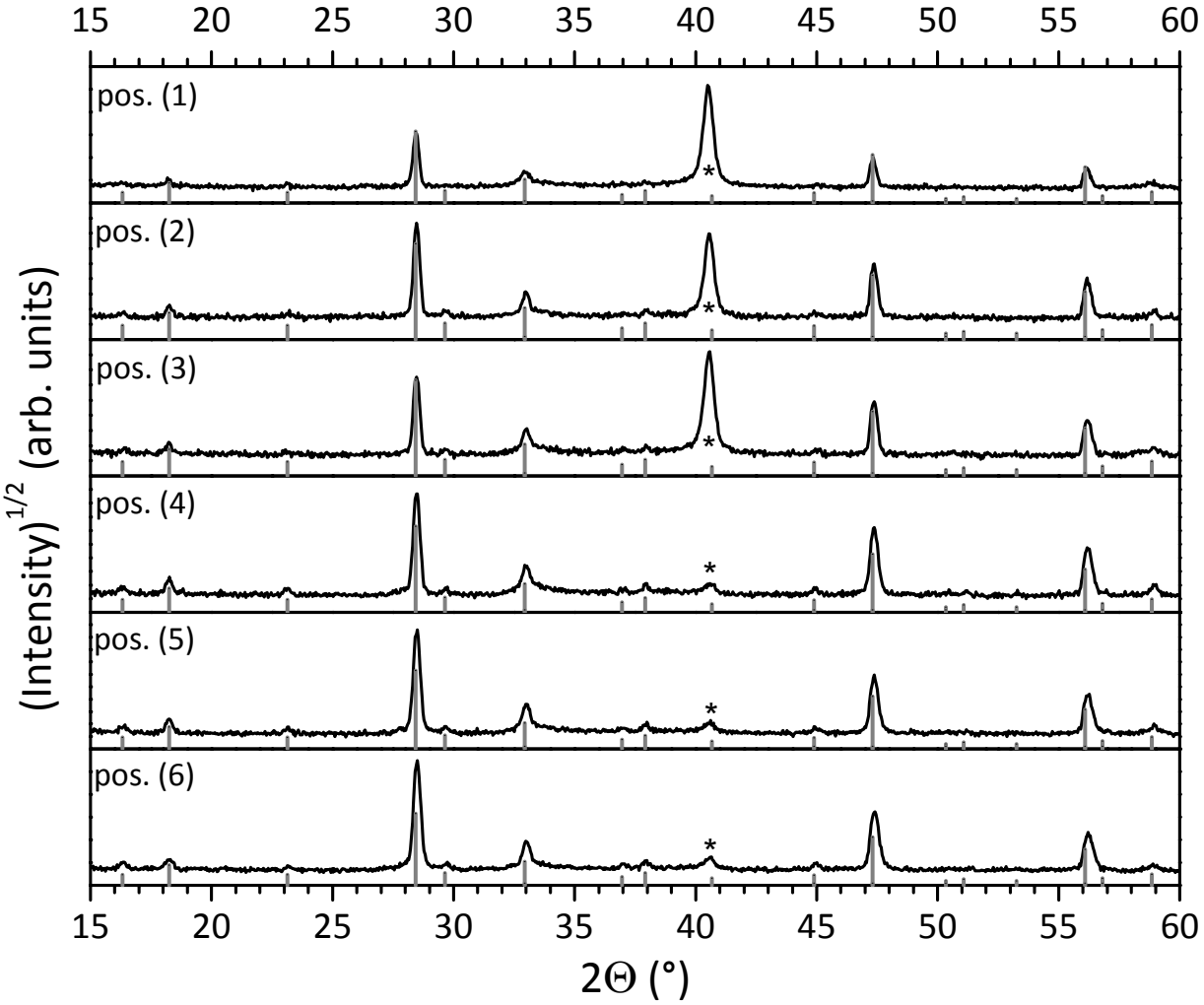

Figure B-1 GIXRD pattern obtained from samples I and J at the different positions (1) to (6) under a grazing angle of 1 °.The grey vertical lines indicate the position of the reference peaks for CZTS according to the following JCPDS file: 01-075-4122, while the "*" indicates the peak due to the Mo substrate (JCPDS: 04-001-0059) [23].

C. Refinement results of the GIXRD patterns of samples I and J

Figure C-1 shows the refined patterns of the best refinements as obtained from the different positions (1) to (6) on samples I and J. Please refer to section 4.12.4 and Table 4-6 for more detailed results of the respective refinements.

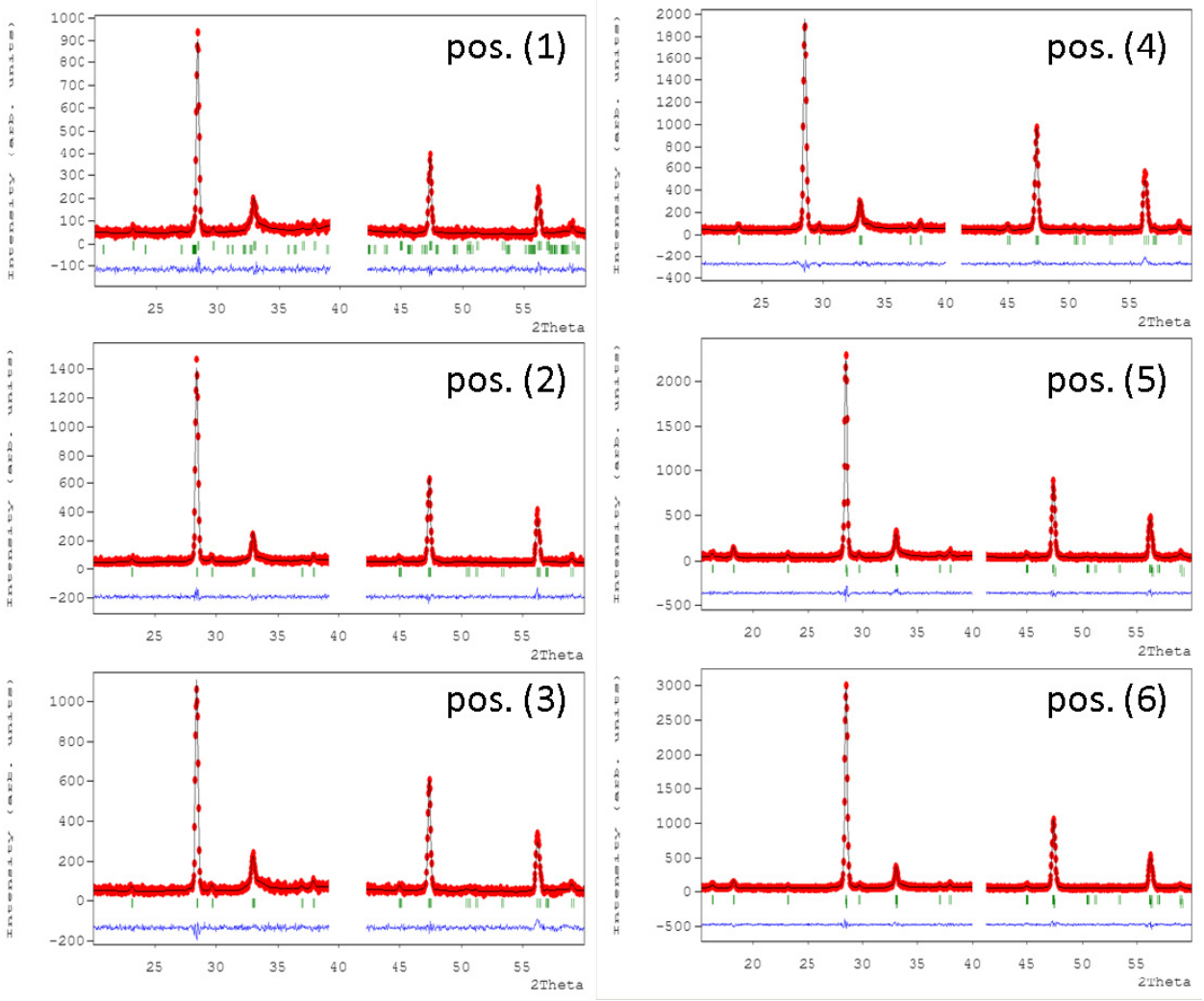

Figure C-1 Refined GIXRD pattern obtained from positions (1) to (6) on samples I and J. The red points represent the measurement, the black lines indicate the calculated respective patterns, and the blue lines indicate the difference between the measured and calculated respective patterns. The small green vertical lines indicate the position of the ZnS, CTS, or CZTS phase that was refined.

D. Proof of principle of CZTSSe formation from a Mo/Cu/Zn stack

To prove that SnSe(g) can be incorporated into a Mo/Cu/Zn stack the same way as SnS(g) does by an annealing in a selenium **and** SnSe(g) containing environment, a sample (very similar to sample O) has been prepared electrochemically, as described in section 5.4. In the following, this precursor was annealing under the standard conditions together with elemental selenium pellets and tin selenide powder. The obtained thin film was characterized by various methods as listed in section 5.4.

Compositional analysis revealed that the amount of chalcogen in the annealed film consisted of 80 % selenium and 20 % sulfur, although the sample was just annealed in the presence of selenium and tin selenide. The presence of sulfur in the film can be explained by contaminations, as the graphite box used for the annealing has not been cleaned properly enough, in order to avoid sulfur. Independent of this issue, EDX analysis did prove that the tin incorporation into the film via SnSe(g) from the gas phase did take place in the same way as for tin sulfide (as discussed in section 5.8.1), resulting in Cu/(Zn+Sn) and Zn/Sn ratios of 0.87 and 1.15, respectively.

Figure D-1 (a) shows the XRD pattern obtained from this sample. As 20 % of the chalcogen in the film was sulfur, the raw data of the obtained pattern were slightly shifted in order to overlap with the reference lines (in blue). The angular distance of this shift is in good agreement with the observed S/(S+Se) ratio of around 20 %.

Figure D-1 (b) shows the morphology of the annealed film with partly small and partly large grains of up to 8 μm. In between the grains one can observe pinholes of several micrometer of length. A solar cell device has not been obtained in this study.

These results show that the selenium **and** tin selenide annealing takes place in a similar manner as it was observed for the sulfur **and** tin sulfide case.

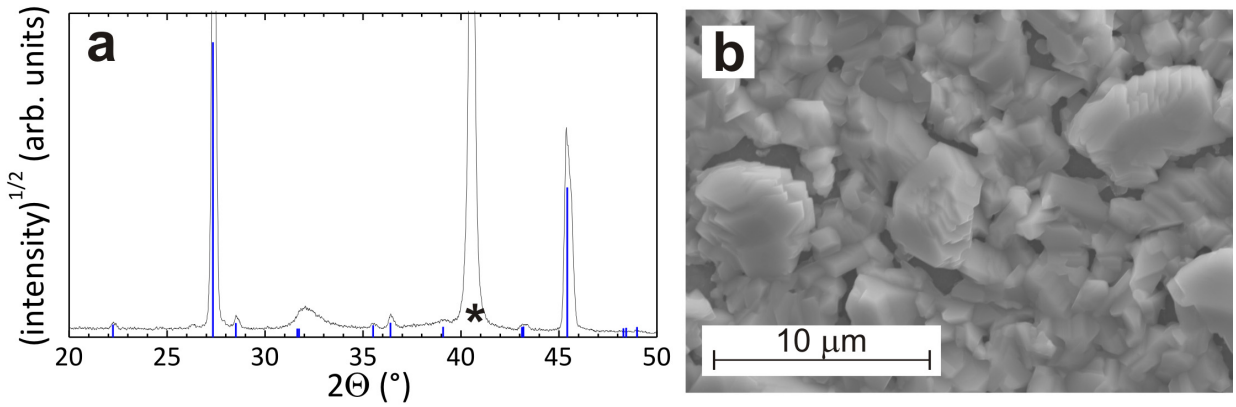

Figure D-1 (a) Slightly shifted XRD pattern obtained from a samples annealed in selenium and tin selenide. (b) SEM top view images from the obtained thin film. "*" indicates the presence of Mo (JCPDS: 04-001-0059) [23].

E. X-ray diffractograms of samples P1 to P4: Study of Sn incorporation

Figure E-1 shows the whole XRD patterns as measured on the samples P annealed in (i) 0 times, (ii) 0.5 times, (iii) 1 time, and (iv) 2.5 times the stoichiometric amount of Sn necessary to form CZTS. As discussed in section 5.8.2, the samples annealed with 1 and 2.5 times the stoichiometric amount of Sn only show peaks that can be attributed to the CZTS phase, aside those that are assigned to the Mo substrate. Hereby, the presence of ZnS and CTS can neither be proven nor disproven satisfactorily, as shown in chapter 4. From these data it seems that all available Zn and Cu from the precursor formed CZTS via the consumption of sulfur and tin sulfide from the gas phase. In contrary, the patterns obtained for 0 and 0.5 times the stoichiometric amount of Sn show the presence of a $Cu_{1.765}S$ phase, indicating that ZnS is also present. Furthermore, this result indicates that there was not sufficient Sn in order to convert all available Cu and Zn into CZTS, however, there was enough sulfur to form the binary sulfides.

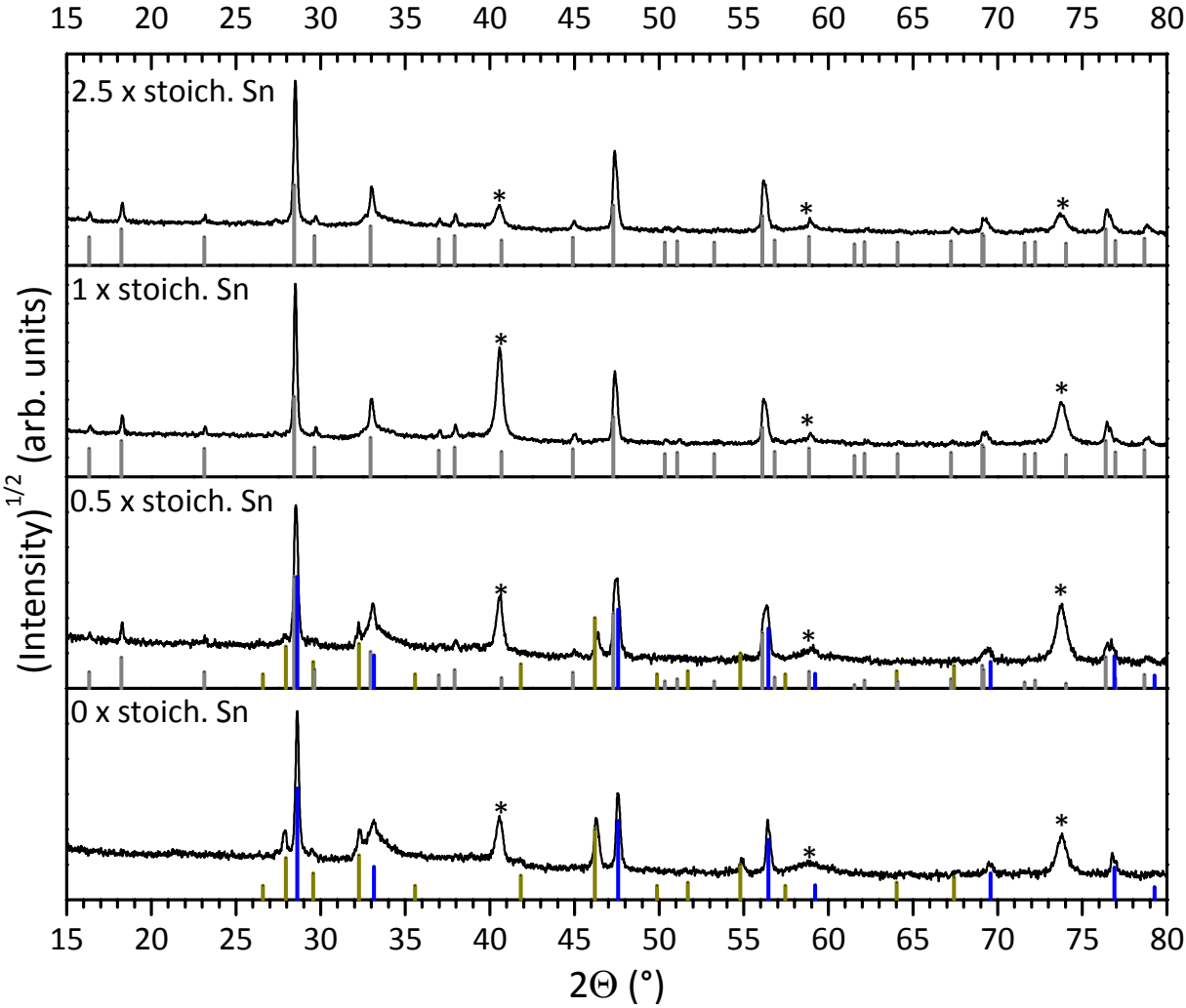

Figure E-1 XRD patterns obtained from the samples P annealed with (i) 0 times, (ii) 0.5 times, (iii) 1 time, and (iv) 2.5 times the stoichiometric amount of Sn necessary to form CZTS. The vertical lines in blue correspond to ZnS (JCPDS: 04-001-6857), those in grey to CZTS (JCPDS: 01-075-4122), and the dark yellow ones to $Cu_{1.765}S$ (JCPDS: 00-023-0960), while "*" indicates the presence of Mo (JCPDS: 04-001-0059) [23].

F. XRD study of Cu_2SnS_3 etching with KCN

Figure F-1 shows the XRD patterns obtained from a Cu_2SnS_3 sample (sample M) that was etched for 0 s, 5 s, 60 s, and 360 s in an aqueous KCN solution, as discussed in section 4.15. From these results it can be seen that the intensity of all peaks stays the same, even after 6 min of KCN etching. Since CZTS samples are typically etched for 30 s to remove Cu-S phases before those phases are processed to solar cells devices, such a 6 min etch is a fairly long timeframe. It can be concluded that within this timeframe Cu_2SnS_3 is not etched.

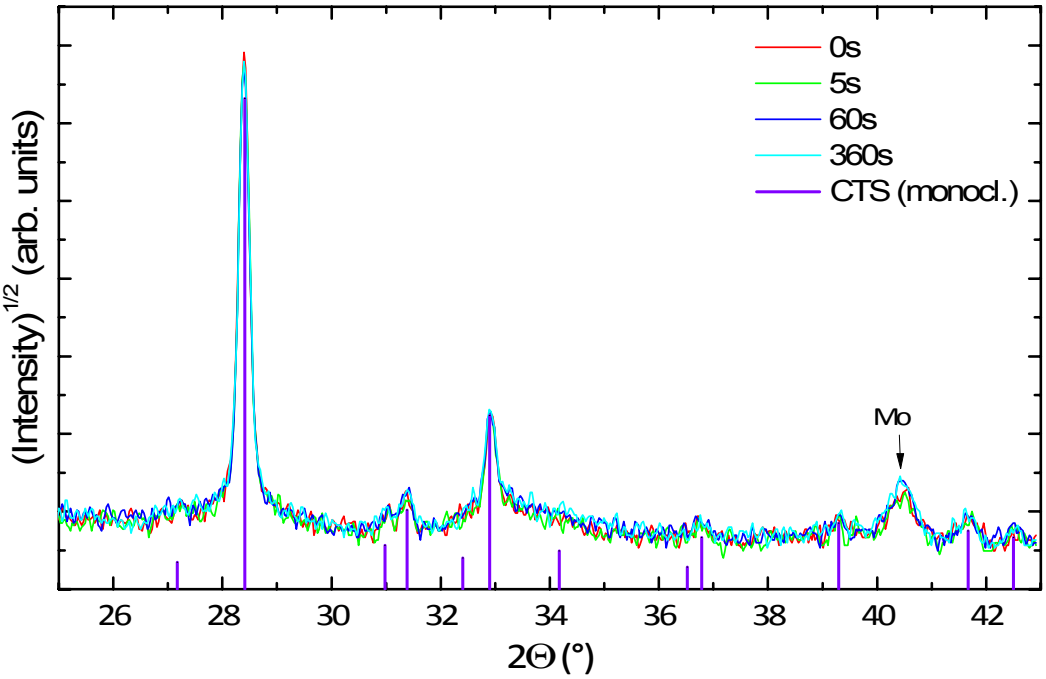

Figure F-1 XRD pattern of sample M before (0 s) as well as 5 s, 60 s, and 360 s after KCN etching, respectively. The violet lines in the XRD pattern indicate the positions of the XRD peaks according to literature (see Table 4-1).

G. Phase diagrams

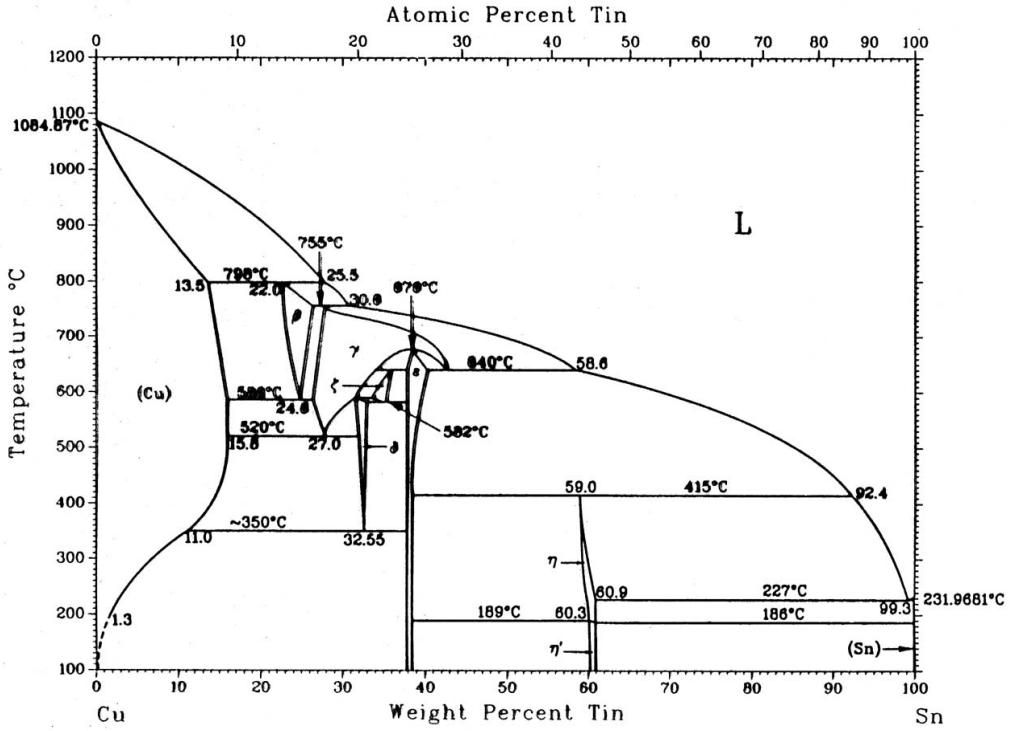

Figure G-1 Phase diagram of the Cu-Sn system, according to [60].

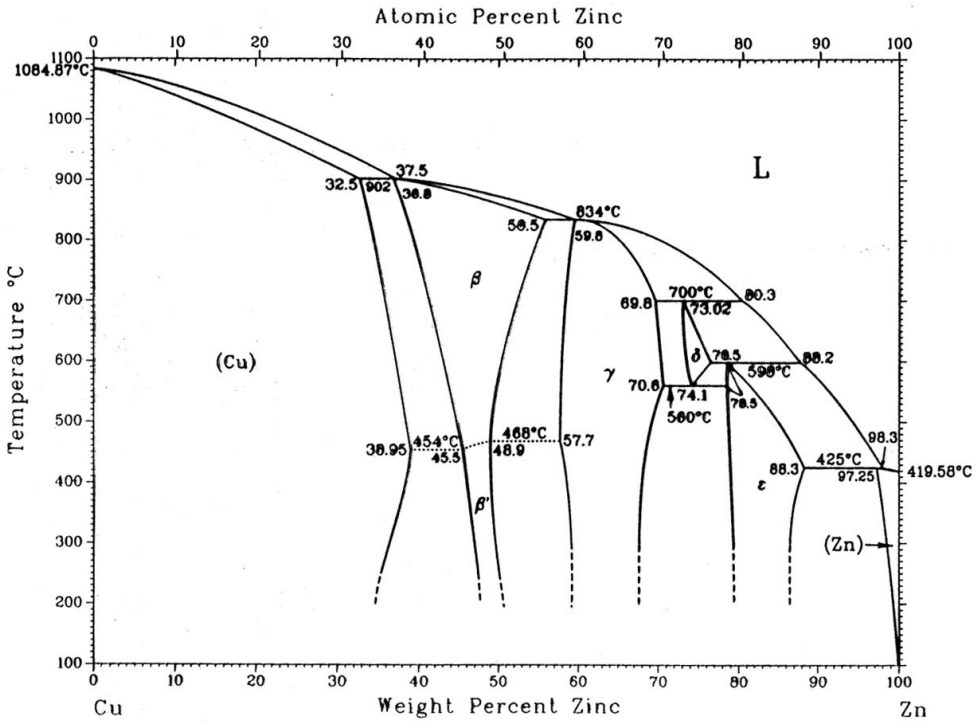

Figure G-2 Phase diagram of the Cu-Zn system, according to [60].

Bibliography

[1] United Nations, Department of Economic and Social Affiars, Population Devision, Population Estimates and Projections Section, 31.10.2011.

[2] M. A. Green, K. Emery, Y. Hishikawa, W. Warta, and E. D. Dunlop, Progress in Photovoltaics: Research and Applications 19:565 (2011).

[3] A. C. Tolcin, U.S. Geological Survey. http://minerals.usgs.gov/minerals/pubs/commodity/indium, 2008.

[4] K. Ito and T. Nakazawa, Japanese Journal of Applied Physics Part 1-Regular Papers Short Notes & Review Papers 27:2094 (1988).

[5] S. Y. Chen, X. G. Gong, A. Walsh, and S. H. Wei, Applied Physics Letters 94:3 (2009).

[6] T. M. Friedlmeier, N. Wieser, T. Walter, H. Dittrich, and H. W. Schock, in 14th European PVSEC, 1997, p. 1242.

[7] C. Persson, Journal of Applied Physics 107:053710 (2010).

[8] J. J. Scragg, P. J. Dale, and L. M. Peter, Electrochemistry Communications 10:639 (2008).

[9] T. Tanaka, T. Nagatomo, D. Kawasaki, M. Nishio, Q. X. Guo, A. Wakahara, A. Yoshida, and H. Ogawa, Journal of Physics and Chemistry of Solids 66:1978 (2005).

[10] T. K. Todorov, K. B. Reuter, and D. B. Mitzi, Advanced Materials 22:E156 (2010).

[11] J. Zhang, L. X. Shao, Y. J. Fu, and E. Q. Xie, Rare Metals 25:315 (2006).

[12] J. Nelson, The Physics of Solar Cells, London: Emperial College Press, 2003.

[13] H. Katagiri, K. Jimbo, S. Yamada, T. Kamimura, W. S. Maw, T. Fukano, T. Ito, and T. Motohiro, Applied Physics Express 1 (2008).

[14] D. Barkhouse, O. Gunawan, T. Gokmen, T. K. Todorov, and D. B. Mitzi, Progress in Photovoltaics: Research and Applications (2011).

[15] I. D. Olekseyuk, I. V. Dudchak, and L. V. Piskach, Journal of Alloys and Compounds 368:135 (2004).

[16] B. M. Basol, M. Pinarbasi, S. Aksu, J. Freitag, P. Gonzalez, T. Johnson, Y. Matus, B. Metin, M. Narasimhan, D. Nayak, G. Norsworthy, D. Soltz, J. Wang, T. Wang, and H. Zolla, in Conference Record of the IEEE Photovoltaic Specialists Conference, 2009, p. 002310.

[17] D. M. Mattox, Handbook of Physical Vapor Deposition (PVD) Processing, ELSEVIER, 2010.

[18] A. Redinger, D. Berg, P. Dale, and S. Siebentritt, Journal of the American Chemical Society 133:3320 (2011).

[19] D. R. Lide, CRC Handbook of Chemistry and Physics, CRC Press/Taylor and Francis, Boca Raton, FL, 2010.

[20] J. Goldstein, D. Newbury, D. Joy, C. Lyman, P. Echlin, E. Lifshin, L. Sawyer, and J. Michael, Scanning Electron Microscopy and X-Ray Microanalysis, Springer, 2007.

[21] M. Birkholz, Thin Film Analysis by X-Ray Scattering, WILEY-VCH, 2009.

[22] S. Schorr, C. Stephan, T. Törndahl, and R. Mainz, in Advanced Characterization Techniques for Thin Film Solar Cells (D. Abou-Ras, T. Kirchartz, and U. Rau, eds.), WILEY-VCH, 2011.

[23] The International Center of Diffraction Data, ICDD, Database (2009).

[24] H. Rietveld, Journal of Applied Crystallography 2:65 (1969).

[25] J. Rodriguez-Carvajal, Gif sur Yvette Cedex, 2001.

[26] G. Caglioti, A. Paoletti, and F. P. Ricci, Nucl. Instrum. 3:223 (1958).

[27] M. Schmitt and J. Popp, Journal of Raman Spectroscopy 37 (2006).

[28] J. Alvarez-Garcia, V. Izquierdo-Roca, and A. Perez-Rodriguez, in Advanced Characterization Techniques for Thin Film Solar Cells (D. Abou-Ras, T. Kirchartz, and U. Rau, eds.), WILEY-VCH, 2011.
[29] G. Bauer and W. Richter, Optical Characterization of Epitaxial Semiconductor Layers, Springer, 1996.
[30] T. Dieing, O. Hollricher, and J. Toporski, Confocal Raman Microscopy, Springer, 2010.
[31] T. Unold and L. Gütay, in Advanced Characterization Techniques for Thin Film Solar Cells (D. Abou-Ras, T. Kirchartz, and U. Rau, eds.), WILEY-VCH, 2011.
[32] L. Gütay, C. Lienau, and G. Bauer, Applied Physics Letters 97 (2011).
[33] H. J. Mathieu, in Surface Analysis - The Principal Techniques (J. C. Vickerman and I. S. Gilmore, eds.), Wiley, 2009.
[34] J. R. Dean, Practical Inductively Coupled Plasma Spectroscopy, John Wiley & Sons, Ltd, Newcastle, UK, 2005.
[35] S. Fonash, Solar Cell Device Physics, ELSEVIER, 2010.
[36] S. Siebentritt, Solar Energy Materials and Solar Cells 95:1471.
[37] W. W. Gärtner, Physical Review 116:84 (1959).
[38] J. I. Pankove, Optical Processes in Semiconductors, Dover Publications, 1971.
[39] A. J. Bard and L. R. Faulkner, Electrochemical Methods, Wiley, 2001.
[40] C. H. Hamann, A. Hamnett, and W. Vielstrich, Electrochemistry, Wiley-VCH, 1998.
[41] J. J. Scragg, in Department of Chemistry, Vol. PhD, University of Bath, Bath, 2010.
[42] H. Araki, Y. Kubo, K. Jimbo, W. S. Maw, H. Katagiri, M. Yamazaki, K. Oishi, and A. Takeuchi, Physica Status Solidi (C) Current Topics in Solid State Physics 6:1266 (2009).
[43] A. Ennaoui, M. Lux-Steiner, A. Weber, D. Abou-Ras, I. Kötschau, H. W. Schock, R. Schurr, A. Hölzing, S. Jost, R. Hock, T. Voss, J. Schulze, and A. Kirbs, Thin Solid Films 517:2511 (2009).
[44] M. Jeon, T. Shimizu, and S. Shingubara, Materials Letters 65:2364 (2011).
[45] M. Kurihara, D. Berg, J. Fischer, S. Siebentritt, and P. J. Dale, physica status solidi (c) 6:1241 (2009).
[46] B. S. Pawar, S. M. Pawar, S. W. Shin, D. S. Choi, C. J. Park, S. S. Kolekar, and J. H. Kim, Applied Surface Science 257:1786 (2010).
[47] S. M. Pawar, B. S. Pawar, A. V. Moholkar, D. S. Choi, J. H. Yun, J. H. Moon, S. S. Kolekar, and J. H. Kim, Electrochimica Acta 55:4057 (2010).
[48] R. Schurr, A. Hölzing, S. Jost, R. Hock, T. Voss, J. Schulze, A. Kirbs, A. Ennaoui, M. Lux-Steiner, A. Weber, I. Kötschau, and H. W. Schock, Thin Solid Films 517:2465 (2009).
[49] J. J. Scragg, D. M. Berg, and P. J. Dale, Journal of Electroanalytical Chemistry 646:52 (2010).
[50] J. J. Scragg, P. J. Dale, and L. M. Peter, Thin Solid Films 517:2481 (2009).
[51] C. P. Chan, Z. Chen, H. Lam, and C. Surya, in Proceedings of SPIE - The International Society for Optical Engineering, Vol. 7411, 2009.
[52] C. P. Chan, H. Lam, K. K. Leung, and C. Surya, Journal of Nonlinear Optical Physics and Materials 18:599 (2009).
[53] C. P. Chan, H. Lam, and C. Surya, in 2009 14th OptoElectronics and Communications Conference, OECC 2009, 2009.
[54] C. P. Chan, H. Lam, and C. Surya, Solar Energy Materials and Solar Cells 94:207 (2010).
[55] C. P. Chan, H. Lam, K. Y. Wong, and C. Surya, in Materials Research Society Symposium Proceedings, Vol. 1123, 2009, p. 105.

[56] X. Zhang, X. Z. Shi, W. C. Ye, C. L. Ma, and C. M. Wang, Applied Physics a-Materials Science & Processing 94:381 (2009).
[57] B. W. Gregory and J. L. Stickney, Journal of Electroanalytical Chemistry 300:543 (1991).
[58] J. L. Stickney, Electrochemical Society Interface 20:28 (2011).
[59] H. Araki, A. Mikaduki, Y. Kubo, T. Sato, K. Jimbo, W. S. Maw, H. Katagiri, M. Yamazaki, K. Oishi, and A. Takeuchi, Thin Solid Films 517:1457 (2008).
[60] T. Massalski, Binary Alloy Phase Diagrams, AMS, Materials Park, Ohio, 1990.
[61] I. A. Carlos, C. A. C. Souza, E. M. J. A. Pallone, R. H. P. Francisco, V. Cardoso, and B. S. Lima-Neto, Journal of Applied Electrochemistry 30:987 (2000).
[62] K. N. Tu, Materials Chemistry and Physics 46:217 (1996).
[63] M. Date, K. N. Tu, T. Shoji, M. Fujiyoshi, and K. Sato, Journal of Materials Research 19:2887 (2004).
[64] I. A. Carlos and M. R. H. De Almeida, Journal of Electroanalytical Chemistry 562:153 (2004).
[65] C. Dominguez-Rios, M. V. Moreno, R. Torres-Sanchez, W. Antunez, A. Aguilar-Elguezabal, and J. Gonzalez-Hernandez, Surface and Coatings Technology 202:4848 (2008).
[66] R. Juakenas, V. Karpaviciene, V. Pakstas, A. Selskis, and V. Kapocius, Journal of Electroanalytical Chemistry 602:237 (2007).
[67] I. T. Bae, Journal of the Electrochemical Society 155:D395 (2008).
[68] G. Zoppi, N. S. Beattie, J. D. Major, R. W. Miles, and I. Forbes, Journal of Materials Science 46:4913 (2011).
[69] R. K. Pandey, S. N. Sahu, and S. Chandra, Handbook of semiconductor electrodeposition, M. Dekker, 1996.
[70] G. Moh, Chemie der Erde 34:1 (1975).
[71] D. B. Mitzi, O. Gunawan, T. K. Todorov, K. Wang, and S. Guha, Solar Energy Materials and Solar Cells 95:1421 (2011).
[72] S. Siebentritt and S. Schorr, "Kesterites - a challenging material or solar cells", submitted (2011).
[73] S. Schorr, in Symposium on Thin Film Chalcogenide Photovoltaic Materials Held at the EMRS 2006 Spring Conference, Elsevier Science Sa, Nice, FRANCE, 2006, p. 5985.
[74] J. Paier, R. Asahi, A. Nagoya, and G. Kresse, Physical Review B 79:8 (2009).
[75] J. M. Raulot, C. Domain, and J. F. Guillemoles, Journal of Physics and Chemistry of Solids 66:2019 (2005).
[76] A. Neisser, Solar Energy Materials and Solar Cells 67:97 (2001).
[77] F. Hergert, Vol. PhD, University of Erlangen-Nürnberg, Erlangen, 2007.
[78] W. Schockley and H. J. Queisser, Journal of Applied Physics 32:519 (1961).
[79] L. M. Peter, Phil. Trans. R. Soc. A 369:1840 (2011).
[80] S. Botti, D. Kammerlander, and M. Marques, Applied Physics Letters 98 (2011).
[81] H. Katagiri, Thin Solid Films, EMRS 2004 480-481:426 (2005).
[82] H. Katagiri, K. Jimbo, K. Moriya, and K. Tsuchida, in Proceedings of 3rd World Conference on Photovaltaic Energy Conversion, Vols a-C, 2003, p. 2874.
[83] H. Katagiri, N. Sasaguchi, S. Hando, S. Hoshino, J. Ohashi, and T. Yokota, Solar Energy Materials and Solar Cells 49:407 (1997).
[84] H. Matsushita, T. Ichikawa, and A. Katsui, Journal of Materials Science 40:2003 (2005).
[85] K. Moriya, K. Tanaka, and H. Uchiki, Japanese Journal of Applied Physics Part 1-Regular Papers Brief Communications & Review Papers 46:5780 (2007).
[86] K. Moriya, K. Tanaka, and H. Uchiki, Japanese Journal of Applied Physics 47:602 (2008).

[87] J. W. Lee, J. D. Cohen, and W. N. Shafarman, Thin Solid Films 480-481:336 (2005).
[88] D. Schroeder, J. Hernandez, G. Berry, and A. Rockett, Journal of Applied Physics 83:1519 (1998).
[89] S. Siebentritt, Thin Solid Films 480-481:312 (2005).
[90] Z. Zhou, Y. Wang, D. Xu, and Y. Zhang, Solar Energy Materials and Solar Cells 94 (2010).
[91] B. Shin, O. Gunawan, Y. Zhu, N. A. Bojarczuk, S. J. Chey, and S. Guha, Progress in Photovoltaics: Research and Applications (2011).
[92] K. Wang, O. Gunawan, T. K. Todorov, B. Shin, N. A. Chey, N. A. Bojarczuk, D. B. Mitzi, and S. Guha, Applied Physics Letters 97 (2010).
[93] C. Wu, Z. Hu, C. Wang, H. Sheng, J. Yang, and Y. Xie, Applied Physics Letters 91 (2007).
[94] X. A. Chen, H. Wada, A. Sato, and M. Mieno, Journal of Solid State Chemistry 139:144 (1998).
[95] L. M. De Chalbaud, J. M. Delgado, and V. Sagredo, in 11th Int. Conf. on Ternary and Multinary Compounds, ICTMC-11, Salford, 1997.
[96] S. Fiechter, M. Martinez, G. Schmidt, W. Henrion, and Y. Tomm, Journal of Physics and Chemistry of Solids 64:1859 (2003).
[97] H. Hahn and H. Schulze, Naturwissenschaften 52:426 (1965).
[98] P. S. Jaulmes, J. Rivet, and P. Laruelle, Acta Crystallographica Section B 33:540 (1977).
[99] M. Khanafer, J. Rivet, and J. Flahaut, Bulletin de la societe chimique de France 12:2670 (1974).
[100] M. Onoda, X. A. Chen, A. Sato, and H. Wada, Materials Research Bulletin 35:1563 (2000).
[101] N. Wang, Neues Jahrbuch der Minaralogie:241 (1976).
[102] P. Fernandes, P. Salome, and A. Da Cunha, J. Phys. D - Appl. Phys. 43 (2010).
[103] P. Fernandes, P. Salome, and A. Da Cunha, Phys. Status Solidi C 1-4 (2010).
[104] P. Fernandes, P. Salome, and A. Da Cunha, Journal of Alloys and Compounds 509:7600 (2011).
[105] D. Avellaneda, M. Nair, and P. Nair, Journal of the Electrochemical Society 157:D346 (2010).
[106] T. Kuku and O. Fakolujo, Solar Energy Materials 16:199 (1987).
[107] M. Bouaziz, M. Amlouk, and S. Belgacem, Thin Solid Films 517:2527 (2009).
[108] M. Bouaziz, J. Ouerfelli, S. K. Srivastava, Bernede J.C., and M. Amlouk, Vacuum 85:783 (2011).
[109] H. Katagiri, N. Ishigaki, T. Ishida, and K. Saito, Japanese Journal of Applied Physics Part 1-Regular Papers Short Notes & Review Papers 40:500 (2001).
[110] Y. Zhai, S. Chen, J. Yang, H. Xiang, X. G. Gong, A. Walsh, J. Kang, and S. H. Wei, (2011).
[111] J. Craig and G. Kullerud, Mineralium Deposita 8:81 (1973).
[112] T. Birther, P. Donohue, W. Cloud, P. Bierstedt, and H. Young, Journal of Solid State Chemistry 1:526 (1970).
[113] M. Burk, Universität Heidelberg, Heidelberg, 1975.
[114] A. Janosi, Acta Crystallographica 17:311 (1963).
[115] H. Rau, Journal of Physics and Chemistry of Solids 28:903 (1967).
[116] Landold and Börnstein, Semiconductors E: Ternary Compounds, Amorphous and Organic Semiconductors, Springer, 2000.
[117] L. Isac, I. Popovici, A. Enesca, and A. Duta, Energy Procedia 2:71 (2011).
[118] S. K. Maji, N. Mukherjee, A. K. Dutta, D. N. Srivastava, P. Paul, B. Karmakar, A. Mondal, and B. Adhikary, Materials Chemistry and Physics 130:392 (2011).

[119] A. U. Ubale, D. M. Choudhari, J. S. Kantale, V. N. Mitkari, M. S. Nikam, W. J. Gawande, and P. P. Patil, Journal of Alloys and Compounds 509:9249 (2011).
[120] S. S. Hegde, A. G. Kunjomana, K. A. Chandrasekharan, K. Ramesh, and M. Prashantha, Physica B: Condensed Matter 406:1143 (2011).
[121] M. Khadraoui, N. Benramdane, C. Mathieu, A. Bouzidi, R. Miloua, Z. Kebbab, K. Sahraoui, and R. Desfeux, Solid State Communications 150:297 (2010).
[122] M. Ristov, G. Sinadinovski, M. Mitreski, and M. Ristova, Solar Energy Materials and Solar Cells 69:17 (2001).
[123] A. Sanchez-Juarez and A. Ortáz, Semiconductor Science and Technology 17:931 (2002).
[124] B. Subramanian, C. Sanjeeviraja, and M. Jayachandran, Bulletin of Electrochemistry 18:349 (2002).
[125] E. Kisi and M. Elcombe, Acta Crystallographica C45:1867 (1989).
[126] M. Öztas, M. Bedir, A. Necmeddin Yazici, E. Vural Kafadar, and H. ToktamIs, Physica B: Condensed Matter 381:40 (2006).
[127] S. Zanettini, F. Bissoli, L. Nasi, P. Ranzieri, and E. Gilioli, Crystal Research and Technology 46:881 (2011).
[128] G. Price, Thermodynamics of Chemical Processes, OUP Oxford, 1998.
[129] J. J. Scragg, T. Ericson, T. Kubart, M. Edoff, and C. Platzer-Björkman, submitted to Chemistry of Materials (2011).
[130] D. J. Vaughan and J. R. Craig, Mineral Chemistry of Metal Sulfides Cambridge University Press: Cambridge, U.K. (1978).
[131] A. Weber, Vol. PhD, Universität Erlangen-Nürnberg, Erlangen-Nürnberg, 2009.
[132] F. Geiger, C. A. Busse, and R. I. Löhrke, International Journal of Thermophysics 8:425 (1987).
[133] J. C. Greenbank and B. B. Argent, Trans. Faraday Soc. 61:655 (1965).
[134] D.-Y. Peng and J. Zhao, The Journal of Chemical Thermodynamics 33:1121 (2001).
[135] V. Piacente, S. Foglia, and P. Scardala, Journal of Alloys and Compounds 177:17 (1991).
[136] O. Tukhlibaev and U. Z. Alimov, Optics and Spectroscopy 88:506 (2000).
[137] H. Rau, T. R. N. Kutty, and J. R. F. Guedes de Carvalho, Journal of Chemical Thermodynamics 5:833 (1973).
[138] T. M. Friedlmeier, Vol. PhD, Universität Stuttgart, Stuttgart, 2000.
[139] A. Redinger, D. Berg, P. Dale, N. Valle, and S. Siebentritt, Journal of Photovoltaics accepted (2011).
[140] A. Redinger, K. Hoenes, X. Fontane, V. Izquierdo-Roca, E. Saucedo, N. Valle, A. Perez-Rodriguez, and S. Siebentritt, Applied Physics Letters 98 (2010).
[141] A. Weber, R. Mainz, and H. W. Schock, Journal of Applied Physics 107:6 (2010).
[142] P. A. Fernandes, P. M. P. Salome, and A. F. da Cunha, Semiconductor Science and Technology 24:7 (2009).
[143] X. Fontane, L. Calvo-Barrio, V. Izquierdo-Roca, A. Perez-Rodriguez, J. Morante, D. Berg, P. Dale, and S. Siebentritt, Applied Physics Letters 98 (2011).
[144] A. Weber, I. Kotschau, S. Schorr, and H. W. Schock, in Symposium on Thin-Film Compound Semiconductor Photovoltaics held at the 2007 MRS Spring Meeting (T. Gessert, K. Durose, C. Heske, S. Marsillac, and T. Wada, eds.), Materials Research Society, San Francisco, CA, 2007, p. 201.
[145] A. Weber, S. Schmidt, D. Abou-Ras, P. Schubert-Bischoff, I. Denks, R. Mainz, and H. W. Schock, Applied Physics Letters 95:041904 (2009).

[146] M. Altosaar, J. Raudoja, K. Timmo, M. Danilson, M. Grossberg, J. Krustok, and E. Mellikov, physica status solidi (a) 205:167 (2008).
[147] J. Alvarez-Garcia, J. Vac. Sci. Technol. A 19:232 (2001).
[148] O. Brafman and S. Mitra, Phys. Rev. 171:931 (1968).
[149] P. A. Fernandes, P. M. P. Salome, and A. F. da Cunha, in Symposium on Thin Film Chalcogenide Photovoltaic Materials held at the EMRS 2008 Spring Conference, Elsevier Science Sa, Strasbourg, FRANCE, 2008, p. 2519.
[150] G. Frey, Phys. Rev. B 60:2883 (1999).
[151] M. Himmrich and H. Haeuseler, Spectrochimica Acta 47A:933 (1991).
[152] H. Katahama, J. Phys. Chem. Solids 44:1081 (1983).
[153] D. Mead, Solid State Communications 20:885 (1976).
[154] B. Minceva-Sukarova, J. Molecular Structure 410-411:267 (1997).
[155] W. Nilsen, Phys. Rev. B 182:838 (1969).
[156] L. Price, chem. Matter 11:1792 (1999).
[157] H. Yoo, Thin Solid Films in press (2010).
[158] M. Ishii, Journal of Solid State Chemistry 105:504 (1993).
[159] C. Munce, Colloids and Surfaces A: Physicochem. Eng. Aspects 295:152 (2007).
[160] K. Hönes, Vol. PhD, University of Luxembourg, Luxembourg, 2011.
[161] D. M. Berg, R. Djemour, L. Gütay, S. Siebentritt, P. J. Dale, X. Fontane, V. Izquierdo-Roca, and A. Perez-Rodriguez, submitted to APL (2011).
[162] A.-J. Cheng, M. Manno, A. Khare, C. Leighton, S. A. Campbell, and E. S. Aydil, Journal of Vacuum Science & Technology A 29 (2011).
[163] R. D. Shannon, in Structure and Bonding in Crystals, Vol. Vol II (M. O'Keefe and A. Navrotsky, eds.), Academic Press, 1981, p. 53.
[164] D. M. Berg, A. Redinger, P. J. Dale, and S. Siebentritt, in Patent pending LU 91754, 2010.
[165] H. Katagiri, Materials Research Society Symposium Proceedings 1165:125 (2009).
[166] G. I. Zoppi, I. Forbes, R. W. Miles, P. J. Dale, J. J. Scragg, and L. M. Peter, Progress in Photovoltaics: Research and Applications 17:315 (2009).
[167] NREL, http://www.nrel.gov/science_technology/pdfs/52659.pdf, 2011.
[168] B.-A. Schubert, B. Marsen, S. Cinque, T. Unold, R. Klenk, S. Schorr, and H. W. Schock, Progress in Photovoltaics: Research and Applications 19:93 (2011).
[169] S. Ahmed, K. B. Reuter, O. Gunawan, L. Guo, L. T. Romankiw, and H. Deligianni, Advanced Energy Materials:n/a.
[170] T. K. Todorov and D. B. Mitzi, in PATENT COOPERATION TREATY APPLICATION, 2011.
[171] Q. Guo, G. M. Ford, W. C. Yang, B. C. Walker, E. A. Stach, H. W. Hillhouse, and R. Agrawal, Journal of the American Chemical Society 132:17384 (2010).
[172] F. Hergert and R. Hock, Thin Solid Films 515:5953 (2007).
[173] A. Weber, R. Mainz, T. Unold, S. Schorr, and H. W. Schock, Physica Status Solidi (C) Current Topics in Solid State Physics 6:1245 (2009).
[174] R. Haight, A. Barkhouse, O. Gunawan, B. Shin, M. Copel, M. Hopstaken, and D. B. Mitzi, Applied Physics Letters 98 (2011).
[175] W. N. Shafarman and L. Stolt, in Handbook of Photovoltaic Science and Engineering, John Wiley & Sons, Ltd, 2005, p. 567.
[176] J. Hedström, in 23rd IEEE Photovoltaic Specialist Conference, 1993, p. 364.
[177] T. Nakada, K. Furumi, and A. Kunioka, Trans. Electron Devices 46:2093 (1999).
[178] S. Mehdizadeh, J. Dukovic, P. C. Andricacos, L. T. Romankiw, and H. Y. Cheh, Journal of the Electrochemical Society 137:110 (1990).

[179] P. C. Andricacos, K. G. Berridge, J. O. Dukovic, M. Flotta, J. Ordonez, H. R. Poweleit, J. S. Richter, L. T. Romankiw, O. P. Schick, F. Spera, and K.-H. Wong, in US 5516412.